Synthesis of Solid-state NASICON Electrolytes for Sodium-ion Batteries

Rebecca Griffin BSc. MRes.

Submitted to Swansea University in fulfilment of the requirements for the Degree of Doctor of Philosophy of Materials Engineering

Swansea University

2024

Abstract

This thesis aims to synthesise the sodium super ionic conductor (NASICON) solid-state electrolyte for sodium-ion battery applications using two methodologies: solid-state and sol synthesis. The objective is to develop NASICON with enhanced chemical properties and minimised secondary phases by employing less energy-intensive techniques. This involves transitioning from conventional oven heating to near-infrared (NIR) radiation sintering, achieved through the fabrication of NASICON as a thin film. All samples were characterised by x-ray diffraction (XRD) and scanning electron microscopy (SEM).

NASICON was successfully synthesised using the solid-state technique, forming dense pellets (density: 2.80 g/cm^3) that are 15 mm in diameter and 2 mm thick (±0.05 mm). The final sintering step was conducted in a tube furnace in an inert environment (argon) at 1180 ºC for 16 hours, with the total oven time for the process being 70 hours and only 1.5% weight fraction secondary phase of ZrO_2. Alumina crucibles and a powder bed were used to prevent the pellet fusing to the crucible (Al^{3+} diffusion) and reduce sodium volatilisation.

The sol method also successfully formed a NASICON powder with a low secondary phase content of <2%, aligned with literature values. The powder was prepared in a conventional oven (in air) with reduced sintering times of 3 hours and temperatures of 1000 ºC. Additionally, NASICON was synthesised as a dense 10 µm thin film on a quartz substrate, utilising a sol spray coating technique. The same sintering times were employed as the powder (3 hours) but at lower a lower temperature of 950 ºC. The spray coating technique allowed the film to dry on a hot plate reducing the overall oven heating time from 16 hours (powder) to 3 hours (thin film).

NIR radiation was successfully employed to synthesise NASICON as a thin film, a novel technique that has not previously been used in this field. This significantly reduced sintering times to 60 seconds, and overall oven/NIR heating times to 2 hours 2 minutes.

Declarations and statements

This work has not previously been accepted in substance for any degree and is not being concurrently submitted in candidature for any degree.

Signed..... [redacted] Rebecca Griffin ....

Date.....23/09/24...

This thesis is the result of my own investigations, except where otherwise stated. Other sources are acknowledged by footnotes giving explicit references. A bibliography is appended.

Signed..... [redacted] Rebecca Griffin ....

Date.....23/09/24...

I hereby give consent for my thesis, if accepted, to be available for electronic sharing

Signed..... [redacted] Rebecca Griffin ....

Date.....23/09/24...

The University's ethical procedures have been followed and, where appropriate, that ethical approval has been granted.

Signed..... [redacted] Rebecca Griffin
....

Date.....23/09/24...

Contents

Acknowledgements

Firstly, I would like to express my deepest gratitude to my supervisor, Professor Jenny Baker. Her guidance, support, and wealth of knowledge have been crucial to my successful completion of this PhD. I could not have asked for a better mentor throughout this journey. I would also like to thank my sponsors, Swansea University for the scholarship and M2A for further funding.

I am also extremely thankful to Dr. Rafael Martí Valls, whose expertise in sol-gel chemistry was invaluable for my research, his support has been truly appreciated. I would also like to extend my sincere appreciation to Dr. Tom Dunlop for his guidance with the XRD analysis, and to Professor Serena Margadonna for her work on Rietveld refinement.

Finally, I would like to thank my parents, whose unconditional love and patience has made all of this possible. I am forever grateful for their unwavering support and belief in me.

I would like to dedicate this thesis to the memory of my beloved Grandad (Bill Griffin) and Granny (Patricia Ross), I know they would have been immensely proud of this achievement.

Papers submitted

(1) Comparative Study of Radiative Heating Techniques for Fast Processing of Functional Coatings for Sustainable Energy Applications. Rebecca Griffin, Katherine Hooper, Cecile Charbonneau and Jenny Baker, *Johnson Matthey Technol. Rev.*, 2022, **66**, 32–43. https://doi.org/10.1595/205651322X16260797478755

(2) Process-Structure-Formulation Interactions for Enhanced Sodium Ion Battery Development: A Review. M. Anne Sawhney,[a] Malik Wahid,[b] Santanu Muhkerjee,[a] Rebecca Griffin,[a] Alexander Roberts, Satishchandra Ogalen and Jenny Baker. *ChemPhysChem* 2022, 23, doi.org/10.1002/cphc.202100860

(3) A new approach for obtaining ceramic NASICON ($Na_3Zr_2Si_2PO_{12}$) films sintered *in situ* by a sol–gel method, using spray deposition and near-infra red sintering. Rebecca Griffin, Rafael Marti Valls, Anne Sawhney, Celina Domingos-Dlofo, Tom Dunlop, Sam Reis, Peter J. Holliman and Jenny Baker. ***J. Mater. Chem. A***, 2024, **12**, 31116-31120. https://doi.org/10.1039/D4TA05747C

List of Figures

Definitions and abbreviations

Alumina – Al_2O_3

Conc – concentration

DI water – Deionised Water

DSC-TGA – Differential Scanning Calorimetry Thermogravimetric Analysis

EIS - Electrochemical Impedance Spectroscopy

EDS - Energy dispersive X-ray spectroscopy

GI-XRD – Grazing Incidence X-ray Diffraction

GOF – Goodness of fit

IPA – Isopropanol or Isopropyl alcohol

Li-ion – Lithium-ion

Na-ion – Sodium-ion

NASICON - Sodium (Na) Super Ionic Conductor ($Na_3Zr_2Si_2PO_{12}$)

$Na_2SiO_3.9H_2O$ – Sodium Metasilicate Pentahydrate

$Na_3PO_4.12H_2O$ – Tri-sodium Phosphate Dodecahydrate

$NH_4H_2PO_4$ – Ammonium Dihydrogen Phosphate

NIR – Near-infrared

N_2 – Nitrogen

O_2 – Oxygen

Quartz substrate - fused silica substrate

SEM – Scanning Electron Microscopy

SiO_2 – Silicon Dioxide

SSE – Solid-state Electrolyte

TA – Tartaric Acid ($C_4H_6O_6$)

UV – Ultraviolet

UV-Vis-NIR – Ultraviolet/Visible/Near-infrared Spectroscopy

Vis – Visible

XRD – X-ray Diffraction

ZrO_2 – Zirconium (IV) oxide or Zirconium Dioxide

$ZrO(NO_3)_2.2H_2O$ – Zirconium Dinitrate Oxide Hydrate

$ZrOCl_2.8H_2O$ - Zirconium Dichloride Oxide Hydrate

Chapter 1 – Introduction

The urgency posed by climate change and diminishing fossil fuel reserves has demanded the shift in energy sources to that of renewable. This transition to alternatives such as solar, wind and tidal is critical in mitigating climate change impacts. Legislative 'net zero' initiatives aimed at reducing carbon emissions, primarily through electrification, intend to assist this this transition.[1] However, given the unpredictable nature of renewable sources there is a need for advanced energy storage systems - enabling the integration of renewables into existing energy frameworks.[2,3,4]

The rapid growth in global population has led to a dramatic surge in energy demand, with global energy use increasing by 39% from 2003-2023[5], emphasizing the importance of both renewable energy sources and efficient energy storage systems.[6,7]A landmark decision at the 2023 United Nations Climate Change Conference (COP28) saw nations agree, for the first time, to transition away from fossil fuels. This represents a significant shift from previous summits, explicitly acknowledging fossil fuels as the primary driver of climate change. The conference also highlighted the pivotal role of battery storage as essential infrastructure facilitating the global transition to clean energy sources, reducing carbon emissions in both electricity and electric vehicle sectors.[8]

There is significant energy storage research focusing on developing battery technologies that offer enhanced safety, extended life cycles, and reduced reliance on finite materials. This thesis contributes to this field by investigating a solid-state electrolyte for sodium-ion (Na-ion) batteries.

While substantial literature has focused on lithium-ion (Li-ion) batteries due to their high energy density, the mining practices associated with its extraction pose significant socioeconomic and environmental challenges. Therefore, research also looks at Na-ion batteries, which utilise an abundant material and offer potential for high ionic conductivity. This research focuses on solid-state Na-ion batteries as a next-generation technology, promising high energy density and improved safety. However, this technology must overcome many hurdles (explained in Chapter 2) to become a viable and competitive commercial alternative to current battery technologies.

This research focuses on sodium (Na) super (s) ionic (i) conductor (c) – NASICON, a ceramic oxide solid-state electrolyte widely studied for Na-ion battery applications. Current challenges in NASICON synthesis include secondary phase formations (unwanted compounds forming at elevated temperatures such as ZrO_2), contact interface resistance with electrodes, and optimising sintering temperature/duration. This work aims to address these challenges through two distinct synthesis routes: solid-state and sol synthesis. The research was further advanced by developing the material as a thin film using the sol technique and spray coating; followed by sintering via near-infrared (NIR) radiation. The outcomes of this thesis demonstrate a reduction in secondary phase formations in both solid-state and sol synthesis of NASICON. Furthermore, NASICON was successfully sintered as a thin film using NIR radiation, which is a novel technique in the field.

The structure of this thesis includes an initial literature review explaining the science foundations of the research, followed by a methodology section detailing the synthesis and characterisation techniques applied. The results are presented in four chapters: Solid-state NASICON synthesis, NASICON sol powder synthesis, Sol thin film NASICON synthesis and Sol NIR sintered NASICON, concluding with a final chapter summarising the findings.

Chapter 2 – Literature Review

Research into electrochemical energy storage systems, including batteries, fuel cells, and supercapacitors, has been pursed with improving existing energy storage capacities as one of its primary objectives. This thesis focuses on electrochemical batteries, distinguished by their comparatively higher energy density, established presence in the commercial market, and potential energy storage applications.

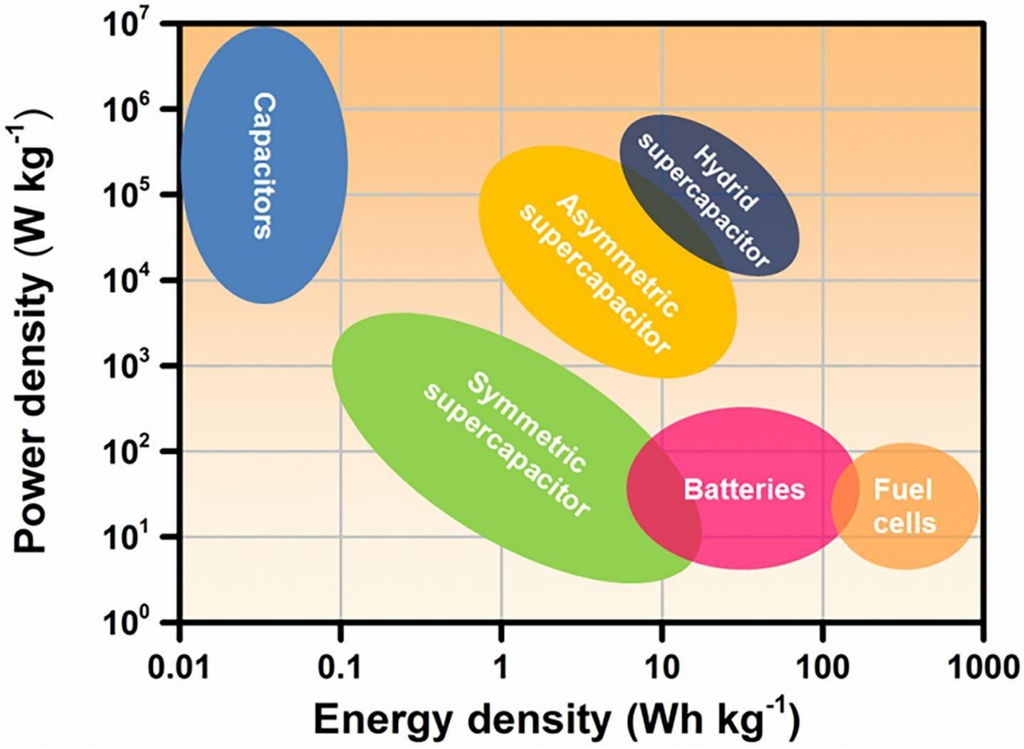

Figure 1: Ragone plot illustrating power density versus energy density for batteries, supercapacitors, capacitors and fuel cells. Reprinted from Liu et al. [9]

Figure 1 compares the energy density across various energy storage technologies, indicating that batteries demonstrate the second highest energy density. This energy-to-power density ratio enables batteries to store substantial energy while maintaining adequate discharge rates for sustained periods, positioning them as suitable long-term energy storage solutions. In contrast, supercapacitors exhibit lower energy density but higher power density, making them more ideal for applications requiring shorter charge/discharge cycles. Notably fuel cells also have an alternative application. Unlike batteries and supercapacitors, fuel cells primarily serve as an alternative to combustion-based technologies, requiring a continuous fuel input (e.g. H_2). This distinction in performance characteristics proves the importance of aligning storage technologies to specific application requirements; it is suggested that all technologies will be required to prevent the energy crisis.[10] However, it is important to note that technology selection must be based on multiple factors beyond energy density alone: including cycle life, efficiency, cost, and environmental impact.[9]

Electrochemical batteries store and convert chemical energy into electrical energy. They consist of two electrodes made of different materials, the anode (e.g. hard carbons) and cathode (e.g. transition metal oxide). Electrodes are typically composed of three materials: active materials (ion storage), conductive carbon which (transports electrons to current collector) and a binder (adhesive); which are deposited on a current collector which ensures electron transfer to the external circuit. The cathode serves as the positive terminal, while the anode is the negative terminal, with an electrolyte facilitating ion movement between the two. When connected to an external circuit, ions migrate through the electrolyte, while electrons flow through the external circuit, generating an electric current.

A battery cycle is one full discharge (from 100% to 0%), and the cycle life is the number of times a battery can be charged and discharged before losing some/certain performance (previously defined) - Figure 2. The typical operation of an electrochemical battery relies on a redox (oxidation-reduction) reaction, wherein both processes occur simultaneously. During battery discharge, the anode material undergoes oxidation, resulting in the removal of electrons. These electrons are transferred through the external circuit and integrated into the cathode material via a reduction reaction. Simultaneously, ions migrate from the anode towards the cathode through the electrolyte, facilitating the flow of current and completing the electrochemical circuit. During the charging phase, this process is reversed: the anode undergoes a reduction reaction while the cathode undergoes oxidation, and ions migrate from the cathode towards the anode.

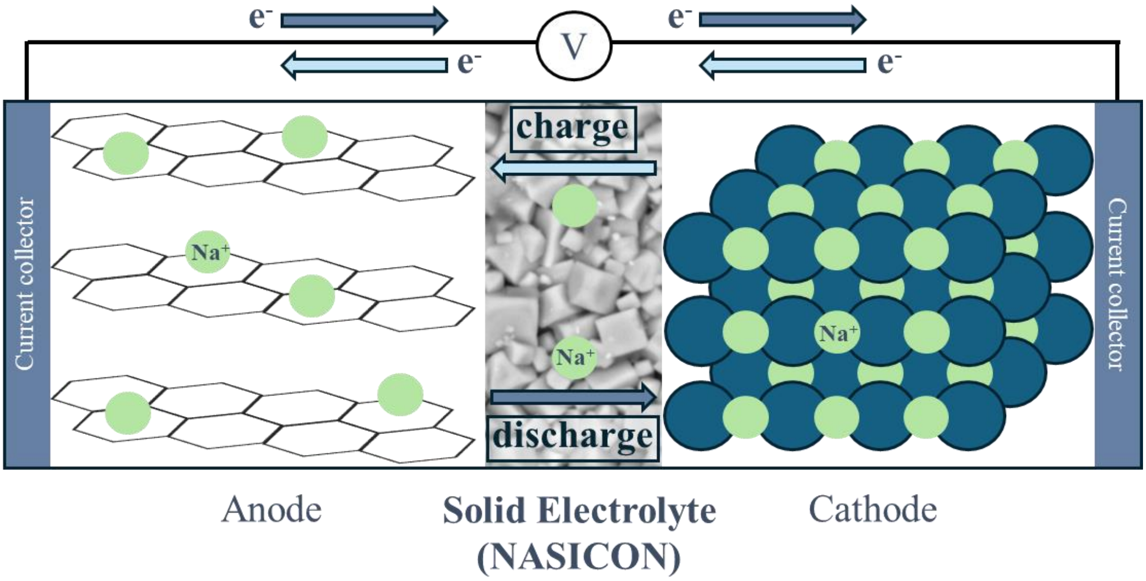

Figure 2: Schematic of Na-ion solid state battery during charge and discharge.[11]

2.1 Current battery technologies

Current battery technologies predominantly utilise liquid electrolytes due to their high ionic conductivity, excellent contact area with electrodes and relative affordability. However, a major disadvantage to this technology is its poor thermal and chemical stability, with the electrolytes being highly volatile and flammable.

The two liquid electrolyte batteries commercially used are lead-acid and lithium-ion batteries. Developed by the French physician Gaston Planté in 1860, lead acid batteries were created first.[12] Although they do not perform as well as newer battery technologies, they remain a prevalent commercial option available in many applications. Lithium-ion batteries are preferred over lead-acid due to their increased cycle life, reduced charging times and greater usable capacity. Yet, the extraction of lithium and other materials essential for lithium-ion batteries rely on scarce natural resources and often involves unethical mining practices, raising significant environmental and societal concerns. This illustrates the importance of exploring various materials and chemical compositions in battery research.[13,14,15]

The necessity for energy storage solutions has increased the development of sodium-ion liquid batteries. This technology offers potential advantages over Li-ion counterparts due to low cost (Na-ion battery cost have fallen by 97% since 1991)[16,17,18] and promising cycle performance (capacity retention (0°C, 200 cycles): Na-Ion battery 52% and Li-ion battery 29%[19]). An advantage of Na-Ion technology is its compatibility with existing Li-ion production methods, allowing for rapid scalability. Furthermore, sodium's (Na) abundance and availability in salt form (which reduces extraction costs) offers significant advantages for Na-ion battery technology, improving long term materials selection and reducing costs. [20,21,22,23] Material substitutions inherent to Na-ion batteries, such as replacing copper with aluminium, and lithium with sodium, creates a 4.5% cost reduction.[21]

Na's chemical properties make it a favorable candidate for battery technology due to its classification as a Group 1 alkali metal, similar to Li. Its single valence electron facilitates the formation of +1 cations which is a suitable redox potential for ion conduction. While

Na exhibits higher reactivity than Li, its larger atomic radius reduces ion mobility comparatively. Other physicochemical differences include coordination preferences in compounds and desolvation energies.[13]

Due to these chemical differences Na-ion technology is applied in different sectors to Li-ion: including stationary energy storage and low-cost vehicles. Na-ion batteries have been commercialised by several companies such as Faradion[21] and Tiamat[21,24], nonetheless further research into underlying physical and chemical processes is needed in this technology to compete with Li-ion equivalents.

In a sodium-ion battery, the cathode is composed of a material that can accommodate sodium, the anode is typically made of carbon and the liquid electrolyte contains sodium ions - used to carry and store energy. Liquid electrolytes are expected to continue to be used commercially as they provide a lower cost and improved sustainability; however, they are inherently flammable, toxic and volatile, raising safety concerns.[13,25,26]

2.2 Solid-state Na-ion Electrolytes

Solid-state batteries represent the next generation of energy storage systems, offering significant advantages over tradition liquid electrolyte batteries. They have improved safety with thermal stabilities of approximately 200°C compared to liquid electrolytes that cannot exceed 70°C.[27] As well as a longer theoretical lifetime, with research aiming for a 10-year lifetime with 1000 cycles.[27,28,29] As an example, they have the potential to decrease the charging time, increase mileage and address safety concerns for electric vehicles. Delivering such performance requires a solid electrolyte that can efficiently transport ions and have chemical passivity. Li-ion battery manufacturing techniques are the foundation of the majority of Na-ion work; however, Na solid-state electrolytes (SSEs) were studied before Li-ion SSEs.[30]

2.2.1 Types of SSE’s

SSEs for Na- and Li-ion batteries include: inorganic solid electrolytes (ISE), solid polymer electrolytes (SPE) and composite polymer electrolytes (CPE) (Table 1).[31]

SPE’s are typically composed of a polymer matrix, sodium salt and organic solvent.[20] These materials exhibit characteristics such as flexible mechanical properties and ease of processing, which enables good interface contact with the electrodes.[32,31] Due to these properties, SPE’s are particularly well-suited for applications in portable and wearable devices.[20] Common examples of polymers used in SPE’s include poly-ethylene oxide (PEO)[33] and poly (vinylidene fluoride) (PVDF)[34].[20,31] While SPE’s demonstrate numerous advantageous characteristics, particularly with regard to contact resistance, it is important to note that they exhibit lower room temperature ionic conductivity compared to ISEs.[35,20]

CPE’s can consist of ceramic particles uniformly dispersed in a polymer matrix, which effectively incorporates active or inactive fillers into SPEs.[31,20] This design aims to combine the advantage of ISEs (high ionic conductivity) and SPEs (low contact resistance) while mitigating the shortcomings of both materials.[31,36,37] CPEs are utilised to enhance safety, achieve high ionic conductivity, and ensure flexible mechanical properties through a multiple-path ion conduction mechanism.[36,37,20] The addition of ceramic particles can increase the amorphous regions in polymers, thereby promoting ion conductivity.[31] While the overall performance of CPEs is higher than SPEs, the room-temperature ionic conductivity is lower than commercial requirements.[20]

ISEs demonstrate superior ionic conductivity and high Na^+ transference numbers in comparison to SPEs and CPEs.[20] The category of inorganic electrolytes encompasses several structural types including: garnet-type, perovskite-type, and sodium superionic conductors materials.[38,26]

This thesis focuses on ceramic oxide-based SSE’s, specifically sodium superionic conductors.

Table 1: Summarising the nature of ISEs, SPEs and CPEs.

	ISEs	SPEs	CPEs
Typical Material	Garnet-type	*Polymer matrix, sodium salt and organic solvent*	*Particles dispersed in a polymer matrix*
	Perovskite-type	PEO	Oxide/ceramic-polymer based
	Superionic conductors	PVDF	
Strengths	Superior ionic conductivity	Low contact resistance	Improved ionic conductivity
Limitations	High contact resistance	Room temp conductivity lower than ISEs and commercial values	

Recent advancements have demonstrated that Na ceramic solid electrolytes now possess the potential to deliver sufficient ionic conductivity for solid-state batteries.[37,13] Currently some scientific research attention is directed towards garnet-type structures, due to the crystal structure being favourable for experimentation with novel chemistries (e.g. cation dopants) to enhance ionic conductivity in SSE's.[39,40,41,42,13] Research by Thangadurai et al.[43] demonstrated that Ba-doped $Li_6BaLa_2Ta_2O_{12}$ achieves a total ionic conductivity of 4.0×10^{-5} Scm^{-1} (22°C), performing at levels similar to other efficient lithium ion conductors ($x10^{-5}$ Scm^{-1} range).[44] NASICON-type oxide SIEs, which are the focus of this work, are also hugely researched. This superionic conductor shows remarkable advantages including: small grain boundary resistance, high mechanical strength, ease of synthesis, excellent thermal, chemical and electrochemical stability, high room temperature ionic conductivity and good electrochemical/chemical compatibility with common electrodes.[35,20]

However, a significant barrier to the commercial adoption of oxide-based materials is the need for further improvement in ionic conductivity and manufacturing. Additional challenges of ISE's also include high interfacial resistance and dendrite formation; the advantages and challenges of ISEs will be discussed in detail later in this chapter. [35,20,13]

The ionic conductivity of ISE's is dependent on variables associated with the materials ion-transport mechanisms, this includes: [35,31]

1. Carrier type: chemistry defects determine the type and concentration of carriers.
2. Diffusion pathway: the migration path of the ions in the crystal structure.
3. Diffusion type: the diffusion of ions which can occur through three primary mechanisms: interstitial direct hopping, interstitial knock-off and vacancy direct hopping (Figure 3). In practise, the predominant mode of ion diffusion is typically a combination of these mechanisms.

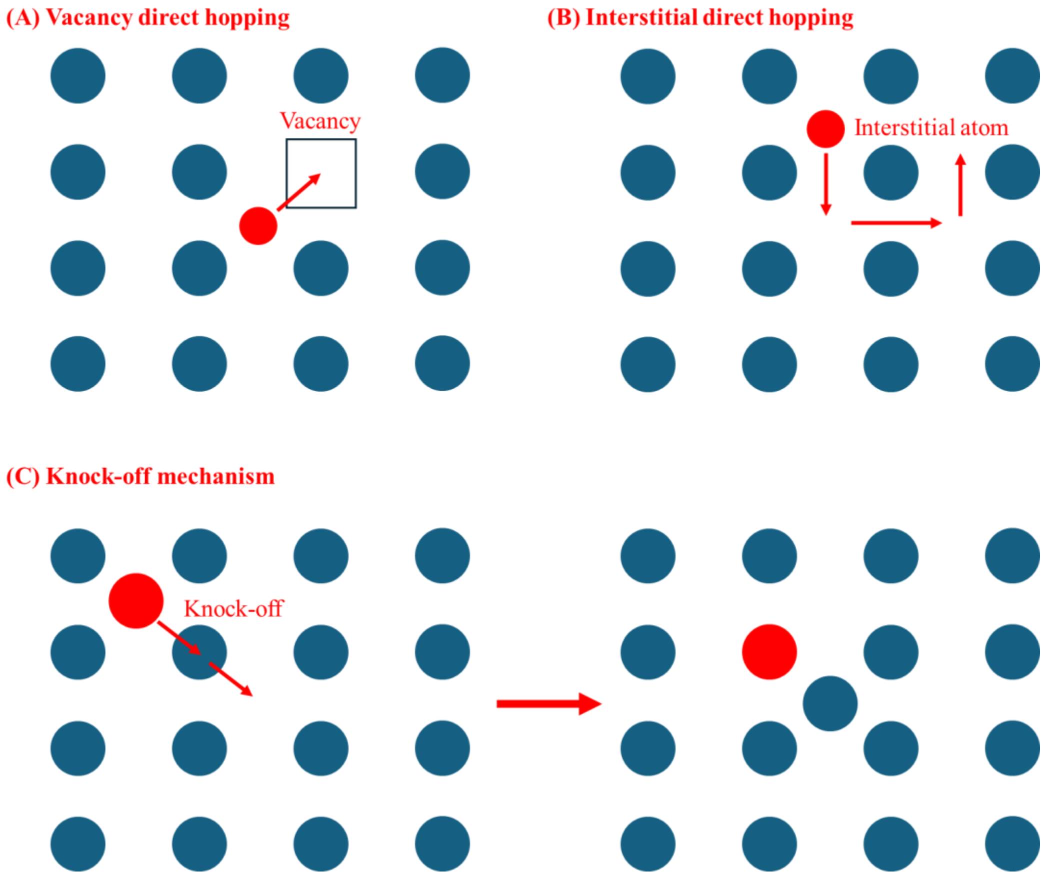

Figure 3: Ion diffusion mechanisms: (A) Vacancy direct hopping (B) interstitial direct hopping (C) Knock-off mechanism.[45]

Abbas et al.[46] explained the activation energies involved in the ion conduction mechanism, where the ions are transferred through bottleneck points of the crystal structure which act as energy barriers. Consequently, there is an inverse relationship between the energy barrier and the ionic conductivity. The literature also identified that the number of vacancies, lattice site occupation and interstitial ion presence also influence ionic conductivity.[46]

2.2.2 Advantages and challenges of SSE’s

This next generation of batteries demonstrate numerous advantageous characteristics, as outlined in Table 2. Among these, the most notable are high thermal stability, high chemical stability, high energy density and the potential for high ionic conductivity.[26,35] Solid-state batteries, particularly Na-ion batteries, have the theoretical potential to achieve high capacity and voltage.[47,20] SSEs can also have enhanced chemical stability and mechanical strength, which in turn can suppress the formation of Na dendrites. This mechanical stability can reduce short circuits and capacity fading.[31,35]

Table 2: Defines the advantages and challenges of SSE's.[35,20,48]

Advantages of SSE’s	Challenges of SSE’s
High energy density	Interfacial resistance
High thermal stability (Less flammable and non-volatile)	Grain boundary resistance
Longer life cycle and fast charging	Mechanical stresses - cracking
High theoretical ionic conductivity (room temperature)	Low practical ionic conductivity (technology in infancy)
High chemical stability	Manufacturing
High electrochemical stability	
Reduce capacity fading and internal short circuits	

Scientific barriers and key research priorities for solid-state batteries include electrode-electrolyte interfaces. Enhancing the anode-electrolyte and cathode-electrolyte interfaces is an active area of research and aimed at improving battery performance and stability. The synthesis and discovery of new solid electrolytes with optimised properties represents another major area of research.

A comprehensive review of literature indicates several requirements that a material must satisfy to be considered a viable SSE:[49,50,51,2520,31,26]

1. High ionic conductivity at room temperature
2. Low electronic conductivity
3. Large electrochemical window
4. Good mechanical properties
5. Excellent thermal, chemical and air stability

6. Compatibility at interfaces with electrodes
7. Environmental friendliness and nontoxic
8. Ease of synthesis, processing and recyclability

At present, solid-state Na-ion batteries have lower current density and ionic conductivity (at room temperature) than required for commercial viability.[52,53,31] These limitations stem from several interconnected challenges, the most important of which includes poor interface contact, cracking/stress and dendrite formation.[35] The subsequent sections will elaborate on these issues.

2.2.2.1 Interface Contact problems, cracking and dendrite formation

The major barriers to viable solid-state batteries arise because of chemical, electrochemical and mechanical problems at the electrode/electrolyte interfaces, causing poor contact and high interfacial resistance.[53] This interface influences the energy storage capacity, cycle stability and charge transfer rate.[54,31,13,20]

Solid-state batteries are particularly susceptible to mechanical stresses and interfacial resistance due to the more rigid contact (no fluidity) between the electrodes and electrolyte, resulting in a poor solid-solid contact.[35] These stresses can lead to capacity fading through mechanical failure at the interface, resulting in active-material loss.[55,37,20,35]

During the charge and discharge of a solid-state battery the movement of ions causes volumetric changes, initiating internal stresses in the material. This can lead to crack formation, contact problems and interfacial resistance at the electrolyte/electrode interface.[31,35,20]

Additionally, chemical side reactions at the interfaces can create new compounds, forming a solid-electrolyte interface layer (SEI). The SEI, often composed of insulating side-reaction products, can cause swelling, develop cracks and significantly increase the interfacial resistance.[35,20]

One of the primary modes of mechanical failure in solid-state batteries is dendrite growth at the interface, which significantly limits critical current density.[56,37,55] Dendrites are needle-like structures that can bridge interfaces, create cracks and interfacial voids. Voids and grain boundaries on solid-electrolyte surfaces are particularly vulnerable to high local current density, promoting dendrites and ultimately causing short circuits.[35,20]

Another challenge in solid-state battery interfaces is the compatibility between the solid-electrolyte and electrode active materials. Incompatibility can result in non-uniform interfacial current distribution, unstable anode interfaces and the promotion of dendrite growth. These issues collectively contribute to large interfacial resistances.[20,35]

Reducing interfacial resistance is critical for minimising ohmic losses in solid-state batteries, therefore there is a pressing need to develop interfaces that exhibit low interfacial resistance but maintain electrochemical stability and high ionic conductivity.[37]

An obvious way to improve interfacial contact is by applying an external pressure or increasing the operating temperature of the battery. However, ensuring constant and equal pressure on the battery is not practical in application; and high temperatures are not desirable/safe commercially.[20] There are several attempts currently in literature to reduce this interfacial resistance, such as ion doing[20], interlayers[55,37,20], regulating surface chemistry[20] and co-sintering in-situ[31].

The main strategy currently researched is the use of interlayers, stopping contact between the solid electrolyte and metal. The material selected for the layer should also improve the wettability towards the electrode surface, as well enhance the chemical and mechanical compatibility/stability of the interface. The interlayer can be deposited between the electrode and electrolyte by a number of methods such as evaporation, sputtering and pulsed laser deposition.[53,55,37]

An example of this is Wang et al.'s[57] work, which used a solid polymer electrolyte (poly(propylene carbonate)-based) as an interlayer in combination with a $Li_{1.5}Al_{0.5}Ge_{1.5}(PO_4)_3$ solid electrolyte for a Li-ion battery. This successfully decreased the interfacial resistance from 3.2×10^4 to 543 Ωcm^2 by reducing the reaction of the electrolyte with the metal electrode.

Another method used to improve contact without an interlayer was carried out by Kehne et al.[58]. They prepared a Na_xCoO_2/NASICON/Na thin film Na-ion battery. This was done by depositing (via pulsed laser deposition) a thin film of Na_xCoO_2 onto a pellet of previously sintered NASICON and attaching a Na metal foil anode. The impedance measurements revealed chemically and microstructurally stable interfaces over 100 cycles, proving this method to be successful.

One method adopted to reduce the problems surrounding interfacial contact is co-sintering in-situ. This method involves sintering the solid-state electrolyte on-top of the electrodes, creating a more intimate contact and reduce interfacial resistance.[31]

One example is Geng et al.[59] successfully in-situ polymerised a 1,3-dioxolane electrolyte at room temperature for 24 hours. However, this involved polymerisation and not sintering, there is no current literature on in-situ sintering of electrolyte by direct deposition approach. This area of work is still in its infancy and shows in a gap in the research that this thesis investigates.

Challenges encountered in this method include the reaction of the electrode and electrolyte particles, void spaces and the formation of undesired phases at elevated temperatures. Therefore, long exposure times at elevated temperatures is unfavourable for this method, this thesis looks to use NIR radiation to avoid this issue.[31]

2.3 NASICON

“before the creation of Li-ion batteries, Goodenough et al. (1976) synthesised a Na super-ionic conductor (NASICON).[30] The common formula of NASICON is $Na_{1+x}Zr_2P_{3-x}Si_xO_{12}$, an inorganic ceramic with a crystal 3D framework which enables high ionic conductivity.

NASICON is widely reported in literature, however, it has several issues that reduce its ionic conductivity: secondary phase formations, charge transfer resistance/interface issues and difficulties in manufacturing. Microstructure (electrolyte porosity and grain size) is shown to impact the electrolytes performance/conductivity and is affected by preparation/synthesis methods.

NASICON is synthesised by two main routes: solid-state reaction and sol-gel synthesis.[60] There are numerous manufacturing processes that affect the outcome of the solid-state reaction, which are related to the size and break-up of the particles, subsequent mixing and the formation of pellets which can be sintered, where time and temperature will differ dependent on article size and pellet geometry.[61]

Sol-gel is a more complex technique compared to solid-state reactions, however both techniques require refining as they do not commonly produce monoclinic phases.[62] As an example, the stoichiometry of NASICON is often modified to alter the electrochemical performance of the electrolyte. Park et al.[63] used an excess of sodium by increasing the ratio of the sodium precursor, which in turn changed the stoichiometry of NASICON. Characterisation indicated an alteration in the grain structure of the electrolyte and an improvement in the total ionic conductivity.[63] Alternatively, the chemical precursors for both solid state and sol-gel synthesis are often substituted to achieve the same effect. Rao&Patro[64] created an excess of Na, by testing two different Na precursors, Na_2CO_3 and Na_3PO_4 both of which also increased ionic conductivity compared to its standard stoichiometric equivalents.

Another example is the variation of deposition methods for sol-gel synthesis. Shimizu&Ushijima[64] successfully used spin coating to make thin film gels, in contrast to Martucci et al.[65] who developed multilayer films via dip coating. Sintering parameters and methods are also variable; demonstrated by Narayanan et al.[66] who explored the trade-off between sintering durations and temperatures. The work suggested that the sintering parameters are a factor in determining the conductivity and density of NASICON, as temperature can influence the volatisation of components.[66]

There are several attempts at synthesising the Li equivalent of NASICON, the first attempt was reported by Hong[67] called, LISICON. The structure has a similar framework, $LiZr_2(PO_4)_3$ however the electrolyte had a lower ionic conductivity than the Na equivalent.[68] Substituting Zr with other cations (e. g. Ge, Ti, Hf) can increase conductivity values, and therefore various variations on this structure have been reported since; for example, LATP, and LAGP.

Across most solid-state electrolyte manufacturing for both NASICON and other types, two main mixing methods have been recognised: mortar and ball milling, both further including wet and dry methods. For example, Deng et al.[69] ball milled dry electrolyte precursors into a powder in one step before pressing into a pellet, while Lan et al.[70] ball milled precursor powder in ethanol as only one of multiple wet steps. The latter design aimed to optimise the cathode/electrolyte interface, since interfacial resistance between the solid electrolyte and cathode is a known performance limitation of SSE Na-ion batteries.[70]

Though promising for next-generation energy storage technology, solid-state batteries are currently limited by insufficient electronic and ionic efficiency. Additionally, mechanically dynamic solid electrolyte/electrode interfaces present unique challenges for design of viable solid-state cells.[71] The particle size, porosity, and thickness of the electrode films also have influence on the overall performance, as explained in the following section.”

– lines are taken from the wording written by the Rebecca Griffin which has also been published within the following article: Process-Structure-Formulation Interactions for Enhanced Sodium Ion Battery Development: A Review. M. Anne Sawhney, Malik Wahid, Santanu Muhkerjee, Rebecca Griffin, Alexander Roberts, Satishchandra Ogale, and Jenny Baker. [72]

2.3.1 Structure

NASICON is characterised by the general formula of AMM'P_3O_{12}. In this thesis, A is the alkali ion Na^+, M/M' sites are the transition metal ion Zr^{4+} and P is partially substituted by Si; resulting in the NASICON composition $Na_{1+x}Zr_2Si_xP_{3-x}O_{12}$ ($0 \leq x \leq 3$). NASICON's crystal structure varies depending on its composition, commonly adopting rhombohedral, monoclinic, triclinic and orthorhombic structures. This thesis focuses on $Na_3Zr_2Si_2PO_{12}$ (Hong-type NASICON)[73,74], which typically exhibits rhombohedral symmetry (space group R3c) except in the intervals $1.8 < x < 2.2$; in these intervals there is a distortion to monoclinic symmetry.[75,76] This formula was selected due its generally higher conductivity than equivalent Na NASICON structures.[77,78,79]

The structure comprises a framework of SiO_4 and PO_4 tetrahedra corners, shared with ZrO_6 octahedra (Figure 4).[80] Conduction pathways within this 3D framework encapsulate the mobile Na^+ ions.[78] The NASICON structure is stabilised by electrons donated by the Na^+, which partially occupy this interstitial space.[81] Na^+ ions can occupy two interstitial sites in a rhombohedral structure, while the monoclinic structure allows for the occupation of three sites, modifying the ion conduction pathways and speed of ion transfer.[82,78,79]

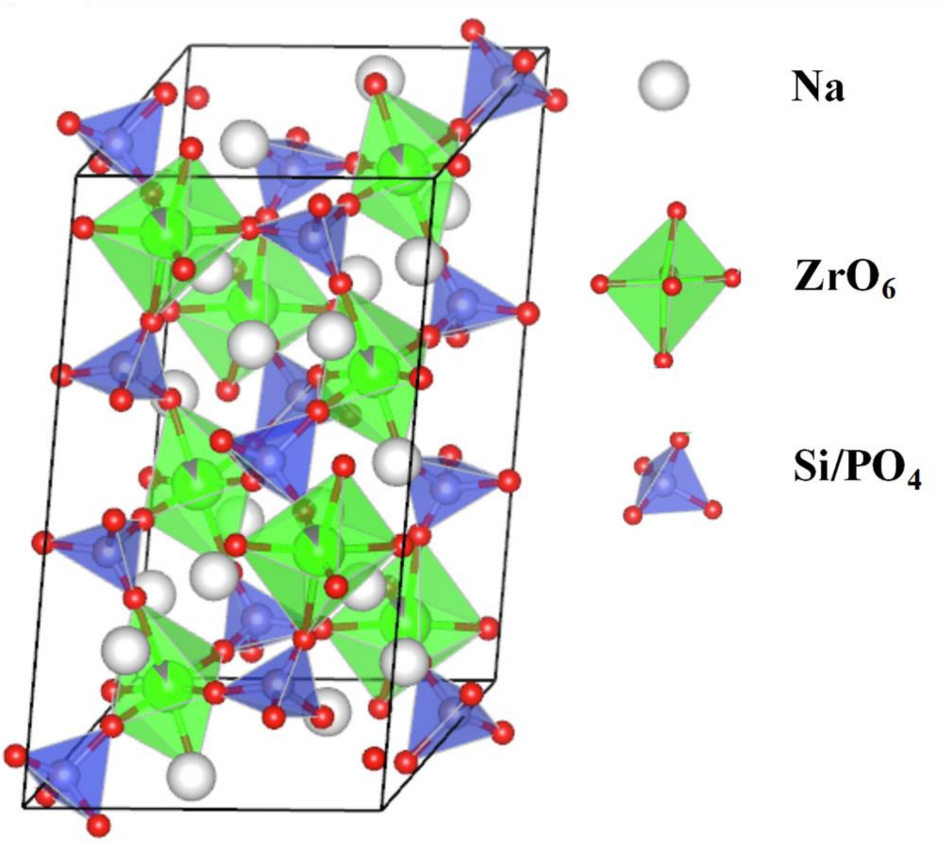

Figure 4: Diagram of NASICON crystal structure. Na^+*,* ZrO_6 *(octahedra) and* Si/PO_4 *(tetrahedra) units labelled. Reprinted from Liang et al.*[83]

Ionic conduction occurs through Na^+ migration in NASICON[37,84] and thermodynamic investigations reveal the preferential occupation of certain Na sites (coordination environment e.g. Na(1) or Na(2)), which influences the stability of the NASICON ground state. Moreover, there is an observed tendency for the rhombohedral structure to transform into the stable (ordered) monoclinic NASICON. Ongoing research by Amores et al.[85] investigates the ion mobility of a new Na-rich double perovskite structure ($Na_{1.5}La_{1.5}TeO_6$) at different temperatures using impedance characterisation. The researchers apply an innovative technique that successfully reduces the activation energy. Their findings demonstrate a significant decrease in activation energy compared to the analogous $Li_{1.5}La_{1.5}WO_6$ double perovskite material: from 0.50(5) eV to just 0.27(2) eV for $Na_{1.5}La_{1.5}TeO_6$, lowering the energy barrier for Na+ diffusion.[85,86]

NASICON demonstrates several favourable properties for application as a Na-ion SSE, including high room temperature ionic conductivity, high energy densities, and notable thermal and chemical stabilities. The extensive research history of NASICON materials provides a robust foundation and Na’s abundancy makes it a good demonstrator material for new techniques.

However, its ionic conductivity still requires further improvement to meet commercial viability standards. A significant challenge in the research lies in obtaining NASICON without glassy and secondary phases.[87]

Secondary phase formation (specifically zirconia) at grain boundaries has been identified as a significant factor in the reduction of ionic conductivity in NASICON materials.[88,89] These impurities act as barriers to ion transport, reducing the overall conductivity of the material. Consequently, minimising the extent of any secondary phases is a proposed strategy for enhancing ionic conductivity.[79]

Therefore, research involving different synthetic routes have been undertaken to improve NASICON chemistry and therefore enhance its ionic conductivity.[37] Common synthetic methods researched include conventional solid-state, spark plasma sintering (SPS), sol-gel and coprecipitation synthesis (Table 3).

Table 3: Illustrating the pros and cons of common current NASICON synthesis methods.[90]

Current synthesis methods	Advantage	Disadvantage	ref
Conventional	Simple chemistry	High sintering temperature	74, 91, 92
		Long sintering time	
		Large particle size	
		Inhomogeneity	
Spark plasma sintering (SPS)	Reduced sintering temperatures	Complex equipment	93, 94, 95
	Fast sintering		
	High relative density		
Sol-gel	Molecular mixing of precursors prior to hydrolysis	Complex chemistry	80, 96, 97, 75
	Good homogeneity	Sensitive reactions	
	Low sintering temperatures		
Coprecipitation	Chemical homogeneity	Careful control of solution parameter	98
	Nano-powder	Post washing and drying procedures	
	Molecular mixing		

Rao et al.[99] conducted a comparative study of NASICON synthesis using both solid-state and sol-gel synthesis methods. The work revealed differences in the microstructure, conductivity and chemistry of NASICON; specifically showing better homogeneity for sol-gel prepared NASICON, but higher ionic conductivity for solid-state NASICON (total conductivity isn’t 6.6 x 10^{-4} Scm^{-1}) due to its higher crystallinity. This indicates the importance of synthesis technique selection in tailoring NASICON properties for specific applications. The work also illustrated other important variables including stoichiometry and sintering temperatures on NASICON crystallinity and secondary phases; where a Na-excess increased ionic conductivity through a predominantly monoclinic NASICON phase.[99]

A substantial amount of research has been undertaken on the use of excess Na in NASICON synthesis; to balance the negative charge of the structure, as well as compensate for Na volatisation during sintering. Park et al.[100] showed excess Na increased bottleneck size in the bulk of the material, which in turn increased Na^+ ion mobility (not Na^+ concentration) and therefore increased the ionic conductivity of the NASICON. He et al.[101] also confirmed that increasing the grain size of NASICON and the associated reduction in grain boundary causes an increase in ionic conductivity.

2.3.3 Solid state synthesis

Solid-state synthesis is a multistep, labour-intensive method, that involves several heating and ball milling steps (Figure 5).

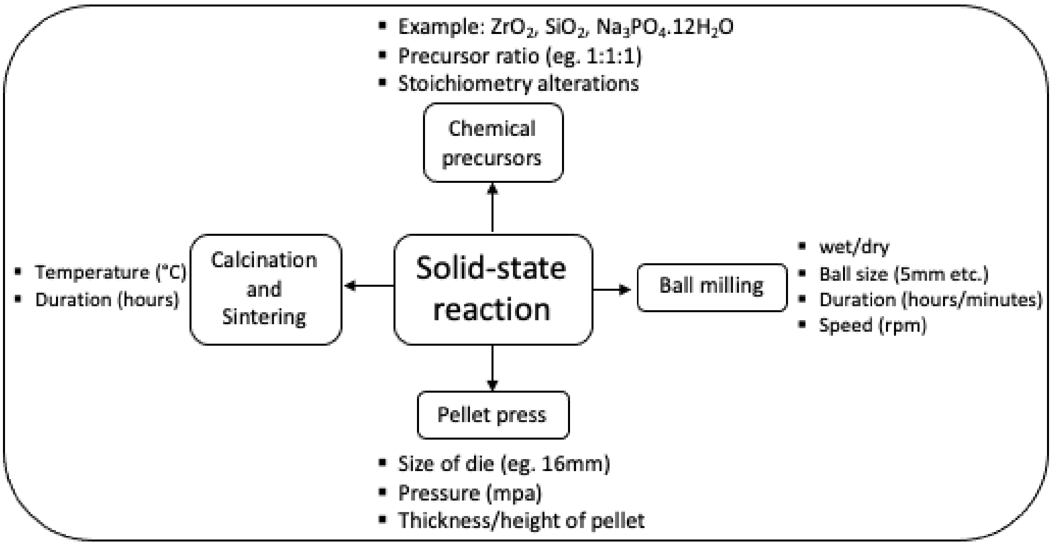

Figure 5: Depicting the variables involved in solid-state NASICON synthesis.

2.3.3.1 Ball milling

Ball milling is a widely employed technique in solid-state NASICON synthesis, used to mix the precursor materials and modify the powder morphology, resulting in smaller and more uniform particles. This reduction in particle size facilitates the formation of smaller grains, which in turn creates shorter ion and electron diffusion pathways.[102] Such microstructure modifications are favourable as they can improve the electrolytes ionic conductivity.

Lee et al.[61] observed that extended ball milling or jet milling post-calcination lead to decreased particle sizes, correlating with improved conductivity.[79] This finding underscores the importance of particle size control in optimising NASICON performance.

There is little literature on the influence of ball milling on the chemistry of NASICON. However, Chong et al.[103] conducted a systematic study into the effects of ball milling duration on NASICON synthesis, investigating periods of 5, 12, 24 and 36 hours at a fixed speed of 350 rpm. The experiment indicated that ball milling for 24 hours was optimal, yielding monoclinic NASICON crystals without lattice distortion and with minimal secondary phase formation. Additionally they observed that density increased with milling time up to the 24-hour mark.[103]

However, it is noteworthy that many studies in literature fail to report the high percentage yield loss associated with the ball milling process. Furthermore, the prevalent use of hand grinding steps in many protocols is a potential source of variation in samples, which may impact reproducibility and scalability of NASICON synthesis.

2.3.3.2 Pellet press

Solid-state synthesis of NASICON is almost exclusively prepared by isostatic cold pressing[104], with the applied pressure usually in the range of 250-370MPa[79,63,75]. However, there are several issues to consider when pellet pressing which are rarely documented in literature: including the material binding to the walls of the die, cracking and crumbling. Solutions to consider, depending on the application of the material, include: the slow release of pressure during pressing, different binder/material selection, use of a lubricant and reducing the particle sizes used.

Hot pressing is often mentioned in NASICON literature; however, it is actually a sintering technique. The method is used to reduce the glassy phase along NASICON grain boundaries and increase material density,[60] therefore reducing grain boundary resistance. The applied pressure causes the glassy phases to flow to outside surfaces, reducing the glassy phase and in turn increasing the ionic conductivity of the material. Kimura et al.[105] successfully used this technique to synthesise $Na_3Zr_2Si_2PO_{12}$ at 1250 ºC.[105]

2.3.3.3 Sintering

The sintering process during NASICON synthesis involves the densification of metal oxide powder particles at sub-melting point temperatures (Figure 6).[106,107,108] Wen et al.[109] demonstrated through XRD analysis of pre- and post-sintered NASICON samples that the crystalline phase formation occurs during the sintering step. The final sintering stage significantly influences the density, phase purity, microstructure and crystallinity of the NASICON material.[62]

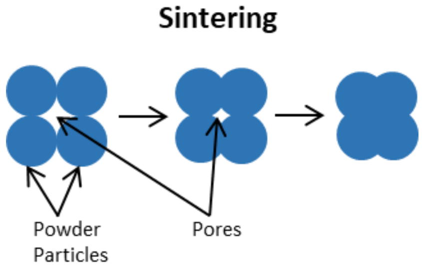

Figure 6: Schematic of the powder particle sintering process at elevated temperatures. Adapted from Griffin et al. [106]

The primary sintering parameters comprise of the temperature employed and duration of exposure to sintering temperatures. Extensive literature has examined the effects of sintering parameters, specifically how the isothermal hold duration and temperature effects the ionic conductivity and the chemistry of NASICON type materials. Wen at al.[109] investigated both parameters experimentally. XRD and IR analysis showed that the crystal structure and chemical bonding of the NASICON, did not change with sintering temperature or time. However, material density and consequently ionic conductivity were significantly influenced by these parameters. Work revealed that the densification of the NASICON sample increased up to 1200 ºC, beyond which the density decreased. Wen suggested this is due to grains fusion into a liquid phase. The isothermal hold duration also proved critical to density. Insufficient dwell times lead to incomplete reactions; whilst extended sintering times (over 15 hours) caused grain expansion and a decrease in density. An ionic conductivity of 7.82×10^{-4} Scm^{-1} (at room temperature) was observed in the ceramic electrolytes sintered at 1200°C for 15 hours.[109]

Fuentes et al.[110] corroborated these findings, confirming the impact of sintering conditions on NASICON microstructure. The research demonstrated an increase in temperature and dwell time enhanced ionic conductivity up to a threshold, beyond which the electrical performance decreased due to liquid phase formation along the grain boundaries.[79,87]

Similarly, Narayanan et al.[66] also demonstrated the need to optimise NASICON sintering parameters and found the optimum temperature to be 1100 ºC for 12 hours, giving a conductivity of 1.13×10^{-3} Scm^{-1} (at room temperature).[87]

Other literature studies suggest that excessive sintering temperatures may promote the formation of secondary phases, specifically ZrO_2, attributed to thermal decomposition and the segregation of zirconia at the grain boundaries.[88,89,79] Furthermore, extreme sintering conditions can potentially lead to volatisation of Na and P, alteration of Si / P arrangement, secondary recrystallisation of NASICON and reformation of secondary phases – leading to a decrease in conductivity.[87,109]

In summation, optimising sintering temperature and duration is critical for achieving high density NASICON with superior conductivities and reduced secondary phase formation.[79,13]

2.3.3.4 Crucibles

A range of different crucibles employed in NASICON synthesis, though often not well reported in experimental methods sections. Among the reported crucibles, alumina (Al_2O_3) is the most frequently utilised crucible.

A significant challenge encountered during the high temperature sintering of NASICON materials is the tendency of the pellet to fuse to the alumina crucible. The fusion of the pellets to the crucibles represents a critical issue in the fabrication process, potentially affecting the purity, structure, and application of the final product, underscoring the importance of crucible selection. The hypothesised reason for the pellet fusing to the crucible may be due to a chemical reaction between the alumina crucible and the NASICON material at these high temperatures.

Kwatek et al.[111] proposed that the mechanism involves the movement of alumina ions (Al^{3+}) from the crucible into the NASICON pellet during sintering, where the Al^{3+} ions diffuse into the grains. A specific reaction mechanism was suggested by Sutton et al.[112] involved the oxidation of elements at the NASICON-crucible interface; where Zr reduces Al_2O_3 to form a ZrO_2 surface layer on the grains of the crucible oxides. In turn, a network of Al_2O_3 forms and propagates from the ZrO_2 base into the NASICON.[112]

An alternative mechanism proposed in literature involves the formation of NASICON eutectic liquids[113] due to decomposition at elevated temperatures, which promotes the breakdown of the alumina oxide crucible.[114] In Al_2O_3-ZrO_3 eutectic compositions, devitrification (change of state from glassy to crystalline) occurs with the nucleation of a ZrO_2 phase, which results in significant diffusion of Al_2O_3.[115] This depicts a similar reaction mechanism to the previous one, however it does not involve oxygen or other oxidants, and is therefore the more likely mechanism for my work in this thesis - due to the reaction occurring in an inert argon environment.

Oh et al.[116] among other scientists utilised a powder bed of pre-sintered powder beneath the NASICON pellet to stop its reaction with the alumina crucible.

2.3.3.5 Chemistry of Solid-state

The experiments in this thesis are based on the macro-precursor experiment in Jalalian-Khakshour's (2020) paper[79], which was completed within Swansea University and investigated how precursor size and sintering times affect NASICON solid-state synthesis.

Equation 1 defines the chemical reaction for the experiment, indicating the chosen macro-precursor chemicals: ZrO_2 (5 µm), SiO_2 (216 µm) and $NaPO_4.12H_2O$ (decomposes at comparatively low temperatures therefore the particle size was not defined). These three precursor chemicals were used in stoichiometric quantities in this paper.

Equation 1

$$ZrO_2 + SiO_2 + Na_3PO_4.12H_2O \rightarrow Na_3Zr_2Si_2PO_{12}$$

The experimental method utilised in this paper is illustrated in Figure 7. Techniques to note include the use of nano and macro precursors and ball milling conditions - wet ball milled in isopropanol (IPA) 120 rpm 2 hours. The paper clarifies the pellets were formed by room temperature uniaxial pressing at 250 MPa (16 mm diameter). It also explains that the method used an extra processing step where the pellets were polished to 1.5 mm, this was not carried out in my work. The sintering times tested in the paper were 10, 24 and 40 hours, with the sintering temperature at 1230ºC.

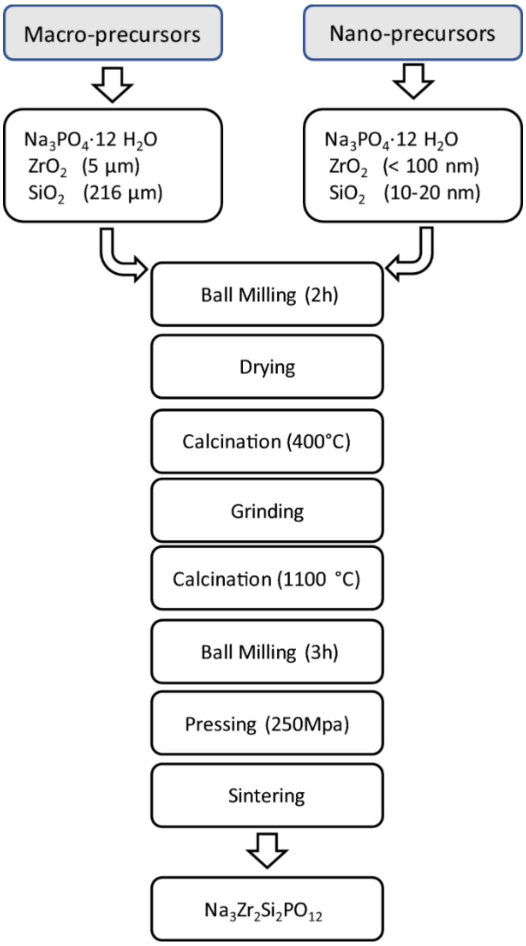

Figure 7: Diagram showing the solid-state NASICON synthesis method used in Jalalian-Khakshour's paper.[79]

Results showed that NASICON was successfully prepared using both particle sizes (nano and macro), as well as all sintering times and temperatures. The most important difference between each sample (to take into my work) was the secondary phases present, shown in Figure 8 and Table 4.

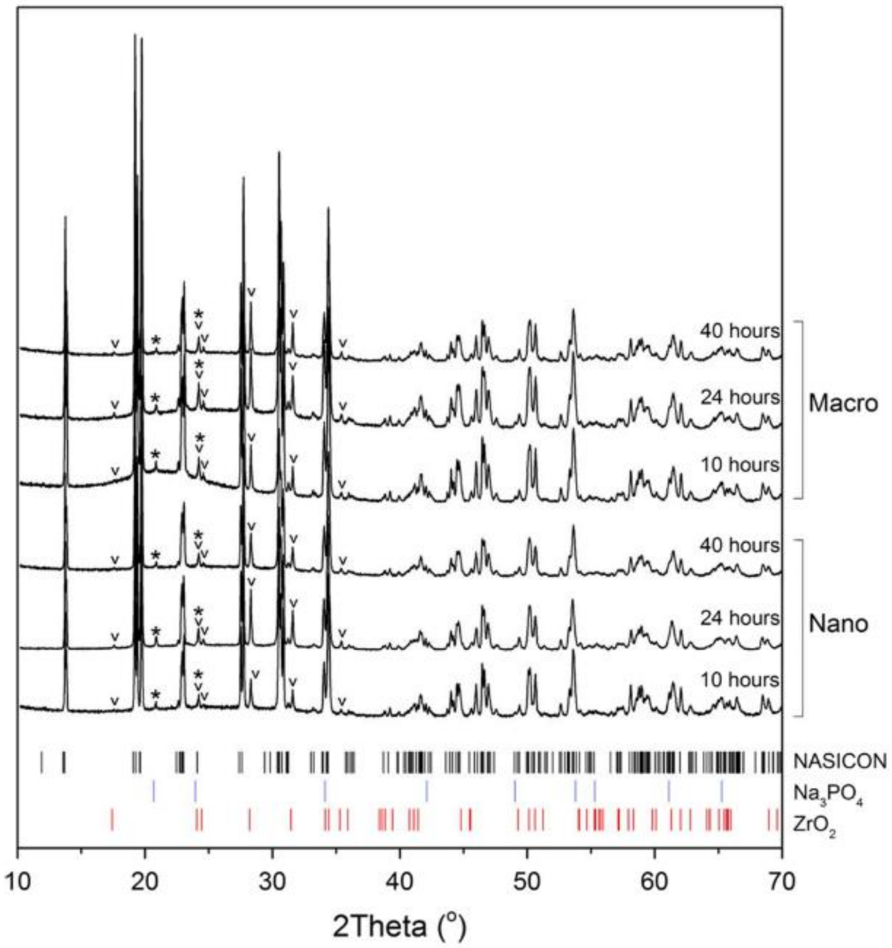

Figure 8: XRD pattern of NASICON from Jalalian-Khakshour's paper[79]*, illustrating* Na_3PO_4 *(*) and* ZrO_2 *(v) secondary phases.*

Table 4: Rietveld refinement XRD data from Jalalian-Khakshour's paper.[79]

	Sintering time (hours)	NASICON	Na_3PO_4	ZrO_2	SiO_2
Nano	10	88.43	3.71	7.83	0.02
	24	80.51	8.09	11.26	0.13
	40	87.46	3.42	8.93	0.19
Macro	10	91.87	2.41	4.64	1.08
	24	86.79	3.47	9.14	0.6
	40	85.404	3.201	11.082	0.312

Secondary phases of Na_3PO_4, ZrO_2 and SiO_2 were present in the XRD's of all the samples. SiO_2 content was higher in the macro-powder derived pellets than the nano-powder derived samples, with a reduction observed in macro-derived samples subjected to extended sintering times. The most abundant secondary phase across all the samples was ZrO_2, showing no reduction with increased sintering duration. Jalalian-Khakshour proposed that the presence of ZrO_2 could be attributed to either unreacted precursor or precipitation resulting from volatilisation during densification.[6] Na_3PO_4 levels were mostly low, except in the nano-derived sample sintered for 24 hours. The number of repeats of this data is not stated, as there is no trend in this data this questions the reproducibility of the work.

Macro-derived powders sintered at 10 hours exhibited the lowest secondary phase content: Na_3PO_4 2.41, ZrO_2 4.64, SiO_2 1.08. The macro-derived sample sintered at 24 hours also showed low secondary phase content compared to the nanoparticle equivalent: Na_3PO_4 3.47, ZrO_2 9.41, SiO_2 0.6. While extended sintering times increased pellet densification, they also led to increased ZrO_2 secondary phase formation. A 16 hour sintering time represents a compromise between the secondary phase formation and density, and was therefore employed in my work.

The microstructure of NASICON is known to influence its overall ionic conductivity;[66] as reduced particle size can enhance the powder reactivity by decreasing surface area/free energy, thereby improving reaction kinetics and increasing material density.[117] However, the difference in secondary phase content between nano- and macro-precursor derived samples was negligible; furthermore, considering the processing time and cost of using nanoparticles, macro-precursors were selected for my work.

While this study provided valuable insights into the solid-state synthesis process of NASICON and reported promising electrochemical data, several crucial methodological details were omitted. The paper lacked specificity in key areas of the synthesis protocol, including:

1. Ball milling parameters: the ball sizes and IPA:precursor powder ratio were not included.
2. Hand grinding process: doesn't specify the material of the equipment used to do this and the criteria for determining when the powder achieved the desired particle size.

3. Crucible specifications: Crucible material and type were not specified for any of the heat treatment steps, particularly the critical sintering stage.

These omissions in the experimental methodology presented a significant challenge in my work when attempting to replicate this experimentally due to lack information. Furthermore, the repeatability of the results is unknown, questioning the consistency and reliability of the work. Only the final sintered pellet was characterised with XRD in this paper, therefore my work focus' on the chemistry at each stage and attempt to reduce the secondary phases.

2.3.4 Sol-gel synthesis

The time line for sol-gel synthesis started with its discovery in 1846 by Ebelmen et al.[118], with its first application in ceramics preparing oxide films in 1930 by Brinker et al.[119] and then latterly employed to synthesise NASICON sol-gels in 1983[120].

The technique involves mixing precursor chemicals in a solvent, where the monomers initially undergo a hydrolysis reaction to form a stable colloidal or polymer sol or gel (Figure 10). Thermal treatment, drying, calcination or sintering, facilitates a phase transition of the sol-gel into a crystalline material.[121] Sol-gel is a favourable synthesis route as the synthesis parameters, and consequently the chemistry can be easily controlled; the reaction can also be effectively conducted at room temperature.

Sol-gel chemical precursors are species that possess the necessary structural framework and appropriate proportions to incorporate the chosen metal ions, in this case Na^+.[122] NASICON is a complex system where the phosphate and silicate tend to form anionic networks of phosphosilicates.[122] NASICON sol-gel synthesis commonly uses metal alkoxide or inorganic metal precursor chemicals to form a metal oxide.

2.3.4.1 Organic Metal alkoxide

Alkoxides are organic compounds in the H^+ of a hydroxyl group is replaced by a metal; [118] and the organometallic materials undergo the elimination of the organic framework during the reaction.[122] The RO^- functional group is a strong base, strong nucleophile and good ligand.[118] During a hydrolysis reaction metal alkoxides react easily with water, releasing an alcohol molecule. If the conditions are correct this can be proceeded by a condensation reaction, where the hydrolysed molecules polymerise and form a 3D network structure/gel.[118] This hydrolysis reaction is illustrated in Equation 2 and Figure 9.

Equation 2 [123]

$$M(OR)_n + H_2O \xrightarrow{hydrolysis} M_2O_n.xH_2O \ + ROH \xrightarrow{drying} M_2O_n \ (xerogel)$$

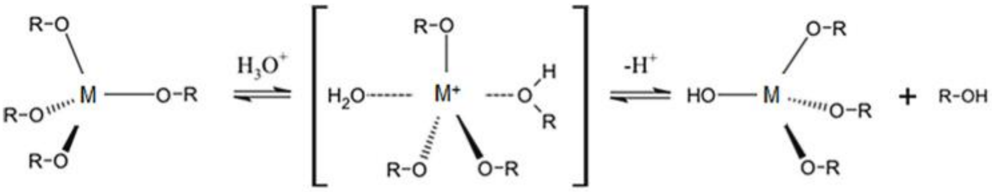

Figure 9: Alkoxide hydrolysis catalysed by an acid.[118]

Metal alkoxides were originally used as in the sol-gel synthesis of metal oxides due to the stability of the colloids obtained during hydrolysis.[123] Metal alkoxides are also favourable due to the ability to control the stoichiometry and homogeneity, as well as employing low temperatures for phase formation.[122] However, several disadvantages of metal alkoxides, such as their cost, handling difficulty, and insolubility, have led to the exploration of alternative materials.[124,125]

2.3.4.2 Inorganic metals

Sol-gel synthesis can prepare high purity NASICON from aqueous solutions of inorganic materials.[124] One example of an inorganic metal used in this field is metal chloride: a transition metal coordinated to chloride ligands.

A sol is a colloidal system, with a liquid dispersion medium and a dispersed phase of fine particles or polymers. Sol-gel processes can be divided into two categories: polymeric and colloidal/particulate (Figure 10). The difference between colloidal and polymeric sol-gel is predominantly related to the rate of hydrolysis.[118] The crystallisation temperatures and reaction times of a sol-gel are reliant on the hydrolysis conditions, specifically the cation/anion environments in the liquid phase and the aggregation of colloidal particles.[121] My work looks at a multi-cation system of chloride or nitrate inorganic precursors.

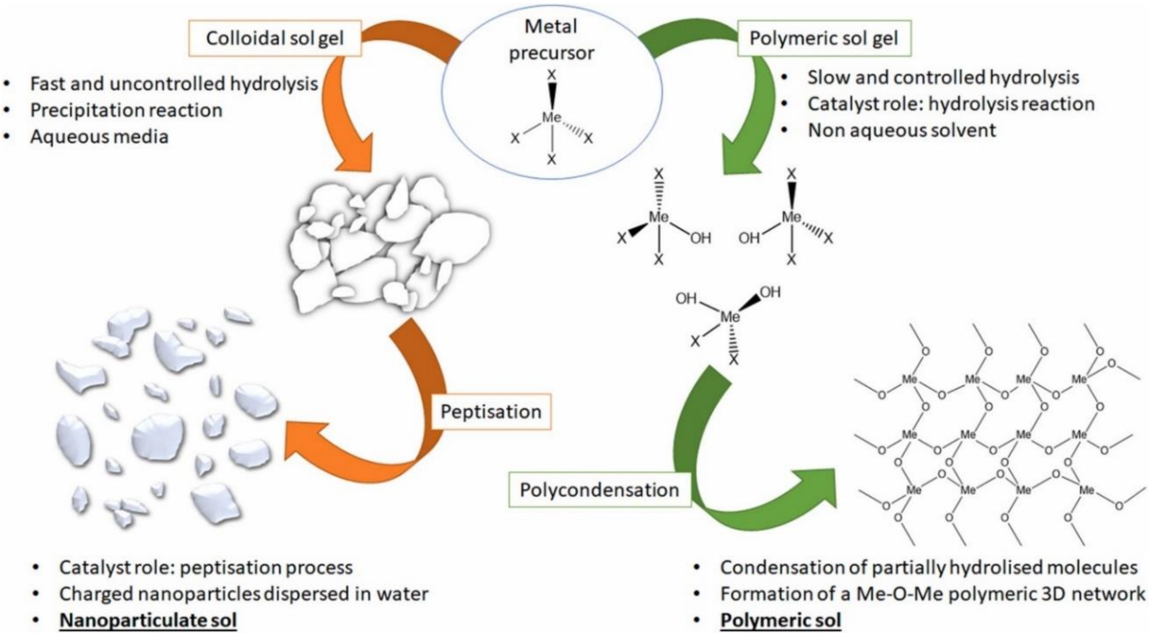

Figure 10: Colloidal and polymeric sol-gel synthesis routes. [118]

2.3.4.3 Polymeric sol-gel

Sol-gel preparation is a hydrolysis and polycondensation reaction of the different metal alkoxides, leading to the formation of a polymeric sol-gel.[119,126]

The polymeric route is a two-step process: the first of which is hydrolysis. The solvent used is a non-aqueous solvent (e.g. alcohol) with an appropriate catalyst, which facilitates a hydrolysis reaction at a slow rate (time dependant on chemicals used), initiating the partial hydrolysis of the metal precursor molecules.

Subsequently, a polycondensation reaction then takes place to obtain a 3D polymeric network via the destabilisation of the particles, covalent-type interactions and the cross-linking between polymeric clusters; where compounds containing metal atoms and oxo- or hydro-oxo bridges form polymers in solution.[126] A gel is a continuous solid network containing a liquid phase, where in this case a metal oxide is formed.[119,118] A condensation reaction occurs when two compounds combine, resulting in the elimination of water. There is some discrepancy in literature on when the condensation reaction occurs, either entirely in the sol or in the solid state during thermal treatments.[80,118]

Differences in NASICON characterisation and properties is observed due to differences in polymeric backbone. Furthermore, the homogeneity of a sol-gel determines the homogeneity of the resultant material – therefore methods are developed to control the precursor polymeric species.[80]

Subsequent thermal treatments complete the conversion of the precursors to the desired metal oxides[119,80] In this thesis a polymeric sol-gel is not utilised as this is not favourable for the spray coating deposition method utilised, as the sol-gel would be too viscous to pass through the nozzle.

2.3.4.4 Particulate sol

In this thesis the solvent used is water, and therefore a colloidal sol reaction is used, summarised in Figure 11. A particulate or colloidal sol is also a two-step process: hydrolysis followed by peptisation. When the solvent is water, the hydrolysis is fast, and therefore there is no time for a polymeric network to grow. Consequently, a nanoparticulate sol (if the right catalyst is used) is obtained through the breakdown of clusters via peptisation.[118]

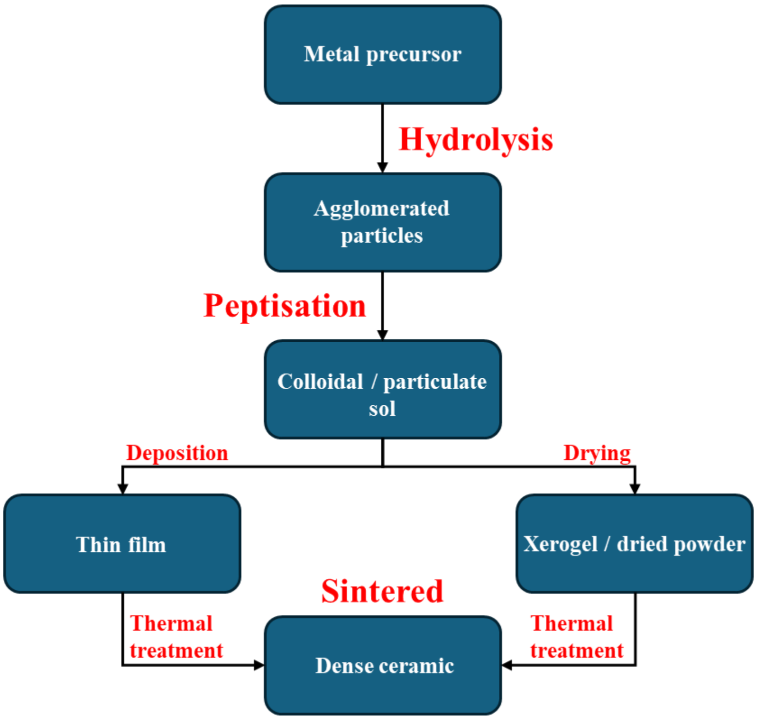

Figure 11: Diagram describing the colloidal/particulate sol synthesis route for NASICON.[118]

A particulate sol can be favourable in NASICON synthesis as it is a multicomponent system and therefore this method allows the atomic mixing of particles that can then be readily sintered. The same as polymer sol-gel's, the homogeneity of the final material is dependent on how homogeneous the sol is.[80]

2.3.4.4.1 Hydrolysis

A colloidal solution is a solid-liquid mixture, in which one substance of dispersed particles are suspended throughout a liquid substance. The colloid is formed starting from precursors containing a metal element surrounded by ligands that do not contain other metals.

Hydrolysis is a decomposition reaction in which a water molecule breaks one or more covalent bonds in the starting compounds. The metal precursors are hydrolysed to metal hydroxide precipitate; an example being metal chlorides which react easily with weak acids, producing an alkoxide. The metal precursor controls the hydrolysis rate and polycondensation degree, it therefore needs to be easily hydrolysed to ensure fast hydrolysis.[118]

The amount of water should always be in excess, allowing the hydrolysis of the metal precursor to occur rapidly, which generates large precipitates; metal precursors hydrolyse faster as the amount of water increases. To ensure pure chemistry of the resultant metal oxide, the entire metal precursor should be completely hydrolysed. [118]

Dispersants are used to control particle size and morphology.[118]Another variable to be aware of is precursor chemicals used in this method can be extremely reactive with water, causing precipitation when water is added.[80]

2.3.4.4.2 Peptisation

The particle clusters generated from the hydrolysis reaction are subsequently broken into aggregates of nanoparticles, a reaction called peptisation, forming a colloidal suspension/sol with high stability. It is defined as the process where a coagulated colloid evolves to its dispersed state.[127,118]

Initially, the breakdown of the particles clusters starts by mechanical stirring. Charge generated by the catalyst on the particles surface breaks down the particle clusters into nanoparticles. During this process, the H^+ ions from the catalyst (in this thesis tartaric acid) interact with the surface of the nanoparticles, creating positive charges. In the case of protons, the positive charges will be created by their adsorption onto the particles surface. The electrostatic repulsion provoked by the originated charges will continue breaking down the agglomerates. When this occurs, the peptisation process can evolve without any mechanical stirring. The acid chosen determines the strength of forces and time needed to complete peptisation reaction.[118]

Once it is finished a nanoparticulate sol is obtained, the optical properties change completely due to the smaller particle size, where the system opaque at the beginning of the process and translucent at the end. The peptisation time is usually estimated by optical inspection, using an excess of time to be sure the process is complete. [118]

Synthesis parameters such as temperature and metal precursor-water ratio determine the chemistry and morphology of the resultant metal oxide. Metal precursor concentration has a strong influence on the peptisation process, determining the particle size and the peptisation time.[127] The decrease in the peptisation time with increasing concentration is directly related with the number of interactions among particles. The higher the concentration is, the higher the probability of particle collisions, breaking down the agglomerates faster.[118]

Peptisation process depends on the adsorption of the protons or the generation of negative charges on the surface of the particles. In the multi-compound system used in this thesis, the different molecules or ions can lead to adsorption competition and side reactions.[118]

Heating the sol can increase the mobility of atoms, molecules and particles, increasing the kinetic energy of the system and creating a faster peptisation process. However, higher temperatures can also stabilise the system causing a higher agglomeration of the particles, as it provides the kinetic energy necessary to overcome the double layer repulsion. Experiments in literature investigate increasing the temperature to reduce the petisation process.[128,129,130] Oppositely, work has been carried out to extended the peptisation time in order to modify the properties of the nanopowders.[131,132,118]

Catalyst concentration is a critical parameter that needs to be adjusted properly. The most frequently used catalysts are acids: including HNO_3, acetic acid and HCl, in this thesis tartaric acid is used.

Furthermore, the catalyst used affects both the hydrolysis and peptisaiton steps, as the catalyst-metal precursor ratio determines the pH conditions of the sol, which can stabilise the resultant ceramic.[118] The catalyst concentration plays a crucial role in generating sufficient charge to disperse particles and stabilise the sol. Inadequate charge leads to uncontrolled sedimentation. Conversely, an excess of catalyst and charge compresses the electrical double layer surrounding the particles, destabilizing the system. This manifests as either the formation of agglomerates (flocculation) or complete system breakdown (coagulation). Thus, precise control of catalyst concentration is essential to maintain colloidal stability within an optimal range. The nature of the catalyst also affects to the particle size and shape.[118]

2.3.4.5 Thermal Treatment - sintering

As alluded to above, following peptisation the sol can be directly used as a thin film or dried and used as a powder. The sol can only be used if it is not destabilised forming agglomerates or coagulation, and if the by-products don't interfere with the synthesis.[118]

The peptised sol can be dried, in an oven, to evaporate water and volatile compounds, forming a xerogel. The solid contains small crystals that can be hand ground into a fine powder, then sintered via a further thermal treatment to form a dense ceramic material.[118]

When used as a thin film it will consist of a nanoparticulate layer.[132] In the case of the films, the same strategy can be followed; however, the substrate stability will determine the maximum temperature that can be applied.[118]

Drying, followed by a thermal treatment (sintering) completes the conversion of the precursor to the desired metal oxide.[80]

The chemistry of the sol chemical precursors determines the reaction mechanism involved in the sintering of the NASICON powders. TGA-DTA data from 3 papers has suggested different sol chemistries are undergo different sintering mechanisms (Figure 12). The TGA data generally shows the mass losses, and the DTA data shows endothermic and exothermic reactions. This is an area I will investigate in Chapter 5 – sol powder.

Figure 12: Summary of TGA-DTA data from NASICON papers. [124,133,134]

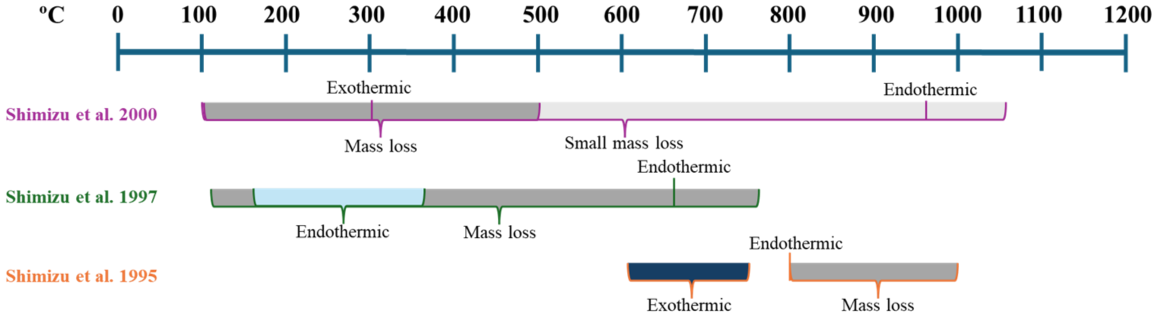

The Shimizu et al. (2000)[124] investigated the thermal behaviour of the xerogel powder synthesised from $ZrO(NO_3)_2.8H_2O$, $NH_4H_2PO_4$ and $Na_2SiO_3.9H_2O$, with tartaric acid.

Significant mass losses were observed between 100-500°C. An exothermic peak at 300°C was attributed to the decomposition of the starting materials containing organic precursor. At 950°C there is an endothermic peak, potentially associated with the evaporation of oxidised carbon from decomposed organic compounds. Small mass losses were noted between 500 and 1050ºC.[124]

Shimizu et al. (1997)[133] utilised $ZrO(NO_3)_2.8H_2O$, $NH_4H_2PO_4$ and $Na_2SiO_3.9H_2O$ precursor chemicals, forming a xerogel powder. TG-DTA data revealed mass losses between 100ºC and 750ºC. An endothermic peak observed at 150-350ºC is visible, suggested to be the evaporation of decomposed materials. A subsequent endothermic peak at 650ºC indicated the crystallisation of the NASICON phase. Mass loss was completed by 750ºC, corresponding to the formation of the purest NASICON phase.[133]

Shimizu et al. (1995)[134] employed $ZrOCl_2.8H_2O$, $(NH_4)_2HPO_4$ and Na_2SiO_3 precursors, and conducted TG-DTA, XRD and FT-IR analysis. Small exothermic peaks were observed between 600ºC and 750ºC, accompanied with small mass losses, indicating the release of decomposed materials. HCl from hydrate salts evaporated at 100ºC, while NH_4Cl decomposed at 340ºC. A sharp endothermic peak at 800ºC was suggested by Shimizu et al. to be attributed to the melting of NaCl, which subsequently decomposed at 801ºC. Weight losses occurred between 800ºC and 1000ºC with an endothermic peak, were associated with the evaporation of decomposed chloride and the partial decomposition of NASICON. $Na(Na_2O)$ and/or $P(P_2O_5)$ evaporation was observed between 600 and 1050ºC.[134]

Collectively the data from these studies show the reaction mechanism is dependent on the precursor chemistry of the sol. All chemistries had in common: exo- or endo-thermic peaks attributing to the evaporation of decomposed material.

2.3.4.6 Chemistry of Sol

The sol synthesis chemistry utilised in this thesis was based on two published papers, however their work implemented a polymeric sol-gel, whereas the research in this thesis employs a particulate sol. The first chemical approach was reproduced from the work of Shimizu's (2000) paper[124] as represented in Equation 3. The chemical precursors used are aqueous inorganic materials, utilising a zirconia nitrate and catalysed by hydroxy acids; in non-stoichiometric compositions with excess Na.

Equation 3

$$ZrO(NO_3)_2.2H_2O + NH_4H_2PO_4 + Na_2SiO_3.9H_2O + C_4H_6O_6 \rightarrow Na_3Zr_2Si_2PO_{12}$$

Two different hydroxyacid catalysts are tested in this paper, citric acid and tartaric acid, as the stability of the gel is dependent on time and the catalyst added. Citric acid maintained a sol-gel stable over 20 days, however it was not viscous. The tartaric acid allowed the sol to gel gradually over 7 days – becoming viscous and a suitable gel for spin coating as a thin film. Shimizu et al. observed that the incorporation of hydroxyacid induced significant physicochemical changes in the mixed aqueous solution, facilitating the formation of a viscous gel exhibiting suitable rheological properties for spin coating applications.

In this thesis spray coating is used as the deposition method, therefore a high viscosity is unwanted. Therefore, a particulate/colloidal sol and do not allow the sol to age to a gel over several days, reducing processing time/energy.
However, the chosen method in this paper utilised the tartaric acid (aged at 2ºC for 7 days) and formed a polymeric sol-gel.

Two experimental approaches were undertaken, one being the formation of a NASICON powder (Table 5).

Table 5: Illustrates the synthesis method post sol-gel formation for NASICON powder synthesis in Shimizu's 2000 paper.

NASICON Powder synthesis		
Synthesis steps	**Time (hours)**	**Temperature (ºC)**
Dried	12	120
Hand ground		
Calcined	1	750
Hand ground		
Sintered	3	1000

Utilising the methodology described in Table 5, a well-crystallized, nearly single-phase NASICON powder was successfully synthesised.

The second approach spin coated the sol-gel onto alumina and quartz substrates (Table 6).

Table 6: Illustrates the synthesis method post sol-gel formation for NASICON thin film synthesis in Shimizu's 2000 paper.

NASICON thin film synthesis		
Synthesis steps	**Time (hours)**	**Temperature (ºC)**
Spin coat		
Dried	unknown	150
Sintered	3	1000

Spray coating of 10 layers of the sol-gel on alumina substrates resulted in the formation of a film. XRD analysis confirmed the successful synthesis of NASICON phase with a minor SiO_2 impurity. Additionally, a thicker film comprising 5 x 50 coats (thickness not stated) was fabricated, yielding NASICON with a secondary phase of monoclinic ZrO_2. This observation suggests that prolonged sintering durations may promote the formation of this secondary phase ZrO_2, potentially due to thermal decomposition or phase segregation.

However, limitations in this paper include XRD's showing a lot of background noise, poor quality SEM images and some experimental values missing (e.g. drying time of film and film thickness).

Equation 4 illustrates the second chemical approach used in the thesis, which was derived from a method outlined in Shimizu's (1995)[135] publication. This sol-gel synthesis method shares similarities with the previous 2000 paper, utilising inorganic materials with an excess sodium stoichiometric composition. However, it differs in its precursor chemistry, employing a chloride-based precursor in contrast to the nitrate-based precursor used in the previously discussed approach.

Equation 4

$$ZrOCl_2 + (NH_4)_2HPO_4 + SiO_3 + C_4H_6O_6 \rightarrow Na_3Zr_2Si_2PO_{12}$$

In this study, polymer sol-gels were synthesised by dehydrating the sol at 80 ºC to form a viscous gel. As described in Table 7 the gel was subsequently dried to form a xerogel powder, which was then pressed into a pellet and sintered at 2 different temperatures: 850 ºC and 1000 ºC.

Table 7: Illustrates the synthesis method post sol-gel formation for NASICON pellet synthesis in Shimizu's 1995 paper.

NASICON pellet synthesis		
Synthesis steps	**Time (hours)**	**Temperature (ºC)**
Dried	12	100
Hand ground		
Calcined	24	600
Hand ground		
Pellet pressed		
Sintered	3	850-1000

The material was characterized by XRD following each thermal treatment, the results of which are shown in Table 8. Shimizu et al. elude that the optimal sintering temperature in this instance is 850 ºC, as this forms the purest phase NASICON.

Table 8: Illustrates the results of XRD characterisation at each stage in the synthesis of NASICON pellet formed from chloride precursor chemistry in Shimizu's 1995 paper.

XRD analysis		
Synthesis steps	NASICON	Secondary phases
Dried (xerogel)	Amorphous phase	NaCl
Calcined	NASICON phase starts to appear	NaCl
Sintered (850ºC)	Hexagonal NASICON	
Sintered (1000ºC)	Hexagonal NASICON and slight monoclinic distortion	Monoclinic ZrO_2

Furthermore, the paper illustrates the most significant finding from this research is the necessity of preparing the sol from separate precursor solutions. It was also highlighted that it is crucial to add these precursor solutions in a specific order, with $ZrOCl_2.8H_2O$ added last. This is due to the higher reactivity of $ZrOCl_2.8H_2O$ compared to the other precursor chemicals, resulting in very different hydrolytic conditions. This methodology was therefore necessary to give the purest phase NASICON and reduce secondary phases such as ZrO_2.

In this paper Shimizu et al. also used nitrate precursor chemistry xerogel paste (composed of xeorgel powder and isoamyl alcohol) to successfully synthesise high purity NASICON thick films on quartz substrates. This method was not employed in the experimental work in my thesis; however, it was interesting to note that this is another viable method to make NASICON films.

Despite the limitations and gaps in the previously described papers, both demonstrated successful formation NASICON using a sol-gel method with limited secondary phases and proved that NASICON can be synthesised as a thin film. Consequently, the work in this thesis investigates both chloride and nitrate chemistries as a foundation for the sol-gel experiments.

2.3.4.7 NIR Sintering

Sintering NASICON via NIR radiation is a novel technique; until this work it was not known if NASICON could be successfully sintered using NIR. Additionally, NIR has not previously been used to synthesise solid oxide electrolytes as thin films, and has not been demonstrated, prior to this work, to achieve temperatures above 500 ºC.

Previous literature shows NASICON has been fast sintered using other non-conventional techniques such as, ultra-fast high temperature sintering[136], spark plasma sintering[89] and microwave sintering[137]. Whilst these papers show potential there are also disadvantages, ultra-fast high temperature sintering requires doping with elements such as Lu, the spark plasma sintering can only sinter a small area at once and microwave sintering is a batch process.

There are several different heating technologies that can be employed to synthesise materials, which are explained in this section.

Conventional heating methods utilise furnaces, where heat is transferred to the sample through three primary mechanisms: conduction, convection and radiation. However, conventional heating is not suitable for many thin film applications due to the selective absorption of energy (substrate vs film).[138,106]

In contrast, fast heating techniques directly heat the material through a radiative method that involves the absorption of electromagnetic radiation. Figure 13 illustrates the wavelengths employed in these rapid heating techniques; where UV, IPL and NIR technologies are of particular use in material processing.

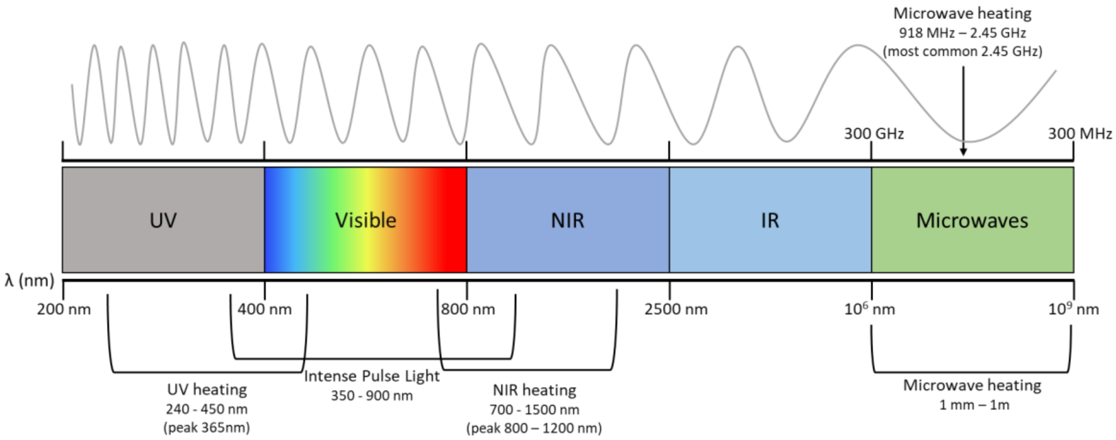

Figure 13: Electromagnetic spectrum with different heating technologies highlighted.[106]

The mechanisms by which these three radiative techniques heat a material are illustrated in Figure 14; where Figure 14(a) shows that UV radiation is absorbed directly into a film, initiating a chemical reaction within the material (crosslinking). The mechanism of IPL is also absorption of radiation within the film (Figure 14(b)), however reflections at the substrate surface and surface of the film also occur. Both techniques cause the material to heat to temperatures up to 300°C, however the temperature reached is dependent on the material and substrate used.[106]

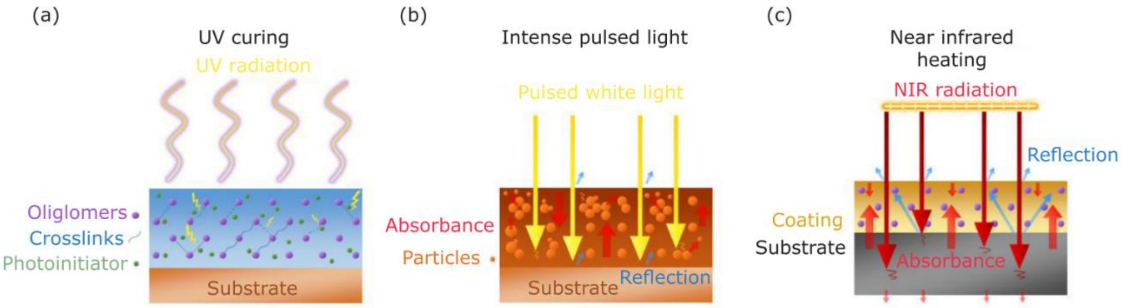

Figure 14: "Interaction of radiation with materials and substrate for: (a) UV curing; (b) IPL; (c) NIR heating" [106]

Figure 14(c) shows that NIR radiation can be absorbed or reflected in the film (similar to the mechanism for IPL) enabling the material to reach higher temperatures commonly up to 500°C[139]. The NIR lamps' energy density and the materials used determine the temperature of the sample. However, materials can be transparent to NIR radiation, allowing the radiation to pass through the film without heating it (e.g. soda lime glass[140]). One solution to this is using a substrate or coating (in direct contact with the material) that does absorb at the given wavelength, allowing the film to be heated. Another approach to overcome transparency issues is to incorporate a compound into the material that absorbs in the NIR region, an example of this is incorporating carbon black[141] or commercially produced NIR adsorbing pigments.[106]

The NIR lamps are typically tungsten-halogen filaments which emit within the wavelength range of 700-1500 nm. The spectrum emitted and lamp power is not a linear relationship, and therefore power settings can alter the wavelength of the radiation emmitted.[142] Heating of the material is dependent on how this emitted radiation is absorbed and the thickness of the material.[143,106]

The radiative heating technique chosen is dependent on the material transformation needed: drying, binder removal, chemical reaction and sintering.[106]

Drying using radiative heating techniques are commonly employed on films, evaporating solvents and (depending on the material) facilitate densification, which in turn can improve the conductivity of a film.[144] IPL and NIR have been used to dry films faster than conventional furnaces.[145]

Chemical reactions can be initiated in a material using rapid heating techniques, in particular applying UV radiation on polymers to form a crosslinked network, UV curing.[146] This technique can be used to solve the contact interface problem in solid-state batteries. Yang et al.[4] in-situ free radical photopolymerised a solid polymer electrolyte on a cathode, creating a 3D polymer network structure via crosslinking. Characterisation showed strong adhesion between the layers, in turn ensuring reduced interfacial resistance and good electrochemical performance.[4] Proton exchange membranes for fuel cells have also been UV cured and crosslinked in-situ using this technique.[3] Photonic sintering[147] and NIR[148] have also initiated chemical reactions in perovskite crystallisation. [106]

For this thesis, radiation is applied as a sintering mechanism. Various radiative heating techniques have been tested on films incorporated in dye-sensitised solar cells (DSSCs). UV radiation has been utilised to sinter titania nanoparticle thin film semiconductors for DSSCs.[149,150] Sandmann et al. demonstrated the efficacy of UV radiation at 325 nm and 30 mW power for sintering TiO_2 photoelectrodes with improved interparticle connectivity.[149]

While photonic sintering has also been applied to titania for DSSCs[151], NIR radiation often proves more effective in this application due to the absorption characteristics of the substrate used (fluorine doped tin oxide), which absorbs in the NIR region but not the visible.[140,139] IPL sintering has been employed across a diverse range of applications [152,153,154,155,156,157,158,159], and could have been a promising initial technique for sintering NASICON films in this work, however the IPL equipment at the University was not operational.

Carnie et al.[139] demonstrated the use of NIR radiation for sintering in DSSCs. The method involved sintering TiO_2 pastes tape cased onto titania metal substrates using NIR. This technique produced fused layers that were sintered in 12.5 s (reduced from 30 mins).[139] Silver nanoparticles have also been sintered using NIR radiation (using polyethylene terephthalate (PET) substrates) in a similar length of time.[160,161]

NIR can be used inline and has proven industrial utilisation in steel plants[143], however it has not been used past 500ºC before, therefore this work gives it a completely new application space.

A review of literature indicates that NIR radiation has not yet been utilised to sinter materials in battery technology. Therefore, the application of this rapid processing technique in this thesis represents a novel approach. An advantage of NIR is that it can reduce diffusion between electrode and electrolyte layers if sintered jointly, which is not possible with conventional heating. Due to the extended sintering times and high temperatures required conventionally for NASICON synthesis, NIR is a suitable radiative heating technique for the synthesis of NASICON thin films. This method offers potential advantages for processing efficiency and material compatibility. The challenge surrounding the NIR technique for the purposes of NASICON thin film synthesis is whether NASICON absorbs radiation in the near infrared region. Furthermore, whether it absorbs enough NIR to heat the material enough to sinter and therefore synthesise NASICON.

The implementation of radiative heating techniques presents several practical challenges that require consideration. A primary concern is the accurate measurement of the material's temperature during processing. Thermacouples[139] and IR cameras[162] are commonly used to estimate the temperatures reached quantitatively. Alternatively, processing temperatures can be qualitatively approximated if a component of the material decomposes at a certain temperature e.g. binder removal.[163] However, all of these techniques are not precise and cannot be employed with all materials.[106]

Another significant practical challenge arises from the rapid nature of these heating techniques, which can induce thermal stresses within the film. This issue is significant in inhomogeneous films, where crack formation can occur. To mitigate these effects, strategies such as pre-heating and post-heating treatments can control the material's heating and cooling rates. Additionally, the use of substrates that absorb radiation at the chosen wavelength can help to reduce thermal stress gradients. The presence of residual solvents in materials subjected to rapid heating can result in defects such as solvent boil[143,145]. Solutions to this include the strategic selection of solvents that exhibit absorption in the chosen wavelength range (e.g. butanol for NIR applications).[143,164,106]

These practical considerations illustrate the complexity of these radiative heating processes, emphasising the necessity for experimental designs tailored to the materials and substrates being processed.

2.5 Gaps in literature this thesis investigates

The issues within Na-ion solid-state electrolyte research and specifically NASICON work stem from the previous mentioned issues of secondary phase formation, long sintering times/temperatures and interface contact resistance. Therefore, my work looks to synthesise NASICON as a thin film in-situ.

A novel aspect of my work is depositing this thin film using a spray coating technique. NASICON has previously been prepared as a thin film[165] via other deposition methods such as dip-coating[166], spin coating[124] and screen printing[167,168]. However, these depositions often don't give unform films of the same thickness, plus the additives required to make the paste can cause unfavourable changes to the chemistry of the NASICON.

Spray coating ensures a uniform coating and thickness, as well as being a scalable technique for industry. A more recent deposition method utilised in NASICON films is powder aerosol deposition[169,170,171], which can successfully synthesise dense NASICON films, however require a calcined powder. In my work spray coating as a deposition method followed by reaction phase sintering of the sol-gel ensures: repeatable films, no additives effecting the NASICON chemistry, reduced processing times and temperatures.

Chapter 3 – Methods

Each method defined in this chapter is the final selected method used for the synthesis of each technique.

3.1 Solid-state synthesis

Solid-state NASICON is prepared in this thesis from conventional solid-state reactions at temperatures >1150 °C. The synthesis involves the three precursors stated in Equation 5 which are micron sized powders (Table 10), and the overall multi-step method is illustrated in Table 9.

Equation 5 [79]

$$ZrO_2 + SiO_2 + Na_3PO_4.12H_2O \rightarrow Na_3Zr_2Si_2PO_{12}$$

Table 9: NASICON solid-state synthesis method employed.

Ball Mill 2 hours, 120 rpm
Dry 16.5 hours, 80°C
Pellet Press
Calcination 5 hours, 400°C
Hand Grind
Pellet Press
Calcination 16 hours, 1100°C
Hand Grind
Ball Mill 3 hours, 120 rpm
Dry 16.5 hours, 80°C
Pellet Press
Sintering 16 hours, >1150°C

Stoichiometric ratios (2:2:1) of Zirconium (IV) oxide (ZrO_2, Sigma Aldrich, 5 µm), Silicon dioxide (SiO_2, Sigma Aldrich, 216 µm) and tri-sodium phosphate dodecahydrate ($Na_3PO_4.12H_2O$, Sigma Aldrich) were used as precursor materials in the solid-state synthesis of NAISCON. They were placed in ZrO_2 grinding bowls (size 250 ml, Fritsch) with 5 mm Ø ZrO_2 grinding balls (number of balls: 1200, Fritsch) and were wet ball milled (Planetary Mill Pulverisette 5, Fritsch) in Isopropanol (IPA, fisher scientific) (Table 11) for 2 hours at 120 rpm (Table 12). The other cup (Cup 2) was filled with 222.38 g sand and 20 mm Ø ZrO_2 grinding balls (number of balls: 15, Fritsch) to balance the planetary mill.

Table 10: Macro-precursor powder sizes.

Particle size		
ZrO_2	**SiO_2**	**$Na_2PO_4.12H_2O$**
5 µm	216 µm	n/a

Table 11: 1st ball milling step quantities of materials placed in Cup 1.

CUP 1		1:3
ZrO_2	15.27 g	20 ml powder
SiO_2	7.45 g	
$Na_3PO_4.12H_2O$	23.56 g	
IPA	47.1 g	60 ml IPA
Balls (ø5 mm, 1200 balls)	490 g	
Total	583.38 g	80 ml

Table 12: 1st ball mill step settings.

120 rpm	Mill (+ reverse)	Pause
Minutes	3	15
Repetitions	40	40
Total (hours)	2	

Subsequently, the materials were sieved and washed using IPA. Then placed in a petri dish and dried in a chamber Furnace (Carbolite Gero, CWF 1200) for 16.5 hours at 80°C, atmosphere air (Figure 15).

Figure 15: NASICON precursor material (a) post 1st ball mill (b) sieved with IPA (c) post 1st dry in petri dish

1 g of dried precursor material was then pellet pressed (PP 25, Retsch) using Pellet press die (16 mm) at 250 MPa (Figure 16).

Figure 16: Pellet pressing NASICON pellet

The pellets were placed in alumina crucibles (Almath) and calcinated in the chamber furnace for 5 hours at 400°C, atmosphere air. The material was then hand ground using an agate mortar and pestle (Sigma Aldrich) (Figure 17) and subsequently pellet pressed. The pellets were placed in alumina crucibles and calcinated in a tube furnace (Carbolite Gero, CWF 1200) for 16 hours at 1100°C, in an argon atmosphere (pureshield argon genie, BOC).

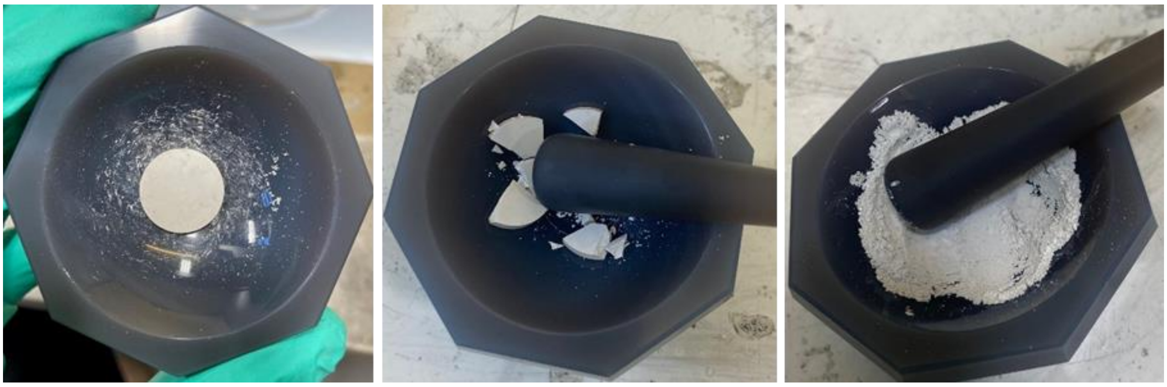

Figure 17: Hand grinding NASICON pellet to fine powder.

Hand ground the pellet once again using an agate mortar and pestle (Sigma Aldrich) and then placed the powder in ZrO_2 grinding bowls (size 45 ml, Fritsch) (Figure 18) with 5 mm Ø ZrO_2 grinding balls (number of balls: 180, Fritsch) and were wet ball milled (Planetary Mill Pulverisette 5, Fritsch) in IPA (fisher scientific) for 3 hours at 120 rpm; described in Table 13, Table 14 and Table 15.

Figure 18: Fritsch 45 ml ZrO_2 ball mill cups

Table 13: 2nd ball milling step quantities of materials placed in Cup 1.

CUP 1 (45 ml cups)		1:3
NASICON precursor material	6.3 g	1.97 ml
IPA	4.48 g	5.70 ml
Balls (ø5 mm, 180 balls)	74 g	
Total	84.775 g	7.67 ml

Table 14: 2nd ball milling step quantities of materials placed in Cup 2.

CUP 2 (45 ml cups)		1:3
NASICON precursor material	6.3 g	1.97 ml
IPA	4.48 g	5.70 ml
Balls (ø5 mm, 180 balls)	74 g	
Total	84.775 g	7.67 ml

Table 15: 2nd ball mill step settings.

120 rpm	Mill (+ reverse)	Pause
Minutes	3	15
Repetitions	60	60
Total (hours)	3	

The materials were then sieved, washed (IPA) and dried in the chamber Furnace for 16.5 hours at 80°C, atmosphere air, and then pellet pressed.

Pellets were then placed in the crucibles, as defined in the experimental chapters, and sintered in a tube furnace for 16 hours at 1180-1230°C, in an inert argon atmosphere (Figure 19).

Figure 19: Tube furnace, Carbolite.

The calculations relating the stoichiometric ratios (2:2:1) to precursor mass and ball milling weight constraints are shown in Table 16 and Table 17.

Table 16: Calculations of precursor chemical mass for 1st ball mill from 2:2:1 molar ratios (250ml cup, 30-125ml capacity).

theoretical density (g/ml)	5.89	2.6	1.62		3.2	
Stoichiometry	2	2	1			12
	ZrO_2	**SiO_2**	**$Na_3PO_4.12H_2O$**	→	**$Na_3Zr_2Si_2PO_{12}$**	**H_2O**
Mr (g/mol)	123.22	60.08	380.12		530.55	18.02
x Stoichiometry	246.44	120.17	380.12		530.55	216.18
				Total	*equation/multiple*	
to 1g	0.33	0.16	0.51	1.000	747	
vol (ml)	0.06	0.06	0.31		*vol=mass/density*	
250ml (80ml)				*1:3 with solvent*		
vol (ml)	2.59	2.86	14.54	20.000	46.298	
Mass (g)	15.27	7.45	23.56			

Table 17: Calculations of material mass for 2nd ball mill (45 ml cup, 3-20 ml capacity).

	Density g/ml	**mass(g)**	**vol(ml) = m/p**
NASICON	3.2	6.3	1.97
IPA	0.785	4.48	5.70
180 Balls (ø5 mm)		74	
Total		**84.775**	**7.67**

3.2 Sol synthesis

As described in Chapter 2, NASICON was also prepared using a particulate/colloidal sol technique. The synthesis method involves the specific addition order of the chemicals to form the correct precursor sol. This work uses a water-based sol precursor made from zirconium dinitrate oxide hydrate ($ZrO(NO_3)_2.2H_2O$) or zirconium dichloride oxide hydrate ($ZrOCl_2.8H_2O$) compounds, the addition of these ZrO precursors must be controlled via stepwise addition.

Zirconium dinitrate oxide hydrate precursors were used to prepare a NASICON sol in Equation 6 (molar ratio of 2:1:2:3), and the addition order of chemicals is displayed in Figure 20.

Equation 6 [124]

$$ZrO(NO_3)_2.2H_2O + NH_4H_2PO_4 + Na_2SiO_3.9H_2O + C_4H_6O_6 \rightarrow Na_3Zr_2Si_2PO_{12}$$

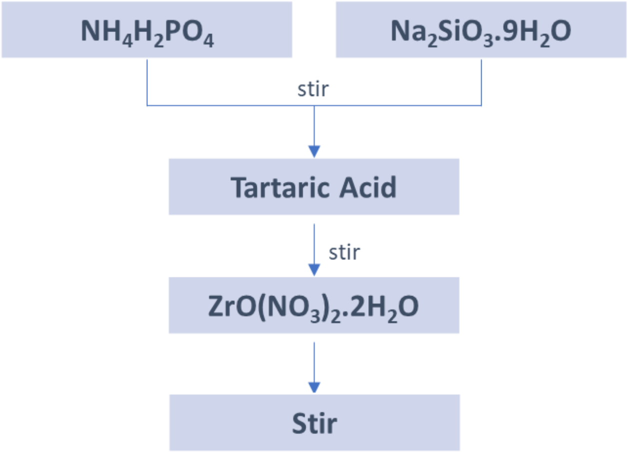

Figure 20: Sol synthesis method of making the Nitrate chemistry sol from separate precursor solutions in H_2O.

A 5% sol solution was formed by the following method. Ammonium dihydrogen phosphate ($NH_4H_2PO_4$, 0.17g, fisher scientific) is stirred and dissolved in H_2O (7.5 g). Sodium metasilicate pentahydrate ($Na_2SiO_3.9H_2O$, 0.85 g, sigma Aldrich) is stirred and dissolved in H_2O (10 g) (Figure 21).

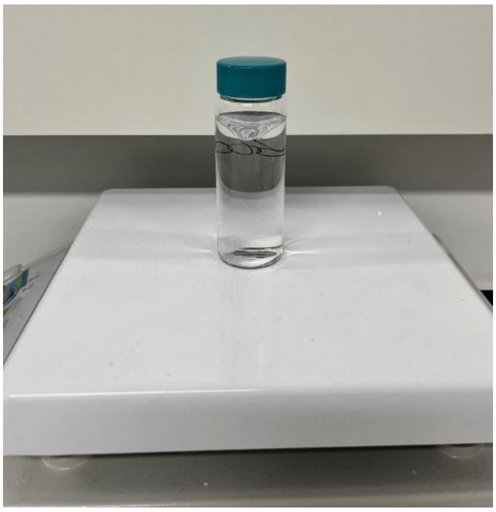

Figure 21: Individual precursor chemicals in H_2O, stirred.

The $Na_2SiO_3.9H_2O$ solution is then added to the $NH_4H_2PO_4$ solution and stirred. Tartaric acid ($C_4H_6O_6$, 0.67g, fisher scientific) is then added and stirred until dissolved.

0.83 g (0.8 g + 4%) Zirconium dinitrate oxide hydrate ($ZrO(NO_3)_2.2H_2O$, fisher scientific) is dissolved in H_2O (30 g) and stirred for a minimum of 48 hours. The $ZrO(NO_3)_2.2H_2O$ was not fully soluble in H_2O, therefore the solution was filtered (fisher scientific, PTFE syringe filter, 0.2 µm). After filtering a 4% loss of the compound was quantified, therefore an extra 4% of $ZrO(NO_3)_2.2H_2O$ was added to every experiment (Figure 22).

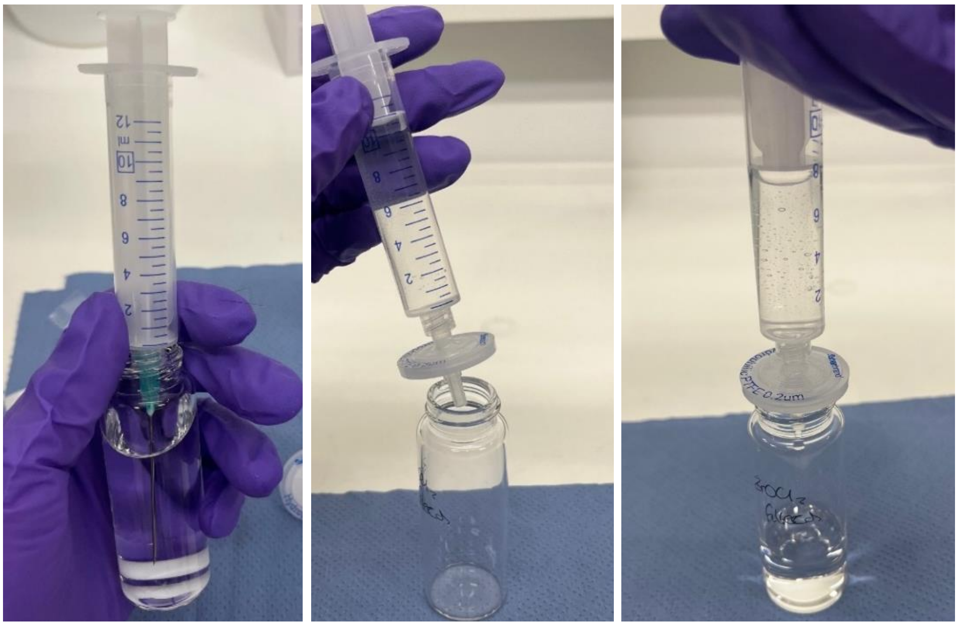

Figure 22: Zirconia precursor chemical solution filtered

Stepwise addition of the filtered $ZrO(NO_3)_2.2H_2O$ is added to the mixture. The final sol is stirred for 1 hour and should look clear before using as shown in Figure 23.

Figure 23: Sol after step-wise addition of filtered zirconia solution, stirred for 1 hour.

$ZrOCl_2.8H_2O$ precursor chemical was also used to prepare a NASICON sol (Equation 7, molar ratio of 2:1:2:3), the addition order of all the precursor chemicals is shown in Figure 24.

Equation 7 [135]

$$ZrOCl_2.8H_2O + NH_4H_2PO_4 + Na_2SiO_3.9H_2O + C_4H_6O_6 \rightarrow Na_3Zr_2Si_2PO_{12}$$

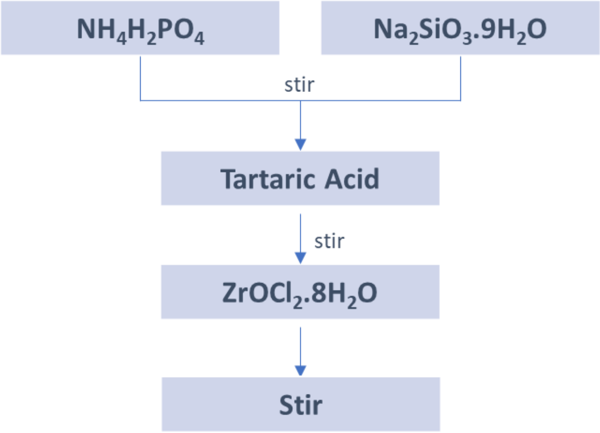

Figure 24: Sol synthesis method of making the Chloride chemistry sol from separate precursor solutions in H_2O.

A 5.33% solution was utilised in this method. Ammonium dihydrogen phosphate ($NH_4H_2PO_4$, 0.17 g, fisher scientific) is stirred and dissolved in H_2O (7.34 g). Sodium metasilicate pentahydrate ($Na_2SiO_3.9H_2O$, 0.85 g, sigma Aldrich) is stirred and dissolved in H_2O (10 g). The $Na_2SiO_3.9H_2O$ solution is then added to the $NH_4H_2PO_4$ solution and stirred. Tartaric acid ($C_4H_6O_6$, 0.67 g, fisher scientific) is then added and stirred until dissolved.

1 g (0.97 g + 4%) Zirconium dichloride oxide hydrate, ($ZrOCl_2.8H_2O$, fisher scientific) is dissolved in H_2O (30 g) and stirred for a minimum of 48 hours. The solution is then filtered (fisher scientific, PTFE syringe filter, 0.2 µm). This filtering step is unnecessary for the chloride sample as the compound is fully soluble in water, however this step was carried out for continuity and replication purposes.

Stepwise addition of the filtered $ZrOCl_2.8H_2O$ is added, and the sol is stirred for 1 hour and should look clear.

Calculations relating the molar ratios (2:1:2:3) with percentage mass to solvent concentrations (for the sol formulations) are shown in Table 18, Table 19 and Table 20. The mass and therefore the concentration changed when altering the degree of sodium metasilicate hydration ($5H_2O$ to $9H_2O$) and when using a different zirconium precursor ($ZrO(NO_3)_2.2H_2O$ and $ZrOCl_2.8H_2O$). Various % concentrations are calculated due to the different formulas used during the thesis; however, the molar ratios of the precursor materials remain constant.

Table 18: Sol calculations for $ZrO(NO_3)_2.2H_2O$ and $Na_2SiO_3.5H_2O$ precursors at 6% and 5% concentrations.

Molar ratio	2	1	2	3		
	$ZrO(NO_3)_2.2H_2O$	$NH_4H_2PO_4$	Na_2SiO_3.5H2O	$C_4H_6O_6$	→	$Na_3Zr_2Si_2PO_{12}$
Mr (g/mol)	267.23	115.03	212.2	150.09	MW (g/mol)	$3Na_2O+4ZrO_2+4SiO_2+P_2O_5$
mols	0.002	0.001	0.002	0.003	123.22	ZrO2
Solubility in water	0.1g/5ml (20g/L)	~40g/dL=400g/L	210g/L	210g/L	61.98	Na2O
30ml min cup					60.08	SiO2
Mass (g)	0.534	0.115	0.424	0.450	283.89	P2O5
Mass (g) 2 (after sintering)	0.24644	0.141945	0.24412	41.5%		
				final weight/initial weight		

6% Solution

Molar ratio	2	1	2	3		
	$ZrO(NO_3)_2.2H_2O$	$NH_4H_2PO_4$	Na_2SiO_3.5H2O	$C_4H_6O_6$	H_2O	Total
grams	1.05	0.23	0.84	0.89	47.00	50.00
g water	30	7	10		47	
					Solids (%) tartaric acid	6.00%

5% Solution

Molar ratio	2	1	2	3		
	$ZrO(NO_3)_2.2H_2O$	$NH_4H_2PO_4$	Na_2SiO_3.5H2O	$C_4H_6O_6$	H_2O	Total
grams salts	0.80	0.17	0.64	0.67	47.72	50.0
g water	30	7.72	10		47.72	
	ZrO2	P2O5	Na2O	SiO2	Solids (%) tartaric acid	4.57 %
grams oxide	0.369	0.213	0.186	0.180		

Table 19: Sol calculations for $ZrO(NO_3)_2.2H_2O$ and $Na_2SiO_3.9H_2O$ precursors at 5% concentration.

Molar ratio	2	1	2	3		
	$ZrO(NO_3)_2$.$2H_2O$	$NH_4H_2PO_4$	Na_2SiO_3 .9H2O	$C_4H_6O_6$	→	$Na_3Zr_2Si_2PO_{12}$
Mr (g/mol)	267.23	115.03	284.2	150.09	MW (g/mol)	$3Na_2O+4ZrO_2+4SiO_2+P_2O_5$
mols	0.002	0.001	0.002	0.003	123.22	ZrO2
Solubility in water	soluble	~40g/dL = 400g/L	210g/L	210g/L	61.98	Na2O
30ml min cup					60.08	SiO2
Mass (g)	0.534	0.115	0.568	0.450	283.89	P2O5
Mass (g) 2 (after sintering)	0.24644	0.141945	0.24412	37.9%		
				final weight/initial weight		

5% Solution

Molar ratio	2	1	2	3		
	$ZrO(NO_3)_2$.$2H_2O$	$NH_4H_2PO_4$	Na_2SiO_3 .9H2O	$C_4H_6O_6$	H_2O	Total
grams	0.80	0.17	0.85	0.67	47.50	50.00
g water	30	7.5	10		47.5	
	ZrO2	P2O5	Na2O	SiO2	Solids (%) tartaric acid	5.00%
grams oxide	0.369	0.213	0.186	0.180		

Table 20: Sol calculations for $ZrOCl_2.8H_2O$ and $Na_2SiO_3.9H_2O$ precursors at 5% concentration.

Molar ratio	2	1	2	3		
	$ZrOCl_2.8H_2O$	$NH_4H_2PO_4$	Na_2SiO_3.9H2O	$C_4H_6O_6$	→	$Na_3Zr_2Si_2PO_{12}$
Mr (g/mol)	322.25	115.03	284.2	150.09	MW (g/mol)	$3Na_2O+4ZrO_2+4SiO_2+P_2O_5$
mols	0.002	0.001	0.002	0.003	123.22	ZrO2
Solubility in water	soluble	~40g/dL=400g/L	210g/L	210g/L	61.98	Na2O
30ml min cup					60.08	SiO2
Mass (g)	0.645	0.115	0.568	0.450	283.89	P2O5
Mass (g) 2 (after sintering)	0.24644	0.141945	0.24412	35.6%		
				final weight/initial weight		

5% Solution

Molar ratio	2	1	2	3		
	$ZrOCl_2.8H_2O$	$NH_4H_2PO_4$	Na_2SiO_3.9H2O	$C_4H_6O_6$	H_2O	Total
grams	0.97	0.17	0.85	0.67	47.34	50.00
water (g)	30	7.34	10		47.34	
	ZrO2	P2O5	Na2O	SiO2	Solids (%) tartaric acid	5.33%
grams oxide	0.369	0.213	0.186	0.180		

3.2.1 Sol synthesis: Powder

Chapter 5 involves the synthesis of NASICON powders, prepared from the two sol's described above (3.2). The preparation of the powders involves conventional furnace processing steps outlined in Table 21.

Table 21: Oven heat steps for sol powder synthesis.

dry (oven)	
Ramp (20°C/min)	10 mins
120°C	12 hours
Sinter (oven)	
Ramp (20°C/min)	37.5 mins
750°C	1 hour
Sinter (oven)	
Ramp (20°C/min)	50 mins
1000°C	3 hours

When forming a NASICON powder, the sol solution is placed in glass petri dish and heated in a chamber furnace (Carbolite Gero, CWF 1200) for 12 hours (10 mins ramp) at 120°C, atmosphere air (Figure 25).

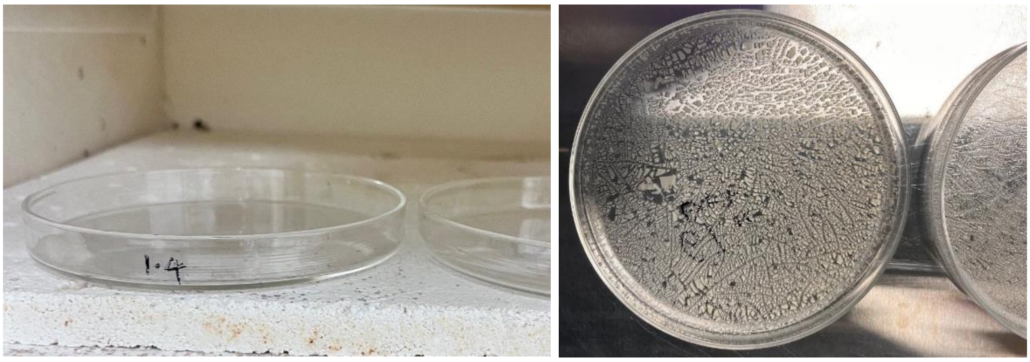

Figure 25: NASICON precursor sol dried to form xerogel powder

Powder is hand ground in an agate mortar and pestle (Sigma Aldrich) into a find powder. This is then placed in an alumina crucible (almath) and heated in a chamber furnace (Carbolite Gero, CWF 1200) for 1 hour (37.5 mins ramp) at 750°C, atmosphere air (Figure 26).

Figure 26: NASICON precursor powder after 750ºC calcination treatment.

After the 750ºC calcination step powder samples containing tartaric acid (TA) turn black at this point (left image) and samples without tartaric acid remain white (right image). The powder is then hand ground in an agate mortar and pestle (Sigma Aldrich).

The powder is placed in an alumina crucible (almath) and heated in a chamber furnace (Carbolite Gero, CWF 1200) for 3 hours (50 mins ramp) at 1000-1100°C, atmosphere air.

Figure 27: NASICON powder after sintering at 1000-1100°C

The NASICON powder should appear white in colour after sintering for all samples (with or without TA) and does not stick to the alumina crucible, shown in Figure 27.

3.2.2 Sol synthesis: thin layer

The two sol's described above in 3.2 are also used to prepare thin films on substrate in Chapters 6 and 7. The substrate preparation and chosen deposition technique (spray coating) is outlined in this section.

Substrates alumina (almath) or quartz (25 mm x 1.5 mm, agar scientific) are cleaned using a toothbrush and a 1-2% Hellmanex in deionised (DI) water solution. They are then rinsed with DI water and dried using nitrogen gas (N_2). The hellmanex solution is used for a second clean. The substrates are then rinsed with DI water, Acetone and IPA; and dried with nitrogen after each step. They are then plasma cleaned (diener electronic, using oxygen (O_2)) for 15 minutes (Figure 28).

Figure 28: Quartz glass in plasma cleaner post cleaning process.

A hot plate is set to 120°C or 150°C and substrates are placed on top. The sol is poured into a spray gun (Fengda, FE-130) with 0.5 nozzle. The sol is sprayed onto the heated substrates at 4 bar pressure (nitrogen genie, BOC) 20 cm from the hot plate (Figure 29). 1 vertical single pass is applied and wait 1 minute (layer heated) before 1 horizontal single pass (wait 1 minute, layer heated). These steps were repeated for a set number of passes, defined in the experimental chapters, dependant on the desired thickness.

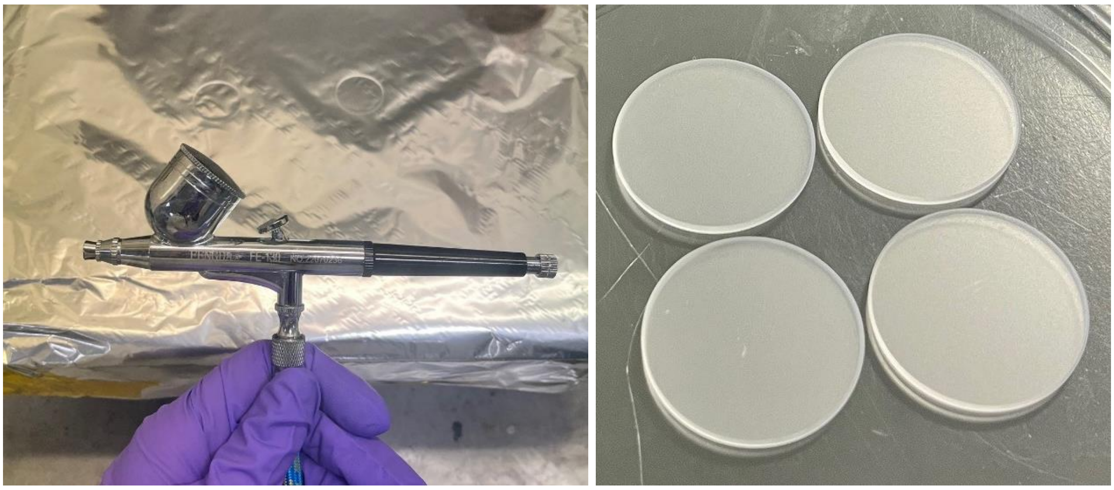

Figure 29: Quartz substrates spray coated using spray gun on hot plate.

After the sol has been deposited and dried on the substrate (alumina or quartz), the thin films are then heated conventionally or by NIR. If conventionally sintered they are placed in in a chamber furnace (Carbolite Gero, CWF 1200) in air and heated at 950-1000°C for 3 hours, with a ramp of 50 mins (20°C/min).

3.2.3 Sol synthesis: thin film NIR sintering

Once the sol (3.2) has been deposited and dried on the substrate (3.2.2) as a thin film, it is heated via the adphosNIR® 6 × 6 kW ceramic based NIR machine (Figure 30) machine using near infrared radiation.

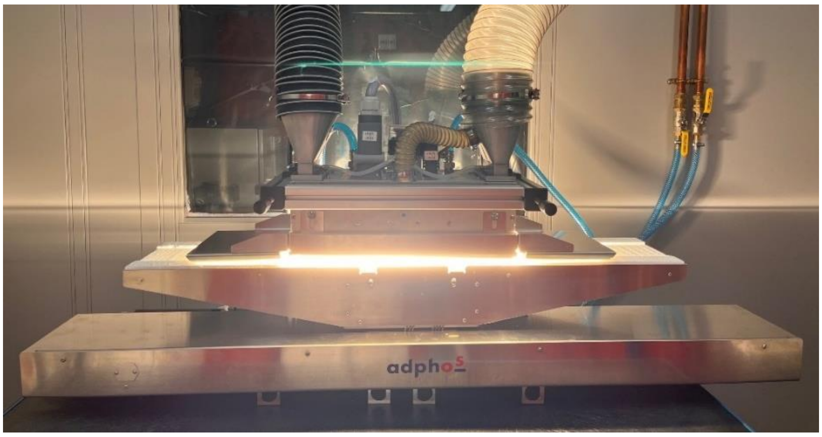

Figure 30: Adphos NIR machine

The NIR machine has a polytetrafluoroethylene (PTFE) platform on a conveyer belt, this material is utilised as it does not strongly absorb the NIR radiation and has good heat resistance. This is advantageous as it allows a greater lamp power to be used (critical in ceramic sintering) and minimises additional heating from the platform.

The NIR machine has a total power output of 36 kW, emitted from tungsten filament halogen lamps which intensity and radiation can be controlled (0-100%). The peak wavelengths of the emitted lamps are between 800 and 1200 nm, illustrated in Figure 124 in Chapter 7. In this work the lamps were operated at 90% or 100% power output for 15-60 seconds, exact parameters chosen are detailed in the experimental section (Chapter 7). The lamps are actively cooled, and there is a small distance between the lamps and the sample; this configuration allowed the NIR machine to heat the samples to temperatures >1000°C.

A temperature sensor was integrated into the NIR setup to determine the temperature the sample reached. However, due to calibration issues, rapid cooling of samples and the high power of the lamps used, it was not accurate for this work.

The output emissions of the NIR lamps, presented in Figure 124 Chapter 7, was carried out by Katherine Hooper. The analysis employed Ocean Optics spectrometers (HR2000+

UV/VIS and NIRQUEST256 NIR) to analyse output emissions at 200-2000 nm wavelengths, and the lamps absolute irradiance was measured for 25 seconds at wavelengths in this range. The spectrum was obtained from a different NIR machine (AdPhos NIR Coil Lab LV2 unit) to the one used in this thesis; however, this equipment uses lamps very similar to the NIR machine employed for this work.[172]

3.3 Characterisation techniques

3.3.1 X-ray Diffraction (XRD)

X-ray diffraction (XRD) was utilised in this thesis as the primary characterisation technique to determine if NASICON had formed. XRD is a non-destructive method that probes the crystal structure of a material at an atomic level. This technique involves directing an incident x-ray beam directed at a sample and measuring the scattered x-ray intensities (Figure 31).

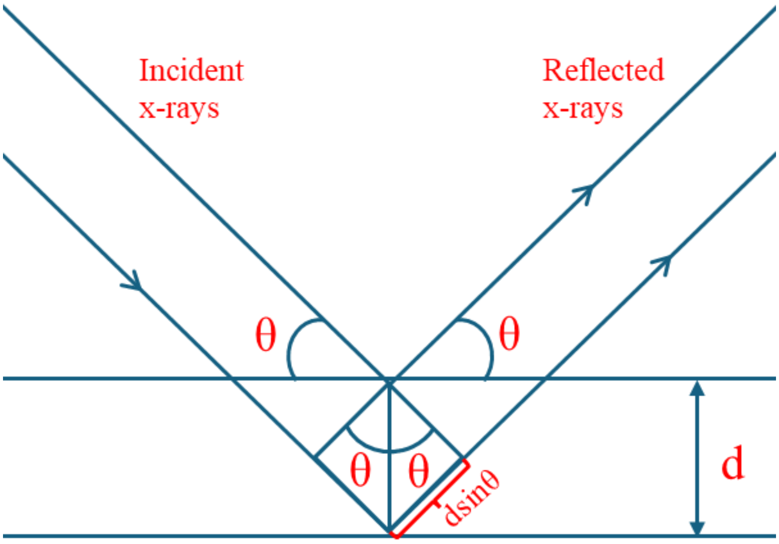

Figure 31: X-ray diffraction from crystal planes.

Bragg's Law describes the conditions necessary for constructive interference in x-ray diffraction; this occurs when the reflected waves combine to form a diffracted beam, the order of diffraction being an integer (n). Powder samples are commonly used in XRD characterisation as they contain millions of crystals in different orientations, this ensures some crystals will have the correct orientation for constructive interference and therefore diffraction to occur.[173] Bragg's law relates the angle between parallel incident and diffracted beams (2θ) to the wavelength (λ) of the x-rays and interplanar spacing (d) in the crystal lattice (Equation 8).[174]

Equation 8

$$n\lambda = 2d\sin\theta$$

For simple crystal structures the XRD peak positions indicate interatomic distances between atoms or crystals in a sample. 2θ can be related to the cell parameters, where larger d-spacings producing peaks at smaller 2θ angles.[174]

XRD peak intensities relate to the scattering factor of a sample, the types of atoms and their positions, providing qualitative information about sample chemistry and crystallinity. However, this relationship is more complex in multiphase samples, generally the greater the intensity of the peak the greater number of molecules in that phase or spacing.

In this work XRD was performed using two XRD machines: Bruker D8 discover and Bruker D8 Advance Figure 32. Both XRD's were used on powder and pellet samples, but the Bruker discover was used for thermal analysis and grazing incidence experiments.

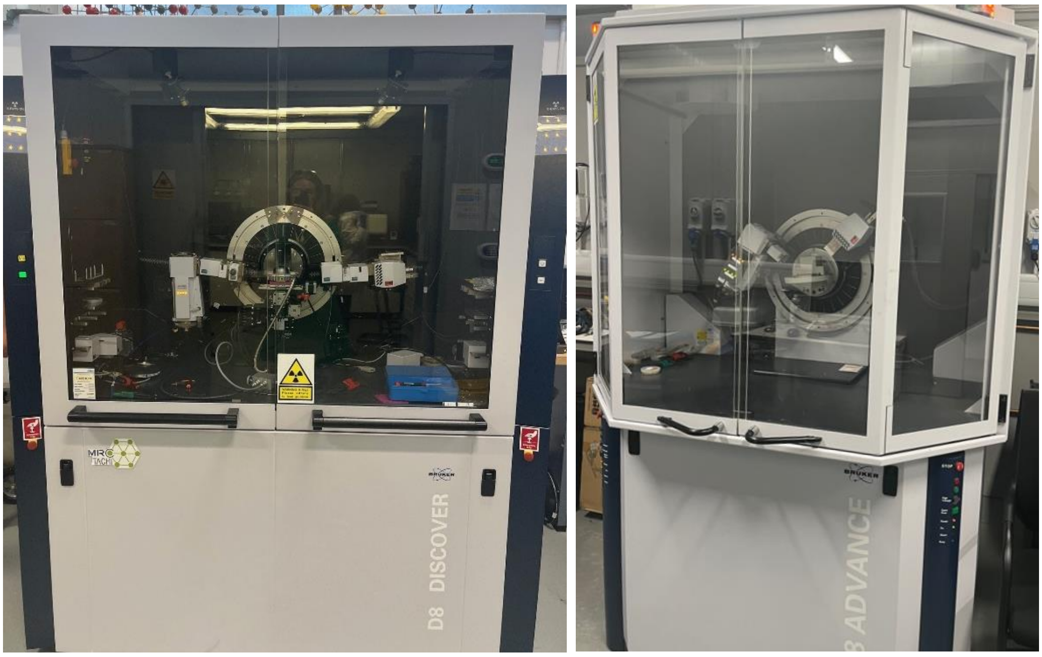

Figure 32: LEFT: Bruker D8 discover, RIGHT: Bruker D8 advance.

3.3.1.1 XRD scan

The crystallinity of the powders and films sintered was analysed by Bragg-Brentano diffractometer Bruker D8 Discover XRD using Cu-Kα radiation source (40 kV, 40 mA, $\lambda = 1.5406$ Å, angle range $2\theta = 10-60^{\circ}$) with a step size 0.02º, steps 2548, time/step 192 s, continuous scan. The samples were also analysed by the Bruker D8 Advance XRD using Bragg-Brentano diffractometer with a Cu-Kα radiation source (40 kV, 40 mA, $\lambda = 1.5418$ Å, angle range $2\theta = 10-60^{\circ}$) with a step size 0.02º, steps 2533, time/step 155 s, continuous scan.

3.3.1.2 Thermal stage XRD

Thermal XRD experiments were carried out in air using a DHS 1100 (Anton-Paar) mounted onto the D8 Discover, the set-up is shown in Figure 33. The equipment employs thermocouples to heat samples at rates of either 2°C/min or 20°C/min within a graphite dome. No cooling mechanism was required for this work and the precise experimental parameters are detailed in Chapter 6. Measurements were performed using a point source, a polycapillary optic, and a 2 mm collimator.

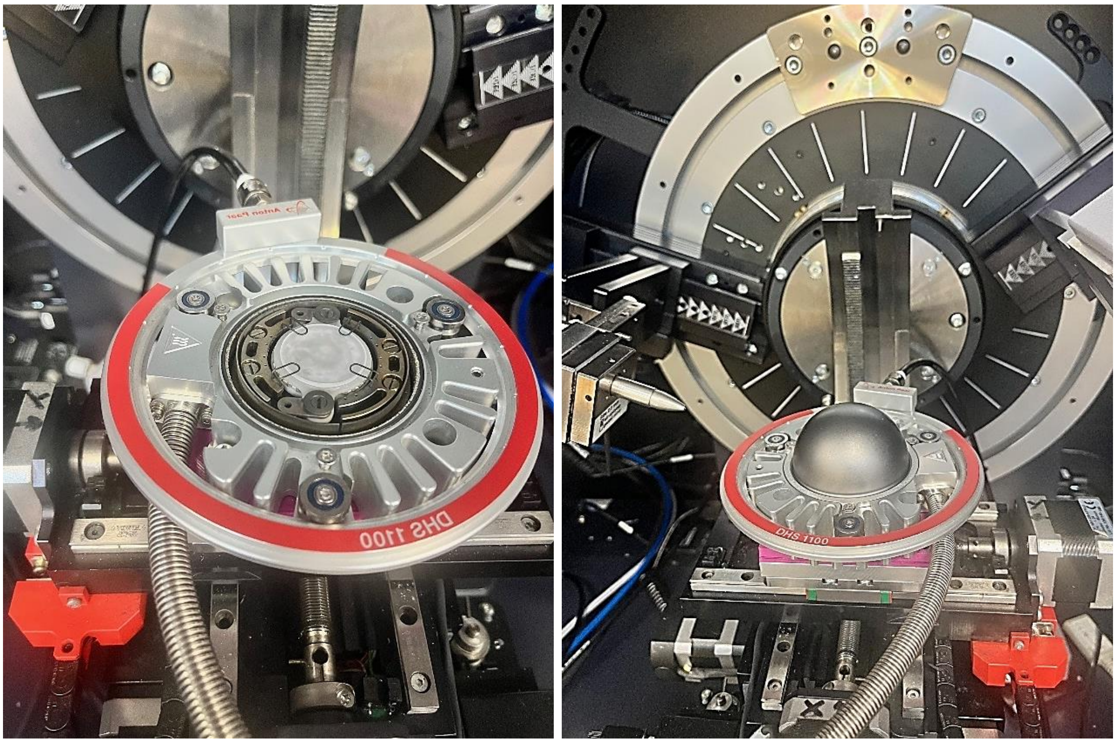

Figure 33: XRD thermal stage set up

3.3.1.3 Grazing Incidence XRD

Glancing Incidence XRD (GI-XRD) was measured in a true parallel beam mode. A Goebel mirror optic and axial soller system was used with the incidence angle fixed at 0.5°, 1.5°, 2.5°, 3.5° and 4.5° to control interaction depth.

3.3.1.4 Rietveld refinement

Rietveld refinement was employed to fit a calculated XRD pattern to the experiential data, to give quantitative analysis of the crystal phases present. The XRD powder data was analysed by Rietveld refinement using GSAS-II software by Professor Serena Margadonna. Initial input structural data, including the space group, atomic positions and site occupancies, was obtained from the Diffrac Eva software (using published sources) and the Crystallography Open Database (COD). The refinement process involved optimising several parameters: the scale factor, background (modelled using a Chebyshev polynomial function), atomic positions, site occupancies, and thermal displacement parameters. The site occupancies were constrained to the chosen chemical formulas, with oxygen atom occupancies fixed at 1. Peak shapes were described using Gaussian functions with both Gaussian and Lorentzian components refined. The refinement was considered complete when the goodness-of-fit indicators reached satisfactory values (Rwp and χ^2) and the difference plot showed minimal deviations. The lattice parameters for the 3 refinements are stated in Table 22, Table 23 and Table 24.

Table 22: Lattice parameters for solid-state NASICON pellet data.

NASICON	**a**	**b**	**c**	**alpha**	**beta**	**gamma**	**volume**
Value	15.631243	9.044577	9.211191	90.000	123.730	90.000	1083.037
sigmas	0.000715	0.000427	0.000399	0.000	0.002	0.000	0.040
ZrO_2	a	b	c	alpha	beta	gamma	volume
Value	5.146674	5.190416	5.329443	90.000	99.214	90.000	140.530
sigmas	0.003189	0.004340	0.004358	0.000	0.028	0.000	0.061

Table 23: Lattice parameters for powder data, sol Chloride NASICON powder (1000°C).

NASICON	**a**	**b**	**c**	**alpha**	**beta**	**gamma**	**volume**
Value	15.627076	9.037722	9.220632	90.000	123.877	90.000	1083.178
sigmas	0.001218	0.000743	0.000516	0.000	0.003	0.000	0.042
ZrO_2	**a**	**b**	**c**	**alpha**	**beta**	**gamma**	**volume**
Value	5.137693	5.214098	5.321108	90.000	99.118	90.000	140.743
sigmas	0.006690	0.010169	0.009094	0.000	0.048	0.000	0.101

Table 24: Lattice parameters for powder data, sol Nitrate NAISCON powder (1100°C).

NASICON	**a**	**b**	**c**	**alpha**	**beta**	**gamma**	**volume**
Value	15.702254	9.081259	9.195111	90.000	124.225	90.000	1083.138
sigmas	0.001340	0.000698	0.000637	0.000	0.004	0.000	0.086
ZrO_2	**a**	**b**	**c**	**alpha**	**beta**	**gamma**	**volume**
Value	5.144450	5.177874	5.339930	90.000	99.251	90.000	140.391
sigmas	0.003665	0.004093	0.004589	0.000	0.029	0.000	0.066

3.3.2 Optical Microscope

Optical images were acquired with SmartZoom Zeiss Primotech microscope, at magnifications <1000 x (camera 3 MP).

3.3.3 Scanning electron microscopy (SEM)

Scanning electron microscopy (SEM) analyses the surface topography of the samples in this thesis, offering superior depth of field and image quality at high magnifications compared to the optical microscope used.

The morphology of the NASICON pellets and films (oven and NIR sintered) were analysed by scanning electron microscopy (SEM, JEOL 7800F FEG-SEM). Beam parameters of 5 kV to 10 kV at 8-10 mm working distance. Samples were prepared for SEM by sputter-coating with 10 nm of Au/Pd. Both planar and cross-sectional sample images were captured.

Cross-sectional SEM image analysis was performed on selected samples. Preparation involved bisecting the sample using a laboratory glass cutting machine by means of a carbide wheel. No additional surface processing or polishing was carried out before sputter coating (10 nm Au/Pd) and mounting it into an SEM sample holder, with the cross-sectional surfaces orientated upward for imaging.

3.3.3.1 Energy dispersive Spectroscopy (EDS)

A number of samples were also characterised via Energy dispersive X-ray spectroscopy (EDS) with an Oxford Instruments Aztec EDS system, integrated onto the SEM.

3.3.4 UV-Vis-NIR

UV-Vis-NIR Spectrometer (Perkin Elmer, Lambda 750) was used to measure the absorbance of the fused silica substrate (quartz), graphite substrate and the different 'NASICON' films prepared. Spectra were collected using transmittance (%T) and reflectance (%R) modes in the wavelength range λ = 500-2000 nm (tungsten and D2 lamps). The detector used was InGAs (gain 20, response 0.20 s), slit width of 2 nm at data intervals of 5 nm.

3.3.5 DSC-TGA

Thermogravimetric Analysis - Differential Scanning Calorimetry (DSC-TGA, Seteram Labsys Evo (STA)) measurements were carried out on a xerogel powder, made as a sol and dried at 120°C for 12 hours. This characterisation was carried out in air in small alumina crucibles; and the temperatures employed were 25-1200ºC at a step size of 20ºC/min.

3.3.6 EIS

Electrochemical impedance spectroscopy (EIS) uses alternating current (AC) modulation over a chosen frequency range to observe the response at a steady state. In this work EIS is used to characterise ionic transport in the solid electrolyte NASICON pellet. This is done using a Nyquist plot that studies the impedance values and behaviour over a range of AC frequencies.

EIS was conducted on three distinct samples: a solid-state NASICON pellet (Chapter 4), a sol thin film sample (Chapter 6) and an NIR processed thin film (Chapter 7). Measurements were performed using a Gamry Potentiostat (Gamry, Reference 600+), selected for its capacity for fast, low-current measurements with reduced noise due to the use of short cables.

NASICON pellets (15 mm diameter x 2 mm thickness) were prepared by sputter coating platinum through a mask and applying silver conductive paint (RS PRO) to the pellet surfaces (Figure 34(a)), ensuring nothing is coated on the edges of the pellet. Gold pins (held with silver conductive epoxy – RS PRO resin) were used for robust crocodile connection.

Sol thin film samples (both oven and NIR processed) deposited on quartz substrates (25 mm x 1.5 mm), underwent similar preparation (Figure 34(b)); including platinum sputter coating, silver conductive paint application and copper foil attachment for robust crocodile clip connections. A mask was utilized to ensure a gap between the two electrodes remained uncoated.

This sample preparation served as the contact electrodes for the 3 samples (Figure 34); the connections have a much higher conductivity than the NASICON, so they tend to zero.

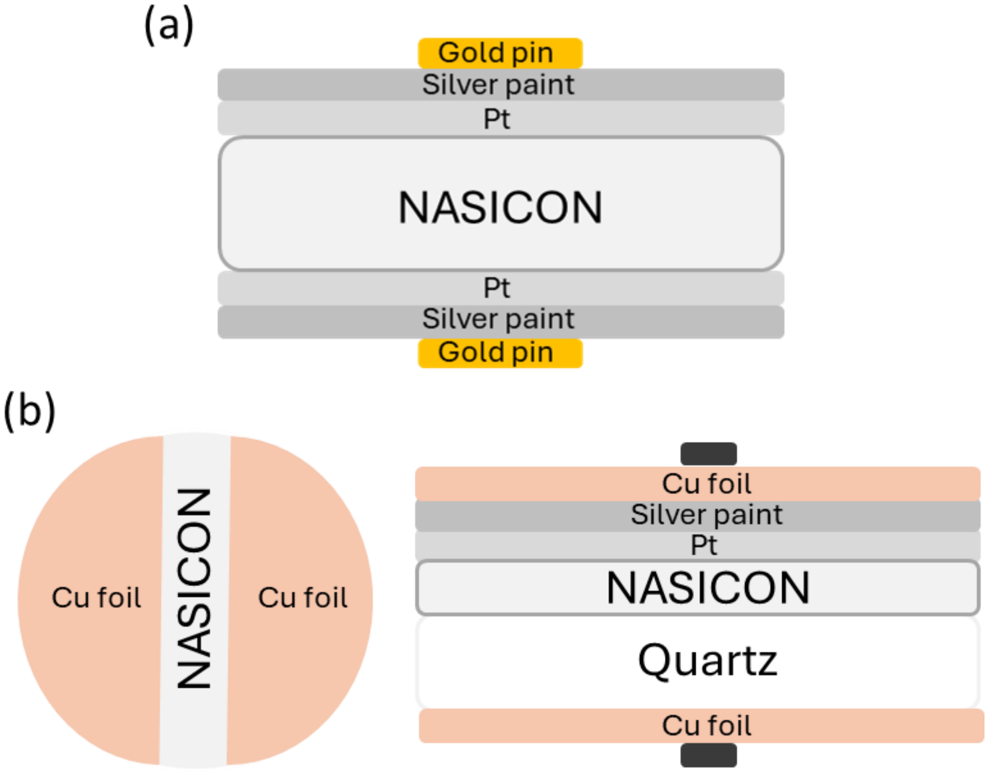

Figure 34: How contacts are made for (a) NASICON solid-state pellets and (b) NASICON thin films on quartz (oven and NIR processed).

All cells used a 2-electrode set-up and samples were placed in a faraday cage (Faraday Shield, Gamry) to reduce noise from stray signals (Figure 35). EIS was carried out at an amplitude of ±10mV with a frequency range of 1Hz and 3MHz.

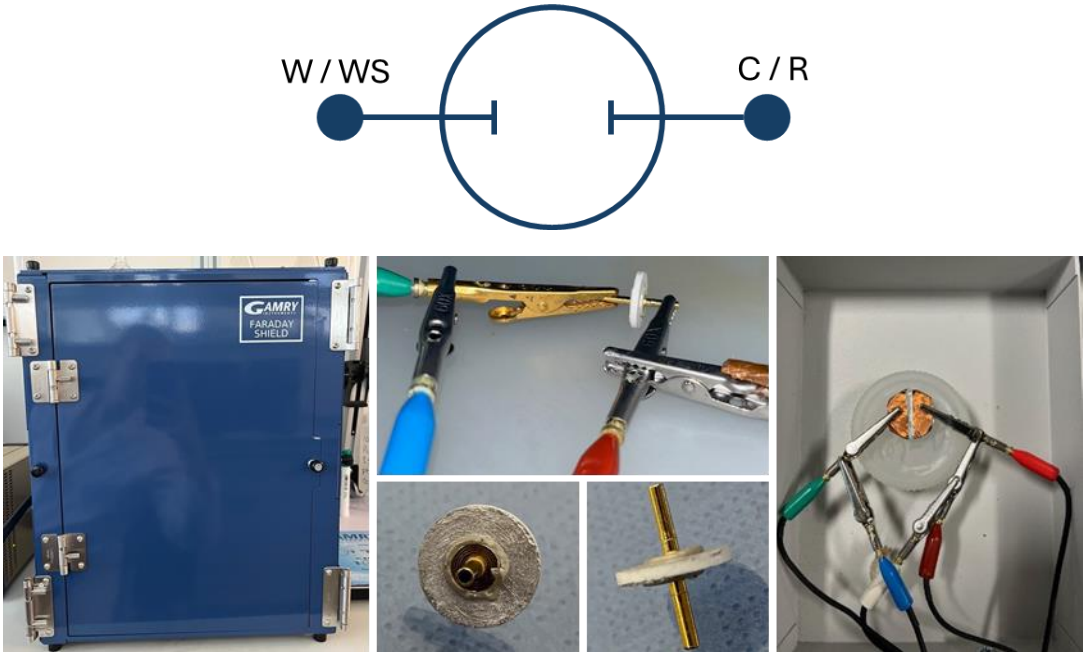

Figure 35: (1) diagram showing 2 electrode set up (2) image of faraday shield (gamry) (3) EIS set up for solid-state pellet samples (4)+(5) Sample preparation for solid-state NASICON pellet EIS (6) EIS set up for thin-film NASICON on quartz samples.

The EIS data was plotted as a Nyquist plot and modelled using Zview; the equivalent circuit used to fit the impedance data is shown in Figure 36.

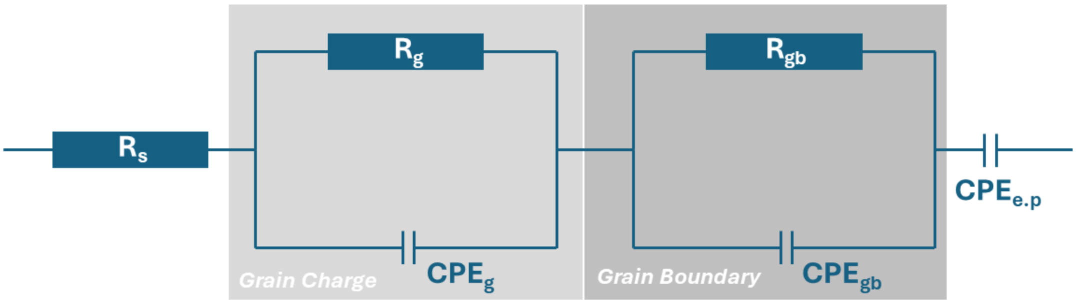

Figure 36: Equivalent circuit used to fit EIS Nyquist plot.

The ionic conductivity of the pellet was determined from the Zview/Nyquist plot data.[175]

Chapter 4 – Solid-state NASICON Synthesis

4.1 Introduction

This chapter involves the formation of a NASICON electrolyte by employing the solid-state synthesis technique. The origins of the process were from the macro-precursor experiment in Jalalian-Khakshour's (2020) paper[79], in which NAISCON pellets were synthesised via a solid-state reaction with a final sintering step of 1230°C, previously described in Chapter 2.

The aim of this chapter is to further understand the solid-state synthesis of NASICON, and to optimise the production of a NASICON pellet for Na-ion battery applications.

Equation 9

$$ZrO_2 + SiO_2 + Na_3PO_4.12H_2O \rightarrow Na_3Zr_2Si_2PO_{12}$$

Equation 9 defines the chemical reaction for the experiment, indicating the chosen precursor chemicals. The following experiments use stoichiometric ratios (2:2:1) of reactant chemicals, to determine whether NASICON can form in the desired composition without excess quantities of reactants (eg. excess Na). Micron sized precursor chemicals (ZrO_2 – 5 µm, SiO_2 - 216 µm) were used in this work, compared to nanoparticle equivalents, due to safety and the cost of material for industrial scale up.

Solid-state synthesis is a multistep, labour-intensive method, that involves several heating and ball milling steps. Table 25 defines the nomenclature used to identify different stages in the solid-state synthesis method.

Table 25: Nomenclature used to identify different stages in the solid state-synthesis method.

1.1	1st ball mill + dry (80°C) 16.5 hours
1.2	1st calcination (400°C) 5 hours
1.3	2nd calcination (1100°C) 16 hours
1.4	2nd ball mill + dry (80°C) 16.5 hours
1.5	Sintering step (1150 – 1230°C, final sample) 16 hours

In this work, the total thermal processing time required for drying, calcination, and sintering of NASICON to produce a solid-state pellet (using a conventional oven and tube furnace) was 70 hours. The solid-state synthesis technique is energy intensive due to the high temperatures required, this can cause elemental evaporation or the formation of unwanted phases.[89] Therefore, after each experimental stage, characterisation was carried out to determine the chemistry of the material – to understand the stage at which NASICON crystals and secondary phases begin to form. XRD determined the crystalline structure and chemical composition, while SEM was used to invesitgate the surface morphology of the crystals.

This method has a low % yield due to material loss after the ball milling step, the average % yield loss after ball milling is 65%. The final sintering step was the most challenging, with temperature and crucible selection significantly impacting the NASICON pellet synthesised.

4.2 Initial experiments

The aim of the initial experiments was to further understand the impact of each of the steps in NASICON formation using the solid-state synthesis technique to aid future process optimisation. The sintering step (1.5) in this experiment was carried out at 1230°C for 24 hours. The Covid-19 global pandemic caused difficulties in obtaining platinum foil, which was the standard method used previously Jalalian-Khakshour's (2020)[79], and therefore ceramic porcelain crucibles alone were used at this stage.

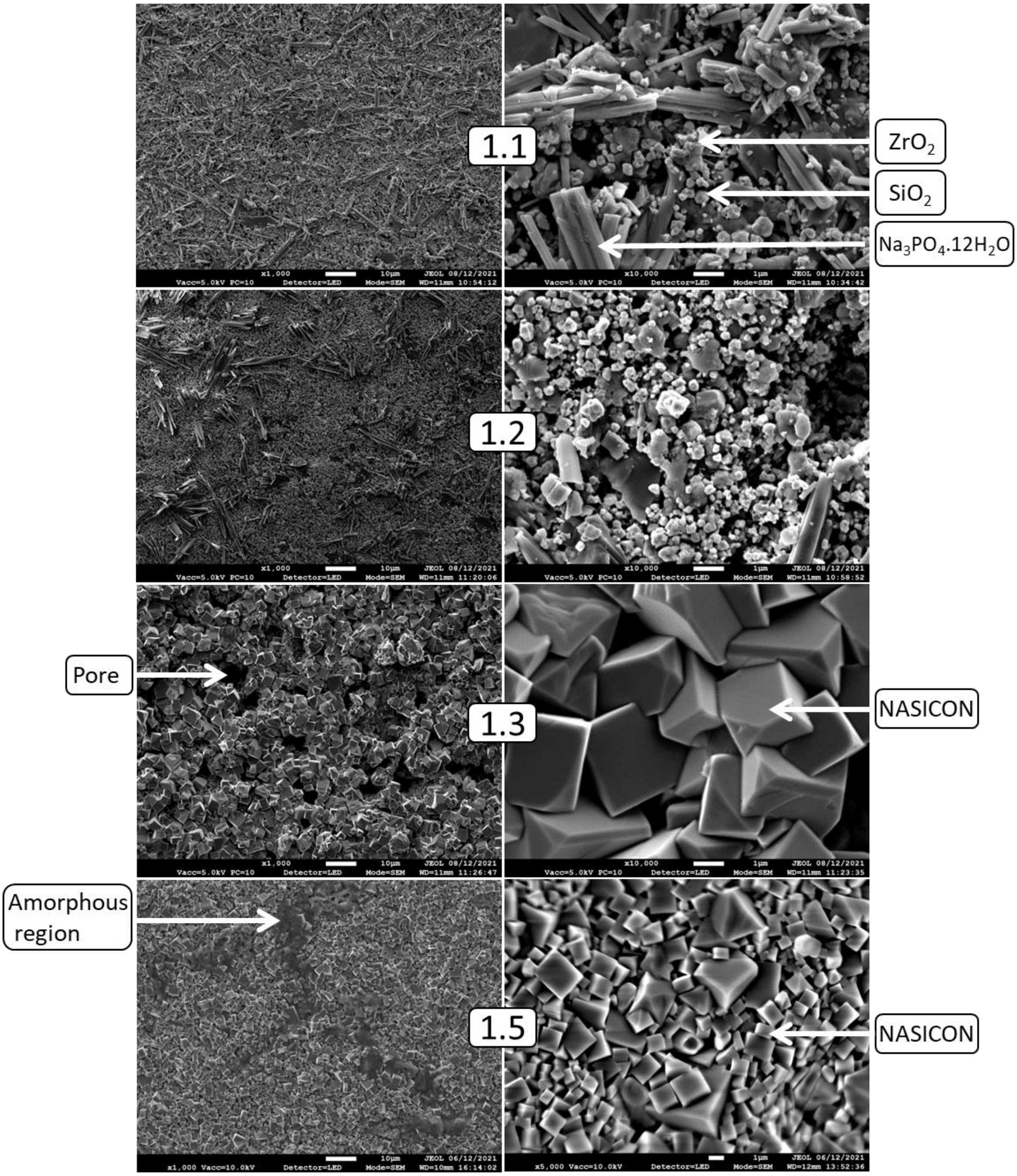

Figure 37:SEM images of NASICON precursor pellet. Pellet at 1.1, 1.2, 1.3 and 1.5 stage: 1st ball mill (2 hours, 120 rpm), sieved, dried (80°C, 16 hours conventional furnace), pellet pressed, 1st calcination (400°C, 5 hours conventional furnace), hand grind, pellet pressed, 2nd calcination (1100°C, 16 hours, argon tube furnace), hand grind, ball milled (3 hours, 120 rpm), sieved, dried (80°C, 16 hours conventional oven), pellet pressed and sintered (1230°C, 24 hours, argon tube furnace).

After the first mixing stage (1.1) the SEM images suggest the precursor chemicals are apparent in the powder (Figure 37). By comparing with SEM images in literature, it is possible to identify the smaller irregular shaped particles observed as ZrO_2[176] and SiO_2[177]. Additionally, $Na_3PO_4.12H_2O$ is documented in the literature as having long, tubular shaped particles[178], which are also visible in the SEM images.

Post 1st calcination (1.2) the pellet contains particles with very similar morphologies to that of the 1.1 powder. These chemicals are the unreacted precursor chemicals; however, during the 400°C calcination the tubular crystals reduce in quantity (Figure 37).

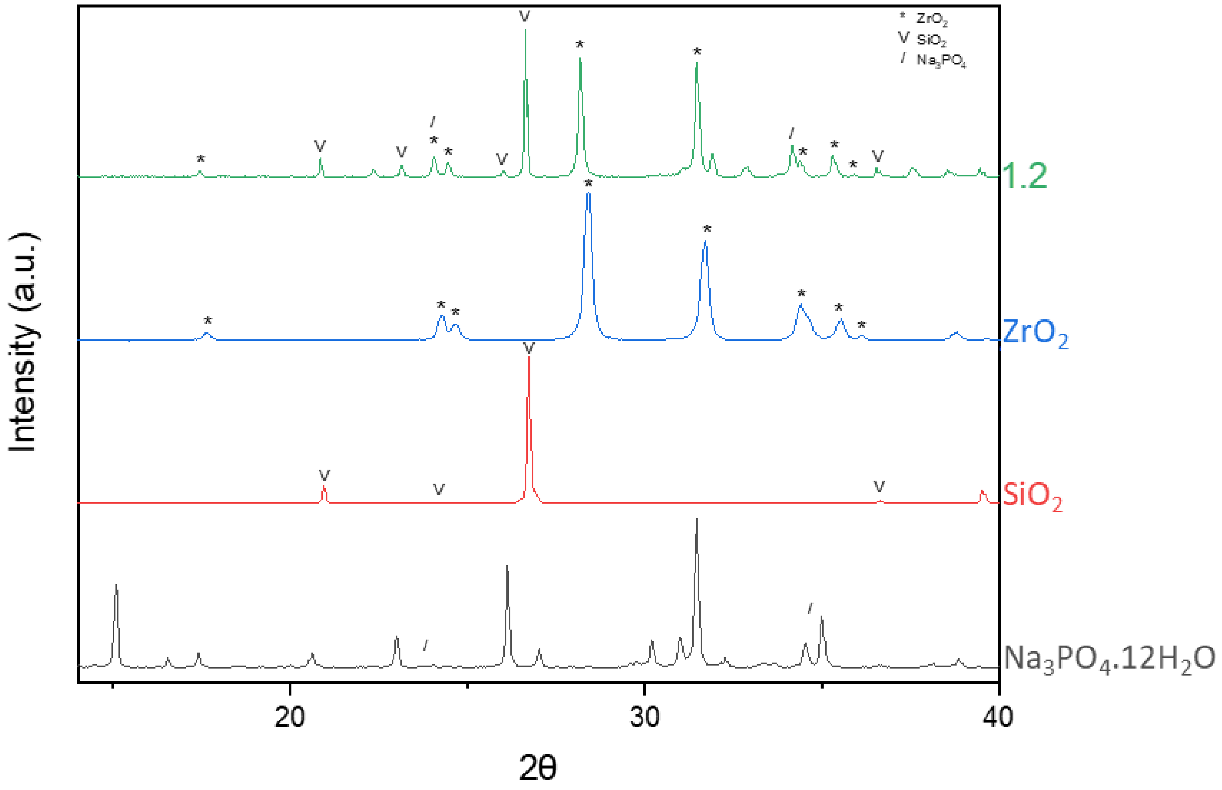

Figure 38: XRD pattern of precursor chemicals ($Na_3PO_4.12H_2O$, SiO_2 and ZrO_2) versus intermediate 1.2 stage pellet.

To validate conclusions drawn from the SEM images and determine the composition of the pellet, Figure 38 compares XRD's of the 400°C calcinated pellet (1.2) to the powders of the starting chemicals. It can be confirmed that the data is dominated by the precursor chemicals:

- ZrO_2: (Space group (SG) 14, Crystallography open database ID (COD) 9007485[179]) 17.5º, 24º, 24.5º, 28.2º, 31.5º, 34.4º, 35.3º, 35.9º.
- SiO_2: (SG 119, COD 4124645[180]; SG 152, COD 1011097[181]; SG 154, COD 1535066[182]) 20.8º, 23.1º, 26º, 26.6º, 36.5º.

- Na_3PO_4: (SG 225, COD 1525646[183]) 24°, 34.1°.

This substantiates the conclusions drawn from the particles observed in the 1.1 and 1.2 SEM images. In this work, it appears ball milling and the 400°C heating has initiated the growth of some $Na_2O_7Si_2Zr$ (SG 2, COD 9012687[184]) crystals at 22.3° and 32.9°; this could attribute to the glassy phases seen in the SEM images. The investigation of ball milling in relation to NASICON crystal formation has not been documented in literature thus far. Overall, it appears that limited reactions occur during ball milling and at these thermal conditions, compared to the latter calcination and sintering steps.

Many of the $Na_3PO_4.12H_2O$ peaks (particularly the 15° and 30° peaks) are no longer present in the calcinated pellet; the volatility of the compound and the loss of structural water. To confirm this is the correct conclusion, future experiments are needed involving vacuum drying the powder and XPS analysis.

The second calcination step at 1100°C (1.3) SEM images have shown a significant change in morphology (Figure 37), resulting in the formation of cubic hexahedron crystals. Gaps between grains are also present, revealing pores in the NASICON precursor, which if exist in the final pellet would be detrimental to conductivity and electrical performance.[103]

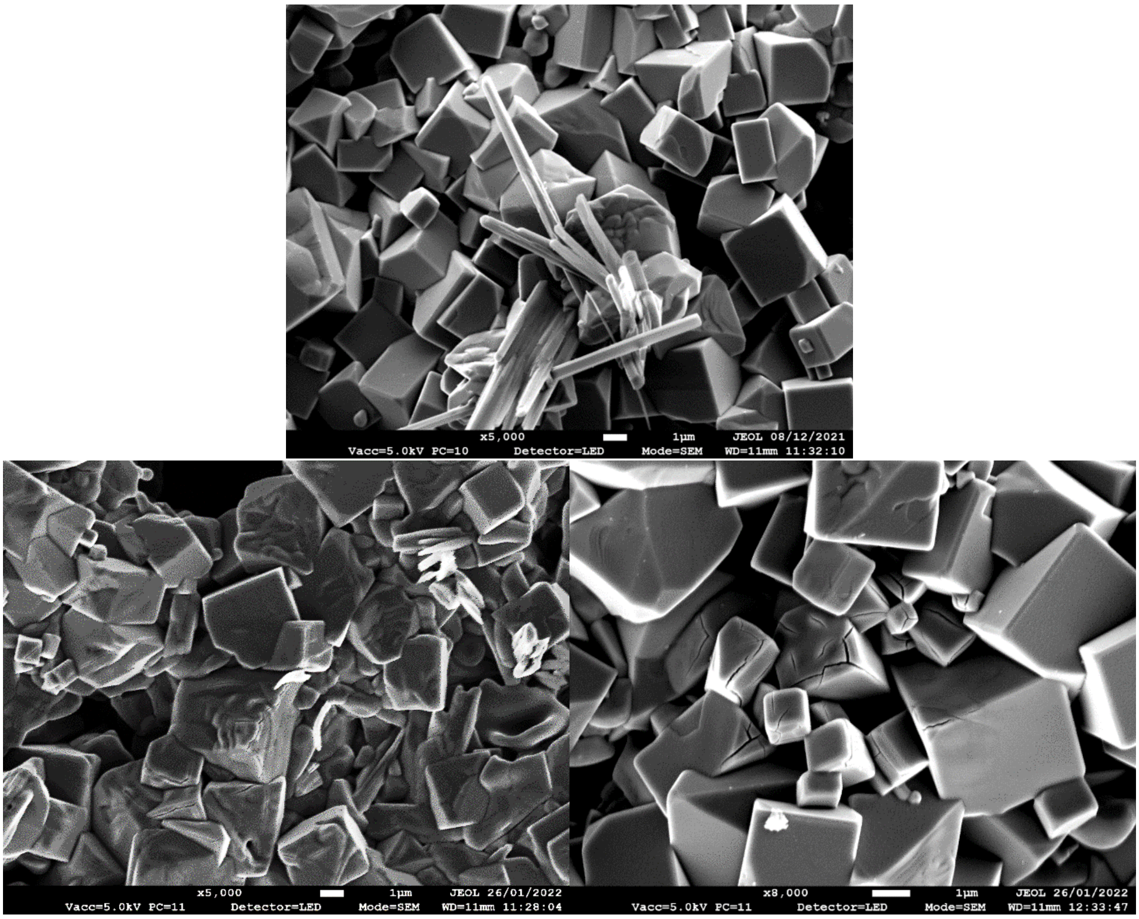

Figure 39: SEM image of pellet at 1.3 intermediate synthesis stage, depicting cubic crystals and unreacted precursor chemicals.

The cubic crystals are present at this stage (1.3), while the assigned long tubular particles ($Na_3PO_4.12H_2O$) and smaller irregular shaped particles (ZrO_2, SiO_2) remain present (Figure 39). This suggests some precursor chemicals have not fully reacted after the second calcination step.

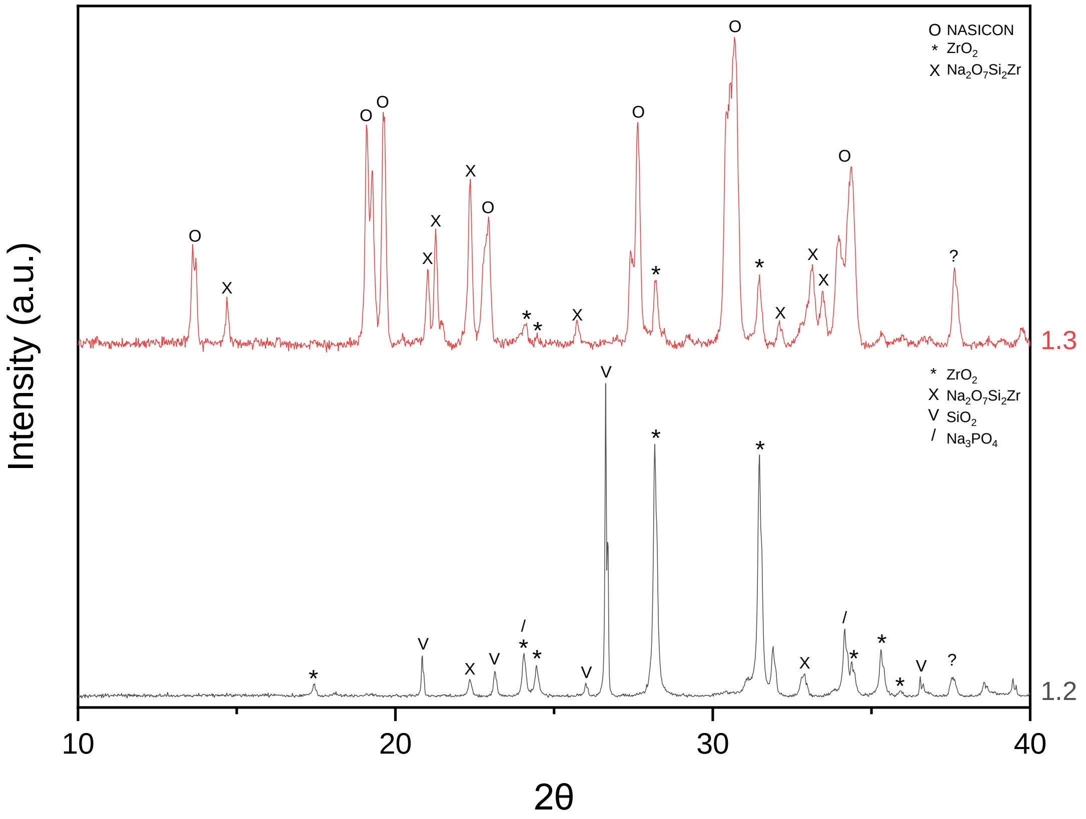

Figure 40: XRD of pellet after first calcination at 400°C (1.2) vs 2nd calcination at 1100°C (1.3).

XRD data for the 1.3 pellet (Figure 40) illustrates some NASICON (SG 15, COD 1530659[185]) peaks have begun to form at 13.7º, 19.2º, 19.7º, 22.9º, 24.1º, 27.6º, 30.6º and 34.4º. This verifies the cubic crystals in the 1.3 SEM images (Figure 37) and evidences that the composition of the 1.3 pellet is no longer primarily precursor chemicals. There are secondary phases of ZrO_2 (SG 14, COD 1528984[186]) at 24.5º, 28.2º and 31.5º. As well as the presence of $Na_2O_7Si_2Zr$ (SG 2, COD 9012687[184]) 14.7º, 21º, 21.3º, 22.4º, 25.7º, 32.1º, 33.1º and 33.5º; all the SiO_2 appears to have transformed into this intermediate structure.

There is high reproducibility of the solid-state reaction process up to 2nd calcination stage (1.3), proven by many repeats carried out, verified by XRD (Figure 42, Figure 50, Figure 55, Figure 59).

An XRD was carried out (Figure 42) to see if chemical changes had occurred after the second ball milling step (1.4). The 1.3 and 1.4 XRD are extremely similar, suggesting no chemical change took place. The main difference between the two stages is the intensity of some of the secondary phase peaks which have increased after ball milling and drying. This may simply be due to the XRD orientation or due to smaller grain sizes after ball milling.

The final sintering step (1.5) and finished pellet in Figure 37 indicates the conversion of precursor chemicals (no longer present) and the formation of NASICON crystals. The SEM images show NASICON of different grain sizes. Pores between crystal grains appear to have decreased from the 1.3 stage, suggesting the density of the pellet has increased. This is evidenced by the reduction in mass of the 1.3 pellet vs the 1.5 pellet, as well as from the approximate density calculations (Table 26).

Table 26: Illustrating the volume (measured using a caliper, Facom), mass (measured using an analytical balance, Fisher Scientific) and density (calculated, ρ = m/v) of NASICON 1.3 and 1.5 pellets.

	Thickness (mm, ±0.05)	**Diameter (mm, ±0.05)**	**Mass (g, ±0.0001)**	**Density (g/cm^3)**
Before sintering (1.4)	2	16	1.0251	2.55
After sintering (1.5)	2	15	0.9889	2.80

Furthermore, in the 1.5 SEM images black glassy/molten phases have formed – this is indicative of secondary phase formation.

XRD characterisation (Figure 41) reveals the successful synthesis of NASICON (SG 15, COD 1530661[185]) after the final sintering step (1.5), shown by peaks at 13.5°, 19.3°, 22.7°, 27.4°, 30.4°, 34.1°, 41.4°, 44°, 46.5°, 50°, 53.4° and 58°. Due to the presence of doublet peaks there may be some phase distortion of the NASICON with hexagonal and rhombohedral NASICON phases.

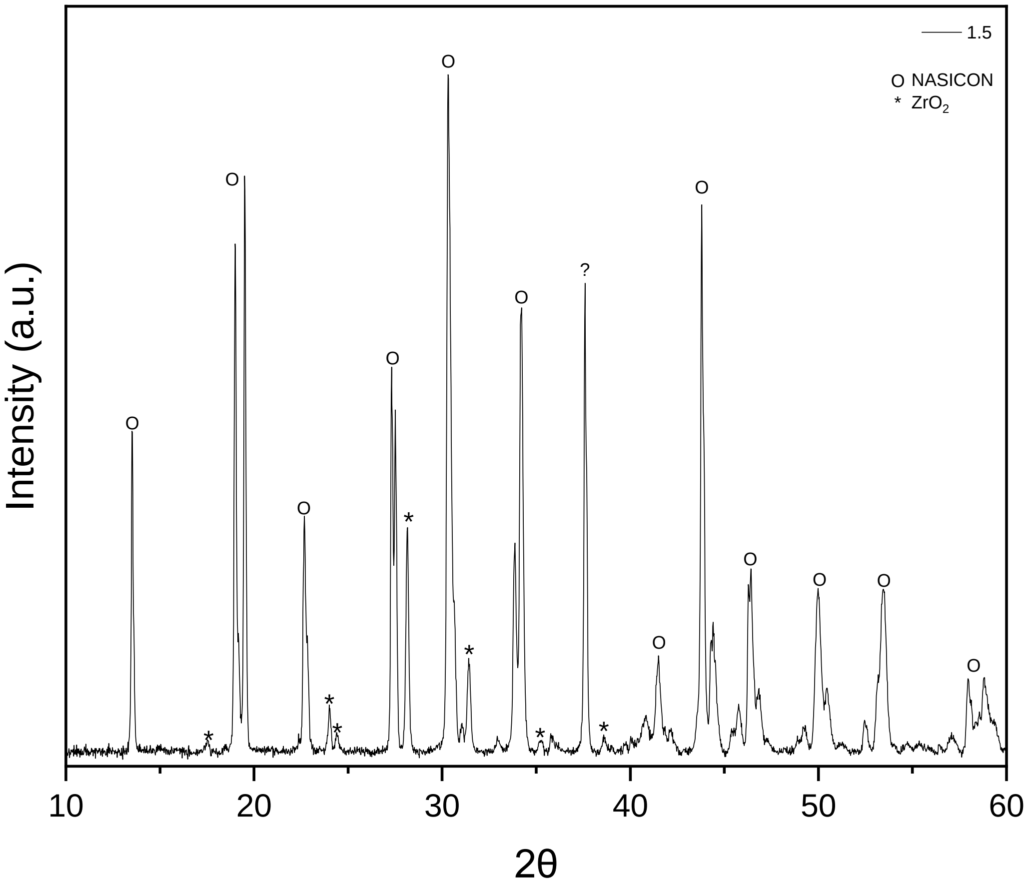

Figure 41: XRD of final NASICON pellet (1.5). Final sintering conditions - 1230°C, 24 hours, in argon (tube furnace) and pellet placed in a ceramic crucible.

Some secondary phases have formed in the final pellet, although the amount has reduced compared to 1.3 XRD (Figure 41). ZrO_2 (SG 14, COD 2108450[187]) secondary phases are present at 17.4°, 24°, 24.4°, 28.1°, 31.4°, 35.2° and 38.6°. There is also an unknown phase at 37.4°, potentially SiO_2 (SG 24, COD 9006301[188]).

ZrO_2 has good thermal stability, compared to Na and P which have high volatility at sintering temperatures (Table 27). Due to the volatility of these elements, ZrO_2 becomes the dominant secondary phase between grains in NASICON formation. Literature shows ZrO_2 is a very common secondary phase, and its presence can reduce ion conduction.[109]

Table 27: Boiling and melting points of precursor chemicals and elements.

	ZrO_2	SiO_2	$Na_2PO_4.12H_2O$	Na	P	IPA
Boiling point	5000°C	2230°C		883°C	280.5°C	82°C
Melting point	2700°C	>1600°C	75°C (elimination of water crystallisation)	97°C	44°C	(-)81.5°C

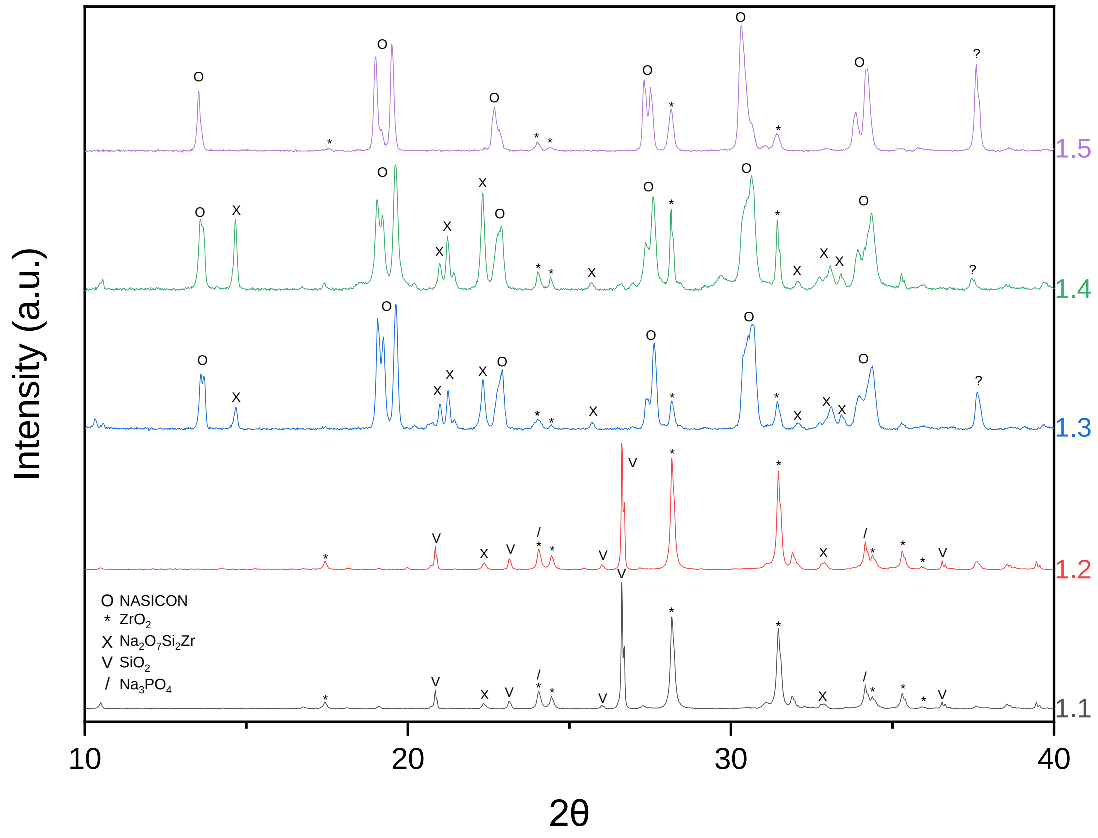

Figure 42: XRD's at different stages in the solid-state synthesis process of NASICON. ***1.1:*** *1st ball mill (2 hours, 120 rpm), sieved, dried (80°C, 18 hours conventional furnace).* ***1.2:*** *1.1 + pellet pressed, 1st calcination (400°C, 5 hours conventional furnace).* ***1.3:*** *1.1 + 1.2 + hand grind, pellet pressed and 2nd calcination (1100°C, 16 hours, argon tube furnace).* ***1.4:*** *1.1 + 1.2 + 1.3 + 2nd ball mill (3 hours, 120 rpm) and dry (80°C, 18 hours conventional furnace).*

The aim of the work was to understand the solid-state synthesis and the point at which a chemical change occurs (Figure 42), Table 28 gives an overview of the conclusions collated from characterisation analysis. The data shows that at 1.1 and 1.2 the peaks are an amalgamation of the precursor chemicals, and at 1.3 and 1.4 stages the data is dominated by secondary phases. Both the figure and the table illustrate that NASICON structures start to form after the first calcination step (1.3) but NASICON is not fully transformed until the final sintering step (1.5). This finding revealed greater depth of understanding regarding the chemical formation mechanism, which had not been previously addressed in the literature. The results demonstrate that to improve the final pellet properties, modifications should be limited to the final sintering step (1.5), thereby reducing the number of variables in future experiments.

Table 28: Overview of characterisation.

	Procedure	**SEM**	**XRD**
1.1	1st ball mill + dry (80°C)	Precursor particles	No chemical change
1.2	1st calcination (400°C)	Precursor Particles	No chemical change
1.3	2nd calcination (1100°C)	Cubic hexahedron crystals	Some NASICON peaks
1.4	2nd ball mill + dry (80°C)	Cubic hexahedron crystals	Some NASICON peaks
1.5	sintering step (final sample)	NASICON crystals (melted)	NASICON formed + secondary phases

4.3 Crucible investigation

The most significant issue during the solid-state synthesis experiments was the pellet sticking to the ceramic crucible during the final sintering step. This is problematic as it means the NASICON pellets cannot be incorporated into Na-ion battery cells as solid electrolytes. A range of experiments were undertaken to investigate the suitability of different crucibles, to prevent the NAISCON from sticking at these high temperatures.

The focus of this work was to understand the impact of crucible type on the formation of NASICON. To do this, variables were introduced in the final sintering step (1.5) to produce a NASICON pellet. The sintering variables altered in these experiments included the temperature, length of time and crucible material - all 1.5 steps were carried out in an inert environment (argon).

In the previous section standard ceramic (low purity) crucibles were employed during the final sintering step, chosen due to the materials high operating temperature necessary in sintering.

Figure 43: Image of NASICON pellet post sintering (1.5) in ceramic crucible.

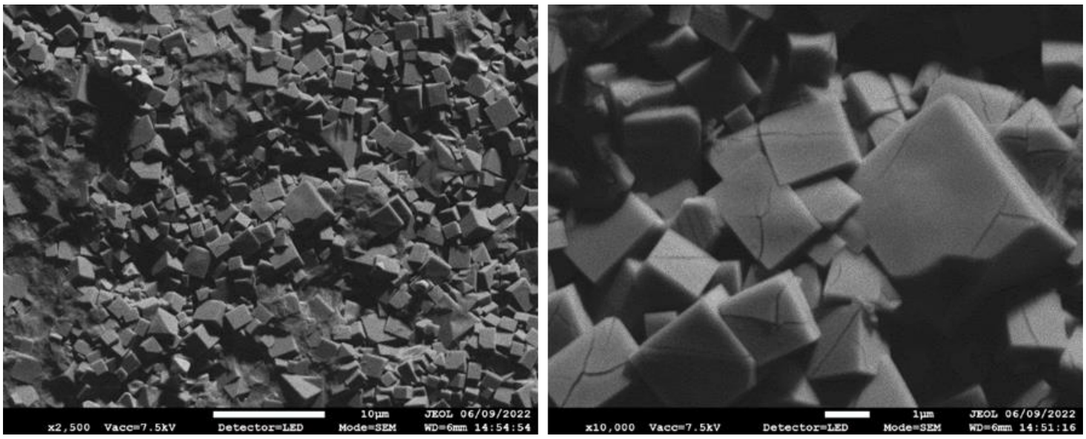

Figure 44: SEM images of NASICON pellet at 1.5 stage: sintered (1230°C, 24 hours, argon tube furnace, ceramic crucible).

The final NAISCON pellet (1.5) was melted/stuck to the ceramic crucible (Figure 43), which is visible to the naked eye. SEM images (Figure 44) illustrate how the surface of the pellet has a large area of molten/glassy phase. Cracks have also developed on the NASICON crystals, which are not present at the 1.3 stage. This suggests the cracks and glassy phases form due to the high temperatures involved in the final sintering step, the temperature and time employed for this experiment was the highest and longest used in this thesis. As previously stated in Chapter 2 (literature review) it is known that extended heating and high temperatures lead to increased secondary phase formation. Furthermore, the fusion of the pellet to the crucible, rendering it virtually inseparable, suggests an interaction between the crucible material and the NASICON pellet during sintering.

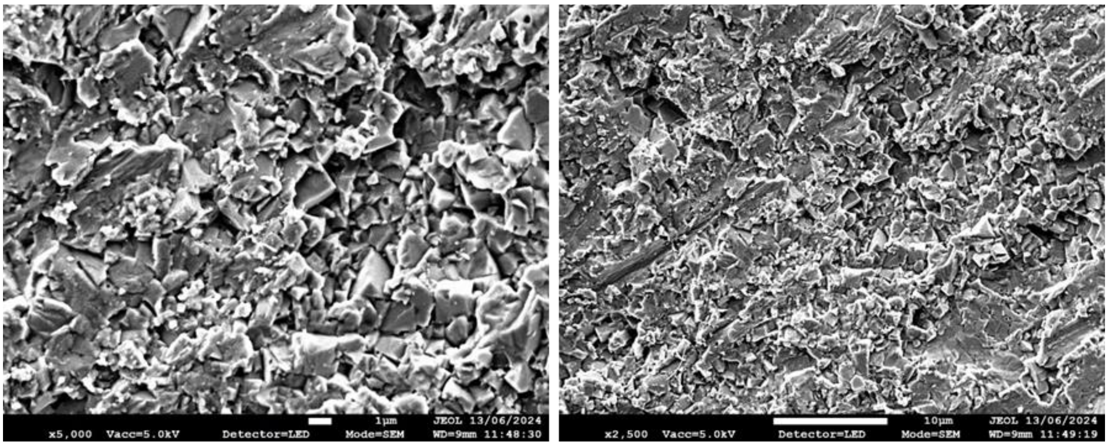

Figure 45: SEM cross section of 1.5 NASICON pellet fused to ceramic crucible – NASICON area captured

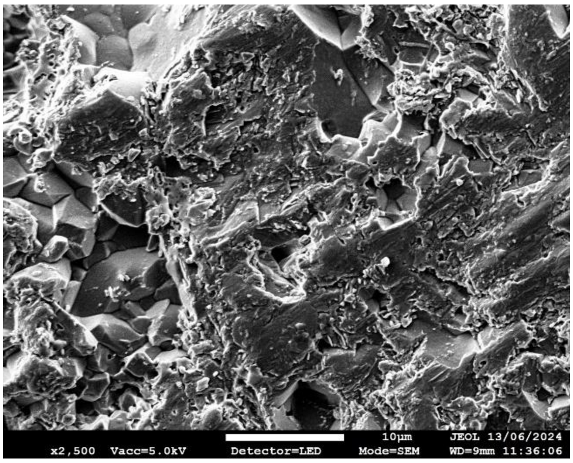

Figure 46: SEM cross section of 1.5 NASICON pellet fused to ceramic crucible – ceramic crucible area captured

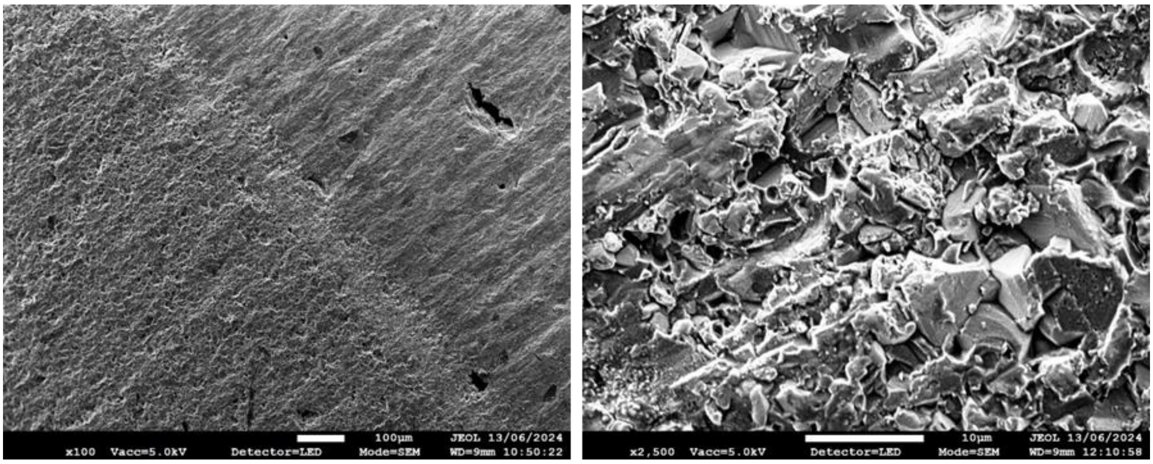

Figure 47: SEM cross section of 1.5 NASICON pellet fused to ceramic crucible – interface NASICON (top right) / ceramic (bottom left).

Figure 45 shows a cross-section of the bulk NASICON, where hexagonal crystals are visible; compared to Figure 46 which illustrates a cross-section of the ceramic crucibles composition. SEM cross sectional images of the interface between the NASICON and the ceramic crucible (Figure 47) do not show a gap or crack between the two materials, instead there is a visible line where an intermediate material appears to have formed (roughly 100 µm) and therefore a chemical reaction has occurred. This is supported by EDS data (Figure 48), which illustrated the intermediate material contained Al as well as Na, Si and P. The analysis indicates no Zr diffusion into the intermediate layer. Additionally, it reveals carbon contamination, likely originating from the carbon tape used during SEM sample preparation.

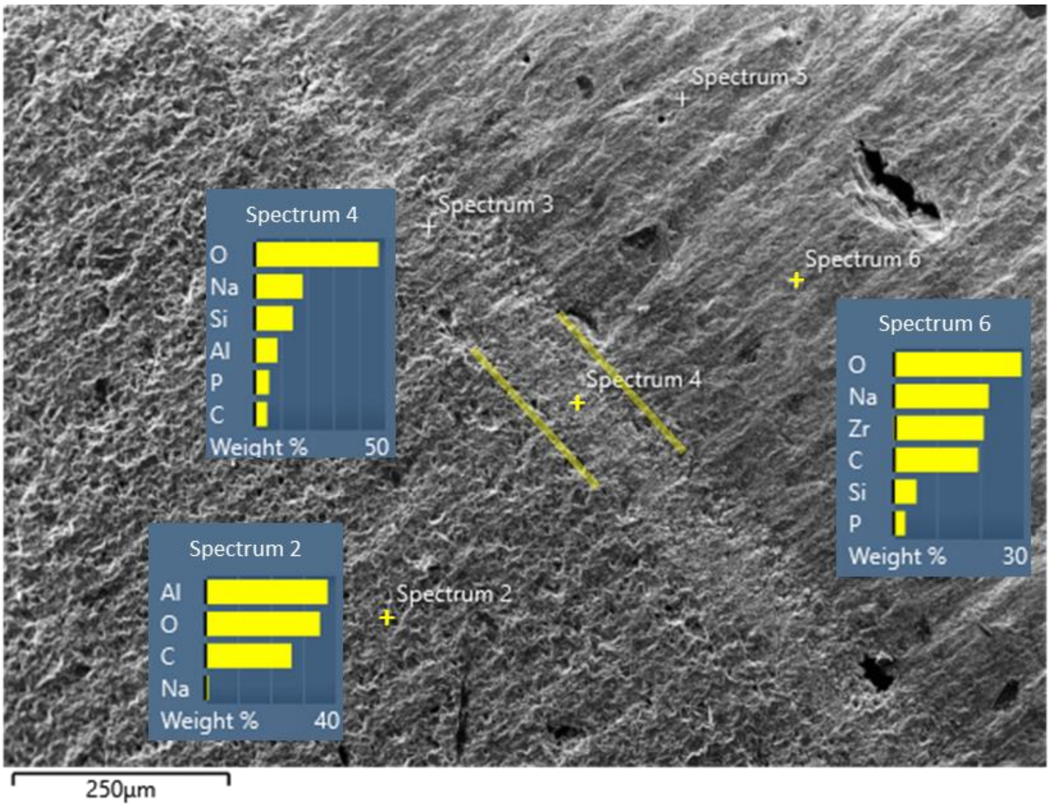

Figure 48: SEM-EDS cross sectional data of NASICON (1.5) pellet fused to ceramic crucible – interface NASICON (top right) / ceramic (bottom left). Yellow lines indicating the region of intermediate material.

Believing the impurity of the ceramic could be causing lower thermal stability of the crucible, a purer ceramic was chosen. Alumina (Al_2O_3) crucible was selected as it can operate at temperatures up to 1750°C and is a dense-single phase ceramic (99.9% purity, almath). The sintering temperature was lowered to 1200°C for this experiment and the pellet was exposed to this temperature for a shorter period - 16 hours.

Figure 49: Image of NASICON pellet post sintering (1.5) stuck to the alumina crucible.

Post sintering the pellet remained adhered to the alumina crucible (Figure 49); however, the proportion of molten material in the pellet has visibly decreased.

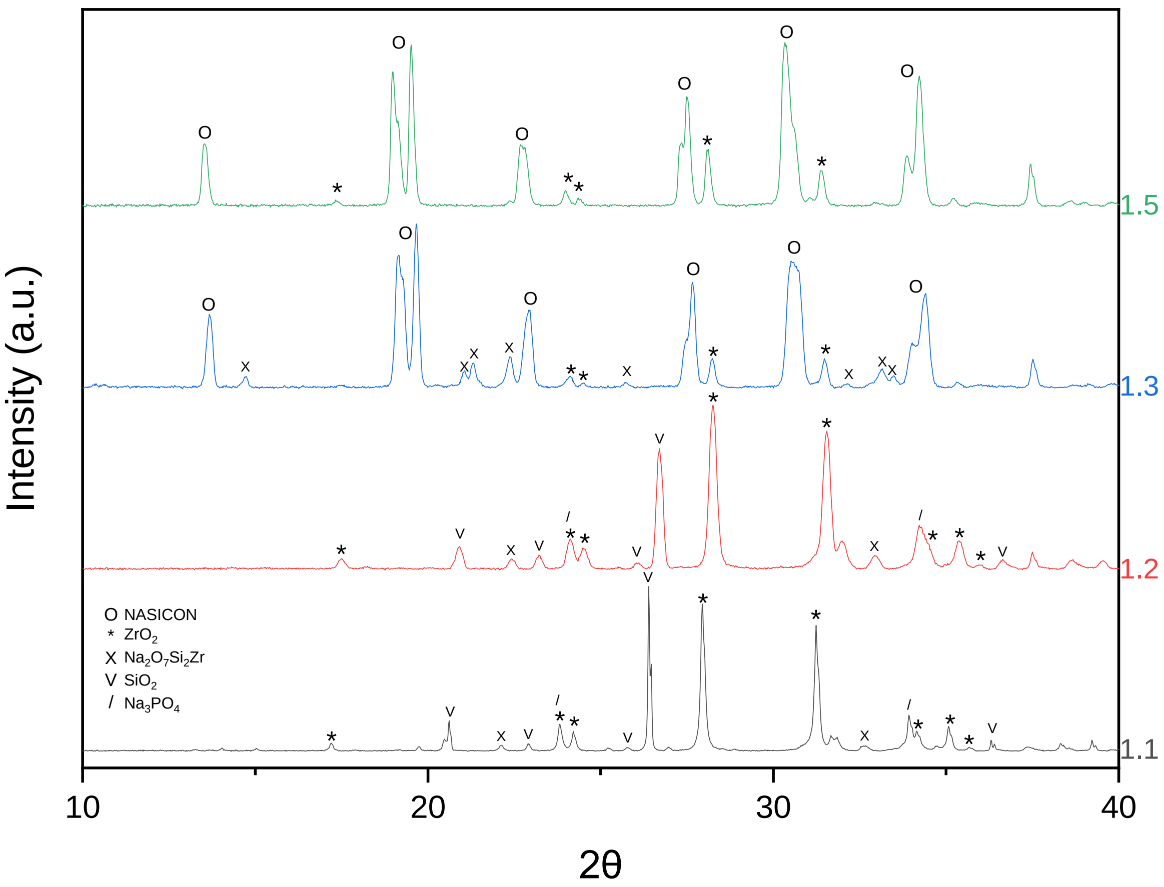

Figure 50: XRD's at different stages in the solid-state synthesis process of NASICON. Final sintering conditions - 1200°C, 16 hours, in argon (tube furnace) and pellet placed in an alumina crucible.

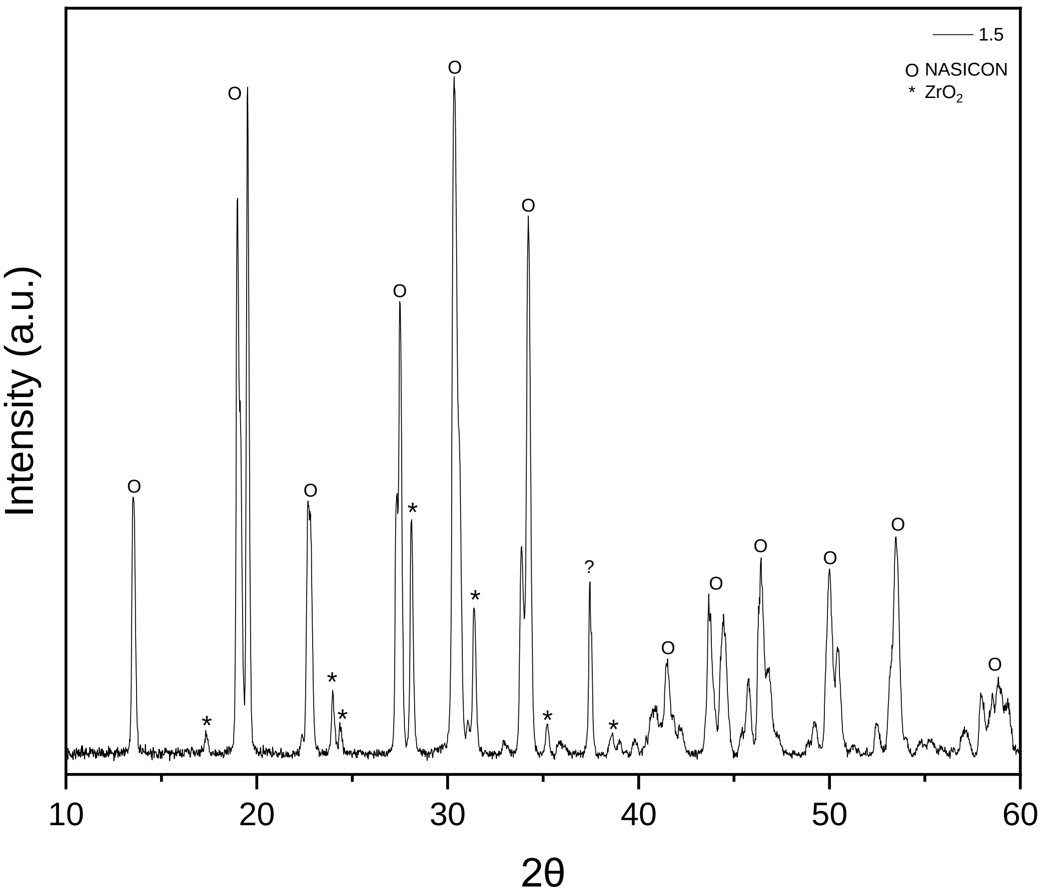

Figure 51: XRD of final NASICON pellet (1.5). Final sintering conditions - 1200°C, 16 hours, in argon (tube furnace) and pellet placed in an alumina crucible.

NASICON phase (SG 15, COD 1530661[185]) has formed in a shorter time frame (16 hours), at a lower temperature (1200°C) and in an alumina crucible. Figure 51 shows that compared to the ceramic crucible experiment similar NAISCON peaks and secondary phases (ZrO_2 (SG 14, COD 2108450[187]) and an unknown phase at 37.5º (potentially SiO_2) have formed, however the intensity of the peaks differ.

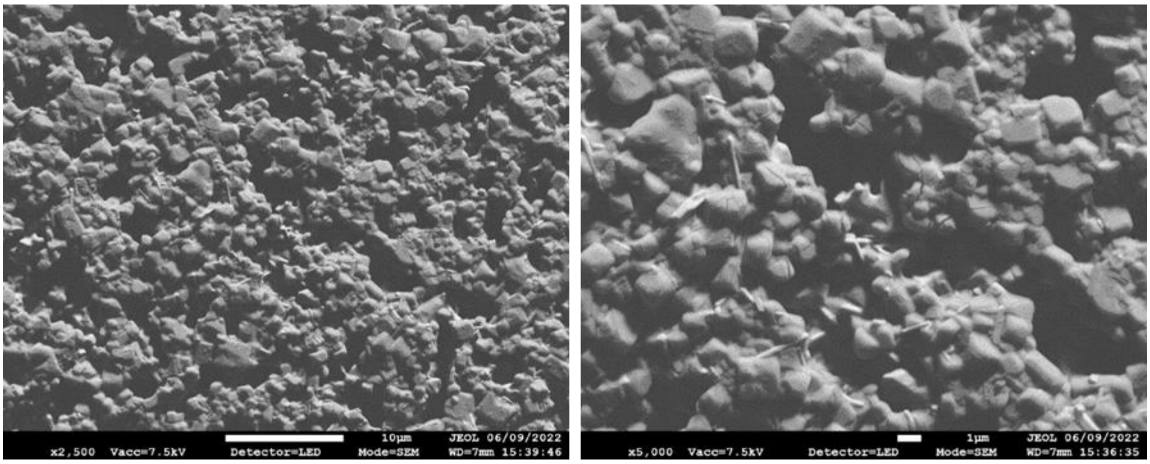

Figure 52: SEM images of NASICON precursor pellet. Pellet at 1.5 stage: 1st ball mill (2 hours, 120 rpm), sieved, dried (80°C, 16 hours conventional furnace), pellet pressed, 1st calcination (400°C, 5 hours conventional furnace), hand grind, pellet pressed, 2nd calcination (1100°C, 16 hours, argon tube furnace), hand grind, ball milled (3 hours, 120 rpm), sieved, dried (80°C, 18 hours conventional oven), pellet pressed and sintered (1200°C, 16 hours, argon tube furnace).

XRD data (Figure 50 and Figure 51) confirms NASICON has formed, however the SEM (Figure 52) illustrates different morphology of grains/particles. The particles are indicative of precursors that have not integrated into the NASICON structure during the sintering step, however they could be the secondary phases visible in the XRD data.

Morphology of the NASICON cubic crystal grains are not well defined, they appear as amorphous glassy grains and seem more molten than the previous standard ceramic low purity crucible experiment. This is evidenced by the NASICON pellets melting/fusing to the alumina crucibles. The reason for the pellet fusing to the crucible may be due to a chemical reaction between the alumina crucible and the NASICON at high temperatures, explained previously in Chapter 2. It is also illustrated in the EDS data (Figure 48), where the weight % shows alumina is present in the alumina crucible (spectrum 2) and the fused intermediate material (spectrum 4), but it is not present in the NASICON material (spectrum 6).

Hypothesising that there could be a diffusion reaction occurring with alumina, another crucible was investigated. Graphite was selected as it has a maximum operational temperature (in an inert atmosphere) of 2760°C (almath crucible). The temperatures employed in this experiment were lowered due to the molten morphology of the

NASICON in the alumina crucible experiment; therefore, final step sintering temperatures of 1150°C and 1180°C in an argon environment were used.

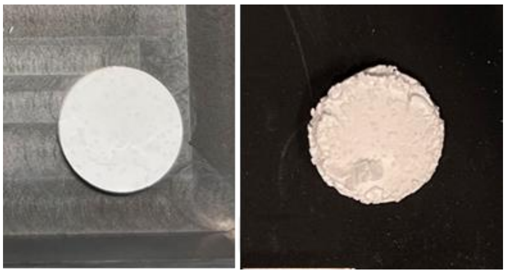

Figure 53: Left hand side image - pellet before sintering (1.4), right hand side image - pellet after sintering step (1.5)

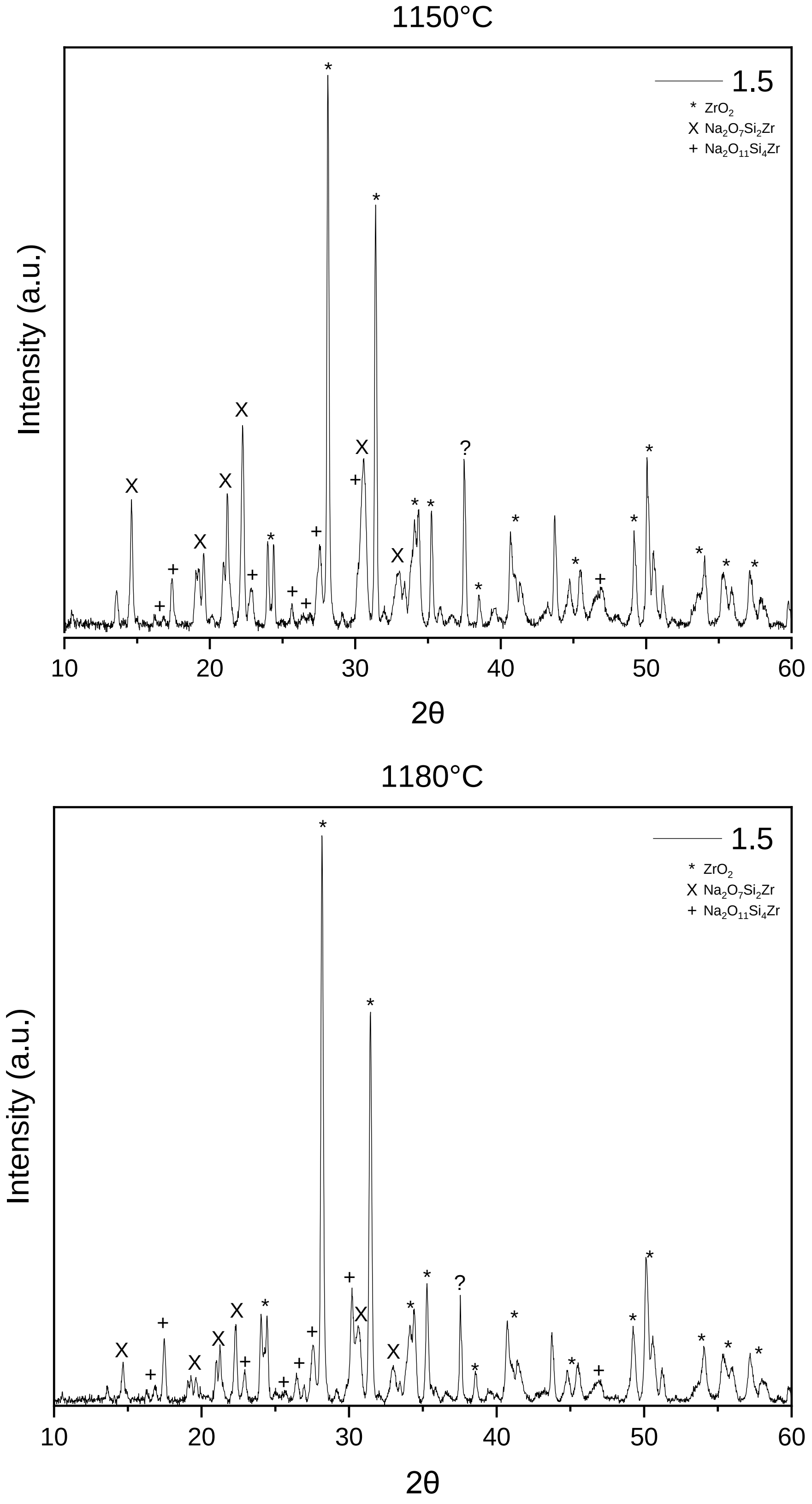

Figure 54: XRD of final NASICON pellet (1.5). Final sintering conditions - 1150°C and 1180°C, 16 hours, in argon (tube furnace) and pellet placed in a graphite crucible.

In both cases the pellets did not stick to the graphite crucibles (Figure 53), however XRD's show at both temperatures (1150°C and 1180°C) NASICON has not formed (Figure 54). Intermediated phases of $Na_2O_7Si_2Zr$ (SG 2, COD 9012687[184]) and $Na_2O_{11}Si_4Zr$ (SG 15, COD 9010607[186]) have potentially formed with ZrO_2 (SG 14, COD 9007485[179]) phases.

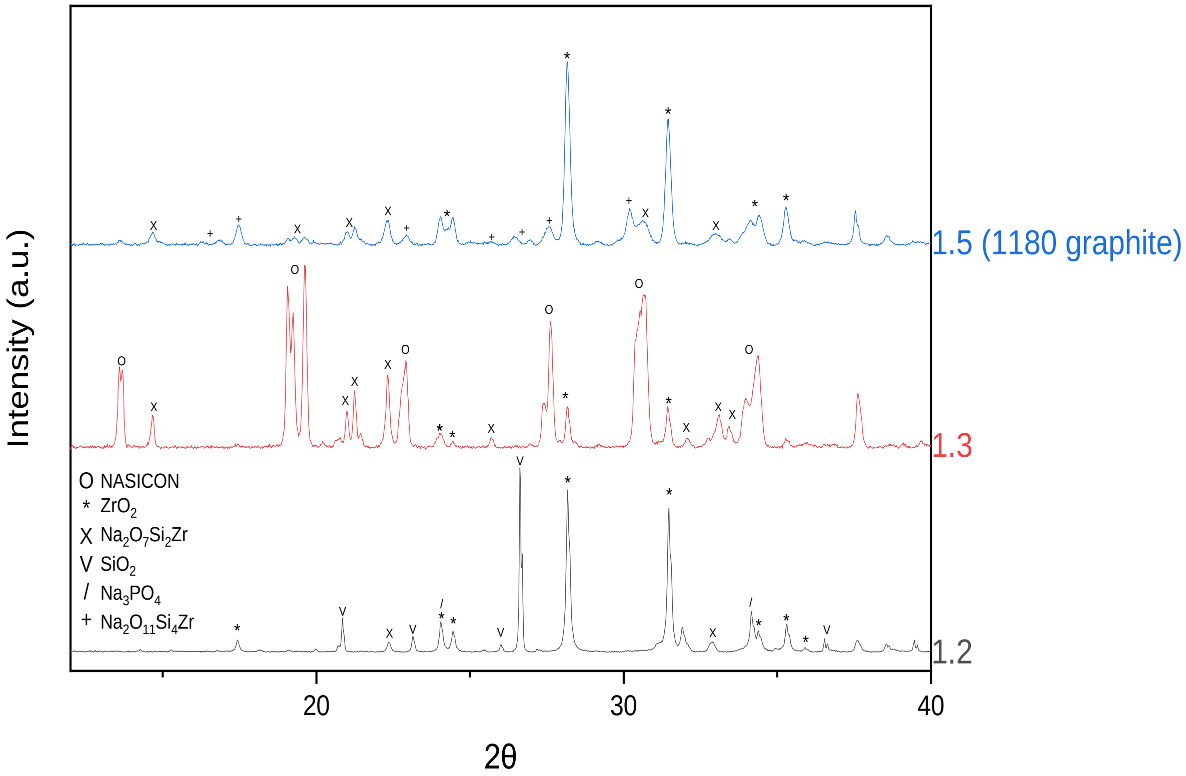

Figure 55: XRD's at different stages in the solid-state synthesis process of NASICON. All conditions for intermediate steps (1.1, 1.2, 1.3 and 1.4) are kept the same. Final sintering conditions - 1150°C or 1180°C, 16 hours, in argon (tube furnace) and pellets placed in graphite crucibles.

XRD pattern's again show repeatability up until the 1.3 stage, where some NASICON peaks have started to form. However, after sintering these NASICON peaks are no longer present (Figure 55). One hypothesis could be that in argon the graphite provides a reducing agent and the NASICON pellet provides oxidant, in turn causing an exothermic reaction. However, the presence of the carbon from the graphite causes a chemical reaction between the Zr and C, hindering the formation of the NASICON phases. To determine if this hypothesis is correct future work could include adding small amounts of alumina or carbon to the powders, then do TGA. Another experiment could include adding the alumina or carbon to the powder, sinter and XRD. The effect of carbon on NASICON formation has been investigated in the sol work in Chapter 5 using tartaric acid as a source of carbon. However, for the solid-state work in this thesis it was more time effective and valuable to look at alternative crucibles/methods.

4.4 Powder bed

Due to the interaction of the crucibles with the pellets, decided to experimentally investigate the use of a powder bed (Figure 56) in which the pellet is embedded during sintering. Powder beds have been used in literature to reduce the sodium volatilisation, but in this case is being employed to stop the NASICON sticking.[109,189,190] The pellet is placed in an alumina crucible, encased (below and above) in 1.4 powder, and the final sintering step was at 1180°C and 1200°C (16 hours, tube furnace). This sintering temperatures and time were chosen due to the previous experiments carried out and literature, stated in literature review Chapter 2.

Figure 56: Image of NASICON 1.4 pellet buried in a powder bed.

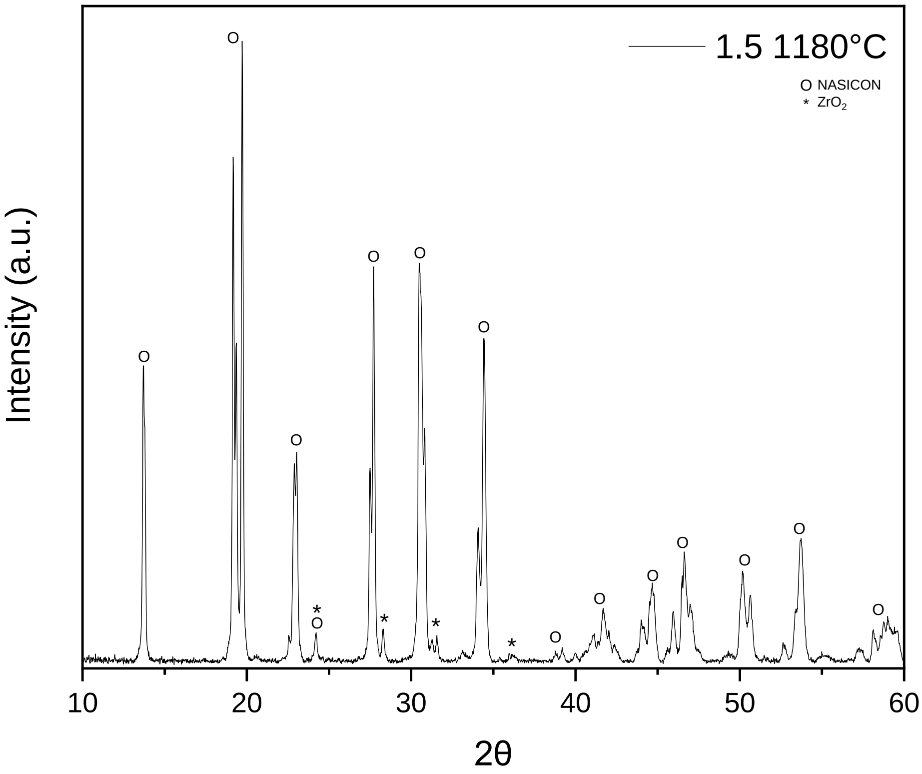

Figure 57: XRD's of final NASICON pellet's (1.5). Final sintering conditions for both pellets - 1180°C, 16 hours, in argon (tube furnace) and pellet placed in alumina crucibles, buried in powder bed.

The experiment was successful as the NASICON has formed in the correct chemistry and the pellet was not attached to the alumina crucible. Figure 57 depicts the XRD of the final pellet at 1.5, showing a NASICON (SG 15, COD 1529665[191]) crystal phase (13.7°, 19.5°, 22.9°, 24.1°, 27.6°, 30.6°, 34.4°, 39°, 41.4°, 44°, 46.5°, 50.4°, 53.6° and 59°). 2 pellets were sintered at 1800ºC and XRD patterns are identical which evinces that the final sintering step at 1180°C in powder bed is reproducible. Some ZrO_2 (SG 14, COD 9007485[179]) secondary phases were present at 24.1°, 28.2°, 31.5° and 35.3°, but were greatly reduced from the previous experiments; furthermore, there was no presence of the unknown 37.5º secondary phase present in the previous samples. Therefore, the layer of powder bed below the pellet stopped/reduced Al^{3+} diffusion, ensuring the pellet formed without chemically adhering to the substrate (Figure 58), and reducing secondary phases.[192]

Figure 58: Image of final pellet (1.5), sintered at 1180°C.

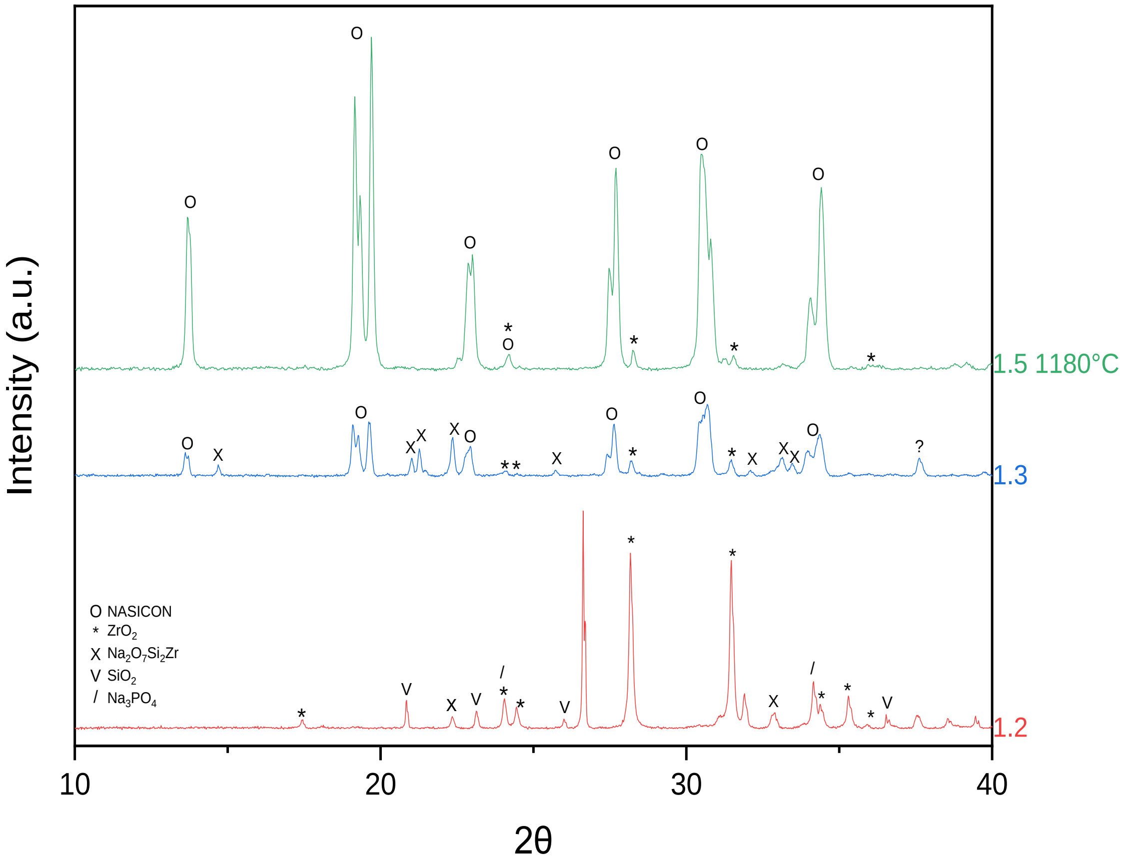

Figure 59: XRD's at different stages in the solid-state synthesis process of NASICON. Final sintering conditions - 1180°C 16 hours, in argon (tube furnace) and pellets placed in alumina crucibles, buried in powder bed.

Figure 59 shows that the intensity of the NASICON peaks significantly increases from the 1.3 to the 1.5 XRD pattern – indicating higher crystallinity. 1.5 data showed NASICON peaks formed at 22.9º and 24.1º, which were not present in the 1.3 data. This is in keeping with the conclusion that NASICON fully forms at the high temperature final sintering step.

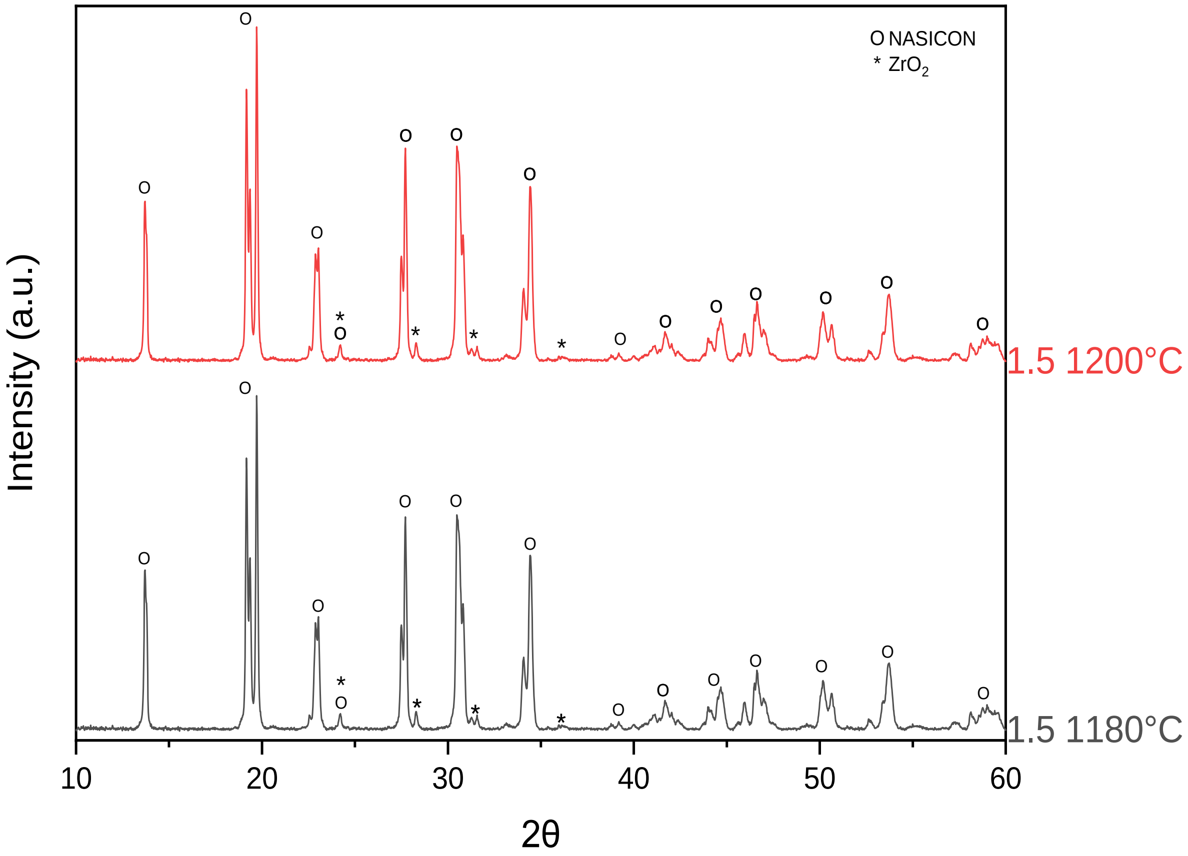

Figure 60: XRD's of final NASICON pellet's (1.5). Final sintering conditions for pellet 1180°C or 1200°C, 16 hours, in argon (tube furnace) and pellet placed in alumina crucibles, buried in powder bed.

At both 1180°C and 1200°C NASICON has formed, however both patterns show some secondary phases of ZrO_2 (Figure 60). The XRD patterns show negligible differences, with peak positions and intensity being extremely similar.

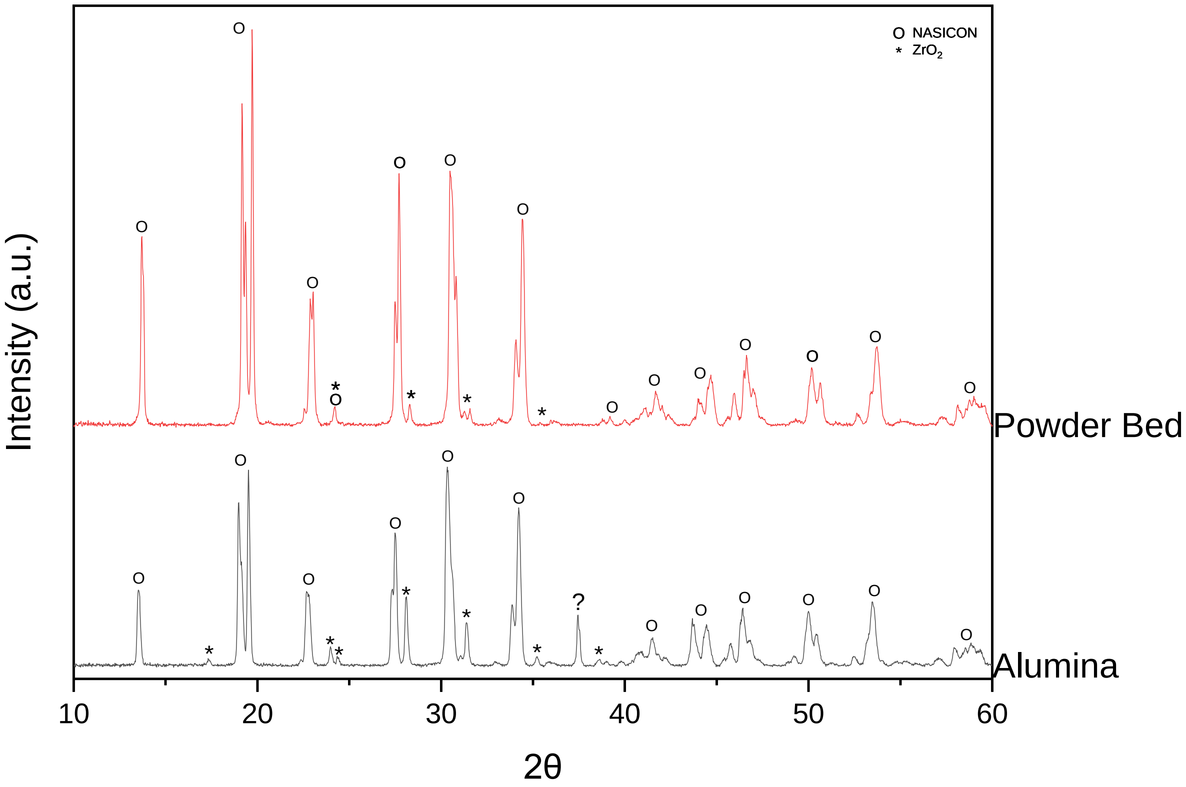

Figure 61: XRD of NASICON sintered using an alumina crucible vs the powder bed method. Both sintered at 1200C for 16 hours.

Compared to previous experiments; involving ceramic, alumina (Figure 61) and graphite crucibles, the secondary phases are decreased for the powder bed samples.

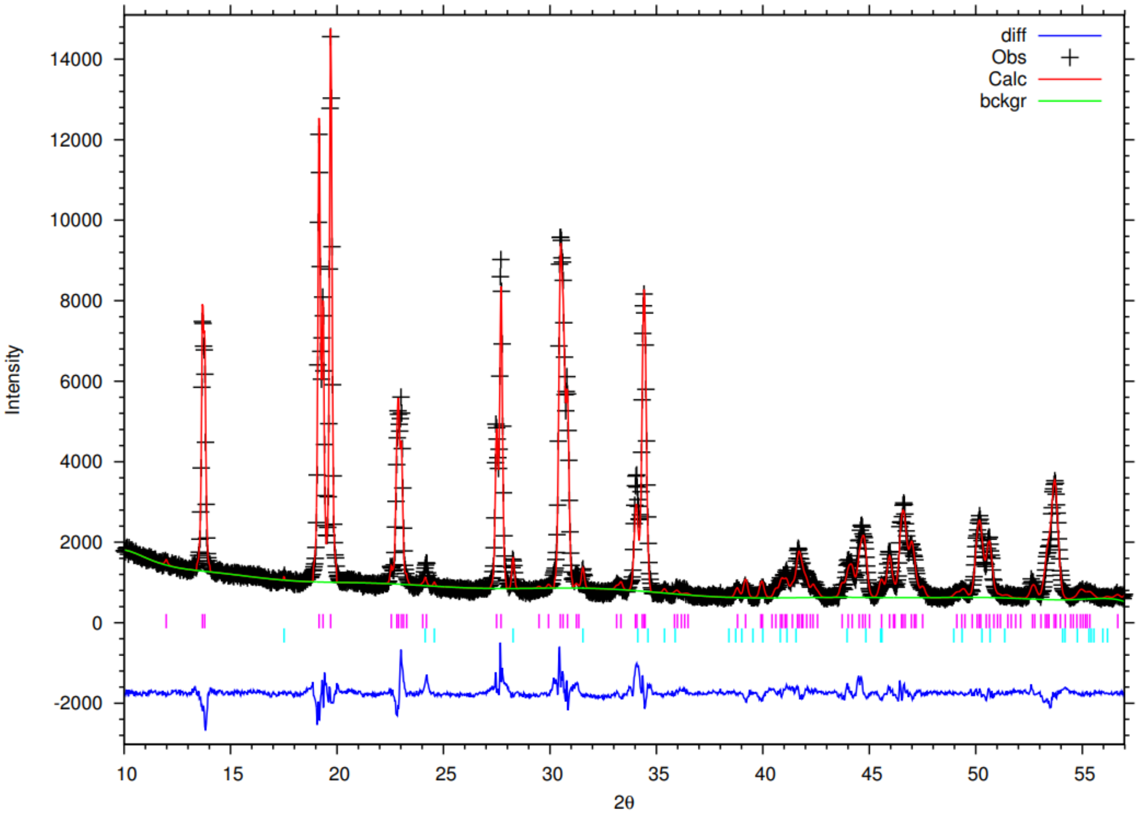

Figure 62: XRD data characterised using Rietveld Refinement (carried out by Professor Serena Margadonna). Purple: NASICON peaks, light blue: ZrO_2.

Table 29: Weight fraction of NASICON and ZrO_2 phases, from Rietveld Refinement.

	NASICON	**ZrO_2**
Weight fraction	98.5%	1.5%
Rwp	7.72%	
Rexp	5.69%	
χ^2	1.62	

Data shows goodness of fit parameters (Rwp and χ^2) fall within acceptable limits, with Rwp<10 (7.72%) and χ^2 reasonably close to the ideal value of 1 (1.62).[193,194]

Rietveld refinement (Figure 62, Table 29) confirms ZrO_2 is the only secondary phase present and quantifies the weight fraction of the ZrO_2 to be 1.5%. This is vastly improved compared to Jalalian-Khakshour's paper[79] which Rietveld refinement (data in Chapter 2) showed after 24 hours of sintering there were 3 secondary phases of Na_3PO_4 (3.47), ZrO_2 (9.14) and SiO_2 (0.6).

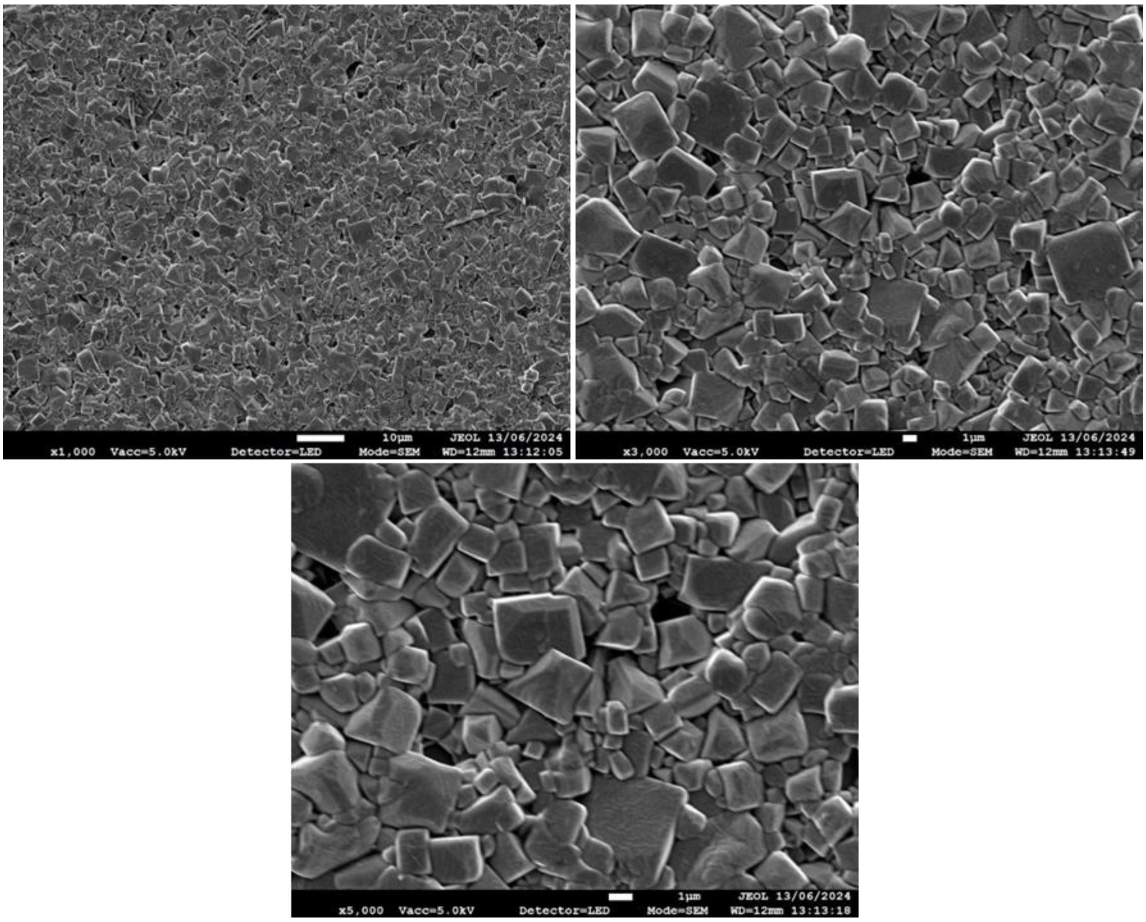

Figure 63: SEM images of final 1.5 sintered pellet (1180ºC Tube furnace, argon environment, 16 hours).

SEM data (Figure 63) validates the XRD data, illustrating NASICON crystals have formed. SEM shows morphology of crystal grains vary in size. Some crystal grains look to have adhered, are close packed.

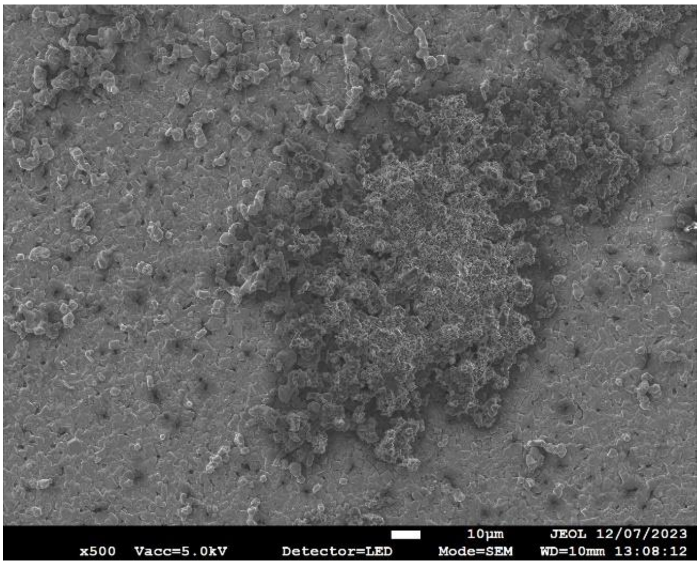

Figure 64: SEM image of the surface of the NASICON 1.5 pellet.

The SEM image (Figure 64) appears to show the NASICON precursor powder chemically bonded to the surface of the NASICON pellet. In the image the fused powder looks to contain amorphous glassy phases, as grain boundaries are not distinct. While this is a disadvantage of having powder bed, this can be removed with polishing before incorporating into a cell. Other impacts of this work are the loss of material when using the powder bed, as some fuses to the crucible.

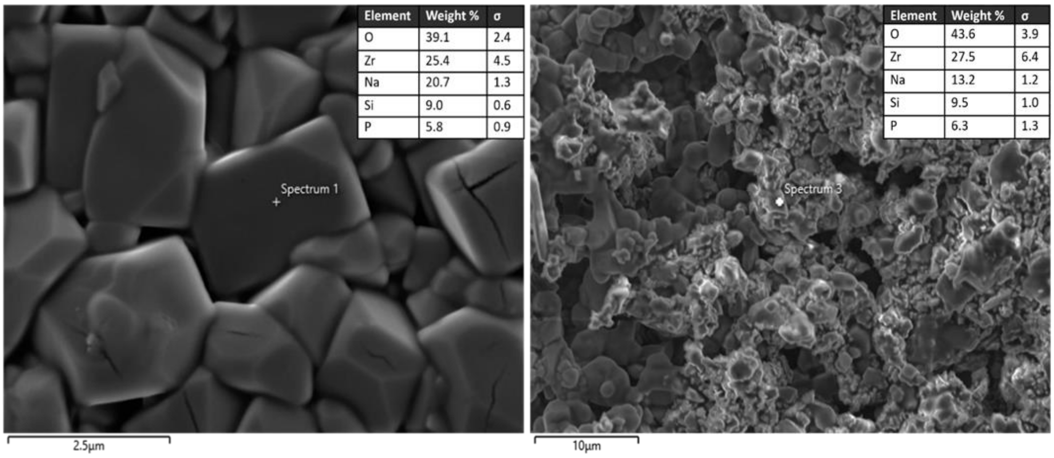

Element	Weight %	σ
O	39.1	2.4
Zr	25.4	4.5
Na	20.7	1.3
Si	9.0	0.6
P	5.8	0.9

Element	Weight %	σ
O	43.6	3.9
Zr	27.5	6.4
Na	13.2	1.2
Si	9.5	1.0
P	6.3	1.3

*Figure 65: EDS of 1180°C pellet. **Left**: NASICON crystals; **Right**: Powder bed fused to surface of pellet.*

EDS data (Figure 65) quantifies the mass percentage of the different elements within the NASICON crystals. The EDS of the powder bed bonded to the surface of the pellet has a lower percentage of Na, compared to the NASICON crystals in the pellet which have a higher percentage of Na compared to the other elements. This suggests the powder bed is retaining the volatile Na in the NASICON crystals.

4.5 Electrochemistry

Electrochemical impedance spectroscopy (EIS) was performed on a synthesised NASICON pellet (sample sintered at 1180ºC, XRD data in Figure 62) to assess its conductivity relative to equivalent NASICON pellets reported in literature. To determine the ionic conductivity of the synthesised NASICON, the pellet dimensions were measured (Figure 66) and reported to be: radius (r) = 0.75 cm, thickness (t) = 0.2 cm and contact area of the electrode ($A = 1.77\ cm^2$).

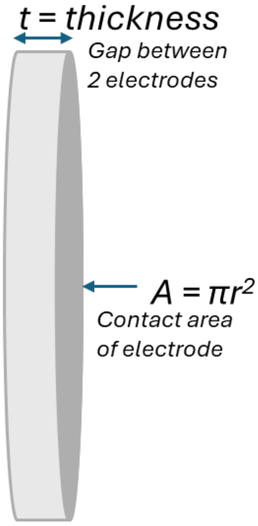

Figure 66: Diagram illustrating the dimensions of the pellet used to calculate the ionic conductivity of the pellet.

The through grain resistance (R_g) and grain boundary resistance (R_{gb}) are visually illustrated in Figure 67 for the NASICON crystals in the pellet.

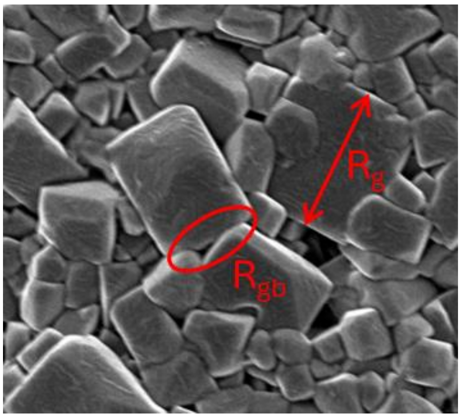

Figure 67: R_g and R_{gb} illustrated on NASICON crystals (SEM image).

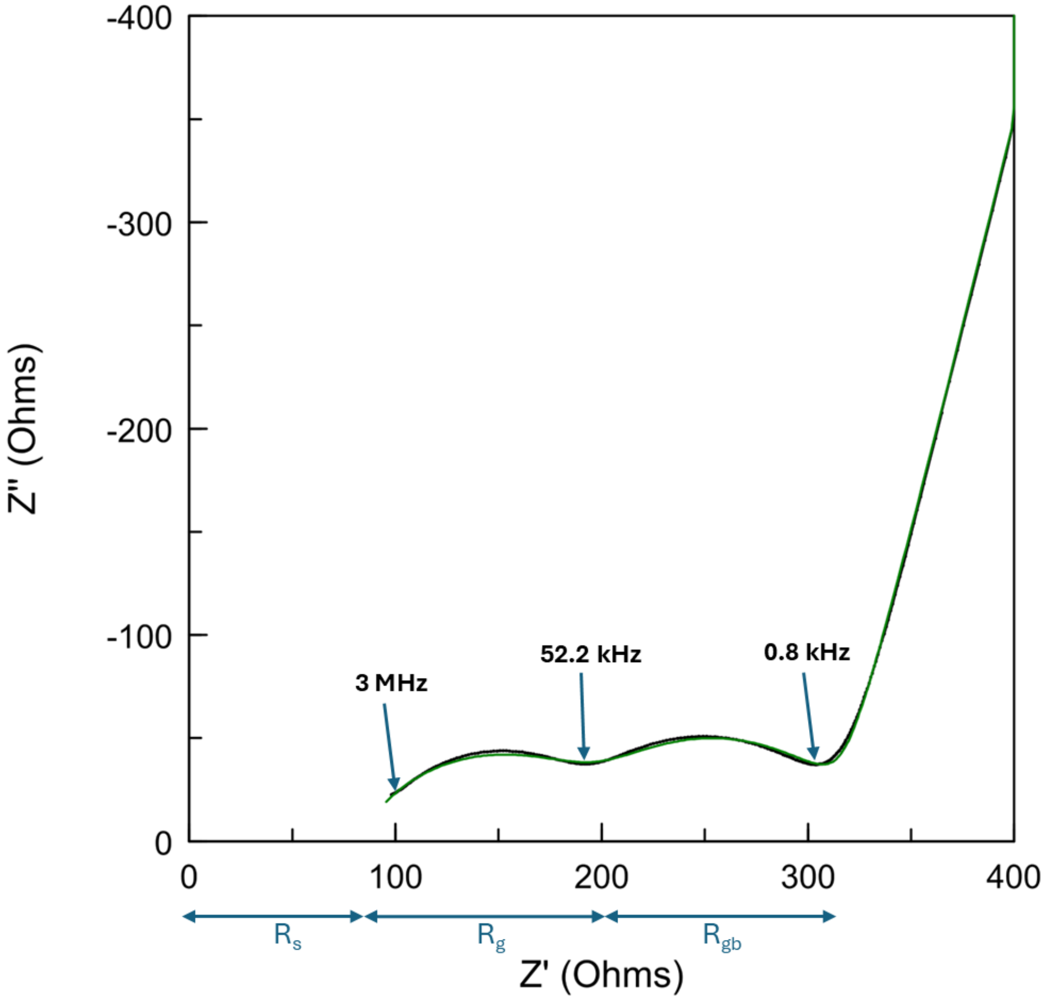

Figure 68: Nyquist plot of EIS data (black line) with corresponding Z-view model fit (green line). Graph illustrates where the R_s, R_g and R_{gb} values are derived.

Table 30: Resistance values and associated error measurements from EIS data modelled using Z-view software (all data and errors outputted by software).

Element	Value	Error	Error %
R_s	82.0	0.5	0.6
CPE1-T	2.6×10^{-7}	2.8×10^{-8}	10.6
CPE1-P	0.71124	0.007	1.07
R_g	120.2	2.05	1.7
CPE2-T	1.9×10^{-6}	1.3×10^{-7}	6.9
CPE2-P	0.8	0.008	1.08
R_{gb}	112.2	1.9	1.6
CPE3-T	4.2×10^{-5}	1.05×10^{-7}	0.2
CPE3-P	0.8	0.0006	0.07

Grain resistance (R_g) and grain boundary resistance (R_{gb}) data is extracted from the Nyquist plot (Figure 68) of the EIS data; where R_s is the resistance in the system set-up. The fitted EIS data (Z-view modelling) give values of $R_g = 120.2\ \Omega$ and $R_{gb} = 112.2\ \Omega$

(Table 30). These values were used to calculate the ionic conductivity of the grain (σ_g) and grain boundary (σ_{gb}) in Equations 10 and 11.[175]

Equation 10

$$\sigma_g = \frac{t}{A \times R_g} = \frac{0.2}{1.77 \times 120.2} = 9.40\ x\ 10^{-4}\ Scm^{-1}$$

Equation 11

$$\sigma_{gb} = \frac{t}{A \times R_{gb}} = \frac{0.2}{1.77 \times 112.2} = 1.01\ x\ 10^{-3}\ Scm^{-1}$$

The total ionic conductivity (σ_t) is the sum of the σ_g and σ_{gb}, illustrated in Equation 12.[175]

Equation 12

$$\sigma_t = \sigma_g + \sigma_{gb} = 1.95\ x\ 10^{-3}\ Scm^{-1}$$

The total ionic conductivity of the synthesised NASICON pellet is 1.95 x 10^{-3} Scm^{-1}. This value falls within the range of high-performance NASICON materials reported in literature at room temperature (in the order of x 10^{-3} Scm^{-1}).[79,175,195] This result indicates that the synthesis and sintering process employed in this work successfully produced NASICON with good ionic conductivity comparable to that reported in literature.

4.6 Conclusion

Table 31 illustrates the overall outcome of each experiment determined by the characterisation techniques. The powder bed experiment was successful in forming NASICON without adhering to the crucible, this was verified by XRD and SEM characterisation. The NASICON pellets were formed as a free pellet, confirming crucibles affect the composition of the NASICON formed, with the powder bed stopping the diffusion of Al^{3+} into the NASICON.

Table 31: Overview of solid-state experiments, identified by the final sintering step.

Temperature (°C)	Time (hours)	Crucible	NASICON?	Stuck/melted?
1230	24	ceramic	yes	yes
1200	16	alumina	yes	yes
1180	16	alumina	unknown	yes
1150	16	graphite	no	no
1150	16	graphite + pt square	unknown	yes
1180	16	graphite	no	no
1230	16	graphite	unknown	not stuck, melted
1180	16	alumina + buried in powder	yes	no
1200	16	alumina + buried in powder	yes	no

Rietveld refinement of XRD data showed 1.5% secondary phase of ZrO_2, a vastly improved composition compared to the secondary phases present in solid-state NASICON pellets synthesised in literature[79]. Data shows the goodness of fit (GOF) parameters fall within acceptable limits (from literature), with Rwp<10 (7.72%) and χ^2 reasonably close to the ideal value of 1 (1.62), providing confidence in with the percentage weight value of 1.5%.[193,194] However, it is important to note that background contribution, preferred orientation effects and refinement errors, can impact the calculated phase percentages and GOF parameters. McCusker et al.[194] indicated how using monochromatic radiation and a rotating horizontally mounted capillary can be used to reduce these effects experimentally and improve the GOF. However, Toby et al.[193] suggests the most reliable method for assessing Rietveld fit quality is through visual comparison of the observed and calculated patterns graphically, alongside verification of the model's chemical plausibility.

Characterisation techniques in this chapter revealed the stages of precursor transformation into NASICON. XRD and SEM data illustrates stages 1.1 to 1.3 are composed of precursor powders. Little to no changes occur in the XRD patterns between 1.1 and 1.2, or 1.3 and 1.4 - confirming ball milling does not alter the chemistry of the precursor and intermediate powders. Chemical changes occur during the high temperature calcination (1100°C) and sintering (>1150°C) steps. Densification occurs during the 1.5 sintering step, which was confirmed by comparison of 1.3 vs 1.5 SEM images, as well as physical volume and density calculations of the pellets before and after sintering.

EIS data showed the total ionic conductivity of the synthesised NASICON pellet is 1.95 x 10^{-3} Scm^{-1}, similar to levels in literature[79,175,195] (in the order of x 10^{-3} Scm^{-1}).

Chapter 5 – NASICON Sol Powder Synthesis

5.1 Introduction

The following chapters investigate the sol technique as a synthesis method to prepare NASICON. The sol route is preferred over the solid-state method due to its shorter processing time, lower sintering temperatures and reduced presence of secondary phases, as well as many more processing benefits. However, the sol route presents a more complex chemistry and involves sensitive reactions, which are challenging for lab-scale synthesis and in turn industrial scale up.

As explained in Chapter 2, the technique involves mixing the chemical precursors in water, which undergo a fast hydrolysis reaction followed by peptisation – forming a particulate sol. This sol is then dried (120°C, 12 hours) to obtain a xerogel and ground. This powder is finally sintered, which facilitates the phase transition into NASICON. DSC-TGA and XRD analysis were carried out in this chapter to identify which precursor chemicals are optimal for the NASICON formation, and to understand the role of the different reactions happening.

The aim of these experiments is to optimise the sol reaction, which will then inform the thin-film process. Different precursor chemicals were investigated to determine which chemistry should be used in thin film application, to form NASICON with limited secondary phases. The aim is to scope out NASICON powder synthesis methods which present minimal secondary phases and to understand the role of tartaric acid (TA) on these processes.

The chemistries employed were inspired by and variations of Shimizu's work (Equation 13, 14, 15, 16, and 17),[124,135] as stated in the literature review (Chapter 2):

Equation 13

$$ZrO(NO_3)_2.2H_2O + NH_4H_2PO_4 + Na_2SiO_3.9H_2O + C_4H_6O_6 \rightarrow Na_3Zr_2Si_2PO_{12}$$

Equation 14

$$ZrOCl_2.8H_2O + NH_4H_2PO_4 + Na_2SiO_3.9H_2O + C_4H_6O_6 \rightarrow Na_3Zr_2Si_2PO_{12}$$

Equation 15

$$ZrO(NO_3)_2.2H_2O + NH_4H_2PO_4 + Na_2SiO_3.5H_2O + C_4H_6O_6 \rightarrow Na_3Zr_2Si_2PO_{12}$$

Equation 16

$$ZrO(NO_3)_2.2H_2O + NH_4H_2PO_4 + Na_2SiO_3.9H_2O \rightarrow Na_3Zr_2Si_2PO_{12}$$

Equation 17

$$ZrOCl_2.8H_2O + NH_4H_2PO_4 + Na_2SiO_3.9H_2O \rightarrow Na_3Zr_2Si_2PO_{12}$$

The solvent used in this work was water. Precursor chemicals were used in molar ratios of 2:1:2:3 (sodium excess to improve NASICON phase formation[196]), with concentrations of % mass to solvent, the calculations are shown in Chapter 3 - Method. The mass and therefore the concentration changed when going from $5H_2O$ to $9H_2O$ (calculations shown in Chapter 3).

5.2 NASICON powder synthesis

The next section of this chapter aims to synthesis a sol NAISCON powder using conventional ovens with different chemistries. All experiments were carried out in air, improved processing compared to solid-state technique which required an inert argon environment. The total heating processing time is 16 hours (Table 32), which is also significantly reduced from the solid-state method.

Table 32: Heat processing times of NASICON sol powder synthesis.

Synthesis steps	Time (hours)	Temperature (°C)
Dried	12 *(10 min ramp)*	120
Calcined	1 *(37.5 min ramp)*	750
Sintered	3 *(50 min ramp)*	1000-1100
Total	**16 hours** *(+ ramp time)*	

Table 33 lists the experiments performed in this chapter, the following variables were investigated: formulation, impact of TA, concentration, and crucibles.

Table 33: List of sol powder experiments carried out.

Formulation			Acid Catalyst	Conc (%)	Crucible	Dry (°C)	Sintering (°C)
$ZrO(NO_3)_2.2H_2O$	$Na_2SiO_3.5H_2O$	$NH_4H_3PO_4$	TA	5%	graphite	120	750 + 1000
$ZrO(NO_3)_2.2H_2O$	$Na_2SiO_3.5H_2O$	$NH_4H_3PO_4$	TA	6%	graphite	120	750 + 1000
$ZrO(NO_3)_2.2H_2O$	$Na_2SiO_3.9H_2O$	$NH_4H_3PO_4$	TA	5%	alumina	120	750 + 1000
$ZrO(NO_3)_2.2H_2O$	$Na_2SiO_3.5H_2O$	$NH_4H_3PO_4$	TA	5%	alumina	120	750 + 1000
$ZrO(NO_3)_2.2H_2O$	$Na_2SiO_3.9H_2O$	$NH_4H_3PO_4$	none	5%	alumina	120	750 + 1000
$ZrOCl_2.8H_2O$	$Na_2SiO_3.9H_2O$	$NH_4H_3PO_4$	TA	5%	alumina	120	750 + 1000
$ZrOCl_2.8H_2O$	$Na_2SiO_3.9H_2O$	$NH_4H_3PO_4$	none	5%	alumina	120	750 + 1000
$ZrO(NO_3)_2.2H_2O$	Na2SiO3.9H2O	$NH_4H_3PO_4$	TA	5%	alumina	120	750 + **1100**
$ZrO(NO_3)_2.2H_2O$	Na2SiO3.9H2O	$NH_4H_3PO_4$	TA	5%	alumina	120	750 + 1150

5.2.1 Concentration – 5% vs 6%

The aim of this first optimisation was to synthesise NASICON powder at two concentrations (5% and 6%) and to understand the concentration at which the NASICON chemistry has the least number of secondary phases. These concentrations were selected from scoping experiments, where 5% and 6% sols had the highest concentration of solids in solution without precipitation, increasing the rate of reaction. Furthermore, reducing the amount of solvent (H_2O) in the mixture reduces the amount of solvent evaporating during the drying step, which can improve homogeneity. At these concentrations the solution is fully saturated, and sedimentation is not observed; this is explained in more detail in Chapter 6.

The experiments synthesised NASICON by drying the NO_3 with tartaric acid sol precursor (120°C) to form a xergoel powder, which was then hand ground using a mortar and pestle (agate). The powder was hand ground before each heating step: before 750°C heating and final 1000°C sintering. For this experiment graphite crucibles were used in air.

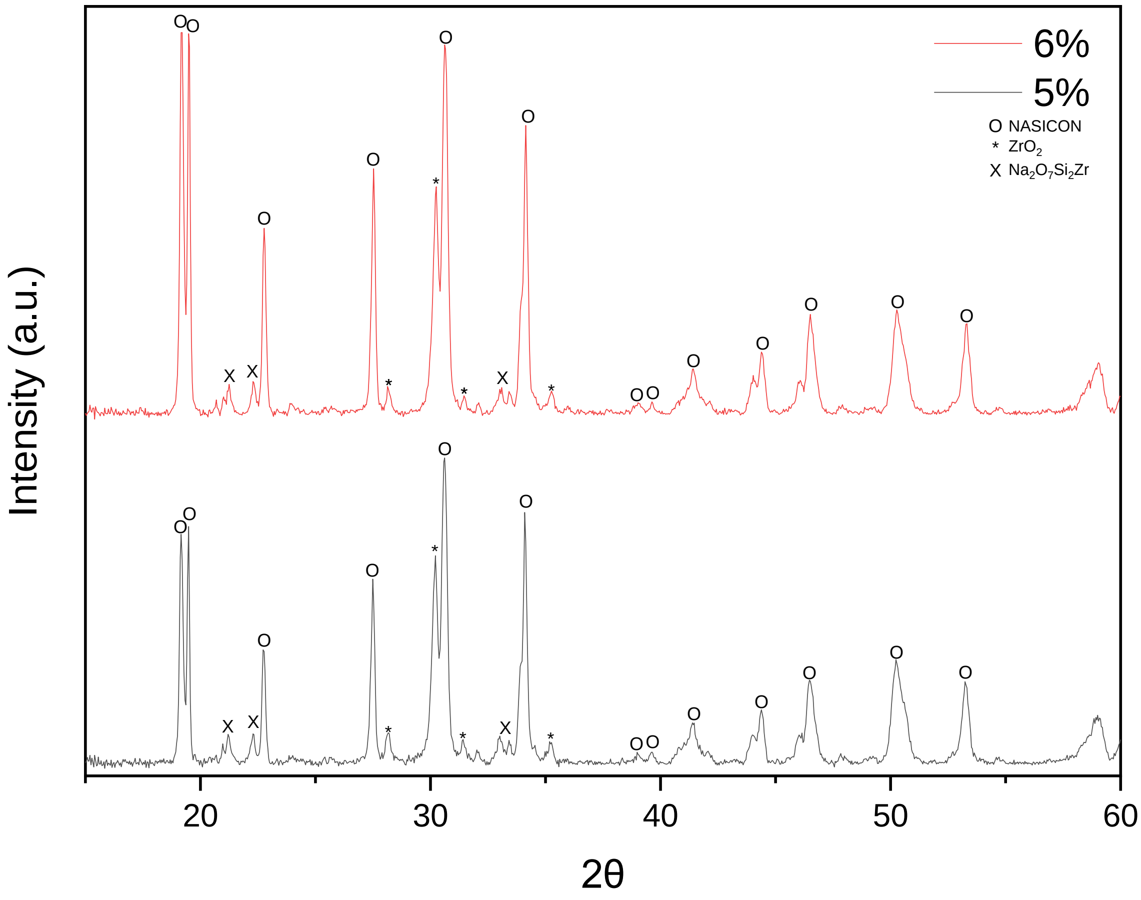

Figure 69: XRD of 5% vs 6% NASICON sol powder, sintered at 1000°C in a graphite crucible.

The powder samples (Figure 69) show NASICON has formed (SG 15, COD 1529665[191]) at 19.2°, 22.8°, 27.5°, 30.5°, 34.1°, 39°, 39.5°, 41°, 44°, 46.5°, 50.5° and 53°. There are secondary phases for both concentrations: ZrO_2 (SG 137, COD 1525706[197] and SG 14, COD 1522143[198]) at 28.1°, 30.2°, 31.5°, 35.2°; and $Na_2O_7Si_2Zr$ (SG 2, COD 9012687[184]) at 21.1°, 22.3°, 33°. The presence of $Na_2O_7Si_2Zr$ could suggest the NASICON phase has not completely formed.

The intensities of the peaks for the 5% and 6% samples are different (Figure 69). In the 6% sample the peak with maximum intensity is at 19º and in the 5% sample is 30º; which could be related to the amount of secondary phase formation. The patterns suggest that the 5% sample could be a less sodium-rich (but still rich) NASICON phase than the 6%.

This experiment was successful because both the 5% and 6% concentrations synthesised NASICON, with similar secondary phases. The 5% sample was a more stable sol which is necessary for thin film synthesis, there was no presence of sediments after mixing the precursors and its gelation time was longer, therefore this concentration was selected for future powder synthesis work.

It was noticed after these experiments that the graphite crucibles had oxidised at the high 1000ºC temperature. It could have affected the sintering process of NASICON (e.g. increase the present of secondary phases). From now on, alumina crucibles will be used to conduct the new experiments with the aim to prevent crucible degradation.

5.3.2 Chemistry

Once the concentration was ascertained, 5%, the aim of the following experiments was to determine which precursor chemicals enabled the fabrication of NASICON. To be precise this work looked at the impact of Cl versus NO_3 precursors, and the impact of the tartaric acid catalyst; as well as understanding whether the hydrated state of the silicate impacted NASICON formation. Therefore 5 powder samples of different chemistries were synthesised (Table 34); the key variables in precursor materials that were experimentally investigated included:

- $ZrO(NO_3)_2.2H_2O$ vs $ZrOCl_2.8H_2O$
- Tartaric acid vs no tartaric acid
- $Na_2SiO_3.9H_2O$ vs $Na_2SiO_3.5H_2O$

$Na_2SiO_3.9H_2O$ was used in the literature but had very long lead times when ordering; therefore, experiments were also carried out on $Na_2SiO_3.5H_2O$ as this was easily accessible.

Table 34: Illustrating the notation of the experiments in this section.

Experiment Number	Formulation			Acid
1.1	$Na_2SiO_3.9H_2O$	$ZrO(NO_3)_2.2H_2O$	**1.1**	$Na_2SiO_3.9H_2O$
1.2	$Na_2SiO_3.5H_2O$	$ZrO(NO_3)_2.2H_2O$	**1.2**	$Na_2SiO_3.5H_2O$
1.3	$Na_2SiO_3.9H_2O$	$ZrO(NO_3)_2.2H_2O$	**1.3**	$Na_2SiO_3.9H_2O$
1.4	$Na_2SiO_3.9H_2O$	$ZrOCl_2.8H_2O$	**1.4**	$Na_2SiO_3.9H_2O$
1.5	$Na_2SiO_3.9H_2O$	$ZrOCl_2.8H_2O$	**1.5**	$Na_2SiO_3.9H_2O$

To try to understand the chemistry of the different experiments, DSC-TGA analysis was carried out. The xerogel powders tested were all made from 5% concentration sols, the chemicals used for each experiment are shown in Table 34 and the DSC-TGA parameters are stated in Chapter 3.

DSC-TGA experiments gave quantifiable data in terms of mass loss percentage during heating (Table 35).

Table 35: % mass loss of xerogel DSC-TGA samples

Experimental number	1.2	1.3	1.4	1.5
Initial (mg, ±0.1)	11.34	8.41	10.61	11.83
Final (mg, ±0.1)	5.45	5.39	4.28	8.63
Mass Loss	51.94%	35.92%	59.66%	27.05%

The data showed a higher percentage mass loss for the two xerogels containing tartaric acid, compared to the materials without it. A higher mass loss % is expected for the samples containing tartaric acid (experiments 1.2 and 1.4) since all the acid will be evaporated during the DSC-TGA analysis. Furthermore, for the tartaric acid samples there was a higher mass loss percentage for the chloride xerogel (1.4) compared to the nitrates one (1.2), a difference of 7.72%. The sample with the lowest percentage mass loss was the chloride without tartaric acid precursors (1.5) at 27.05%.

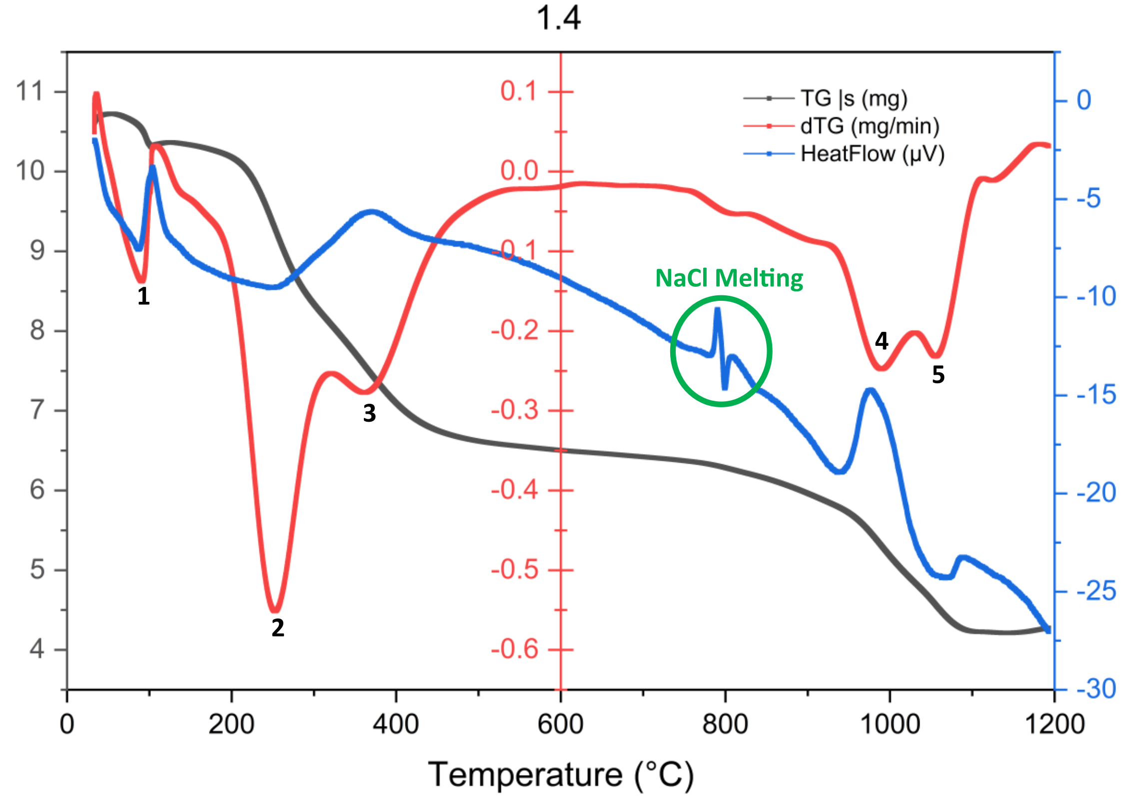

Figure 70: DSC-TGA curves of sol xerogel 1.4 Cl chemistry with tartaric acid powder.

An in-depth graph of the DSC-TGA data for the 1.4 sample is displayed in Figure 70, annotated with numbers that correspond to key thermal events. The analysis of each point is explained below.

1: 5.5% of physically absorbed water is lost up to 100ºC[199], this is associated with an endothermic peak in the DSC data.
2: A dTG peak at 255°C is related to loss of ammonia due to the decomposition of $NH_4H_2PO_4$ [199] and loss of unbound tartaric acid[200] (its theoretical boiling point), a change in gradient in the TG data indicates the 2 mass losses; this is associated with an endothermic peak.
3 and 4: At 366°C and 977°C there are exothermic carbon combustion reactions related to the loss of organic molecules coordinated to Zr^{4+}. Metal attached organic compounds are removed at higher temperatures than their boiling points.[200] Sharp endothermic peak at 800°C in the DSC curve is attributed to the melting of NaCl.[135]
5: At 1055°C the dTGA shows a mass loss associated with an endothermic peak in the DSC data which could be related to the evaporation of NaCl.[135] The evaporation temperature of NaCl is 1465ºC; however the exothermic reaction at 950ºC could increase the total temperature and NaCl with other metals in the system could enable evaporation.

This loss of Na explains the small secondary phases in the sintered powders (XRD data), the NaCl comes from the NASICON structure (decomposition), which therefore assists ZrO_2 formation.

There is no specific peak related exactly with NASICON formation, it requires the desired ions in close proximity, the absence of other material which might interfere and sufficient energy for the ions to reorganise themselves in the correct configuration. The presence of carbon hinders the formation of NASICON (as it is attached to Zr), so when the carbon is removed the structure can form/grow – after 977°C. However, the energy obtained from the exothermic reaction (combustion of the carbon) helps to form the NASICON structure. Once all the carbon is removed around 977°C, the NASICON phase starts to crystalise.[201] This is in accordance to the thermal stage XRD results, in Chapter 6.

In comparison, Figure 71 looks at how the reaction mechanism changes for the chloride without tartaric acid dried sol solution.

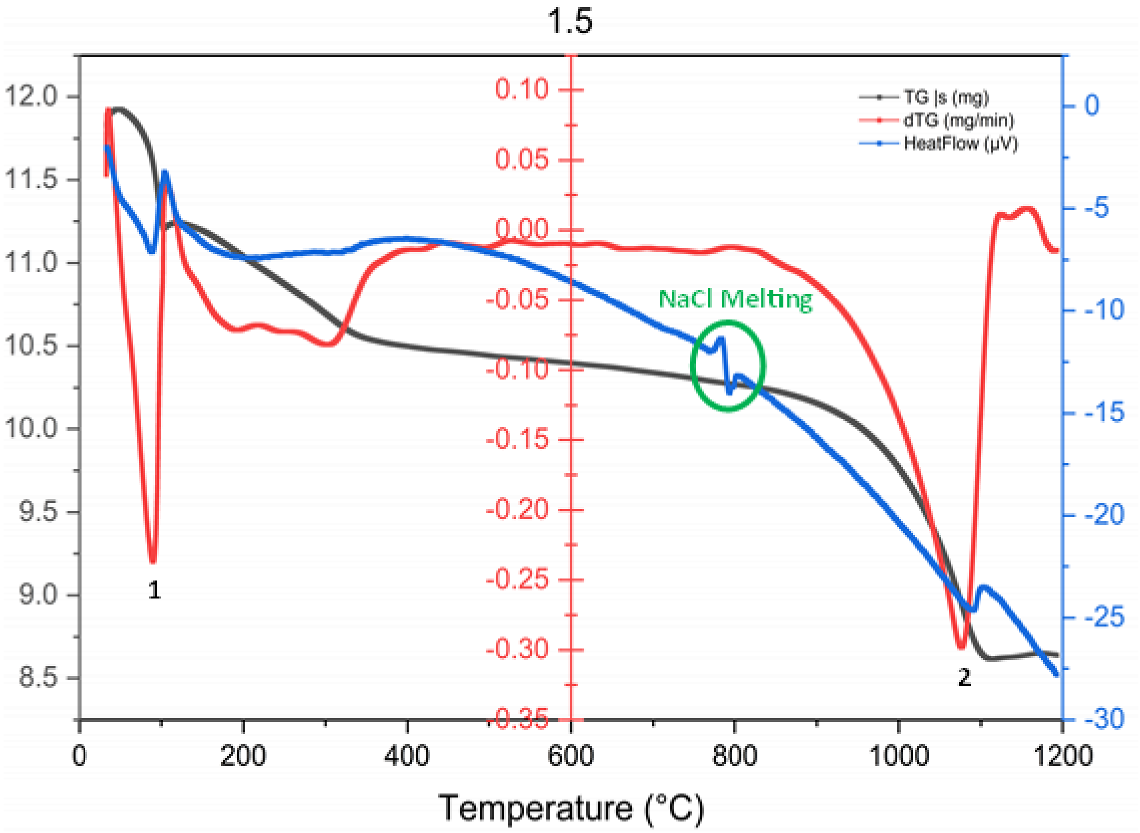

Figure 71: DSC-TGA curves of sol xerogel 1.5 Cl chemistry without tartaric acid powder.

1: Up to 100°C there is a dTG peak which is the loss of physically absorbed water[199], this is associated with an endothermic peak in the DSC data.

The loss of mass observed from 100-300°C can be linked to the loss of ammonia from $NH_4H_2PO_4$ and the remaining structural water.[199]

Sharp endothermic peak at 800°C in the DSC curve is attributed to the melting of NaCl.[135]

2: At 1055°C the dTGA shows a mass loss associated with an endothermic peak in the DSC data which could be related to the evaporation of NaCl.[135]

Figure 72 directly compares the DSC-TGA data for the two chloride samples with and without TA, showing the mass loss and heat flow differences. The data shows quite similar heat flow and dTG curves are obtained for samples with and without TA (e.g.the physically adsorbed water is removed at temperatures up to 100ºC for all samples). The main differences observed between 1.4 and 1.5 curves are related to the presence of tartaric acid, which generates additional peaks in both curves of sample 1.4

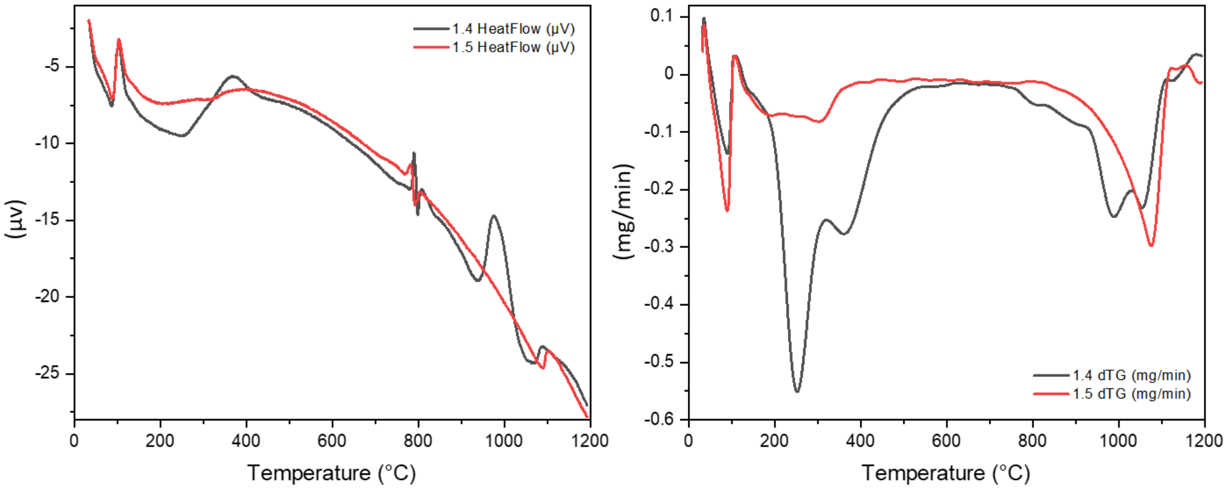

Figure 72: DSC-TGA data of Cl with tartaric acid (1.4) and Cl without tartaric acid (1.5) xerogels.

In comparison, the DSC-TGA data of nitrate chemistry xerogels are a lot more complicated, the data is difficult to analyse and therefore come to a definitive conclusion on the mechanism.

Figure 73 depicts the DSC-TGA data for the nitrates xerogel with tartaric acid.

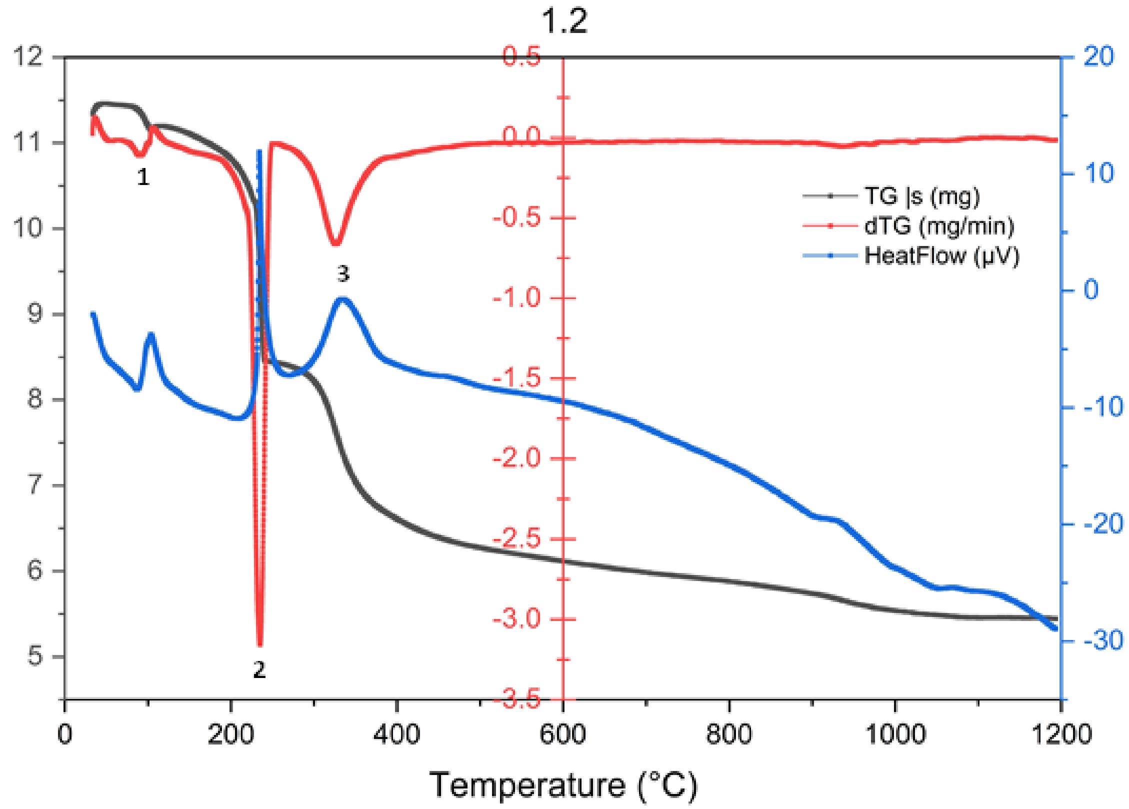

Figure 73: DSC-TGA curves of sol xerogel 1.2 NO_3 chemistry with tartaric acid powder.

Below is a suggested explanation of the chemical mechanism for the DSC-TGA data. Large weight losses occurred between 100°C and 400°C.

1: Up to 100°C there is a dTG peak which is the loss of physically absorbed water[199], this is associated with an endothermic peak in the DSC data.

2: The greatest mass loss occurred at 210°C, where the DSC data also shows a large sharp exothermic peak, this attributes to the combustion between nitrate, ammonia and tartaric acid, since combustion reactions present sharp peaks and a sudden loss of mass.[202]

3: 350°C tGA peak shows combustion of remaining carbon/ammonium nitrate associated with an exothermic peak.

Smaller weight loss occurs between 500°C and 1000°C.[124] At higher temperatures the heat flow is constant, only a small exotherm just above 900ºC. Nitrate is a combustion catalyst; therefore, the loss of compounds and carbon occurs at lower temperatures.

Then investigated the NO_3 without tartaric acid xerogel, however the DSC-TGA data is extremely complex (Figure 74).

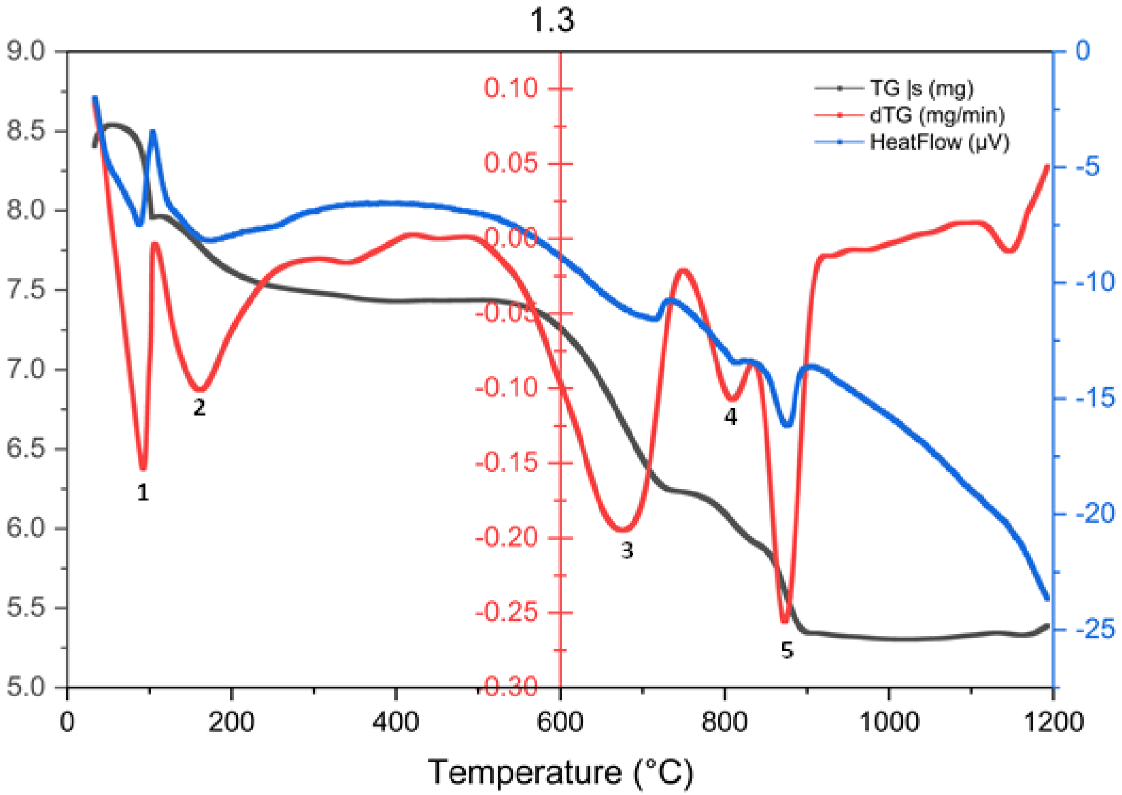

Figure 74: DSC-TGA curves of sol xerogel 1.3 NO3 chemistry without tartaric acid powder.

1: Loss of the remaining structural water, up to 100°C, associated to an endothermic peak.

2, 3 & 4: Endothermic peaks at 160°C, 790°C and 880°C associated with evaporation and loss of compounds. This could include ammonia and oxides.

As explained in the analysis above, there are different exothermic and endothermic peaks (and mass loss) at different temperatures for chloride and nitrate samples with and without tartaric (Figure 75). This means that the reaction mechanisms taking place are different, which could lead to different results (i.e. when a NASICON phase is obtained). The absence of tartaric acid means the material reacts in response only to the external heat source supplied, and any exo- or endo-therms generated by the material, therefore reactions are occurring at higher temperatures.

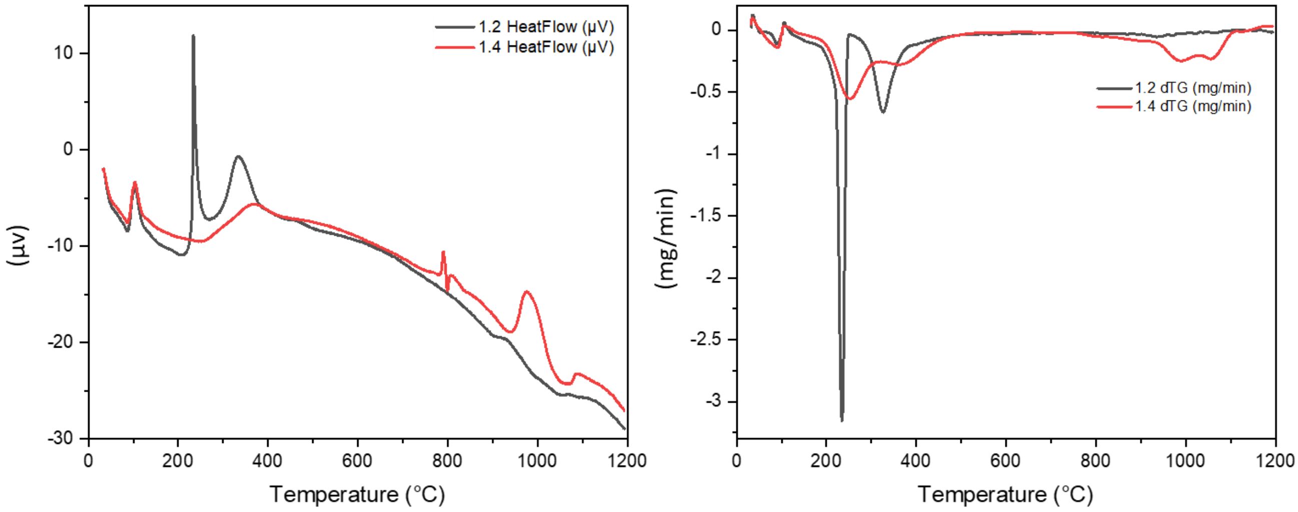

Figure 75: DSC-TGA data of tartaric acid chemistry xerogels, comparing Cl (1.4) and NO_3 (1.2) chemistries.

This DSC-TGA analysis was then used to explain the XRD results obtained for the sol NASICON samples, this comparison is explained within this and the following chapters.

XRD data (Figure 76) illustrates the different NASICON powders synthesised in the experiment, formed from different precursor chemistries. This data will be explored in more detail later in this section; however, it outlines that for these experiment parameters (1000ºC sintering, in air and alumina crucible), only the Cl precursor chemistries formed NASICON.

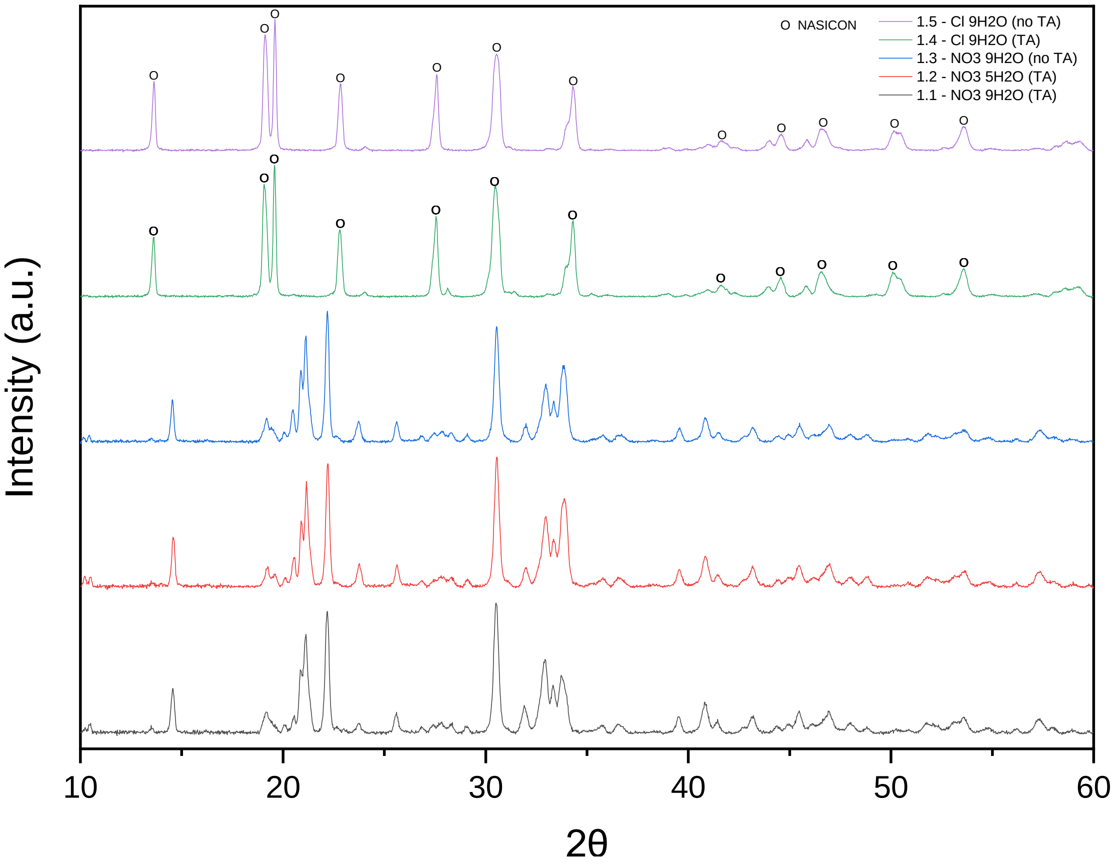

Figure 76: XRD of sol NASICON powders formed with different chemistries in a conventional oven and alumina crucible. Black: $Na_2SiO_3.9H_2O$ Red: $Na_2SiO_3.5H_2O$ Blue: $Na_2SiO_3.9H_2O$ (without tartaric acid) Green: $ZrOCl_2.8H_2O$ Purple: $ZrOCl_2.8H_2O$ (without tartaric acid)

The primary chemistry investigated was the difference in synthesis between $ZrO(NO_3)_2.2H_2O$ compared to $ZrOCl_2.8H_2O$ precursor chemicals as shown in Figure 77.

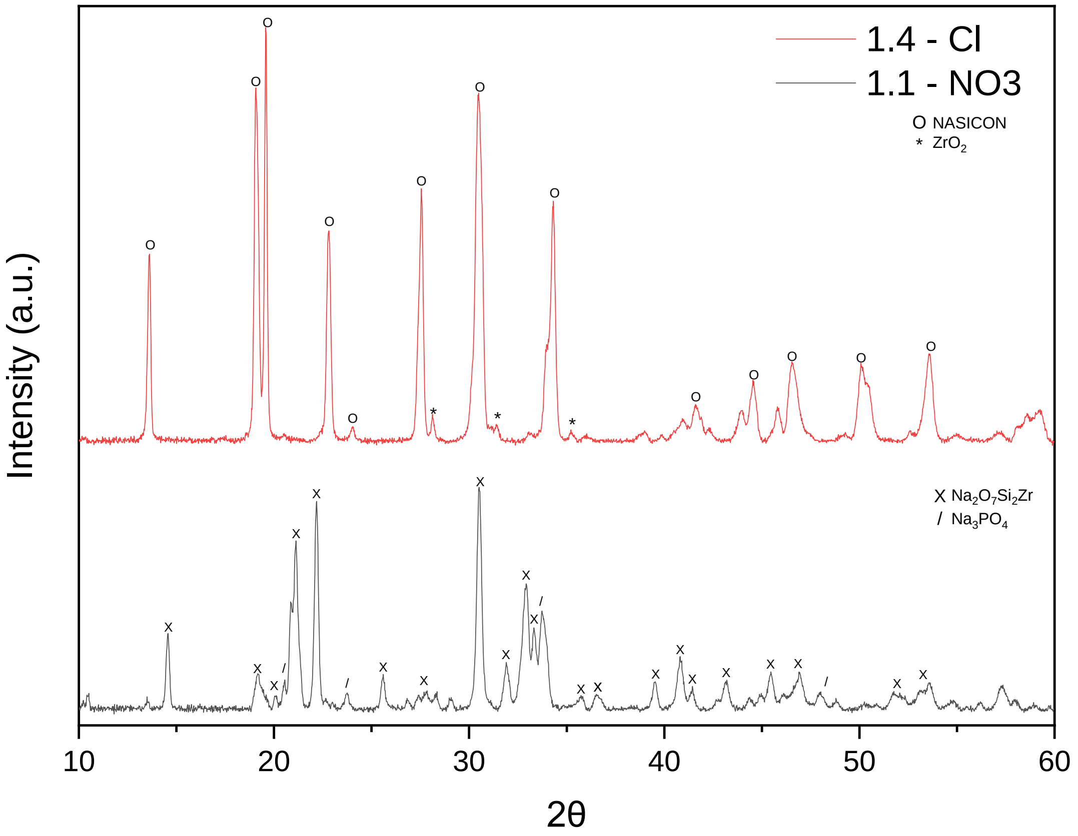

Figure 77: XRD of sol powders of different chemistries - $ZrO(NO_3)_2.2H_2O$ vs $ZrOCl_2.8H_2O$ (both $Na_2SiO_3.9H_2O$). Sintered at 1000°C, in alumina crucibles.

XRD data in Figure 77 illustrates the formation of NASICON (SG 15, COD 1530661[185]) at 1000°C from the $ZrOCl_2.8H_2O$ precursor. Limited secondary phases of ZrO_2 (SG 14, COD 9016714[203]) at 28.1°, 31.4°, and 35.2° have formed, with low intensities. The loss of oxides due to the partial decomposition of NASICON shown in the DSC-TGA data (Figure 70) could explain the presence of small secondary phases in the sintered powder. The chloride chemistry powders in Figure 76 (1.4 and 1.5), show that they have also formed NASICON. The Cl chemistry of both powders formed less secondary phases compared to that of the powder sintered in a graphite crucible (Figure 69). Both samples have NASICON peaks with limited secondary phases detected. ZrO_2 phases are also likely to have formed due to the long sintering times (3 hours), which can cause this secondary phase.[124]

However, NASICON does not appear to have formed at 1000°C for the $ZrO(NO_3)_2.2H_2O$ precursor (Figure 77). 1000°C might not be the right temperature to obtain NASICON with the nitrates sample, a higher temperature could be needed. Phase analysis of the NO_3 XRD data in Figure 76 (1.1, 1.2 and 1.3) suggested the formation of $Na_2O_7Si_2Zr$ (SG 2, COD 9012687[184]) and Na_3PO_4 (SG 225, COD 1524983[204]), confirming NASICON has not formed in the correct phase. The main difference between this XRD data and the data in Figure 69 is the crucible it was sintered in; Figure 69 powder was sintered in graphite crucibles, compared to Figure 76 which was carried out in alumina crucibles. The phase $Na_2O_7Si_2Zr$ was seen in the graphite crucible NO_3 experiments at lower intensities, this suggests that the oxidation of the graphite crucible (combustion exothermic reaction) enabled higher temperatures, converting some of the precursors into NASICON. However, in the alumina crucibles, 1000°C was an insufficient temperature to convert the precursors into NASICON, resulting in the formation of alternative compounds such as $Na_2O_7Si_2Zr$. Additional experiments at higher temperatures were carried out in the next section to confirm it.

Another reason the NO_3 chemistry does not form NASICON at 1000ºC (in alumina), could be due to the exothermic reactions seen in the DSC-TGA data (Figure 73). These exothermic reactions could promote the early formation of crystalline metal oxides and lead to the early evaporation of necessary elements. This could be confirmed with future TGA-FTIR experiments.

These experiments also investigated the $ZrOCl_2.8H_2O$ precursor chemical reaction with and without the presence of tartaric acid, and how this affected the formation of NASICON (Figure 78).

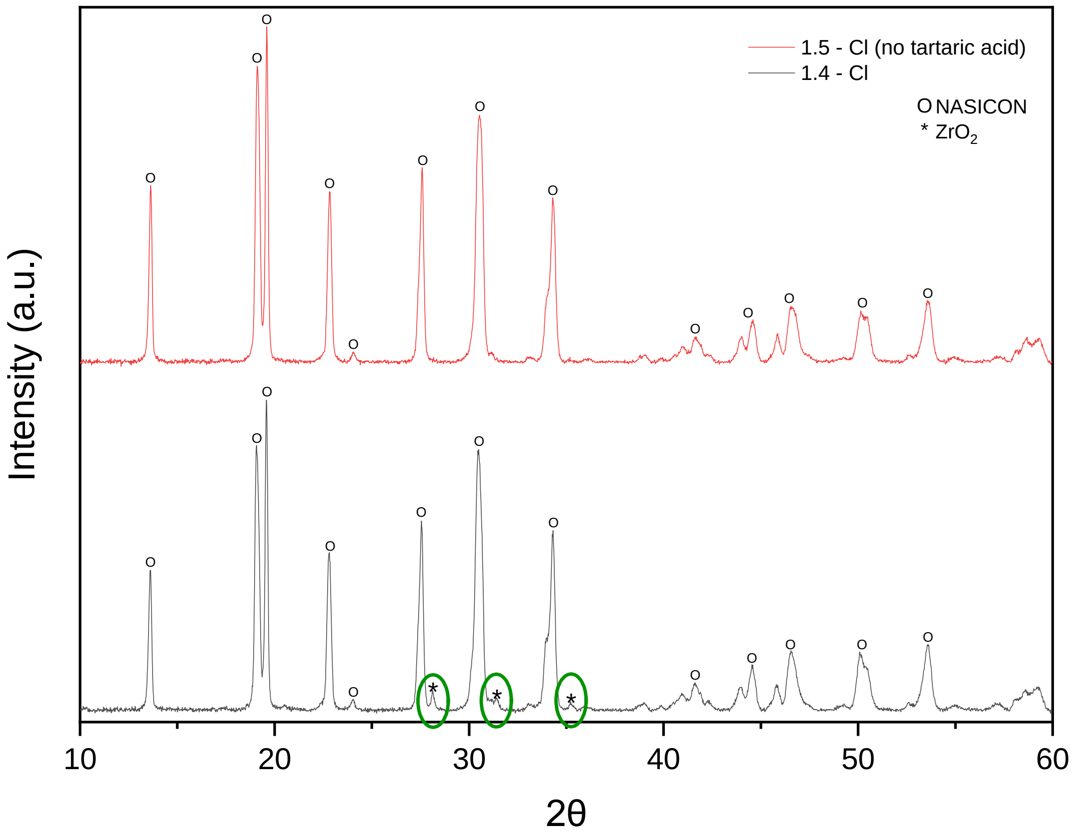

Figure 78: XRD of $ZrOCl_2.8H_2O$ sol powders with tartaric acid (black line - 1.4) and without tartaric acid (red line - 1.5) at 1000ºC in alumina crucibles.

The XRD's for the powder synthesised with and without tartaric acid (Figure 78) are almost identical, and in both cases have formed NASICON. The chloride chemistry NASICON without tartaric acid (SG 15, COD 1530659[185]) formed with negligible secondary phases. The secondary phases, formed in the NASICON formulated with tartaric acid (SG 15, COD 1530661[185]), at 28.1º, 31.4 º, and 35.2º are ZrO_2 (SG 14, COD 9016714[203]); and the intensity of these secondary phases are very low. XRD patterns of 1.4 and 1.5 (Cl chemistry with and without tartaric acid) are not significantly different; the nitrate XRD's are also very similar for 1.1, 1.2 and 1.3 (Figure 76). The patterns are similar regardless of the presence of tartaric acid. DSC-TGA data of the chloride sample with tartaric acid (1.4) presents an exothermic peak close to 1000ºC (977ºC), this exothermic peak increases the overall temperature (real or experimented temperature is higher than 1000ºC) leading to ZrO_2 secondary phase formation. Literature shows the presence of the ZrO_2 (monoclinic) phase increases at temperatures above 1000ºC.[196]

However, for the purposes of developing NASICON thin films in battery solid electrolyte fabrication, the tartaric acid is a necessary additive. As stated in detail in Chapter 2 (literature review), the tartaric acid ensures the stability of the sol by controlling the peptisation reaction.[124] Therefore, it stops the viscosity of the sol from being too high, which is critical to allow the passage of the solution through the gun during spray coating. This instability of sol is visibly apparent, as illustrated in Figure 79.

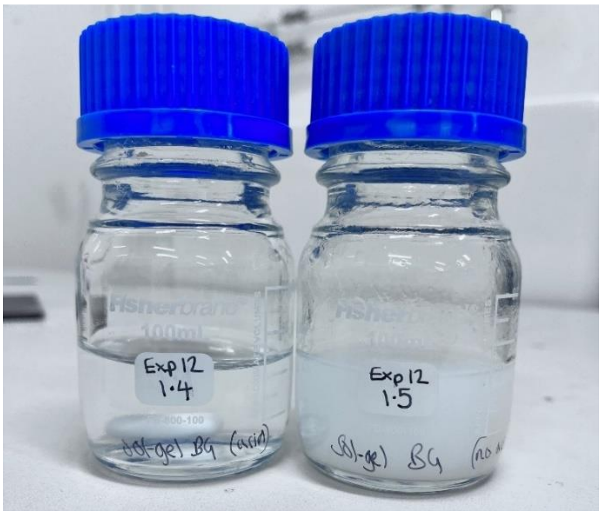

Figure 79: LEFT: Chloride chemistry sol with tartaric acid, RIGHT: chloride chemistry sol without tartaric acid.

Therefore, as the tartaric acid catalyst enables spray coating, the favoured chemistry was the $ZrOCl_2.8H_2O$ precursor in the presence of tartaric acid (Figure 80).

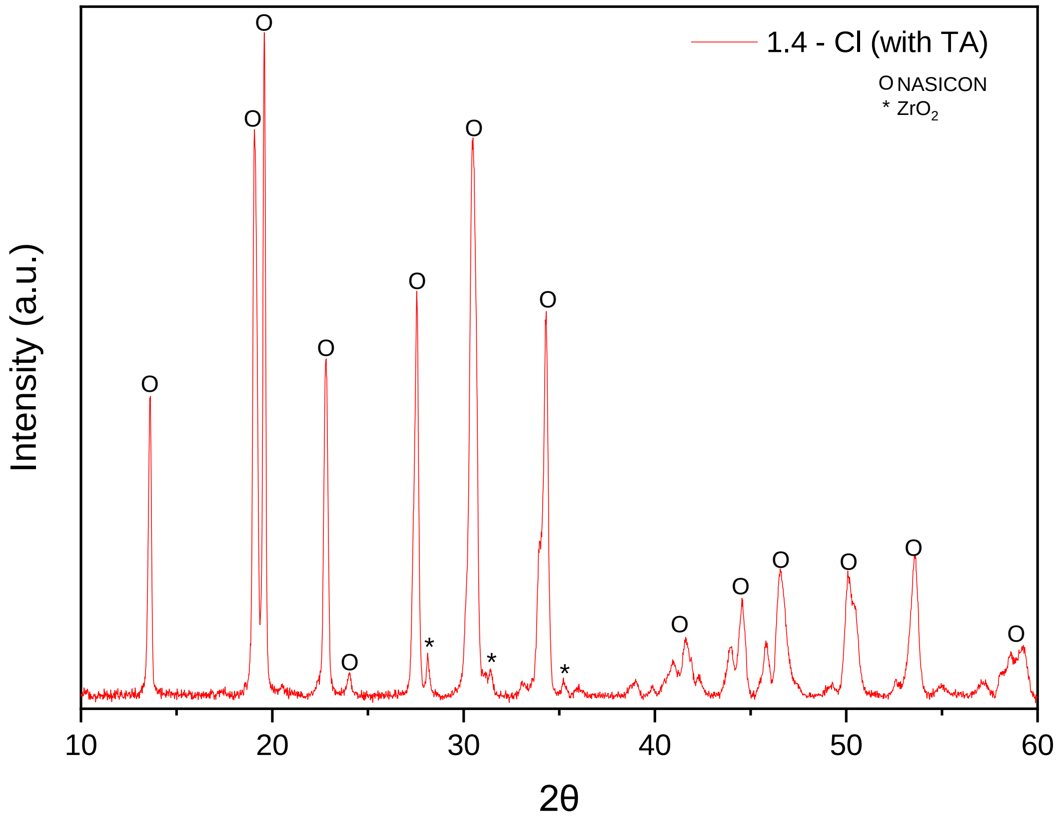

Figure 80: XRD of $ZrOCl_2.8H_2O$ (with tartaric acid) sol powder.

5.2.3 Crucible vs Temperature

Previous experiments (Figure 77) showed NO_3 chemistry samples in alumina crucibles at 1000ºC failed to produce NASICON powder. This experiment investigates whether increasing the sintering temperature to 1100°C yields successful NASICON synthesis.

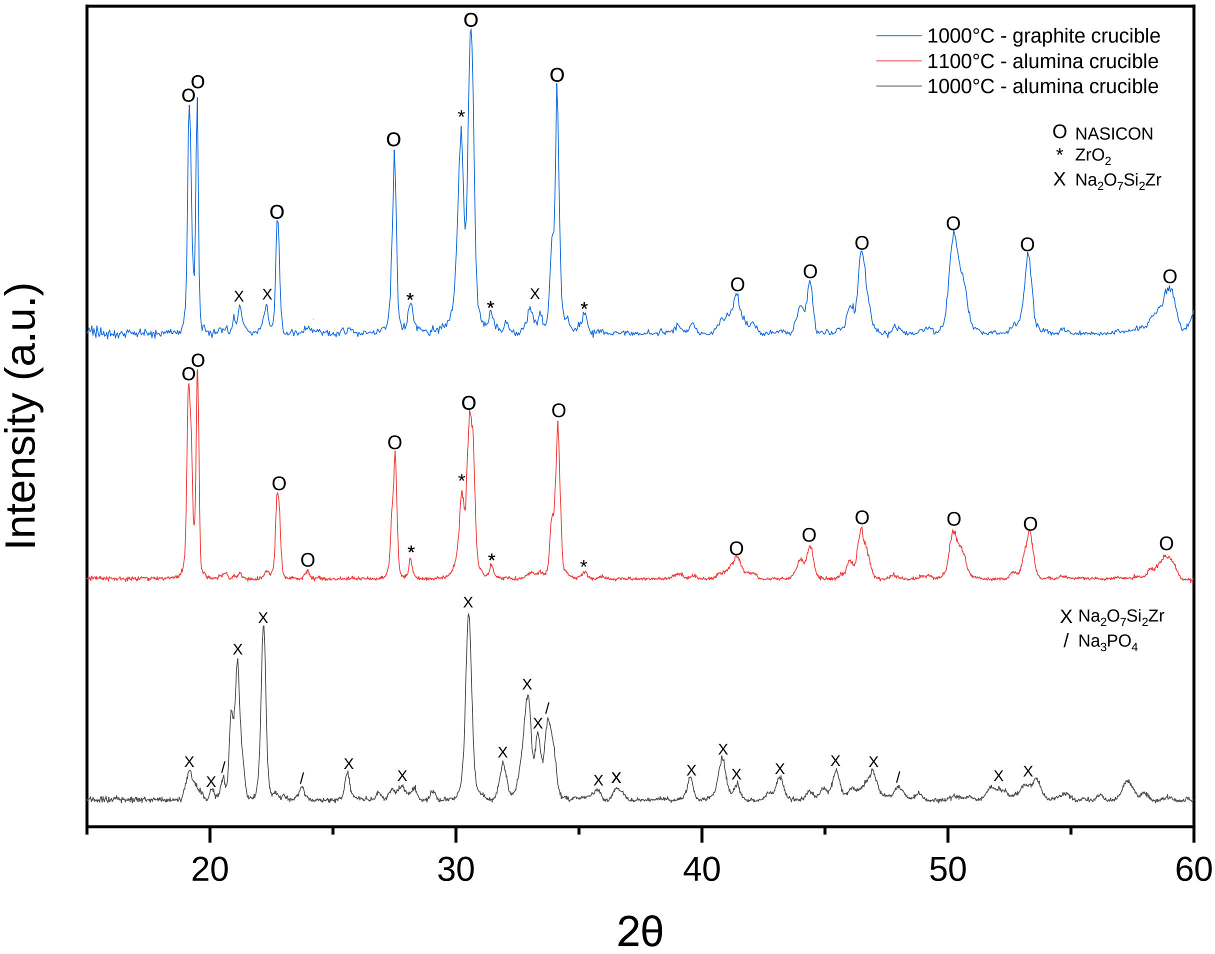

Figure 81: XRD of NO_3 chemistry sol powders sintered in different crucibles and at different temperatures. Black: alumina crucible, 1000°C; Red: alumina crucible, 1100°C; Blue: in a graphite crucible, 1000°C.

NASICON was successfully synthesised at 1100°C using NO_3 chemistry in an alumina crucible (Figure 81); as NASICON (SG 15, COD 1529665[191]) with potentially some hexagonal NASICON (SG 167, COD 1538807[205]) phase distortion. The material also contained secondary phases of ZrO_2 (SG 14, COD 2300544[206] and SG 137, COD 1525706[197]).

In the previous experiment a graphite crucible was used, due to the combustion of carbon in air the degraded graphite crucible reached a higher temperature (or generated extra energy) than the equivalent alumina crucible, this meant that the $ZrO(NO_3)_2.2H_2O$ precursor chemistry NASICON could be formed at 1000°C due to the transferred heat from the graphite's exothermic reaction. This experiment has shown that at the higher temperature of 1100°C NO_3 NASICON can be formed in an alumina crucible (Figure 81).

By comparison, the $ZrOCl_2.8H_2O$ sol forms NASICON at the lower temperature of 1000°C in an alumina crucible. This difference in sintering temperatures between the NO_3 and Cl NASICON materials is due to the difference in chemistry between the precursors used, in turn resulting in different chemical mechanisms during sintering; this is confirmed by the DSC-TGA data Figure 75.

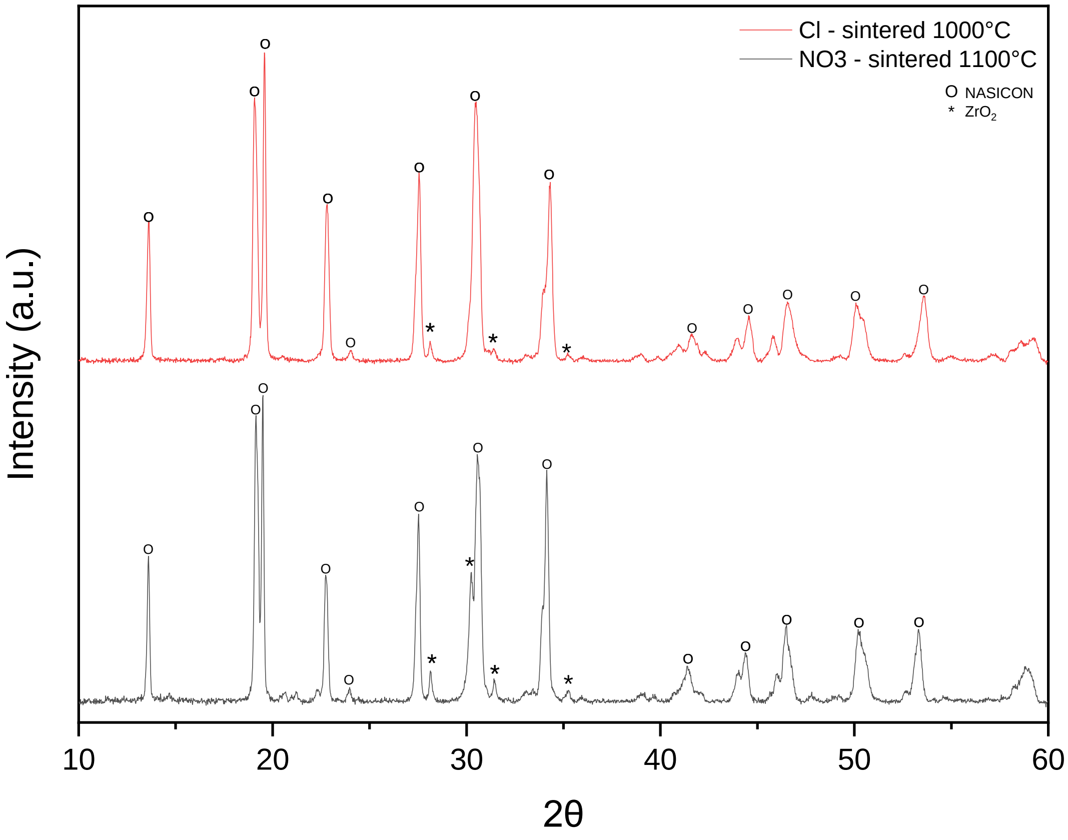

Figure 82: XRD of sol NASICON powder ($ZrO(NO_3)_2.2H_2O$ chemistry) sintered at 1100°C in an alumina crucible. Compared to the XRD of sol NASICON powder ($ZrOCl_2.8H_2O$) sintered at 1000°C in an alumina crucible. NASICON (O) and ZrO_2 (*) phases present.

Figure 82 compares the XRD data of Cl (1000°C) and nitrate (1100°C) powders that have both formed NASICON. The data for both chemistries are very similar, the differences include the intensities of some of the peaks and more secondary phase peaks for the NO_3 chemistry NASICON; a particular feature to note is the ZrO_2 secondary phase peak at 31.5° which is not present in the chloride chemistry. As stated in the literature review (Chapter 12), increased sintering temperatures correlate to an increase in the resultant secondary phases, which is evidenced in the experimental analysis shown here. To reduce the ZrO_2 secondary phase formation further, future work using larger excess Na molar ratio could be carried out.[196]

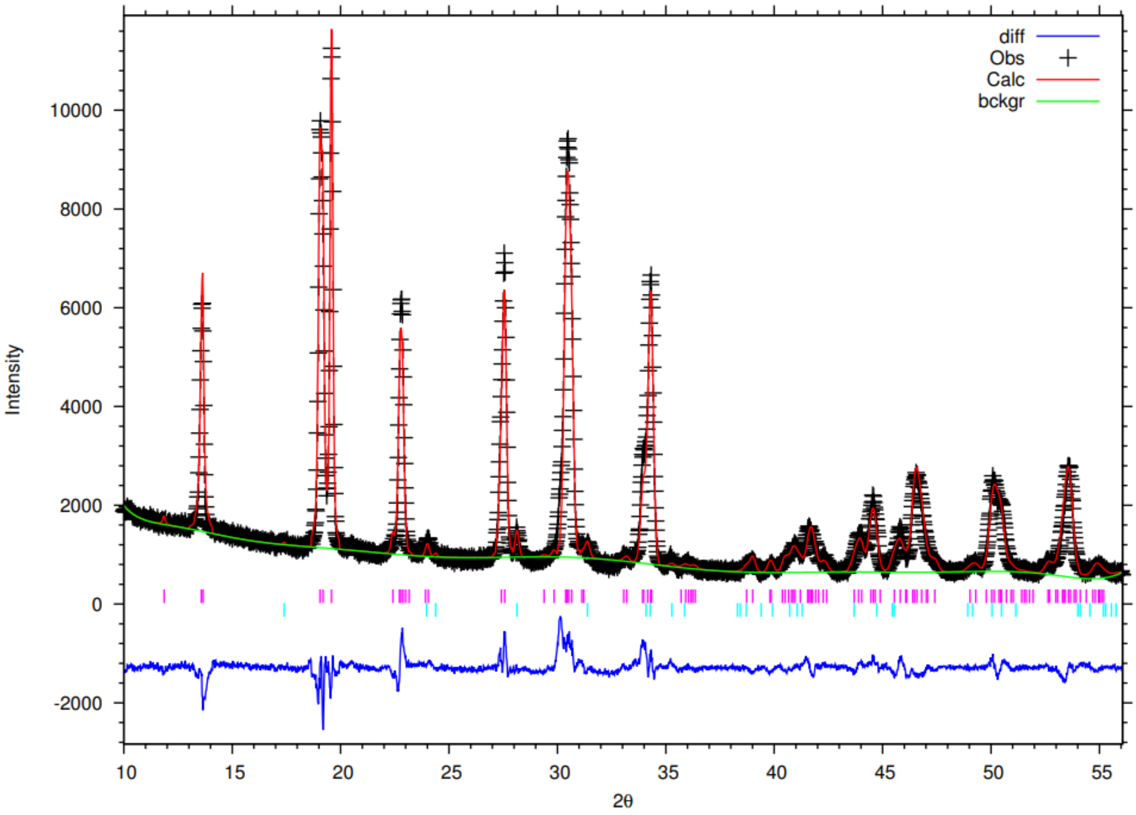

Figure 83: XRD chloride (1000°C) data characterised using Rietveld Refinement (carried out by Professor Serena Margadonna). ***Purple:*** *NASICON peaks,* ***light blue:*** *ZrO_2.*

Table 36: Weight fraction of chloride NASICON and ZrO_2 phases, from Rietveld Refinement.

	NASICON	ZrO_2
Weight fraction	98.2%	1.8%
Rwp	8.47%	
Rexp	6.65%	
χ^2	1.84	

The data confirms adequate goodness of fit parameters, with Rwp below 10 (8.47%) and χ^2 close to the ideal value of 1 (1.84).[193,194]

Rietveld refinement (Figure 83) confirms ZrO_2 as a secondary phase for the Cl chemistry NASICON powder. This analysis quantifies the weight fraction of the ZrO_2 to be 1.8% (Table 36), with some small peaks that point towards another impurity.

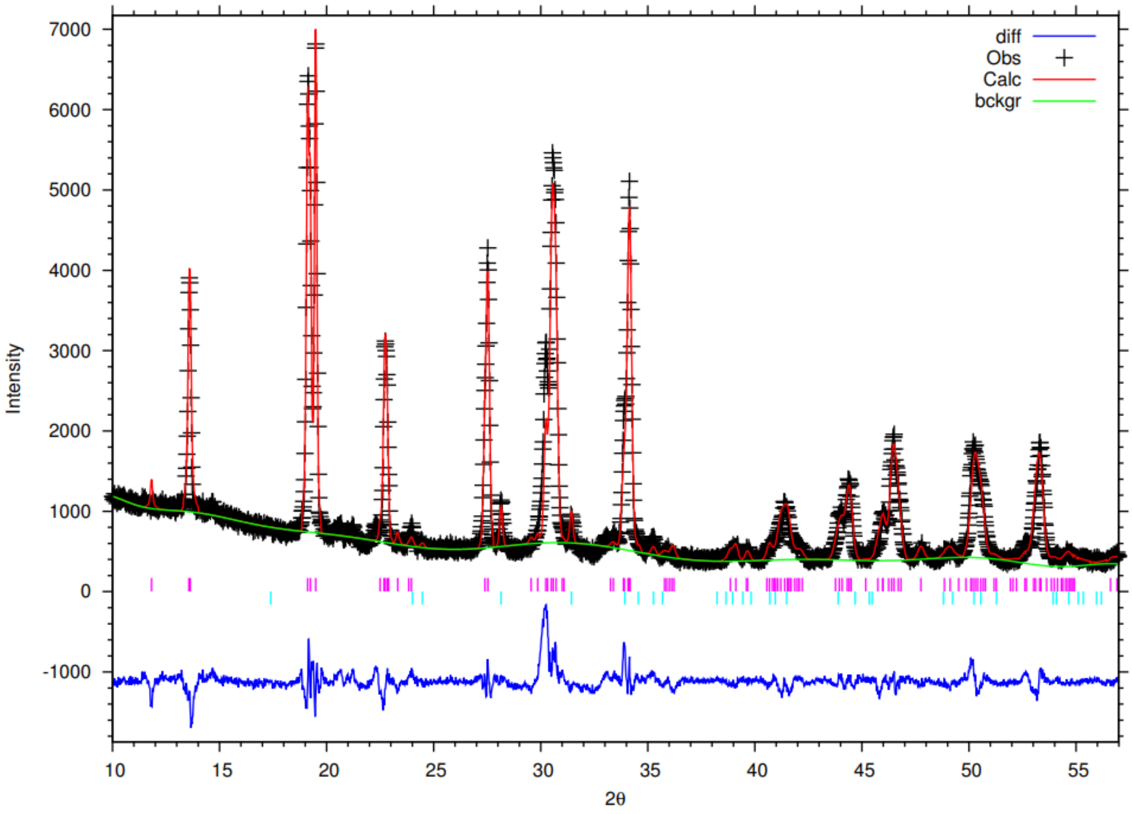

Figure 84: XRD NO_3 (1.4, 1100°C) data characterised using Rietveld Refinement (carried out by Professor Serena Margadonna). Purple: NASICON peaks, light blue: ZrO2.

Table 37: Weight fraction of NO_3 (1100°C) NASICON and ZrO2 phases, from Rietveld Refinement.

	NASICON	**ZrO_2**
Weight fraction	98.5%	1.5%
Rwp	9.69%	
Rexp	6.69%	
χ^2	1.97	

Rietveld refinement (Figure 84) confirms ZrO_2 as a secondary phase for the Cl chemistry NASICON powder, and quantifies the weight fraction of the ZrO_2 to be 1.5% (Table 37). There are more small peaks (than the chloride equivalent NASICON powder) which implies there is at least another 2 different impurities, therefore more secondary phases in the NO_3 powder (overall weight fraction of secondary phases will be greater than 1.5%). This is confirmed by the GOF values (Rwp 9.69% and χ^2 1.97) being greater for the NO_3 chemistry than the Cl. The lattice constants are also bigger than the chloride equivalent (data in Chapter 3 Method), therefore the Cl powder is the preferred precursor chemistry moving forward. Both samples exhibit a secondary phase composition similar to the literature[133,124,135], which also reported small secondary phase distortions of ZrO_2.

The Rietveld refinement shows a similar weight percentage of ZrO_2 to the solid-state synthesised pellets in Chapter 4. This secondary phase of ZrO_2 could potentially be eliminated in the sol work by employing lower sinter temperatures, shorter sintering durations, and the utilising a powder bed. However, given that the primary objective of this thesis was to form NASICON thin films, the presence of <2% secondary phases was deemed beyond acceptable. Further work beyond the scope of this thesis could include longer XRD scans with increased data points to enhance peak definition and improve the goodness of fit for Rietveld refinement analysis.

The XRD's for both sets of data are very similar, however the reduced secondary phases and lower sintering temperatures for chloride-TA precursor NASICON sol is favourable; therefore, future experiments will be carried out using the chloride chemistry. Reduced sintering temperatures ensures less energy use (therefore reduced environmental impacts) and ensures more options for substrate materials that can be employed in thin film synthesis.

5.3 Conclusions

Both chloride and nitrate precursor chemistries form NASICON powder in alumina crucibles, with the presence of <2% ZrO_2 secondary phase peaks (comparable to literature). Cl without tartaric acid forms the purest NASICON, meaning it has the least/no secondary phases. However, the sol is very unstable and starts to gel, and therefore is not usable in future thin film/spray coating work. NO_3 chemistry NASICON exhibits more secondary phases and only forms at elevated temperatures of 1100°C in an alumina crucible, compared to the Cl chemistry (1000°C). Therefore, the chloride and tartaric acid precursor NASICON powder (1.4) is the most suitable chemistry to be employed in subsequent thin film experiments.

This method forms NASICON at reduced sintering temperatures (1000°C) and reduced thermal processing times (total 16 hours) than the solid-state synthesised equivalent pellets (Chapter 4).

This chapter demonstrates the successful synthesis of NASICON powder via the sol peptisation method, as an alternative to the sol method previously reported in literature. This sol technique is essential for informing the subsequent chapter on NASICON thin film synthesis, since the NASICON precursor sol must not gel before deposition. Determining the minimum sintering temperature required for NASICON formation proved valuable, as lower temperatures are preferable when sintering thin films due to substrate temperature limitations. This was further investigated through DSC-TGA work, which indicated the temperatures at which exothermic reactions occur. The study also established baseline understanding of sol synthesis chemistry, identifying the secondary phases that form without substrate interactions and quantifying their presence (% weight phase) through Rietveld analysis.

Chapter 6 – Sol Thin Film NASICON Synthesis

6.1 Introduction

This chapter explores the development of NASICON thin films, applying chemical insights gained from the sol powder experiments presented in Chapter 5. The aim of the experiments is to sinter NASICON after it has been deposited as a film onto a substrate - reaction phase sintering. In this chapter a conventional oven (in air) was used to sinter the films.

The sol technique was employed with water-based sol precursors for the thin film experiments (instead of the solid-state method) because it produced NASICON with low secondary phases at a lower sintering temperature in Chapter 5. In the future when integrating NASICON into the battery (or other devices) as thin films, high sintering temperatures can lead to undesirable reactions with the electrode materials, therefore the lower sintering temperature of sol synthesis is favourable. Furthermore, this thin film method uses a total thermal processing time of 3 hours (plus hot plate and ramp time), dramatically decreased from the solid state (70 hours, Chapter 4) and sol powder work (16 hours, Chapter 5).

Several variables were tested in this chapter to determine the best conditions to form NASICON as a film, including: % concentration, deposition method, substrate used, precursor chemistry and drying/sintering temperatures (Table 38). All variables were considered in relation to secondary phase formation and scalability for industry.

Table 38: Experiments and variables tested for NASICON sol thin film formation.

formulation				conc (%)	substrate	deposition	No. of layers	drying temp (°C)	sintering temp (°C)
$ZrO(NO_3)_2.2H_2O$	$Na_2SiO_3.5H_2O$	$NH_4H_3PO_4$	TA	5	alumina	spray coat	60	150	1000
$ZrO(NO_3)_2.2H_2O$	$Na_2SiO_3.5H_2O$	$NH_4H_3PO_4$	TA	5	alumina	tape cast	4 layers	150	1000
$ZrO(NO_3)_2.2H_2O$	$Na_2SiO_3.5H_2O$	$NH_4H_3PO_4$	TA	6	alumina	tape cast	4 layers	150	1000
$ZrO(NO_3)_2.2H_2O$	$Na_2SiO_3.5H_2O$	$NH_4H_3PO_4$	TA	5	alumina	spray coat	100	120	750 + 1000
$ZrO(NO_3)_2.2H_2O$	$Na_2SiO_3.5H_2O$	$NH_4H_3PO_4$	TA	5	alumina	spray coat	100	120	750
$ZrO(NO_3)_2.2H_2O$	$Na_2SiO_3.9H_2O$	$NH_4H_3PO_4$	TA	5	alumina	spray coat	100	120	1000
$ZrO(NO_3)_2.2H_2O$	$Na_2SiO_3.9H_2O$	$NH_4H_3PO_4$	TA	5	alumina	spray coat	100	120	1180
$ZrO(NO_3)_2.2H_2O$	$Na_2SiO_3.9H_2O$	$NH_4H_3PO_4$	TA	5	quartz	spray coat	100	120	1000
$ZrOCl_2.8H_2O$	$Na_2SiO_3.9H_2O$	$NH_4H_3PO_4$	TA	5	alumina	spray coat	50	120	1000
$ZrOCl_2.8H_2O$	$Na_2SiO_3.9H_2O$	$NH_4H_3PO_4$	TA	5	quartz	spray coat	50	120	1000
$ZrOCl_2.8H_2O$	$Na_2SiO_3.9H_2O$	$NH_4H_3PO_4$	TA	5	alumina	spray coat	50	120	750 + 1000
$ZrOCl_2.8H_2O$	$Na_2SiO_3.9H_2O$	$NH_4H_3PO_4$	TA	5	quartz	spray coat	50	120	750 + 1000
$ZrO(NO_3)_2.2H_2O$	$Na_2SiO_3.9H_2O$	$NH_4H_3PO_4$	TA	5	quartz	Spray coat	50	150	1100
$ZrO(NO_3)_2.2H_2O$	$Na_2SiO_3.9H_2O$	$NH_4H_3PO_4$	TA	5	alumina	Spray coat	50	150	1100
$ZrOCl_2.8H_2O$	$Na_2SiO_3.9H_2O$	$NH_4H_3PO_4$	TA	5	quartz	spray coat	50	150	1000
$ZrOCl_2.8H_2O$	$Na_2SiO_3.9H_2O$	$NH_4H_3PO_4$	TA	5	quartz	spray coat	50	150	1000
$ZrOCl_2.8H_2O$	$Na_2SiO_3.9H_2O$	$NH_4H_3PO_4$	TA	5	quartz	spray coat	50	150	750 + 1000
$ZrOCl_2.8H_2O$	$Na_2SiO_3.9H_2O$	$NH_4H_3PO_4$	TA	5	quartz	spray coat	50	150	750
$ZrOCl_2.8H_2O$	$Na_2SiO_3.9H_2O$	$NH_4H_3PO_4$	TA	5	quartz	spray coat	50	120	950
$ZrOCl_2.8H_2O$	$Na_2SiO_3.9H_2O$	$NH_4H_3PO_4$	TA	5	quartz	spray coat	50	120	1000

6.2 Percentage concentration

The initial experiments looked at the percentage concentration of the sol; as it must contain enough material to chemically react and form NASICON during sintering, but not have a concentration so great that sedimentation and gelation occurs in the sol before deposition.

The concentration of the sol was calculated as the percentage of all the solids in the solvent; the solvent used in the experiments was deionised water. A range of sol's at different concentrations were tested to scope and understand the best concentration range at which the sol film could be deposited. These experiments were carried out using $ZrO(NO_3)_2.2H_2O$ chemistry, at the following concentrations: 2%, 4%, 5%, 6%, 7%, 10% and 20%, in a molar ratio of 2:1:2:3 (Equation 18).

Equation 18

$$ZrO(NO_3)_2.2H_2O + NH_4H_2PO_4 + Na_2SiO_3.9H_2O + C_4H_6O_6 \rightarrow Na_3Zr_2Si_2PO_{12}$$

At the higher concentrations of 7%, 10% and 20% the sol's appeared cloudy, and sediment was observed after stirring overnight. This sediment is likely the ZrO_2 precipitating out of solution, as the Zr material is the only insoluble component in water, it is also the last chemical added and instantly precipitates before stirring. $ZrOCl_2$ is very soluble at very acidic pH (1.85) but if you increase the pH of the medium it precipitates.

From visible inspection 2%, 4%, 5% and 6% solid concentration samples did not appear cloudy and the 5% and 6% concentrations had no sediment after stirring overnight. The highest possible concentration is favoured to facilitate the chemical reaction; therefore, trials were carried out on 5% and 6% concentrations.

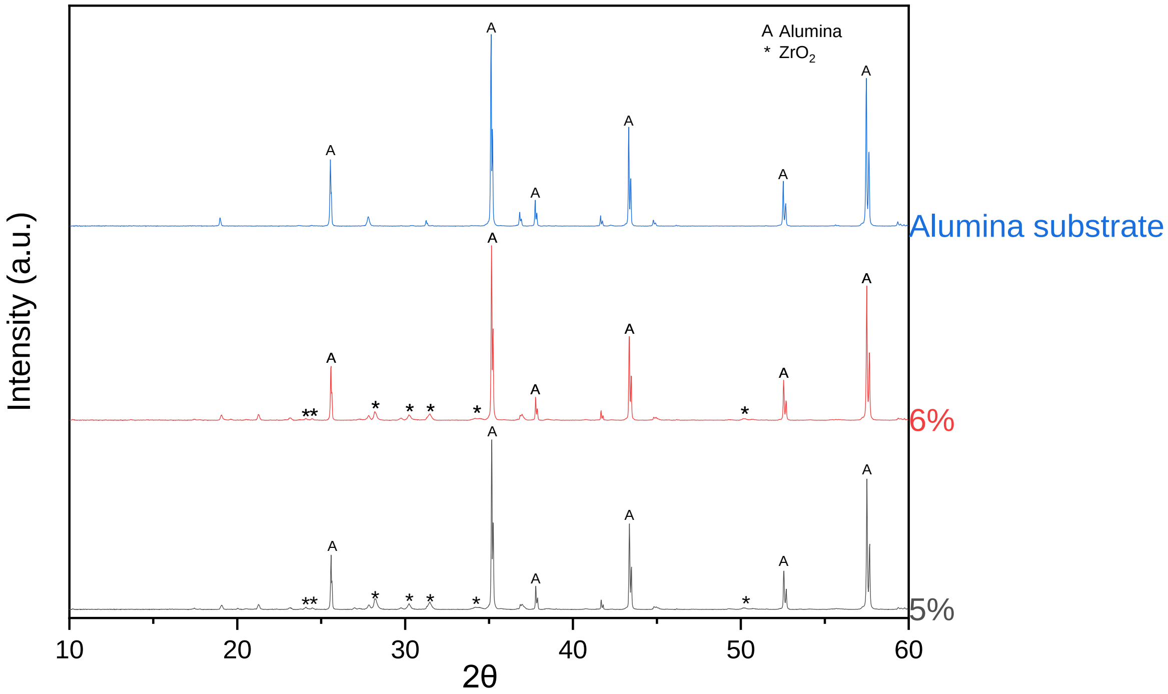

Figure 85: XRD of 5% vs 6% sol NASICON tape casted (4 layers) onto alumina substrate and sintered at 1000°C.

To determine whether the 5% and 6% sol samples were viable as a film, they were tape casted onto an aluminium substrate. The diffraction patterns (Figure 85) illustrate that NASICON has not formed. XRD analysis showed phases of Al_2O_3 (SG 167, COD 2300448[207]; 25.6°, 35.2°, 37.8°, 43.4°, 52.6° and 57.5°) and ZrO_2 (SG 14, COD 2300544[208]; SG 137, COD 2300612[209]; 24.1 °, 24.5 °, 28.2°, 30.2°, 31.5°, 34.3° and 50.2°) are present. Analysis also showed other phases in the sample could potentially be $Al_{0.981}NaO_4Si$ or $Al_{7.2}Na_{7.15}O_{32}Si_{8.8}$.

Previous sol work in Chapter 5 ascertained that NASICON can form as a powder from the same chemical reaction, this suggests that the issues in NASICON thin film formation are due to substrate interaction explained by Al^{2+} diffusion stated in Chapter 2.

Weight loss experiments were also carried out, which showed 4% weight loss at all tested concentrations after filtering. Therefore, an extra 4% of the zirconia precursor chemical was added in every experiment to ensure the same molar ratio, as detailed in the methods section (Chapter 3).

After a few days the 6% showed sediment on the side of the glass beaker and started to gel, compared to the 5% sample which did not. Demonstrating that the 5% solid sample had a higher chemical stability compared to the 6% sample. Therefore the 5% concentration sol was selected for future experiments.

6.3 Deposition method

As explained in Chapter 2 several coating techniques are suitable for the deposition of thin films. Scoping experiments in this research explored tape casting, spin coating, drop casting and spray coating techniques.

Spin coating was chosen as a deposition technique due to its ability to control the thickness of the film, this is done by dropping the sol onto a substrate and rotating it. Variables that effect the homogeneity and thickness of the film include the speed (rpm) and time (seconds) at which the substrate is rotated. The technique formed inhomogeneous films, plus the technique was labour intensive and time consuming - after each layer deposited the sample had to be moved and dried for 1 minute in a conventional oven or on a hotplate. Therefore, this combined with the technique being unfavourable for industrial scale-up, is why spin coating was not used in further experiments.

Another method tested was drop casting, which involved pipetting a drop of sol onto the substrate and allowing it to spread until it coated the entire substrate surface. An inhomogeneous film was observed (coffee ring effect[210]), and the thickness of the film was difficult to control – therefore this technique was not employed in further work.

Two techniques that had potential in the deposition of NASICON sol as a thin film were spray coating and tape casting. This is due to the ability to control film thickness and the potential to make homogeneous films. Experiments were carried out to compare the two techniques, where NO_3 chemistry sol was tape casted and spray coated onto alumina substrates. Both samples were subsequentially sintered at 1000°C in a conventional oven. Some of the scoping work was carried out prior to some of the Chapter 5 experiments, and therefore they were carried out using NO_3 chemistry and 1000ºC sintering temperatures.

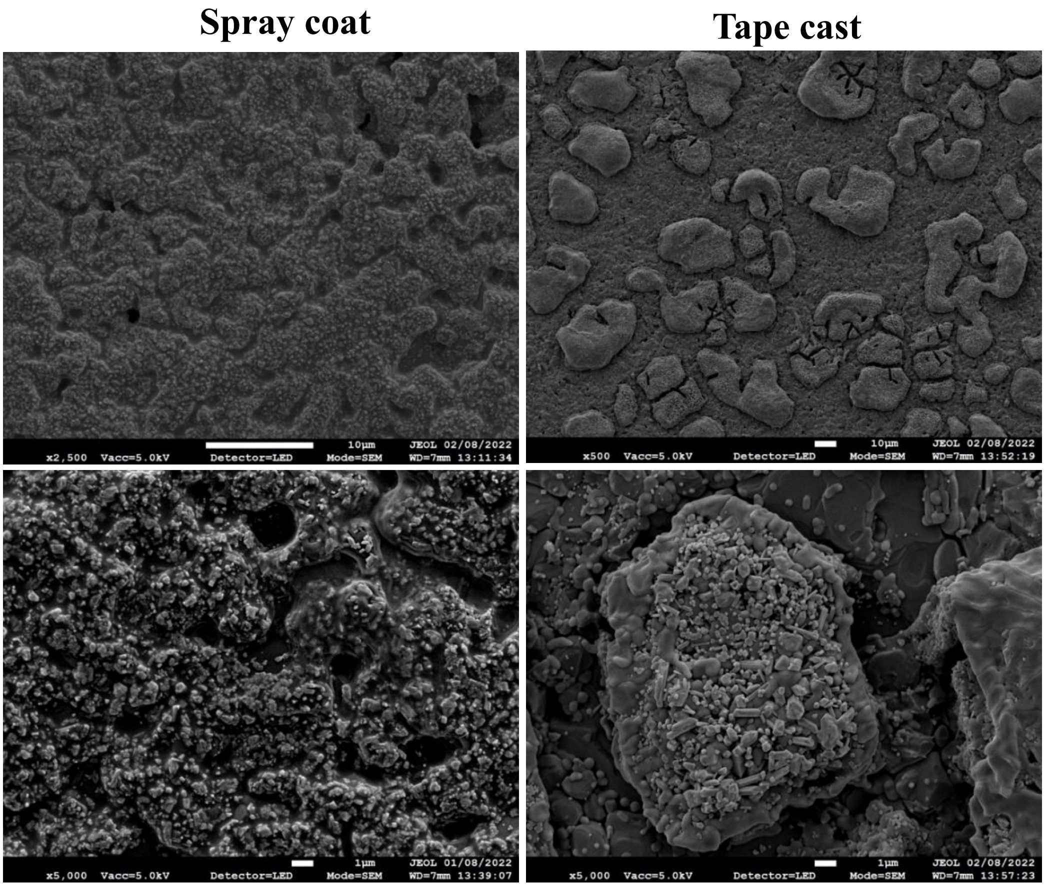

Figure 86: Alumina substrates with 5% sol (NO_3 chemistry) sintered at 1000°C. Images on the left show the film deposited by spray coating, images on the right are of the film deposited by tape casting.

Tape casting involved placing tape on either side of the substrate and pipetting sol onto it, a glass rod was then used to spread the sol over the substrate and remove any excess liquid. This method could make reproducible thin films due to the tape determining the film height, which was removed after drying.[211] However, the films look much less uniform and therefore other methods are more favourable. The film is less homogenous than the spray coating equivalent, as islands appear to have formed (Figure 86).

Alternatively, spray coating involved placing the substrates on a hot plate (120/150°C) and operating a spray gun at a set distance from the samples. Repeated application of a vertical pass (1 minute dwell) followed by 1 horizontal pass (1 minute dwell), allowed the application of precursor films and drying them to remove the solvent – H_2O. This method controlled the film thickness via flow rate of the spray was set using two pressure gauges, one on the gas regulator and one on the spray gun. This made a more reproducible and homogeneous film than the tape casted equivalent (Figure 86) – it is also suitable for industrial scale-up. Therefore, spray coating was the chosen deposition method.

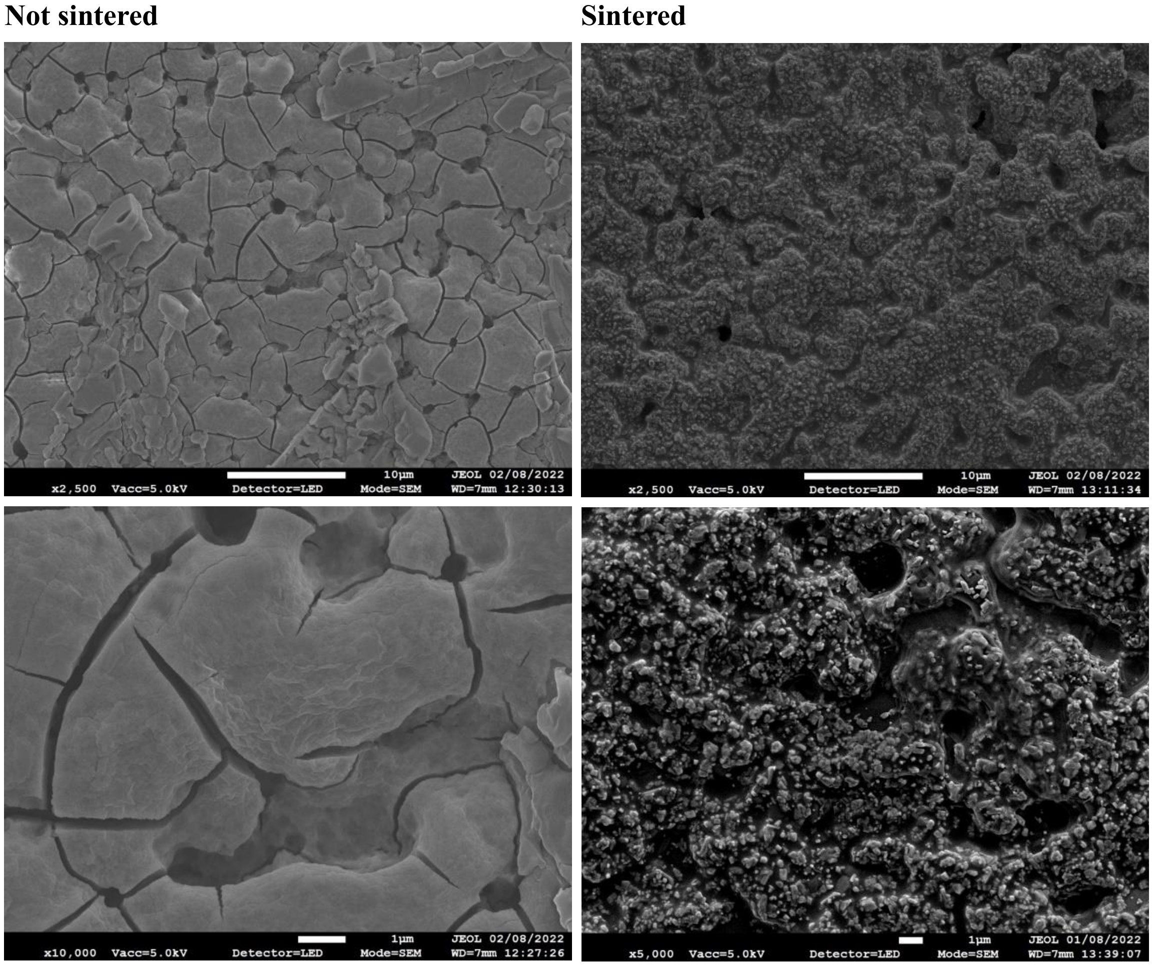

Figure 87: Alumina substrates spray coated with 60 layers of 5% sol NASICON. SEM Images on the left show the film before sintering, images on the right are of the film post sintering.

Comparing SEM images of the spray coated film pre and post sintering (Figure 87) show an even coverage of the sol. The film prior to sintering shows cracks and holes in the film - the DSC-TGA data in Chapter 5 showed that an exothermic reaction happens at 150°C (removal of physically absorbed water), this may have generated the cracks on the surface. Therefore, changing the drying temperature of the hotplate (eg. 120°C) could help this. Homogeneity could be improved by several things such as altering the sol pH and the solvent used, which can subsequently be characterised by contact angle analysis.

One scoping experiment carried out involved adding a small amount of IPA to the sol, however this greatly increased the viscosity, which is unsuitable for spray coating. Another experiment that could be tested involves altering the pH. The sol is stable at a more acidic pH, because SiO_2 gels at acidic pH's; therefore, NaOH could be used to modify the pH of the sol to a more alkaline pH. This could improve homogeneity and reduce SiO_2 secondary phases.[212] Latter experiments have been carried out with NaOH or ammonia as a pH modifier in the sol; showing promise by stopping the gelation for several weeks, and improving the stability and wettability of the sol. More experiments on NASICON sol film homogeneity need to be explored, however this was beyond this scope for this PhD.

The spray coated film post sintering (1000°C) appears to be homogenous and compact (Figure 87), however different shaped crystal structures are present. Previous XRD data (Figure 85) suggests $Al_{0.981}NaO_4Si$ or $Al_{7.2}Na_{7.15}O_{32}Si_{8.8}$ structures may have formed, along with ZrO_2. As previously stated this is due to the influence of the alumina substrate and the thermal stability of ZrO_2, therefore further experiments must explore the impact of the substrate on NASICON thin film formation.

6.4 Substrates: Alumina vs Quartz

Scoping experiments were carried out to determine which substrate facilitates the formation of a NASICON thin film. Two substrates were tested – alumina (Al_2O_3) and quartz (SiO_2), which were chosen primarily due to their exceptional heat resistance/stability and chemical inertness. Alumina was used as a crucible in the previous chapters and has a maximum working temperature of 1750°C; quartz has the following temperature limits: softening Point - 1683°C, annealing Point - 1215°C and strain Point - 1120°C (defined by almath).

Initial work looked at spray coating NO_3 chemistry (5%) sol on alumina substrates, and conventionally sintering in the oven at different temperatures - 1000°C and 1180°C. These temperatures were selected due to the sol powder data (Chapter 5), illustrating a higher temperature is needed for NO_3 chemistry sol NASICON to form in an alumina crucible.

The films were characterised before and after sintering to understand if any chemical changes occur after the high temperature treatment. There are differences between the XRDs before and after sintering (Figure 88), suggesting there has been some phase formation.

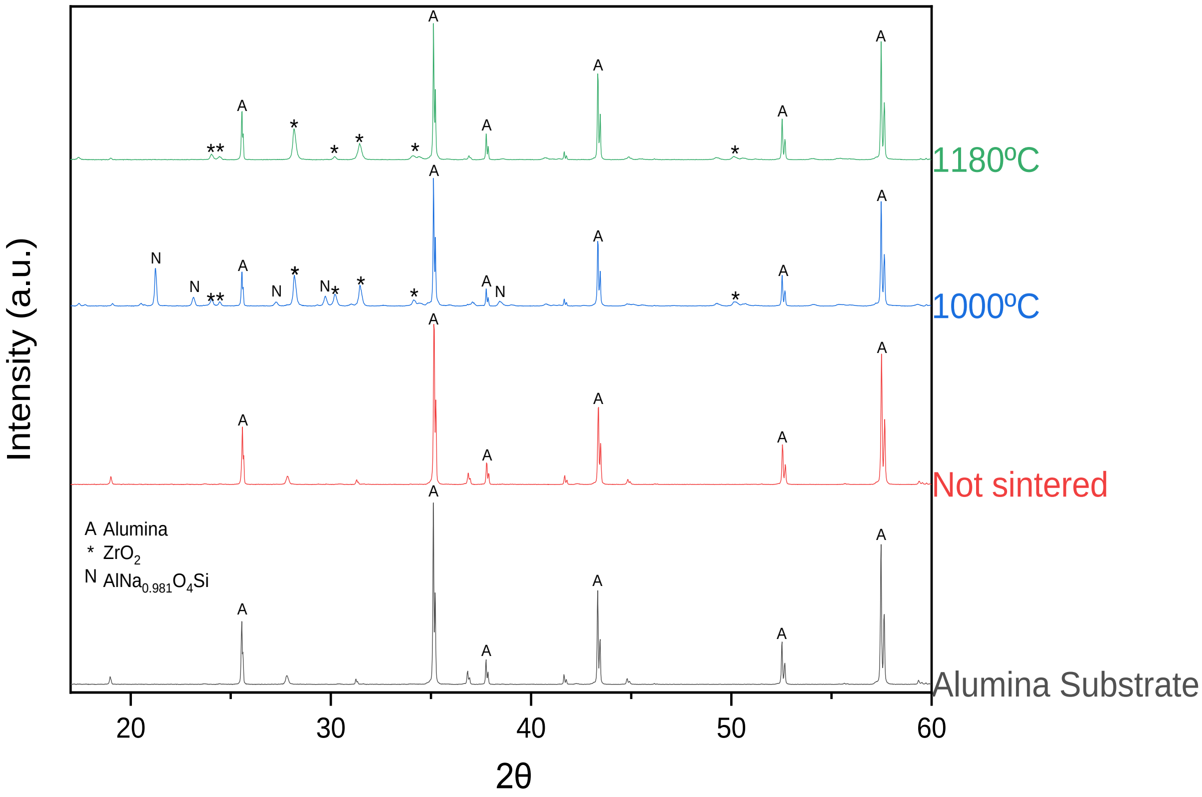

Figure 88: XRD of sol NO_3 NASICON spray coated on alumina substrates and sintered at 1000°C or 1180°C. Compared to the XRD of the alumina substrate. XRD of 5% sol NO_3 NASICON spray coated on alumina substrate sintered at 1000°C vs non-sintered samples.

To understand the peaks present in the sintered thin film, the data was compared to the alumina substrate. Al_2O_3 (SG 4, COD 1000032[209]) peaks are present in all XRDs at 24º, 24.5º, 28.2º, 30.2º, 31.5º and 34.3º. The XRD in Figure 88 suggests that at 1000ºC and 1180ºC NASICON has not formed, the peaks present predominantly correlate to the alumina substrate and a ZrO_2 phase at 25.6º, 35.1º, 37.8º, 43.3º, 52.5º and 57.5º. However, at 1000ºC low intensity peaks present at 21.3º, 23.1º, 27.3º, 29.7º, 38.5º suggest the formation of a $AlNa_{0.981}O_4Si$ (SG 4, COD 9010480[213]) phase, which is not present at 1180ºC.

One explanation for no NASICON peaks present in the XRD data is that the film is 60 layers (later work showed this to be ~10 µm thick) which we believe is thick enough for the XRD to detect NASICON peaks, however it may be that the crystal signal of the alumina greatly outweighs the NASICON signal. Further work, using grazing incidence XRD could confirm this.

A more probable explanation is that there is an interaction between the Al^{3+} in the alumina substrate and the sol film at high temperatures, which in turn stops the formation of NASICON. Al_2O_3 experiences grain growth on sintering, literature indicates there is a diffusion of Al^{3+} ions into the NASICON film which is then incorporated into the NASICON grains.[111] This was also evidenced in Chapter 4 when using alumina crucibles at high temperatures during the solid-state synthesis technique.

To decrease the effects of chemical reactions between the substrate and film, experiments were undertaken on quartz discs (Figure 89). Alumina can react with both acid and bases so can react with the sol, particularly at these temperatures, whereas quartz is more chemically inert.

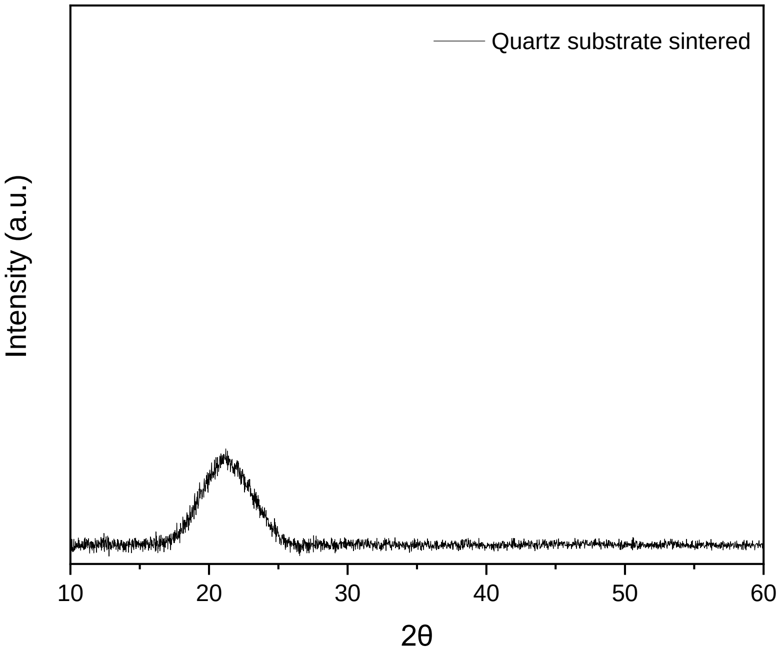

Figure 89: XRD of quartz substrate heated in a conventional oven at 1000°C for 3 hours.

NO_3 chemistry sol (5%) was spray coated onto quartz substrates and conventionally sintered in an oven at 1000°C.

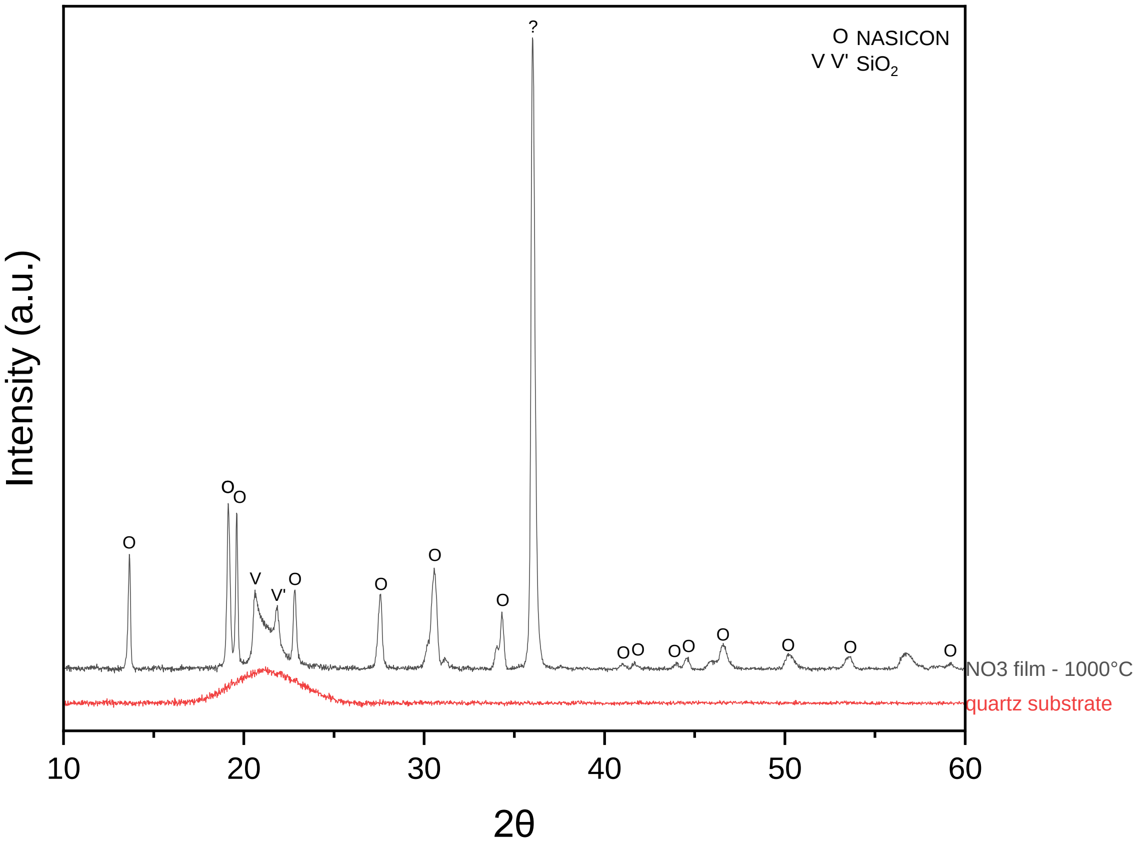

Figure 90: XRD of NO_3 chemistry sol NASICON spray coated and sintered (1000°C) on a quartz substrate, compared to a quartz substrate.

The experiment showed that NASICON has formed using a water-based precursor sol, spray coating and reaction phase sintering - a new way to make films. NASICON (SG 15, COD 1529665[191]) peaks were confirmed via XRD (Figure 90 and Figure 91) at 13.6°, 19.1°,19.6°, 22.8°, 27.6°, 30.6°, 34.3°, 41°, 41.7°, 44°, 44.6°, 46.6°, 50.3°, 53.5° and 59°. SiO_2 secondary phases are present at 20.6° (SG 1, COD 9013393[214]; V - orthorhombic/tridymite) and 21.8° (SG 92, COD 9001578[215]; V' - tetragonal/cristobalite). XRD analysis of the peak at 36° is inconclusive, further experiments need to be carried out to determine this peak.

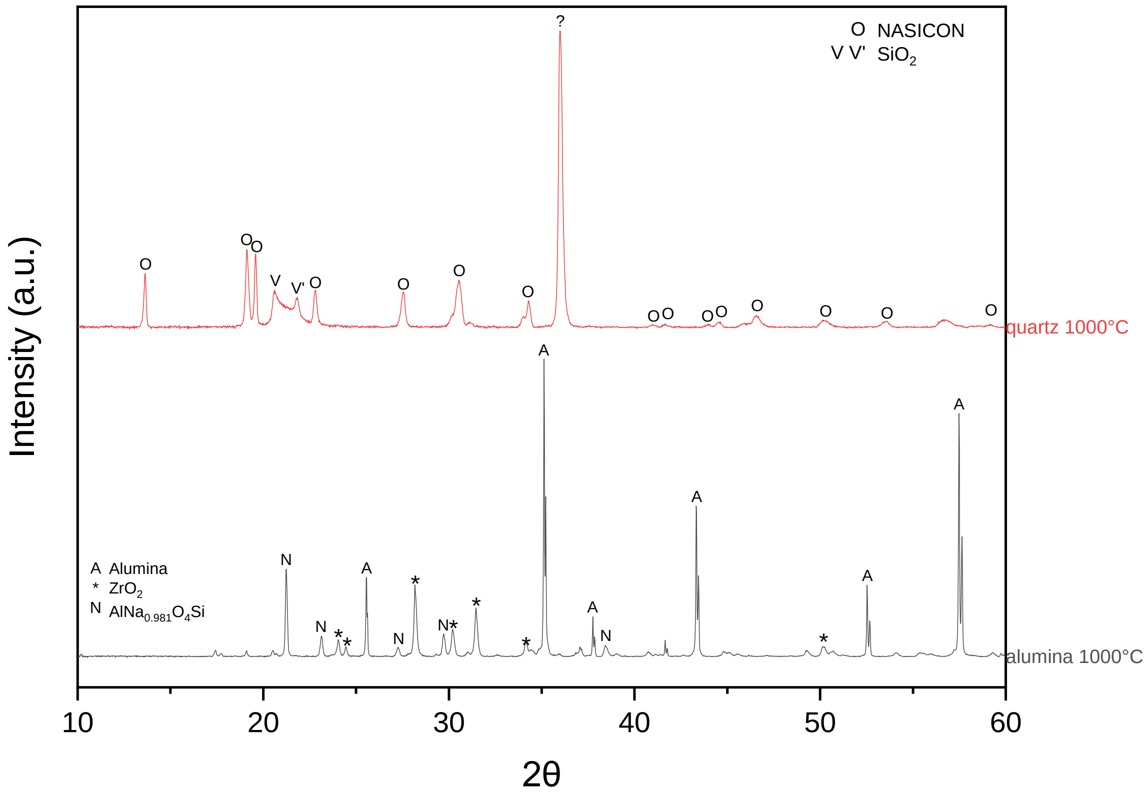

Figure 91: XRD of NO_3 chemistry sol spray coated and sintered on a quartz substrate, vs the same sol spray coated on an alumina substrate.

XRD (Figure 91) shows NASICON forms on the quartz substrate, compared to the alumina sample which does not. As the thickness of both samples are the same, this confirms NASICON has not formed on the alumina substrate due to the Al^{3+} interaction. Therefore, quartz substrates are used for all experiments moving forward.

6.5 Chemistry: Chloride vs Nitrate

Informed from experimental data in Chapter 5, different chemistries were tested to determine the best precursor chemicals used to produce NAISCON thin films on quartz substrates. The main variable tested was $ZrO(NO_3)_2.2H_2O$ (Equation 18) vs $ZrOCl_2.8H_2O$ (Equation 19).

Previous work (Chapter 5) determined that tartaric acid is a necessary component as it stabilises the sol and reduces viscosity to allow spray coating - therefore, this variable remained constant. Furthermore, $Na_2SiO_3.9H_2O$ or $Na_2SiO_3.5H_2O$ can be used as it does not affect the chemistry of the NASICON, but to reduce the number of factors that could affect the outcome of the experiment $Na_2SiO_3.9H_2O$ was selected. The aim of the experiment was to find out if NASICON can form as a thin film using both chemistries and if there are any differences between the two films.

Equation 19

$$ZrOCl_2.8H_2O + NH_4H_2PO_4 + Na_2SiO_3.9H_2O + C_4H_6O_6 \rightarrow Na_3Zr_2Si_2PO_{12}$$

Experiments looked at depositing the NO_3 chemistry sol as a thin film onto quartz using a spray gun and sintering via a conventional oven. Details of the spray coating technique is described in the methods section (Chapter 3). The drying temperature employed is 120°C (hotplate) and the sintering temperature is 1000°C.

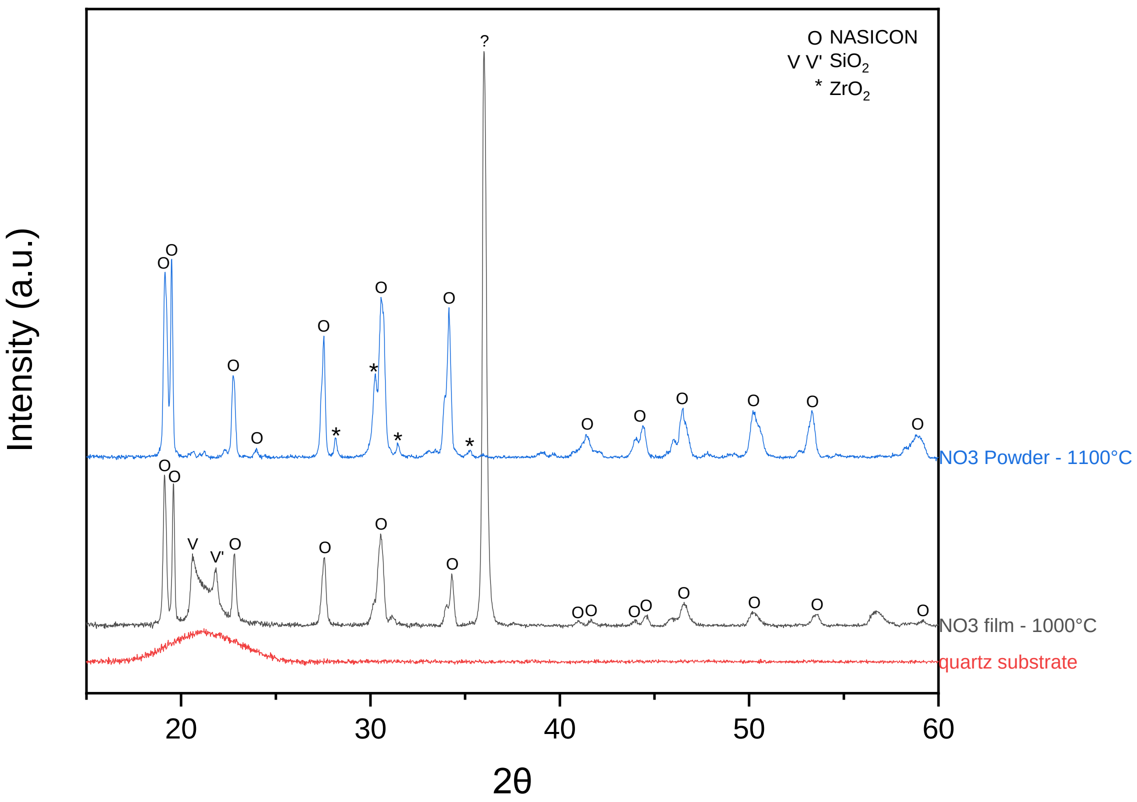

Figure 92: XRD of NO_3 NASICON sol spray coated on a quartz substrate (dried at 120°C) and sintered at 1000°C. XRD of equivalent sol NASICON powder and a XRD of the quartz substrate.

The XRD pattern's (Figure 92) show that the thin film has formed NASICON (SG 15, COD 1529665[191], and is confirmed by comparing it to the NO_3 powder sintered at 1100 ºC. The two samples contain secondary phases, however the powder has predominantly ZrO_2 (*) secondary phases (due to the longer sintering times of 3 hours) compared to the thin film which contains SiO_2 phases. There is still an unknown secondary phase with an extremely high intensity at 36º in the thin film data. Due to the intensity of the peak, this may be the main crystal phase that has formed on the quartz.

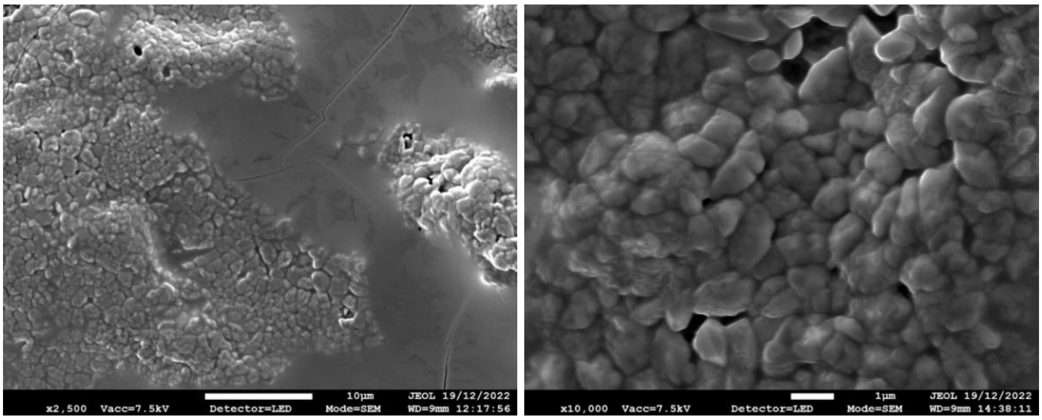

Figure 93: SEM images of sol NO_3 chemistry NASICON spray coated and sintered at 1000°C on a quartz substrate.

SEM images (Figure 93) of the sol coated and sintered show the film is not as homogenous as the alumina equivalent, but NASICON has formed. The crystals appear to have formed islands and the characteristic cubic crystals normally viewed by SEM for NASICON are not present, grains appear molten/less defined.

To directly compare the NO_3 thin film work with the sol powders in Chapter 5, experiments investigated NO_3 chemistry at higher drying and sintering temperatures: 150°C drying temperature and 1100°C sintering temperatures were employed.

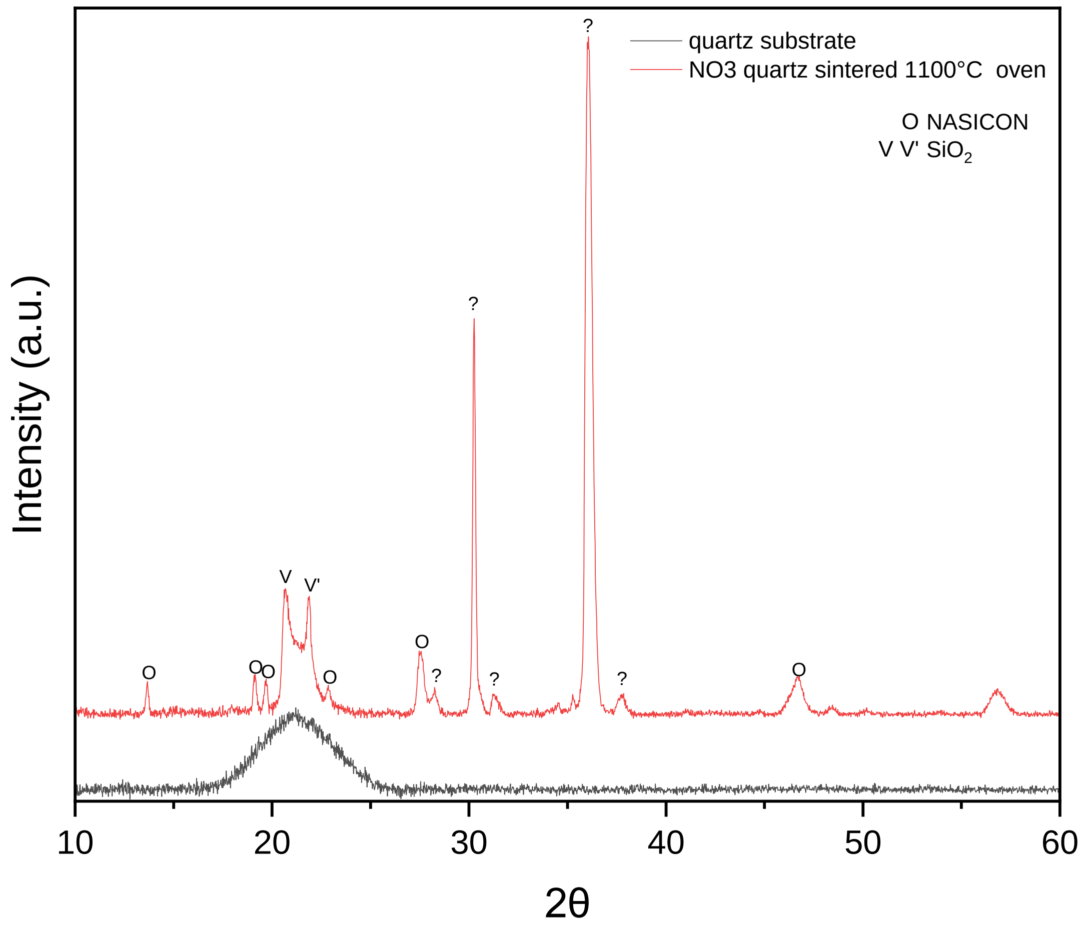

Figure 94: XRD of NASICON sol (ZrO(NO$_3$)$_2$.2H$_2$O) spray coated onto quartz (150°C) and sintered conventionally at 1100°C, compared to the XRD of the quartz substrate.

Figure 94 XRD shows NASICON (SG 15, COD 1530658[216]) has formed at 13.6º, 19.1º, 19.6º, 22.8º, 27.6º and 46.4º. However, the SiO$_2$ (SG 92, COD 9001578[215]; SG 1, COD 9013393[214]) secondary phase peaks at 21.7º and 21.8º are of a high intensity and the NASICON peaks have a lower intensity than Figure 92. The unknown peak at 36º has a very high intensity and more secondary phase peaks are present at 28.3º, 31.3º and 37.8º which are potentially SiO$_2$ or ZrO$_2$.

ZrOCl$_2$.8H$_2$O chemistry sol thin films were then synthesised onto the quartz substrates. Drying and sintering temperatures used were 120°C and 1000°C respectively (conventional oven).

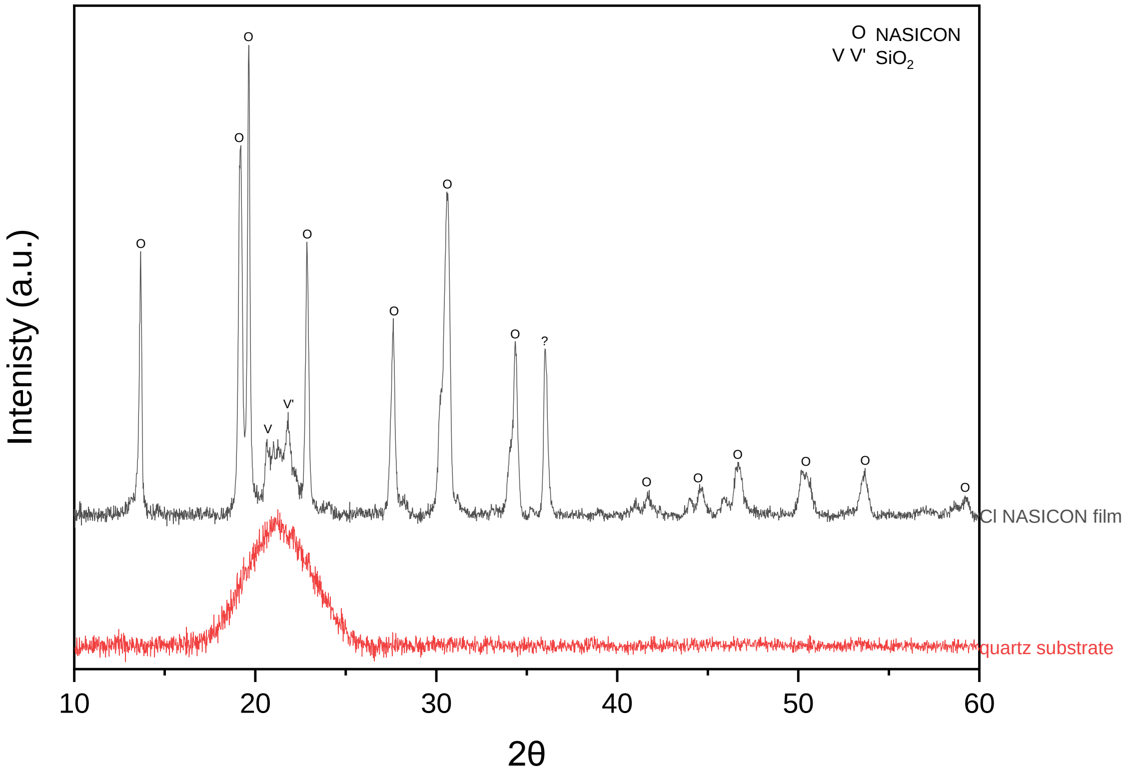

Figure 95: XRD of NASICON sol ($ZrOCl_2.8H_2O$) spray coated (50 layers) onto a quartz substrate (dried 120°C) and sintered conventionally 1000°C. Compared to the XRD of the quartz substrate.

Figure 95 shows NASICON peaks (SG 15, COD 1529665[191]) have formed and are of higher intensity than the NO_3 equivalent. The chloride sample also contains SiO_2 secondary phase peaks at 20.6º (SG 1, COD 9013393[214]; V) and 21.7º (SG 92, COD 9001578[215]; V'), but they appear to be at a lower intensity compared to the NO_3 samples. In particular, the unknown secondary phase peak at 36º has a much lower intensity. However, as we do not know the composition of this peak this could be due to a number of factors including chemistry (NO_3 vs Cl), number of layers, drying temperature or grain orientation.

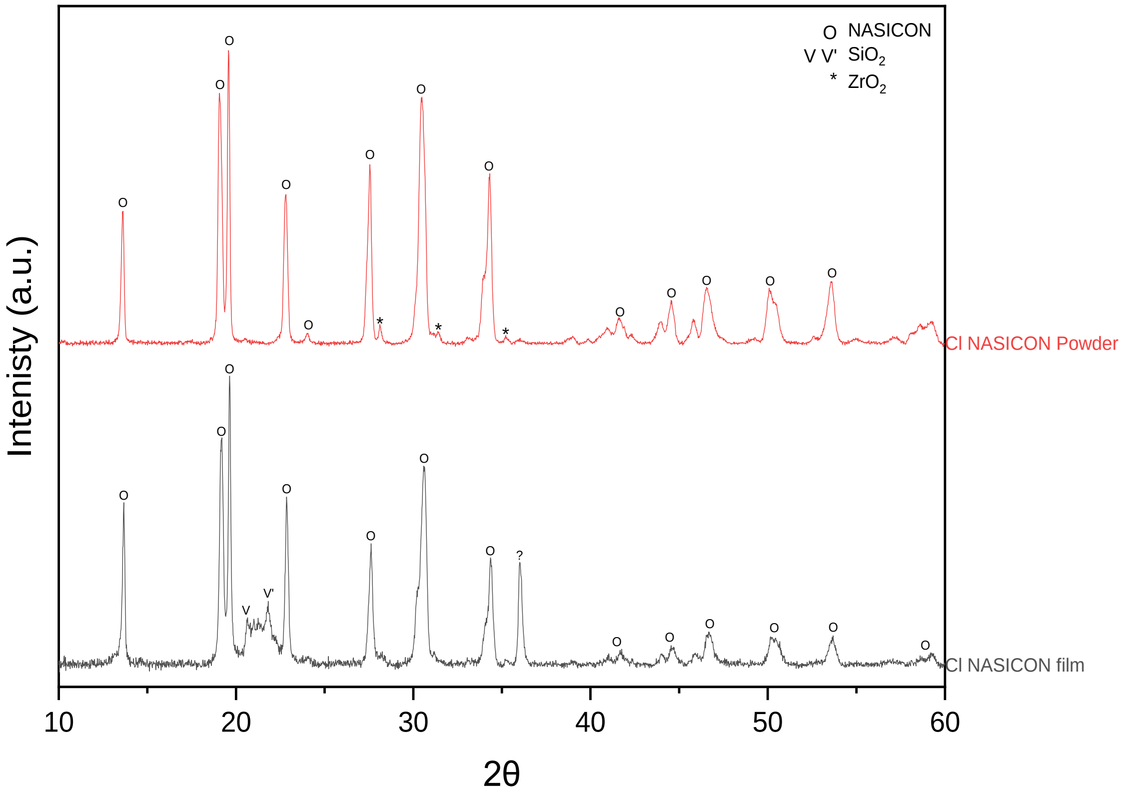

Figure 96: XRD of NASICON sol ($ZrOCl_2.8H_2O$) spray coated (dried at 120°C) and sintered conventionally (1000°C). Compared to the XRD of the equivalent NASICON sol powder.

The XRD data in Figure 96 compares the chloride thin film to the sol powder equivalent, confirming NASICON has formed on the quartz substrate as a film (spray coated 50 layers) as the characteristic NASICON peaks are present. Further investigations at this point are required to understand the nature of the secondary phases.

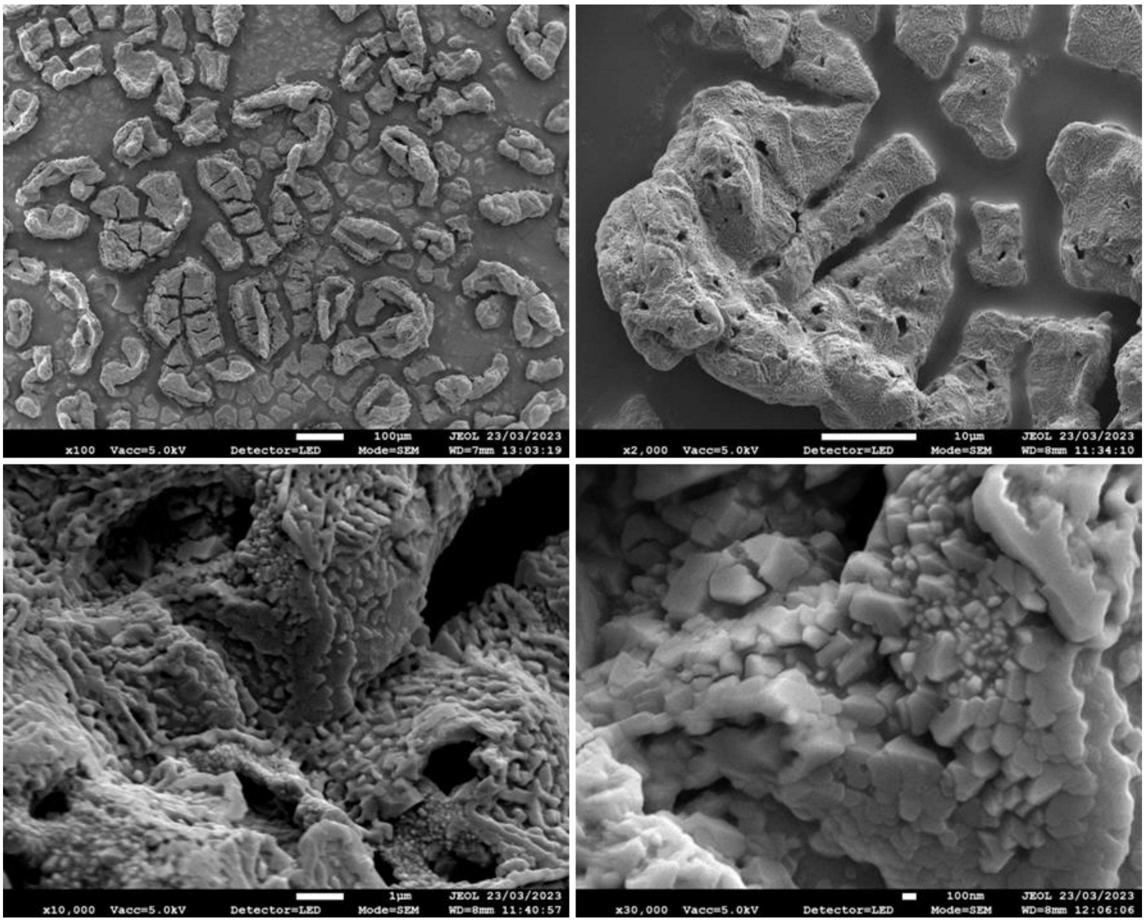

Figure 97: SEM images of NASICON sol ($ZrOCl_2.8H_2O$) spray coated onto a quartz substrate (dried 120°C) and conventionally sintered at 1000°C.

The SEM images (Figure 97) of the Cl chemistry thin film show crystals have formed, hypothesised to be the NASICON phase identified by XRD. These crystals grains are more defined (suggesting higher crystallinity) than the NO_3 sol chemistry crystals in Figure 93. However, you can see the NASICON has formed as islands, the homogeneity of this film needs to be improved, requiring a completely homogeneous and compact film to ensure ionic conductivity for future battery applications.

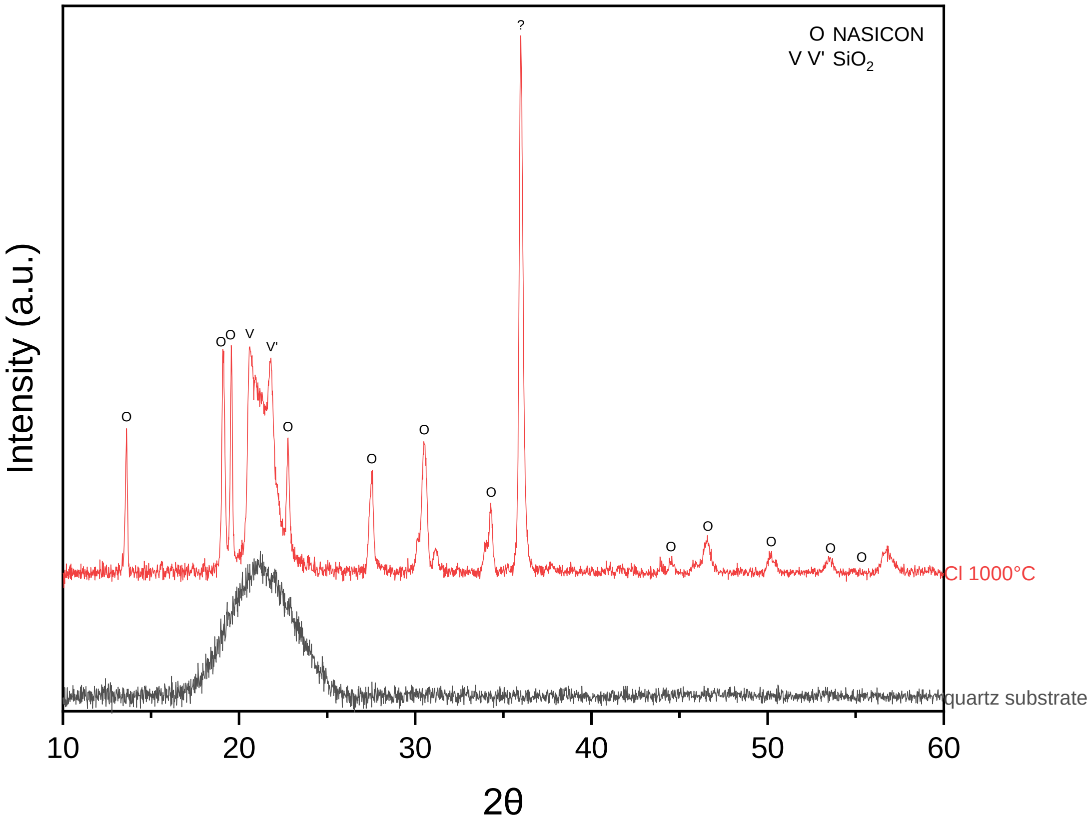

Figure 98: XRD of NASICON sol ($ZrOCl_2.8H_2O$) spray coated onto quartz (dried 150°C) and sintered conventionally at 1000°C, compared to the XRD of the quartz substrate.

Experiments also investigated the chloride chemistry sol film with a higher drying temperature of 150°C (Figure 98). NASICON has formed on the quartz substrate, however the secondary phases at 20.6º, 21.7º and 36º have increased in intensity. The difference between this experiment and the previous one is the drying temperature of the spray coating – at 150°C instead of 120°C and a new gun was used; both variables could impact film thickness and the intensity of this secondary phase peaks. As discussed previously the intensity of these secondary phases could be due to a range of factors.

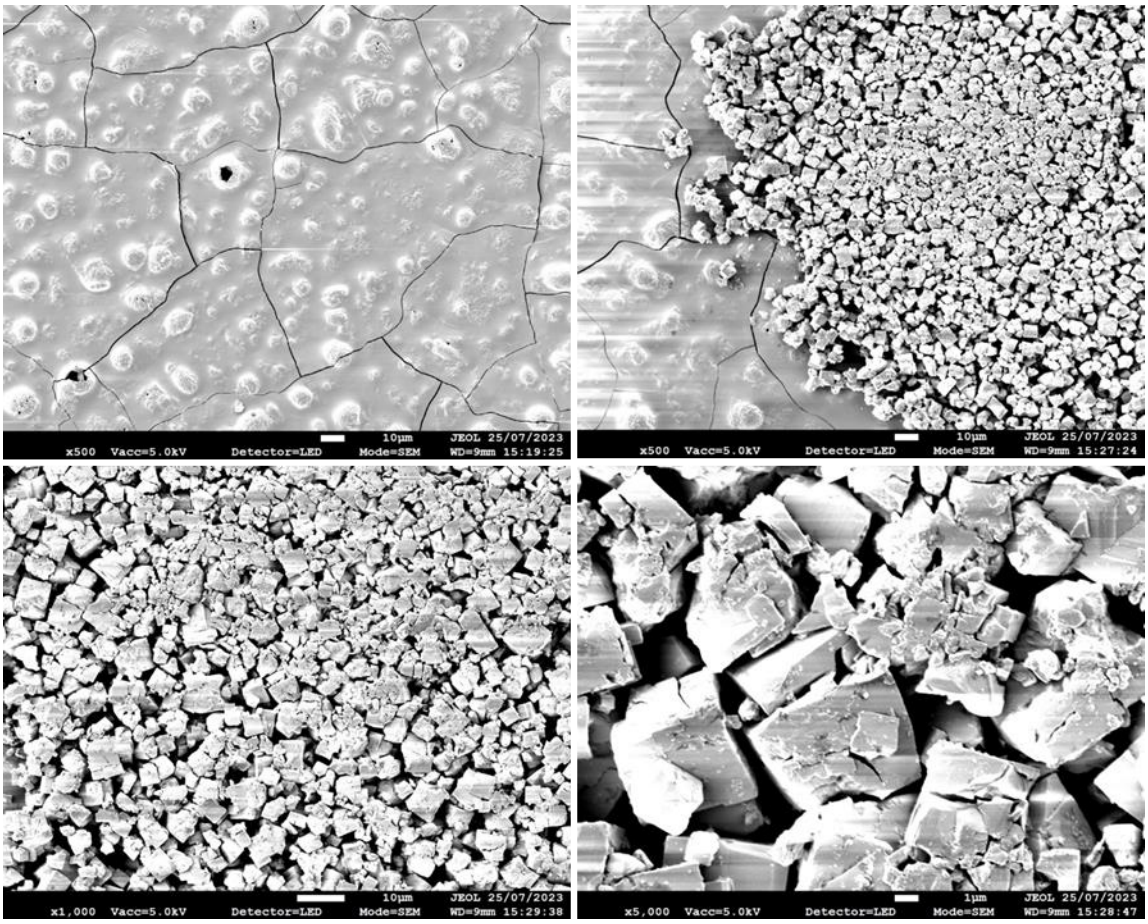

Figure 99: SEM images of NASICON ZrOCl2.8H2O sol spray coated on quartz (dried 150°C) and sintered at 1000°C. Images at x100, x 500, x1,000 and x5,000 magnification.

SEM images (Figure 99) show characteristic NASICON cubic crystal structures, validating the XRD data that NASICON has formed. However, they appear to be on the surface of the film, further work must be done to understand the phases present here.

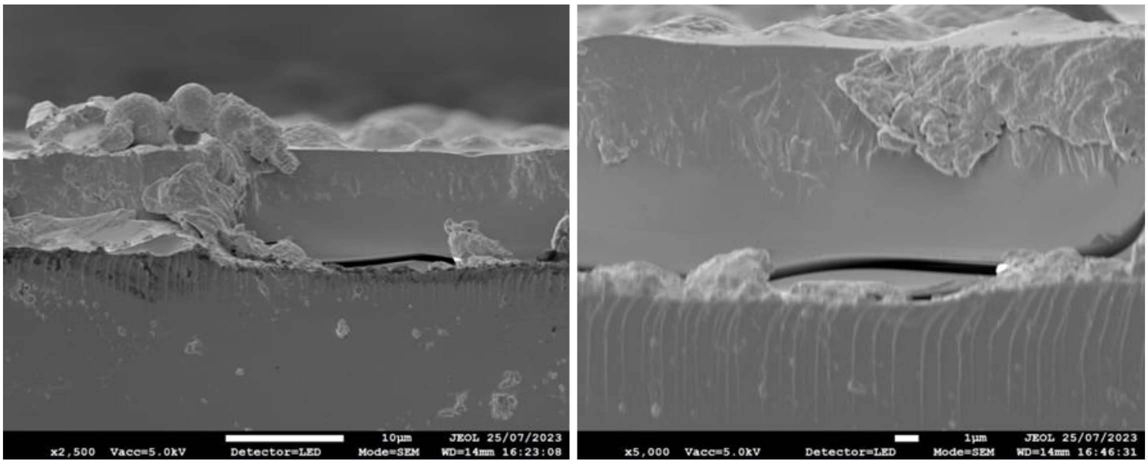

Figure 100: SEM images of NASICON $ZrOCl_2.8H_2O$ *sol spray coated on quartz (dried 150°C) and sintered at 1000°C. Images are cross sections at x2,500 and x5,000 magnification.*

SEM images in Figure 100 show a cross section of the chloride thin film sol on quartz sample. The images show the quartz substrate, with a defined dense film on top and island type structures on the surface of the layer.

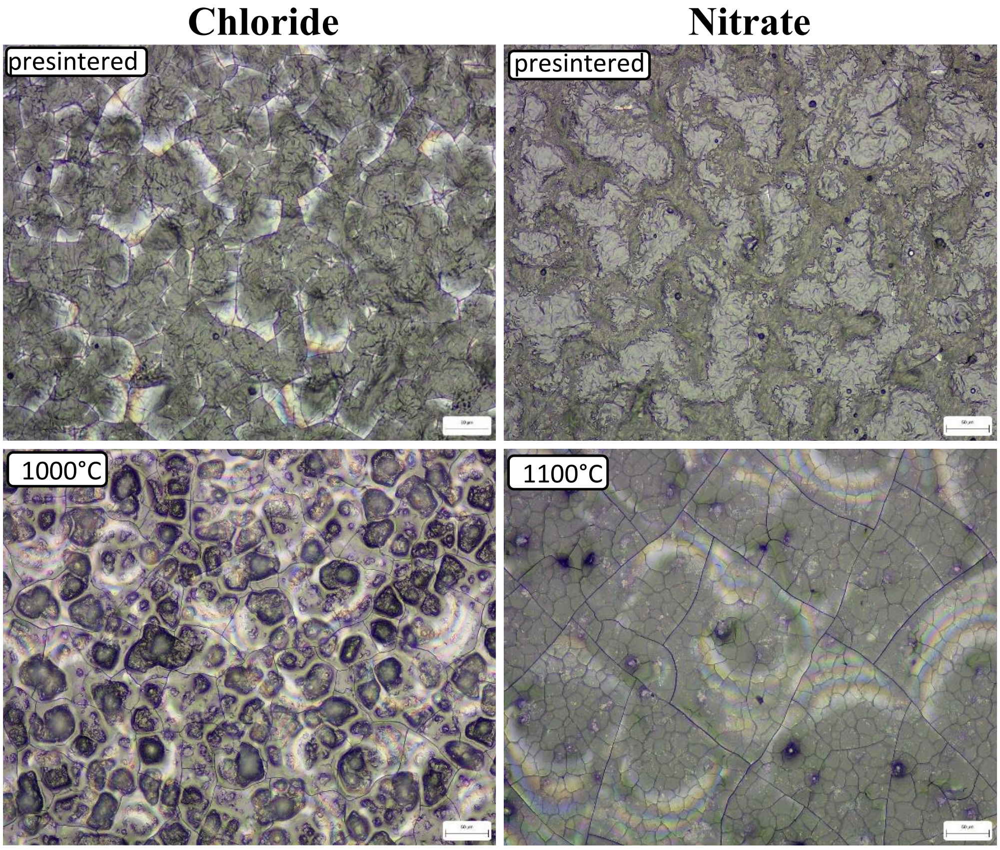

Figure 101: Optical microscope images of NASICON $ZrO(NO_3)_2.2H_2O$ and $ZrOCl_2.8H_2O$ sol spray coated on quartz (50 layers). Sintered at 1000°C and 1100°C in a conventional oven. Images at x20 magnification.

Optical microscope images in Figure 101 shows there are morphological differences in the two different chemistry sol films on quartz. The chloride chemistry shows the formation of more islands than the NO_3 chemistry. These islands could be the formation of NASICON and therefore explains the higher intensity in the NASICON peaks of the chloride chemistry in the XRD data. Both sets of images show inhomogeneous films that appear to contain cracks.

Considering all the information above, the data suggests that we should continue work using the chloride chemistry, as it yields higher intensity NASICON peaks, as well as utilises lower sintering temperatures and appears to form more defined NASICON grains. Therefore, chloride chemistry will be used for all future experiments.

6.6 Sintering temperatures

The aim of this set of experiments is to see how heat treatment temperatures affect the formation of NASICON thin films. $ZrOCl_2.8H_2O$ chemistry sol was used in these experiments, deposited by spray coating on quartz substrates. The sintering and 750°C heat treatment steps were carried out in a conventional oven (air).

6.6.1 Sintering at 1000°C vs 750°C + 1000°C

In the previous sol powder chapter (Chapter 5) three heating steps were employed to form the powder: 120°C drying step, a 750°C treatment and a sintering step of 1000°C. This experiment is looking at replicating these heat treatments to determine whether this improves the chemistry of the NASICON as a thin film compared to just drying and sintering (without 750°C step).

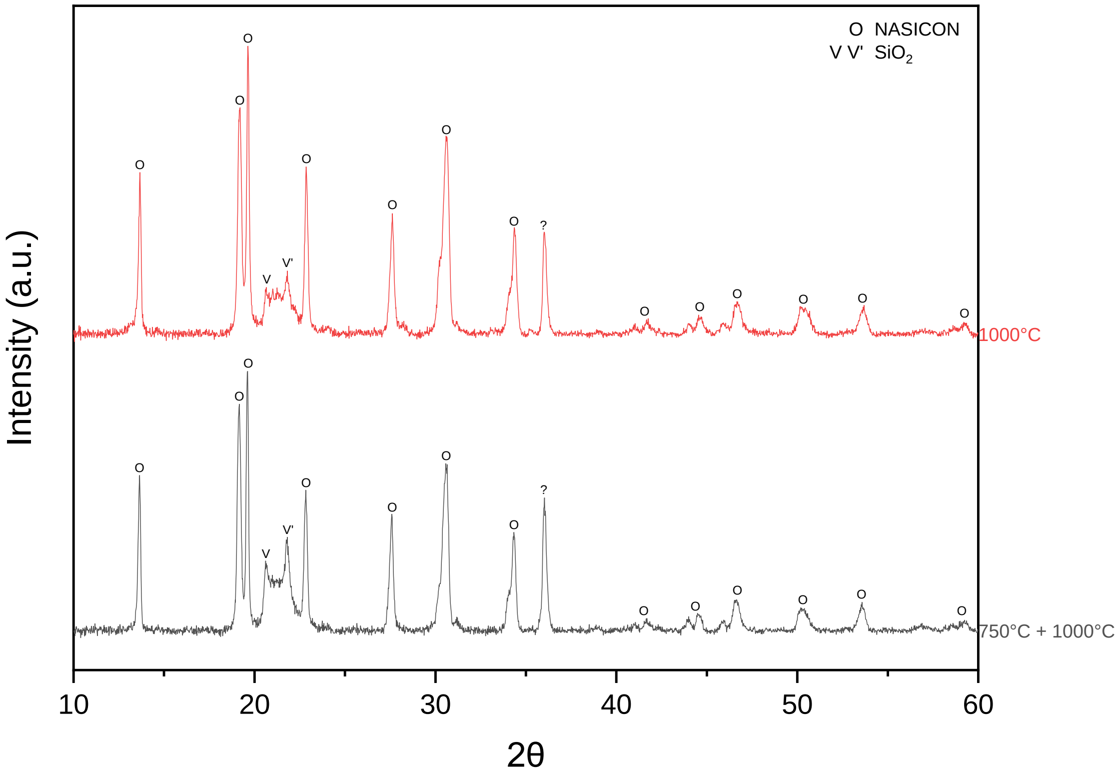

Figure 102: XRD of NASICON sol (ZrOCl2.8H2O) spray coated onto a quartz substrate and sintered conventionally at 1000°C. Compared to the XRD of the equivalent sol sample (ZrOCl2.8H2O) spray coated onto quartz and sintered at 750°C and 1000°C.

The XRD's in Figure 102 show that the samples sintered at 1000°C and at 750°C + 1000°C have formed NASICON. The only difference between the two sample is the intensity of the secondary phase peaks at 20.6º, 21.7º and 36º. There is a slight increase in intensity of the secondary phases for the 750°C + 1000°C sintered sample, however this could just be grain orientation.

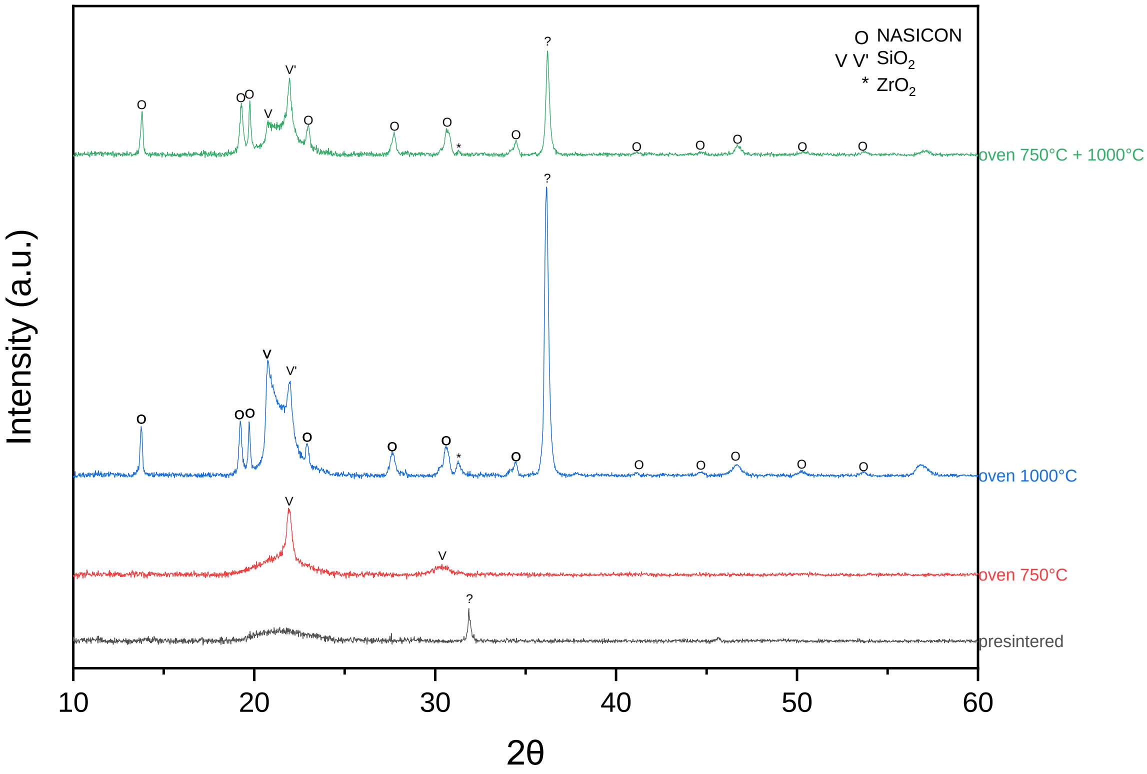

Figure 103: All XRD's are samples with NASICON sol (ZrOCl2.8H2O) spray coated onto quartz. Black XRD: sample before sintering, Red XRD: sample treated at 750°C in conventional oven, Blue XRD: sample sintered at 1000°C in conventional oven, Green XRD: sample heated at 750°C and sintered at 1000°C both in a conventional oven.

Figure 103 compares the XRD data for this experiment, illustrating NASICON does not form in the sol before heat treatments (thin film presintered) or after heating at 750ºC. The presintered sample shows the quartz distortion at 21º and an unknown peak at 31.8º; and the 750 ºC heat treated sample shows SiO_2 peaks at 22.1º (SG 91, COD 9017338[217]) and 30º (SG 136, COD 9007530[218]) both tridymite.

XRD's (Figure 103) show the grain growth/crystal development after conventional heat treatments; the sample treated at 1000°C forms NASICON crystal with secondary phases, and the sample treated at 750°C and 1000°C also forms NASICON crystals, with lower intensity secondary phases. This illustrates the NASICON phase transformation only occurs during sintering at 1000ºC. In both XRD's SiO_2 peaks are present at 20.6º (SG1, COD 9013393[214]) and 21.7º (SG 92, COD 9001578[215]). Secondary phase of ZrO_2 at 31.4º (SG 14, COD 2300544[208]) are also present, as well as the unknown peak at 36º.

During a combustion reaction tartaric acid becomes CO_2 and H_2O (redox reaction, O reduced to -2 and C is oxidised to +4). This reaction usually occurs at ~400ºC, but if bonded to a metal (e.g. Zr) a higher temperature is needed for combustion. After heating at 750°C for an hour the samples turned black. This black coloration is associated with the appearance of carbon (C^0) as a result of an incomplete oxidation of the carbon coming from the tartaric acid (C^{-4}). At higher temperatures, this carbon (C^0) reacts with O_2 (combustion reaction, exothermic) generating CO_2 (C^{+4}) making this black carbon (C^0) disappear. This is observed experimentally during the sintering step at 1000°C where the film turns white again.

The secondary phase at 20.6 º and 21.7º is SiO_2, this could be due to the nucleation of the quartz causing the silicon substrate to recrystalise or could be a secondary phase within the NASICON film itself. The peak at 36º could be analysed with the diffrac database as one of several phases including: ZrO_2, SiO_2 or SiC. We can conclude the 36º peak is not SiC as this peak is not present in the powder results with or without the presence of tartaric acid (Chapter 5). This suggests that the peak does not correlate to SiC, as this 36º peak would be present in the powder results with tartaric acid, as it contributes carbon. One explanation could be that the 36º is a zirconia phase, and the synthesis of thin film NASICON on quartz causes secondary phase formation. Alternatively, this peak could correlate to the underlying silicon, forming a compound such as SiO_2. There could be a renucleation of the quartz substrate, causing the silica glassy/amorphous phase to convert. Meaning the 36º peak is not a secondary phase within the NASICON but is due to the quartz substrate and there is not an issue with the chemistry of the NASICON or its synthesis. More investigation and characterisation must be carried out to determine the nature of this phase.

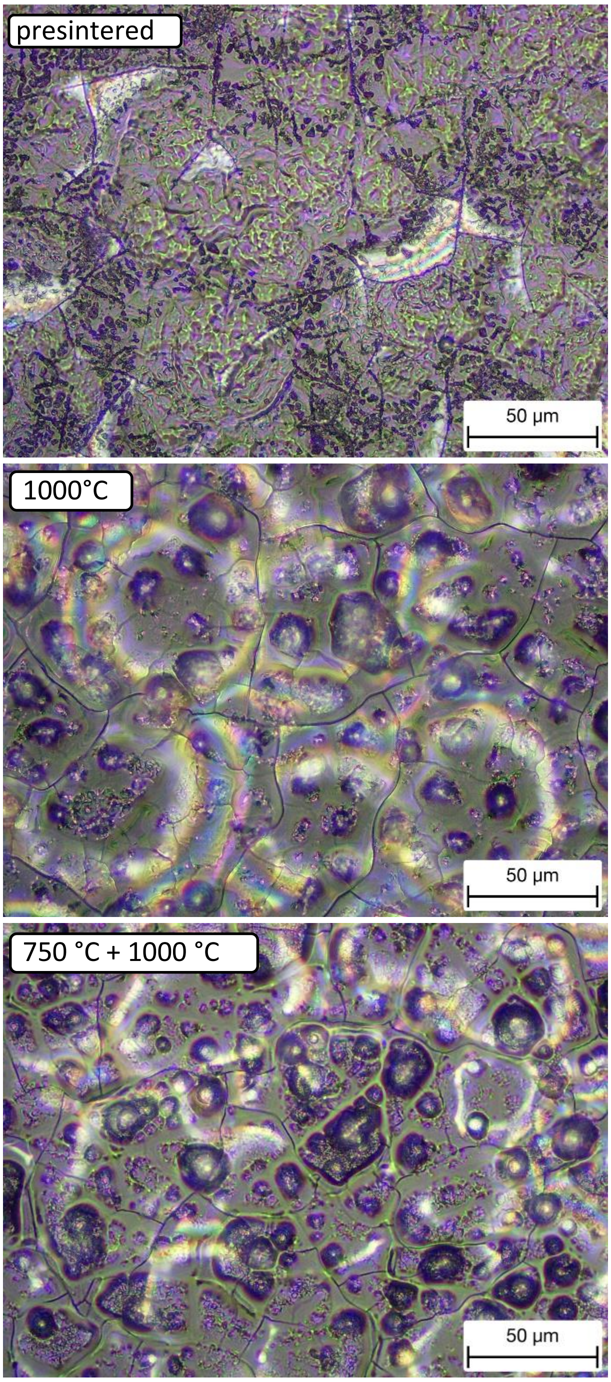

Figure 104: Optical microscope images of NASICON $ZrOCl_2.8H_2O$ sol spray coated on quartz. (1) presintered sample (2) sintered at 1000°C (3) heated at 750°C and sintered at 1000°C. Images at x50 magnification.

Optical microscope images (Figure 104) show the appearance of island formation (darker/black areas) for both the samples– heated at 1000°C, and heated at 750°C and 1000°C.

6.6.2 Sintering at 950°C vs 1000°C

This work investigated if NASICON could form at lower sintering temperatures, to understand if this would affect the chemistry of the film and reduce the opportunity for secondary phases to form. The temperatures tested were: 950°C and 1000°C, carried out in a conventional oven.

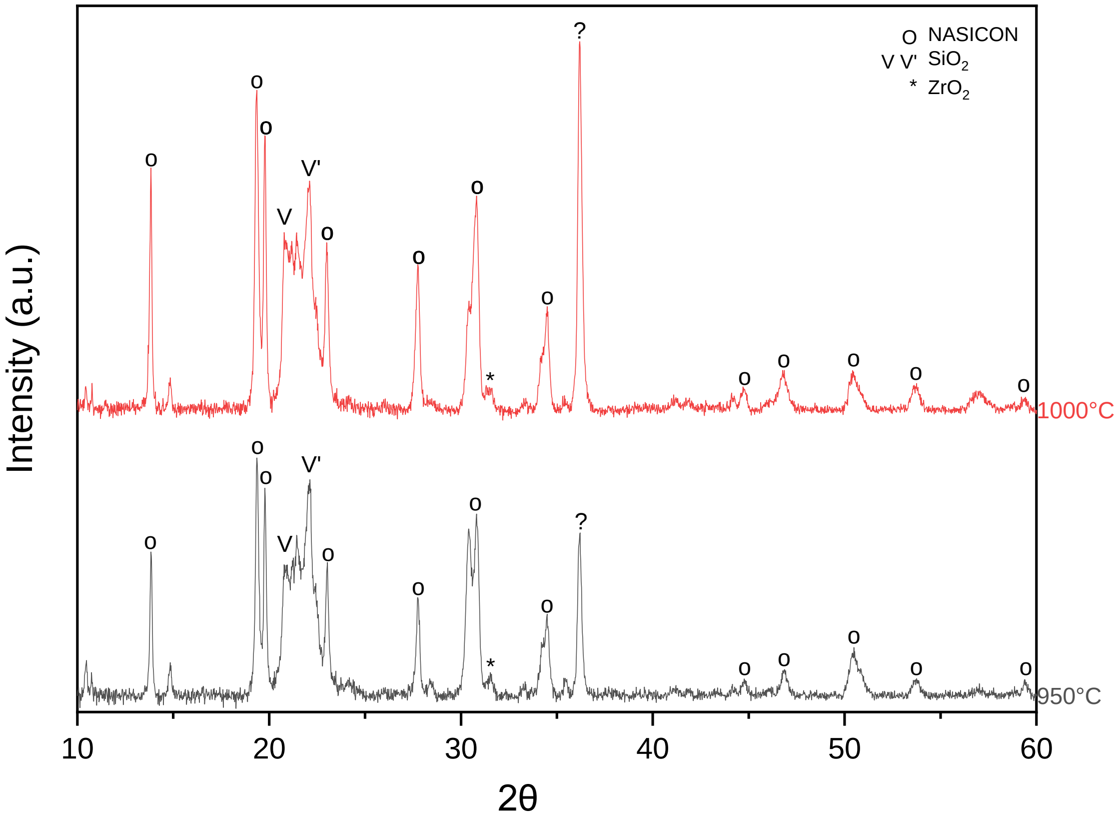

Figure 105: XRD of NASICON sol ($ZrOCl_2.8H_2O$) spray coated onto a quartz substrate (120°C) and sintered conventionally at 1000°C. Compared to the XRD of the equivalent sol sample ($ZrOCl_2.8H_2O$) spray coated onto quartz and sintered at 950°C.

XRD pattern's in Figure 105 show that NAISCON (SG 15, COD 1529665[191]) forms at both 1000°C and 950°C sintering temperatures. Some of the NASICON peaks in the 950°C sample have a lower intensity, however the unknown secondary phase peak at 36º is also lower. Whilst there is a difference in intensity, lack of homogeneity in the film means that it is hard to draw a strong conclusion from this. The next section 6.7 Grazing Incidence XRD looks to determine what this secondary phase is at 36º.

It is very positive that the film can form NASICON at the lower temperature, as it decreases energy requirements, reduces cost and potentially minimises substrate interactions and/or secondary phase formations that occur at higher sintering temperatures. In the 6.8 XRD thermal stage experiment section, further experiments were carried out to determine the optimum temperature for sintering NASICON as a thin film.

6.7 Grazing Incidence XRD

The aim of the grazing incidence XRD is to use different angles to analyse the surface and top layers of the NASICON film deposited on the quartz substrate. In particular this work utilised this method to understand if the secondary phases present in the XRD data are from the NASICON itself or if the quartz/an intermediate layer has caused these secondary phases; specifically, whether the 36º peak is a ZrO_2 or SiO_2 phase. At lower angles (0.5°) the XRD will interact more with the top layers, increasing their signal, and potentially removing the quartz and other lower layers from the XRD data. As the XRD angle increases (4.5°), we increase the XRD penetration so will see more data/signal from the lower layers (e.g. the quartz), but there will always be some interaction with the upper NASICON layer.

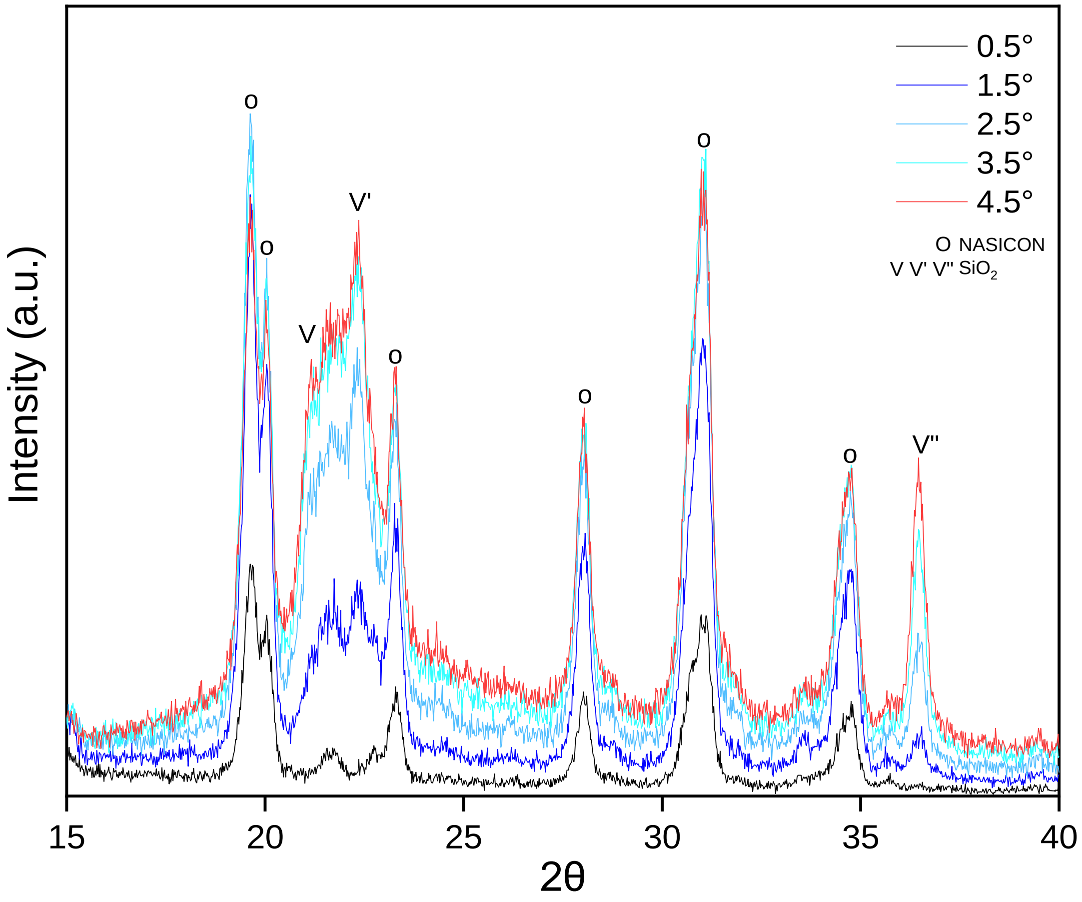

Figure 106: GI-XRD of NASICON sol ($ZrOCl_2.8H_2O$) spray coated onto a quartz substrate (120°C) and sintered conventionally at 950°C. XRD angles used are: 0.5°, 1.5°, 2.5°, 3.5° and 4.5°.

Figure 106 shows NASICON (SG 15, COD 1529665[191]) peaks formed at 19.1º,19.6º, 22.8º, 27.6º, 30.6º and 34.3º when it is sintered at 950°C.

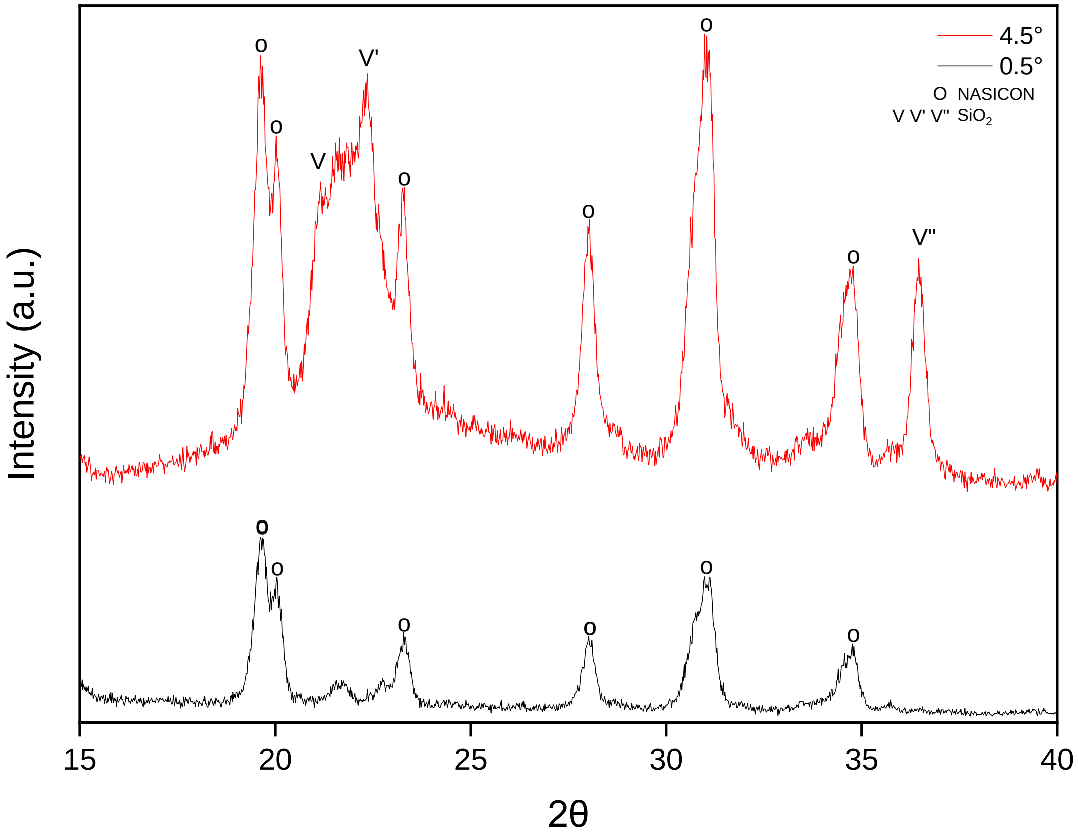

Figure 107: GI-XRD of NASICON sol (ZrOCl2.8H2O) spray coated onto a quartz substrate (120°C) and sintered conventionally at 950°C. XRD angles used are: 0.5° and 4.5°.

Figure 107 shows that at the higher angle 4.5° SiO_2 secondary phases are present at 20.6º (SG 1, COD 9013393[214]; V - orthorhombic/tridymite) and 21.8º (SG 92, COD 9001578[215]; V' - tetragonal/cristobalite), as well as the unknown 36º secondary phase. At 0.5° GI-XRD on the top surface of the sample, there is no secondary phases present, which shows there is a layer of just NASICON on the surface of the sample. If the quartz peaks at 20.6º and 21.8º stayed the same intensity at all angles, this would suggest a transformation of NASICON with integrated SiO_2 secondary phases. However, the intensity of the quartz peak at 20.6º and 21.8º peak both increased in intensity as the XRD angle increased, which suggests the secondary phase is linked to the quartz layer. This is also true for the secondary phase peak at 36º; this peak is present at 4.5° and not at 0.5°, meaning this phase is also linked to the quartz substrate (not the NASICON). Therefore, this peak can also be identified as a SiO_2 phase (SG 92, COD 9001578[215]; V", tetragonal).

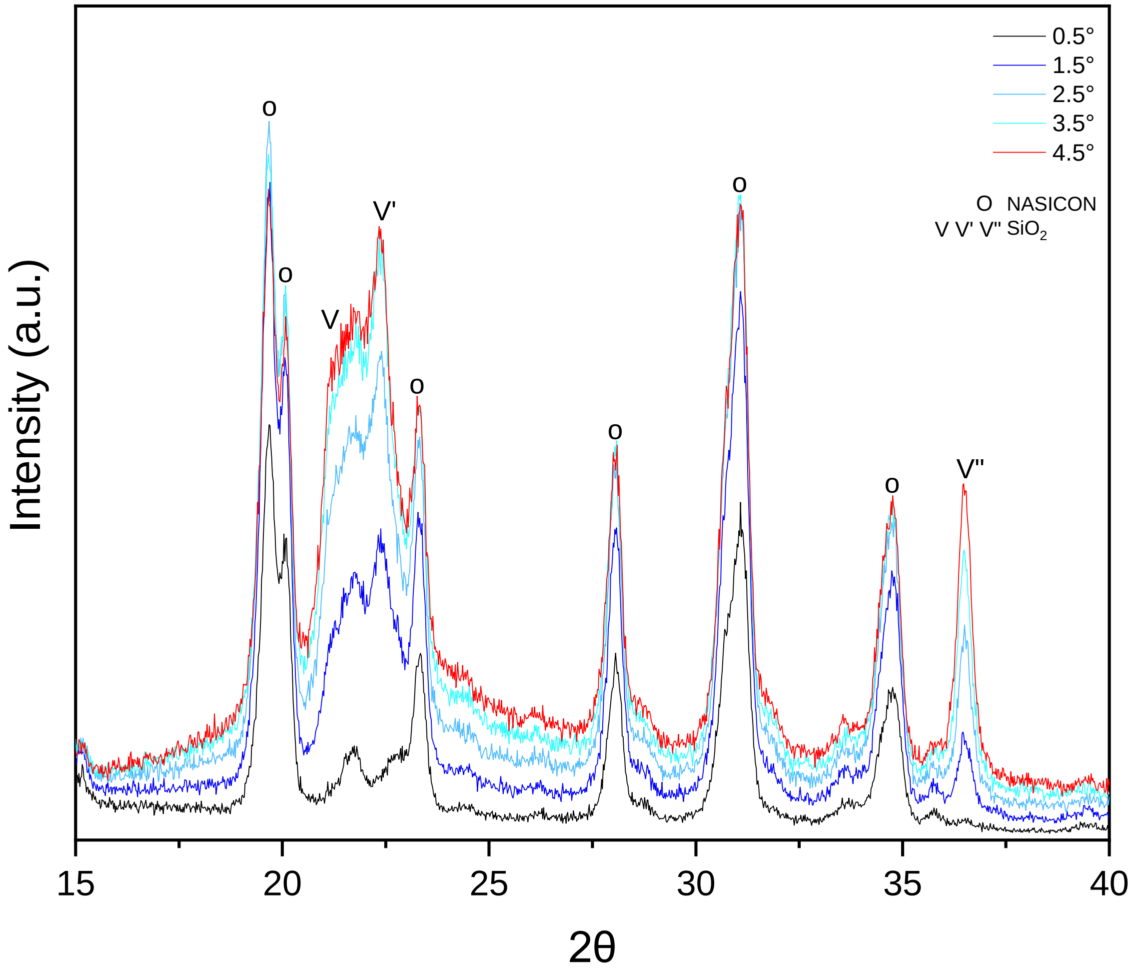

Figure 108: GI-XRD of NASICON sol (ZrOCl2.8H2O) spray coated onto a quartz substrate (120°C) and sintered conventionally at 1000°C. XRD angles used are: 0.5°, 1.5°, 2.5°, 3.5° and 4.5°.

Figure 108 demonstrates that the same thing happens when sintered at 1000°C; silica phases were not present on the top surface of the film and are a result of a silica phase on/near the surface of the quartz substrate or bottom part of the film. Confirmed by the reduction in the intensity of these phases with decreasing XRD angle.

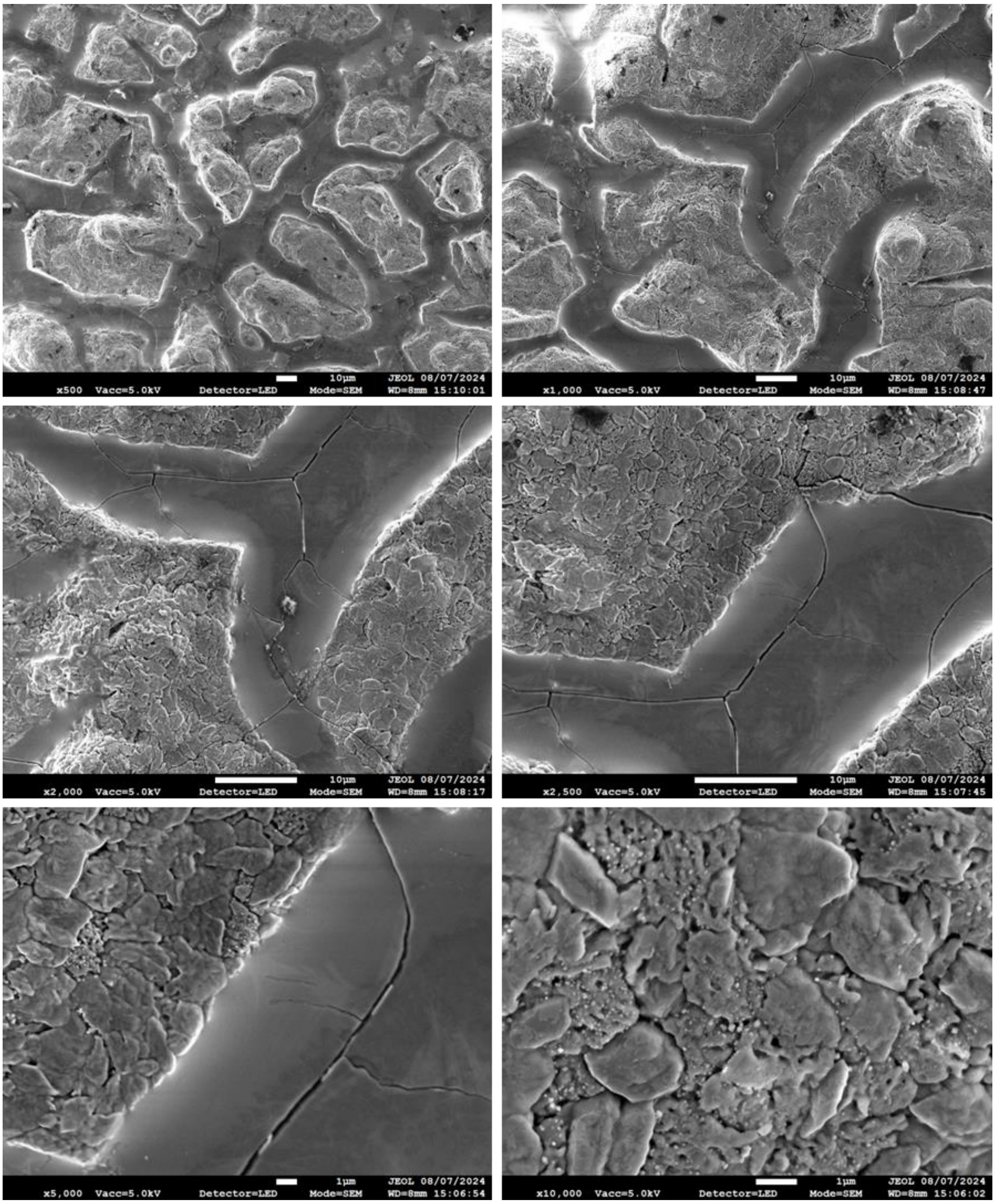

Figure 109: SEM images of chloride sol spray coated 50 layers on quartz, dried at 120°C and sintered at 1000°C.

SEM images (Figure 109) show in homogeneous films at the micron level, with the formation of islands. As the other phases present in the XRD samples is now confirmed as SiO_2 (the valley areas in the SEM images), it can be concluded that these islands are NASICON connected by SiO_2; renucleated/converted quartz silica in the gaps between areas of NASICON. At the submicron level the islands of NASICON show more homogenous grains. This island formation could be due to several things: high temperature phase separation, decomposition or liquid phase shrinking. Therefore, improving the homogeneity of the film could reduce the 36º peak intensity. Furthermore, as we can confirm the peaks are due to the quartz substrate, increasing the thickness of the NASICON film may reduce the intensity of this peak, and could be the reason for the difference of intensities of SiO_2 peaks in the previous XRD data in this chapter.

Initial lab work shows a reduction in the intensity of the SiO_2 XRD peaks as the thickness of the film increases, which supports the analysis that the SiO_2 phases are at the surface of the quartz substrate. However, further work beyond the scope of this thesis is needed to look at the effect of this increase in film thickness and improved homogeneity of the films in reducing the formation of the SiO_2 phases.

However, as stated previously the annealing point (1215ºC) and softening point (1683ºC) of quartz is above 950ºC (the sintering temperature used). Therefore. there are two plausible hypotheses for how the SiO_2 is formed:

1. A higher temperature than 1000ºC is reached due to the presence of carbon in the system. Demonstrated through DSC-TGA analysis, an exothermic reaction happens around 950ºC, causing an increase in energy/temperature which could cause the sample to reach the crystallisation temperature of the SiO_2
2. The presence of Na in NASICON could facilitate the formation of SiO_2 structure at lower temperature than expected – lowering the quartz melting point.

Furthermore, the GI-XRD data alone cannot determine if the SiO_2 peaks are due to the recrystallisation of the quartz or if the Na in the NASICON is forming an intermediate. This intermediate layer could be on the surface of the substrate or the bottom part of the NASICON film, demonstrated by the GI-XRD. But it is certain that a NASICON forms on top of the SiO_2 structure without SiO_2 secondary phases.

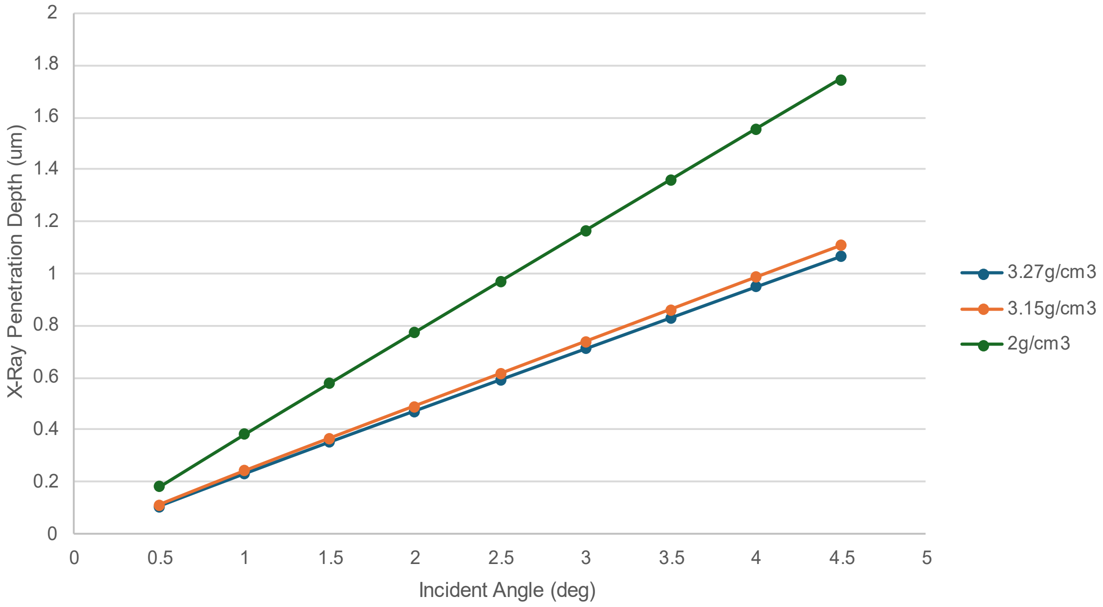

Figure 110: Graph illustrating the scan penetration depth of the XRD at the angles employed, using approximate NASICON densities from literature. Calculations carried out using GIXA web tool.[219]

The graph in Figure 110 shows the depth of XRD penetration for the sample at each angle and shows the only the top 100-200 nm of the sample doesn't have the additional phases and is therefore NASICON.

6.8 XRD thermal stage experiment

To understand peak formation during NASICON synthesis a thermal stage XRD experiment was carried out, using Equation 19 chloride chemistry. The experiments summarised in Table 39 were designed to determine the optimal temperature-time relationship for synthesising NASICON thin films on quartz discs.

2 types of experiments were carried out:

- The first was a ramp scan, where the sample was heated at 2°C/min from 30 to 1000°C. XRD scans were detected at the temperatures shown in Diagram 1.

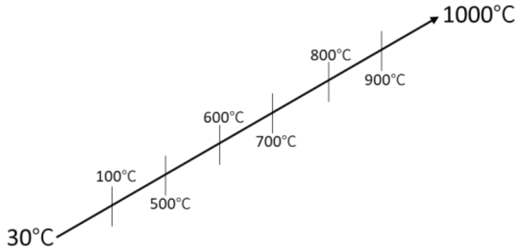

Diagram 1: Thermal XRD ramp experiment.

- The second experiment was a temperature hold. The sample was heated (ramp of 20°C/min) to the desired temperature; 900°C, 950°C or 1000°C. The thermal stage then held the sample at this temperature for several hours and XRD scans were taken at routine intervals (Diagram 2).

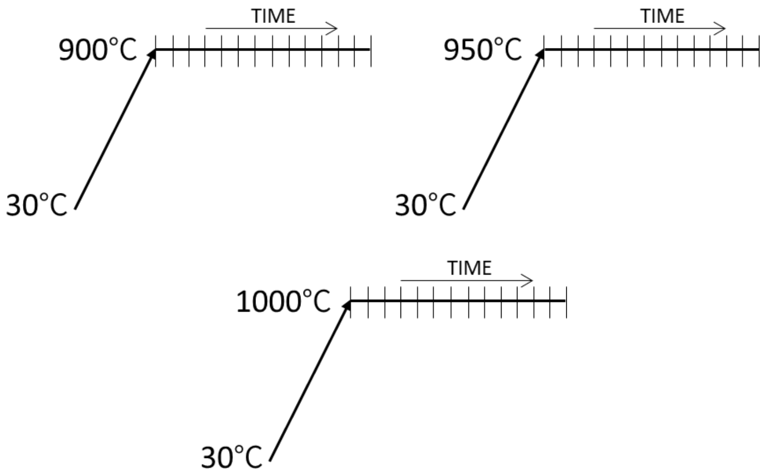

Diagram 2: Thermal XRD temperature hold/time experiment.

Table 39: Thermal stage XRD experiments carried out.

Formulation	Conc (%)	Substrate	Deposition	Number of layers	Temp (°C)
$ZrOCl_2.8H_2O$	5	quartz	spray coat	90	30 to 1000
$ZrOCl_2.8H_2O$	5	quartz	spray coat	90	900
$ZrOCl_2.8H_2O$	5	quartz	spray coat	90	950
$ZrOCl_2.8H_2O$	5	quartz	spray coat	90	1000

6.8.1 Thermal XRD ramp experiment

This experiment took an XRD measurement every 100°C and held this temperature for 10 mins; Figure 111 shows the temperatures at which the measurements were taken. The aim of this experiment is to determine at what temperature NASICON formation occurs.

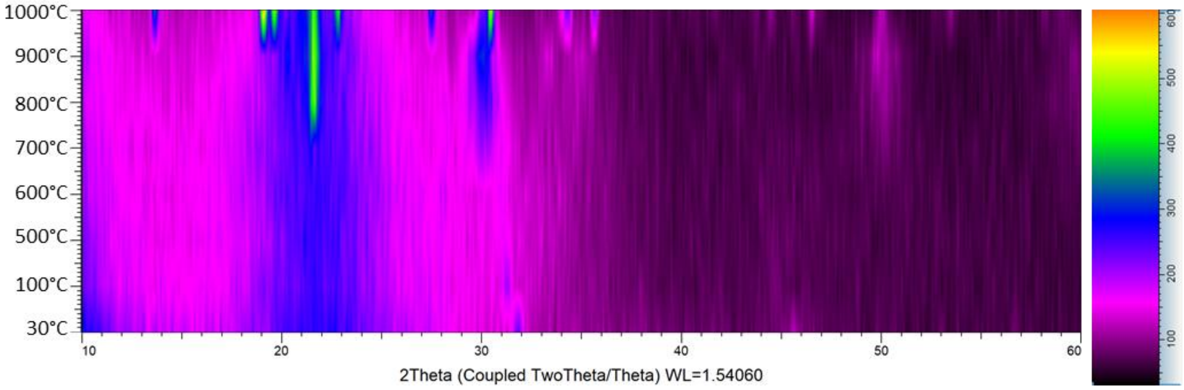

Figure 111: 2D view of XRD thermal stage experiment. XRD scans taken at 30°C, 100°C, 500°C, 600°C, 700°C, 800°C, 900°C and 1000°C, ramp rate 2°C/min.

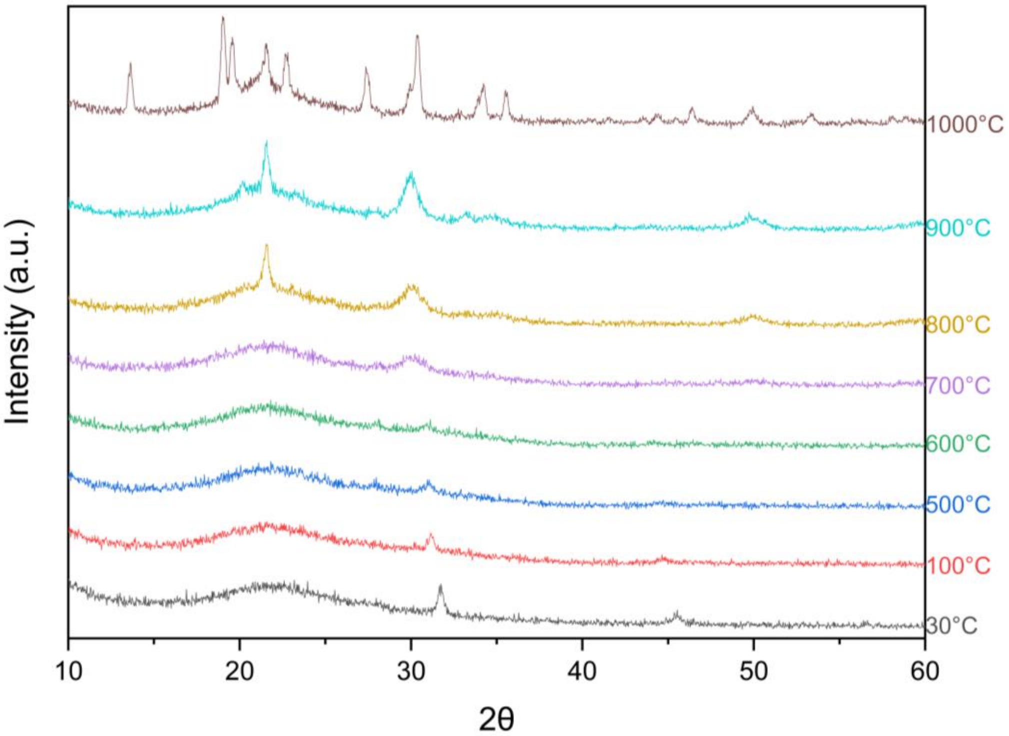

Figure 112: XRD's taken at different temperatures during the thermal stage experiment.

The thermal stage XRD data shows that NASICON only forms at 1000°C (Figure 112), and not at lower temperature scans.

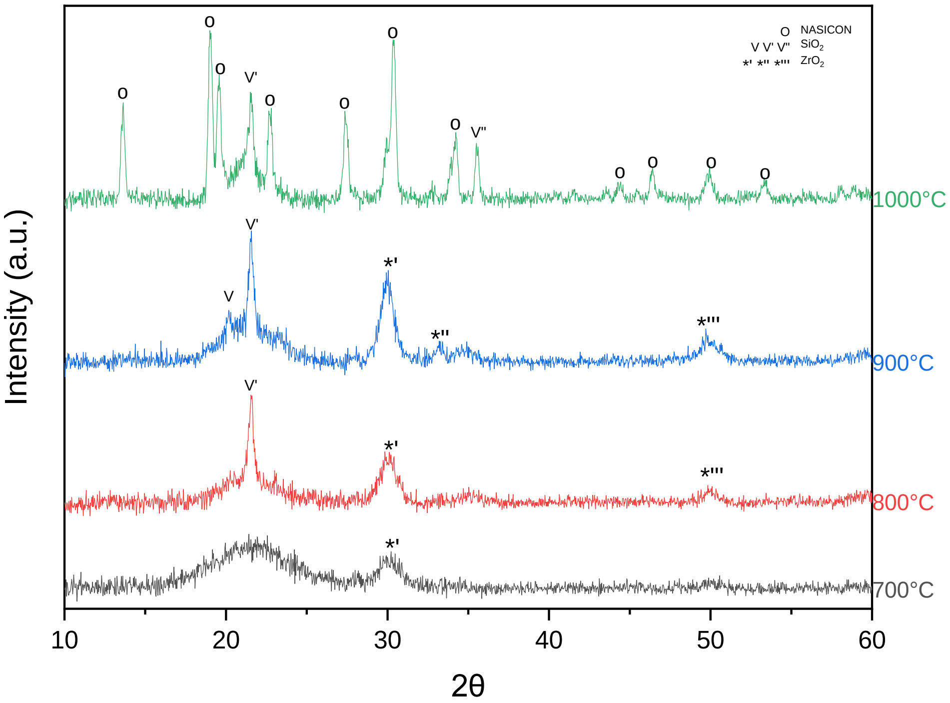

Figure 113: XRD's taken at different temperatures during the thermal stage experiment. Graph shows the evolution of the NASICON peaks.

XRD data Figure 113 illustrates that the SiO_2 peak at 21.7º (V') forms at 800°C, whereas the 20.6º (V) and the 36º (V") SiO_2 peaks form at a higher temperature, potentially 950°C. GI-XRD analysis suggests that this peak is related to quartz and is due to the recrystallisation of the substrate/or intermediate quartz phase. ZrO_2 phase peaks start to fully form at 800ºC (30.3º 31.4º and 50.4º), however they are not present in the XRD at 1000ºC. Tetragonal ZrO_2 phases occur at lower sintering temperatures (or not enough sintering time), and monoclinic ZrO_2 phase occurs at higher temperatures. NASICON peaks form at 1000°C, this formation could be forming at any point after 900ºC but can be dependent on time and temperature/ramp rate.

6.8.2 Thermal XRD hold experiment - 900°C

The aim of this experiment is to see if NASICON can form at 900°C when held at this temperature for a longer period of time. The ramp rate is faster for this experiment 20°C / min, until it reaches 900°C hold. Each scan takes 15 minutes and the time at which each scan started is shown on the y-axis of Figure 114.

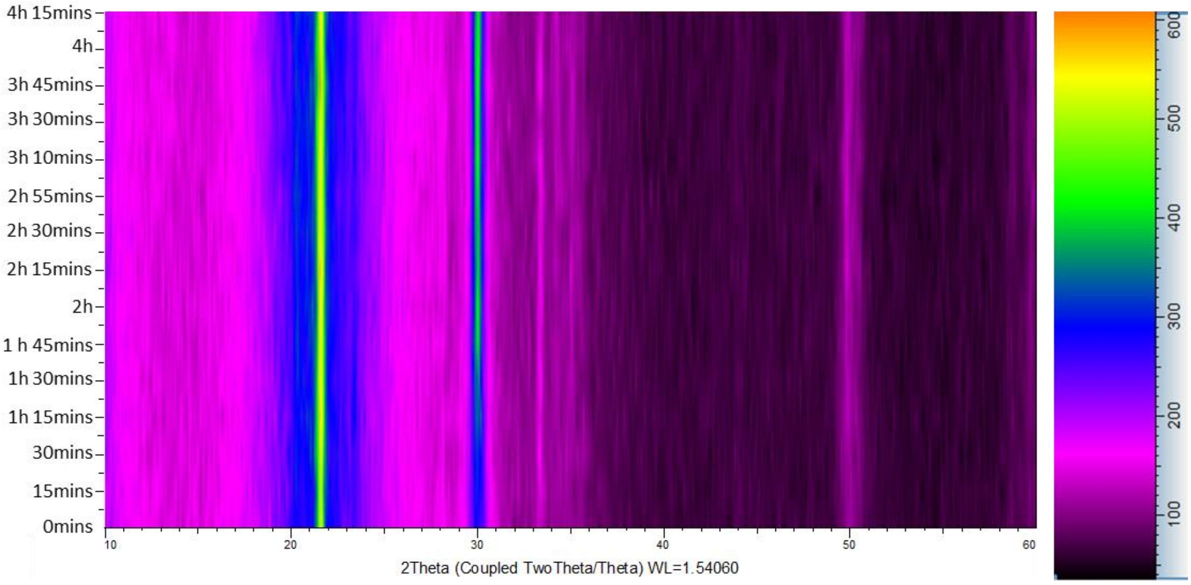

Figure 114: 2D view of XRD thermal stage experiment. XRD scans taken once the stage had reached 900°C, the left axis shows the time at which each scan was recorded.

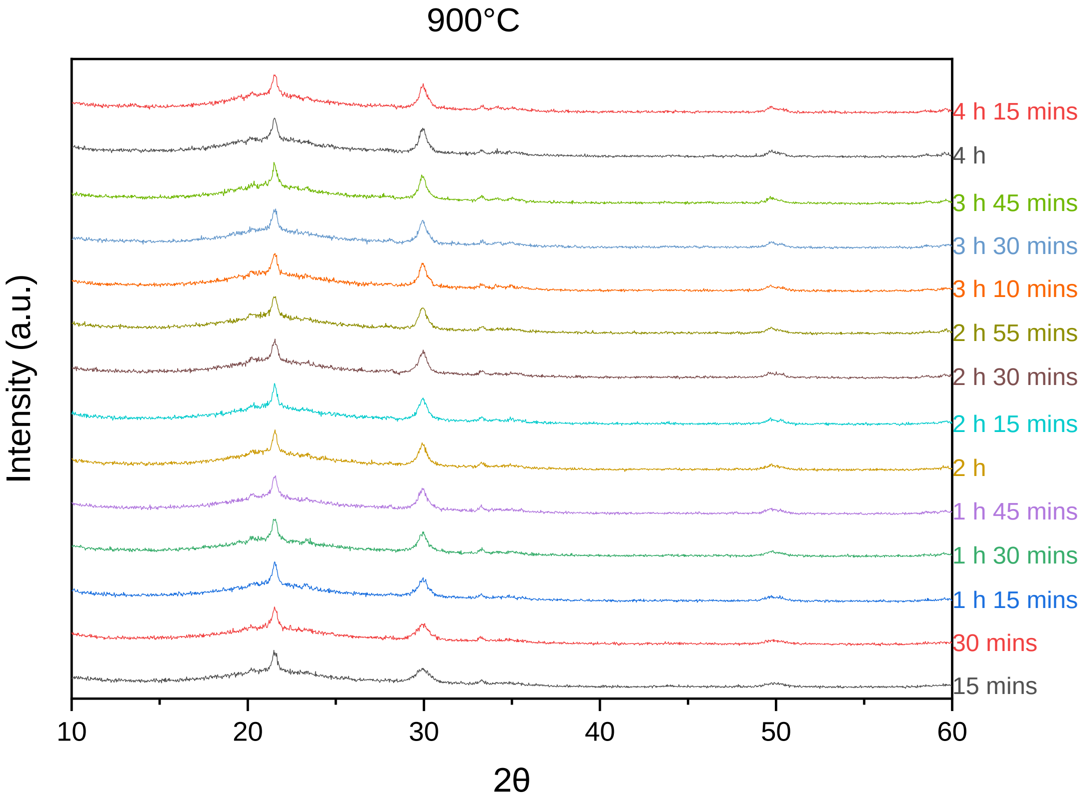

Figure 115: XRD's taken at time intervals during the thermal stage experiment.

XRD data (Figure 114 and Figure 115) show that NASICON does not form at 900°C over 4 hours 15 mins, some ZrO_2 and SiO_2 phases have started to form at 20.6° and 30.6° respectively.

6.8.3 Thermal XRD hold experiment - 950°C

The aim of this experiment is to see if NASICON forms at 950°C, and if so, at what hold time crystallisation starts to occur. The ramp rate for this experiment is also 20°C / min, until it reaches 950°C hold. Each scan takes 15 minutes and the time at which each scan started is shown on the y-axis of Figure 116.

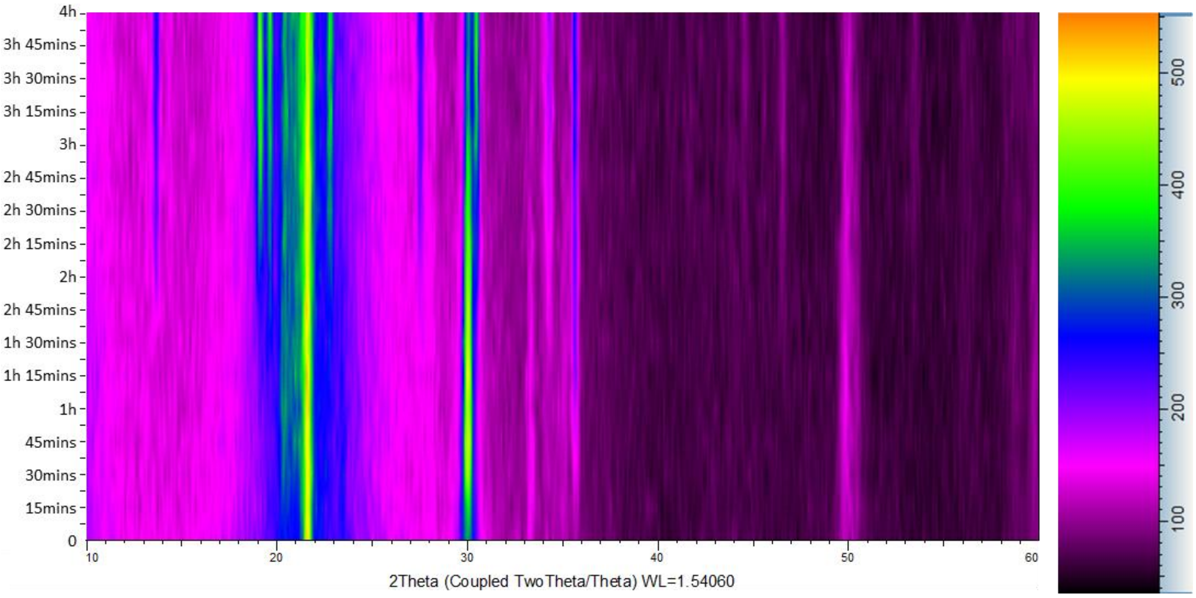

Figure 116: 2D view of XRD thermal stage experiment. XRD scans taken once the stage had reached 950°C, the left axis shows the time at which each scan was recorded.

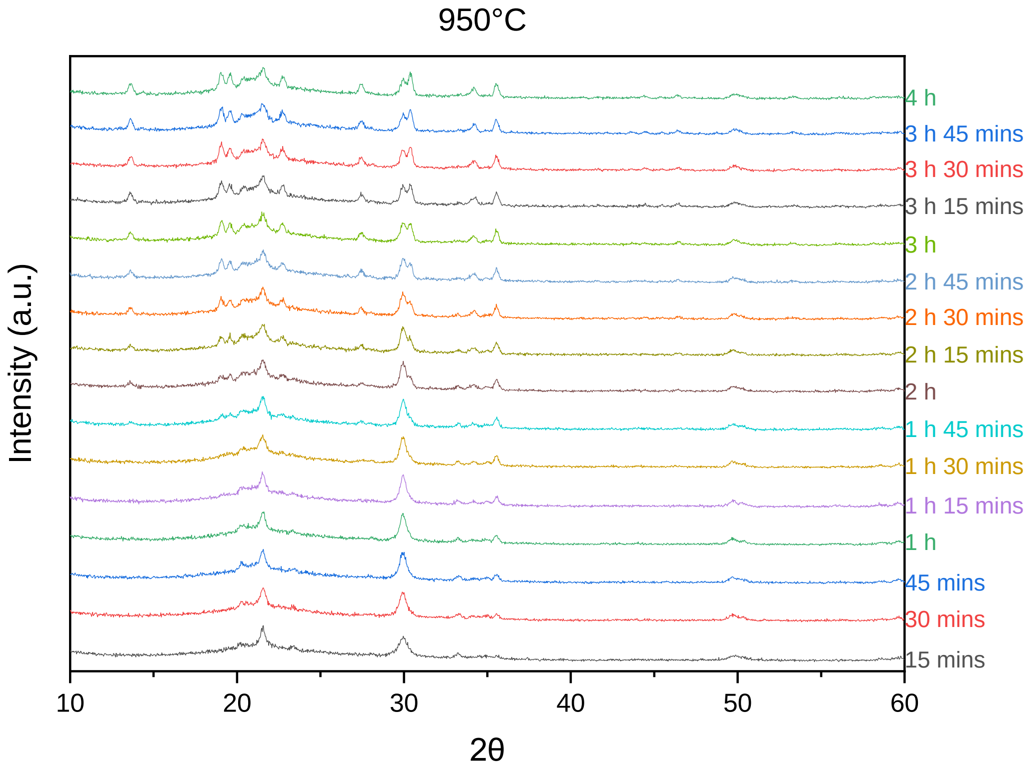

Figure 117: XRD's taken at time intervals during the thermal stage experiment.

Figure 117 depicts V’ (21.7º) SiO_2 tetragonal peak (SG 92, COD 9001578[215]) forms instantly at 950ºC. The V (20.6º) orthorhombic SiO_2 (SG 1, COD 9013393[214]) and V” (36º) SiO_2 tetragonal peak doesn’t form at 950ºC until roughly 1 hour. After 2 hours the intensity of the secondary phase peaks doesn’t increase over time.

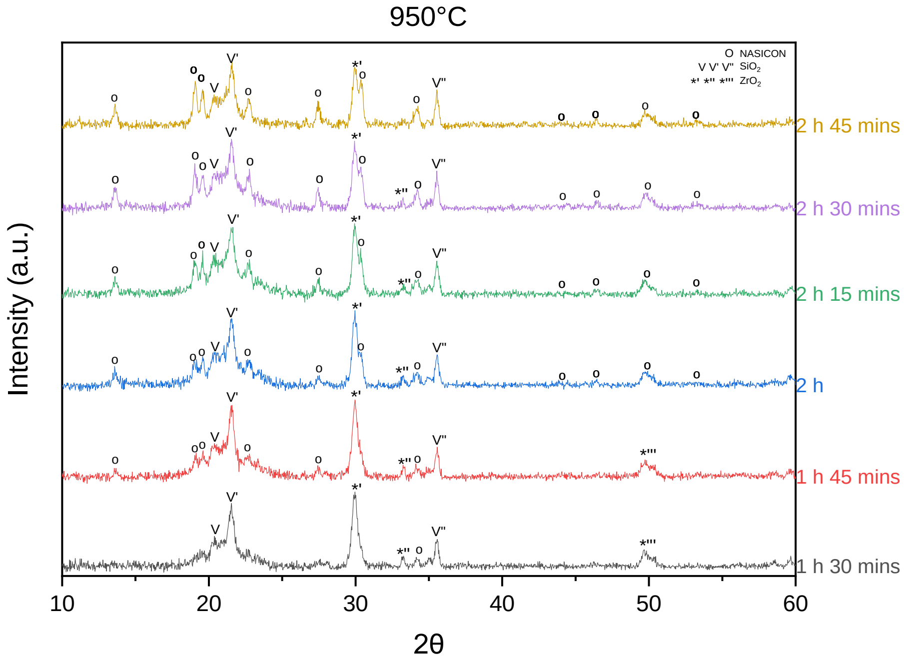

Figure 118: XRD's taken at time intervals during the thermal stage experiment. Graph shows the evolution of the NASICON peaks.

XRD data (Figure 118) shows NASICON formation initiates at 950ºC after 1 hours 45 minutes, and the NASICON peaks have formed/reaction is noticeable after 2 hours, with peaks intensity continuing to increase over time. ZrO_2 phases are present at 30.3º, 31.4º and 50.4º; however the only ZrO_2 phase present in the final scan is the doublet peak at 30.3º, the other ZrO_2 secondary phases are no longer present.

6.8.4 Thermal XRD hold experiment - 1000°C

The aim of this experiment is to see if NASICON forms at 1000°C, and if so, how long it takes for crystallisation to occur. The ramp rate for this experiment is 20°C / min, until it reaches 1000°C hold. Each scan takes 15 minutes and the time at which each scan started is shown on the y-axis of Figure 119 and Figure 120.

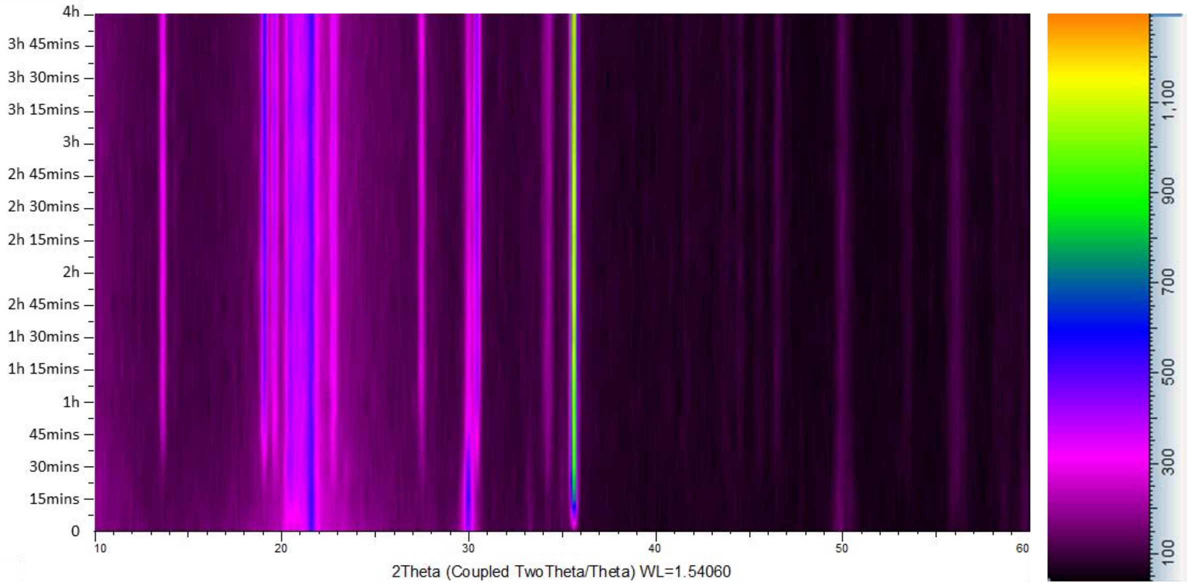

Figure 119: 2D view of XRD thermal stage experiment. XRD scans taken once the stage had reached 1000°C, the left axis shows the time at which each scan was recorded.

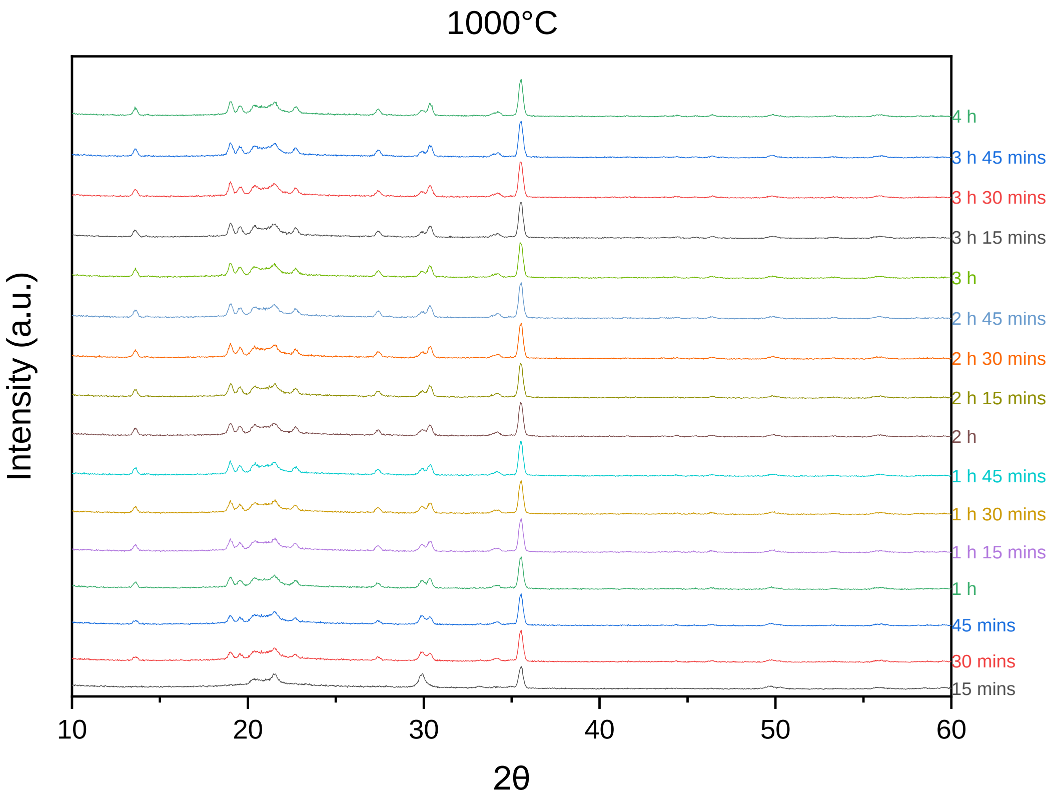

Figure 120: XRD's taken at time intervals during the thermal stage experiment.

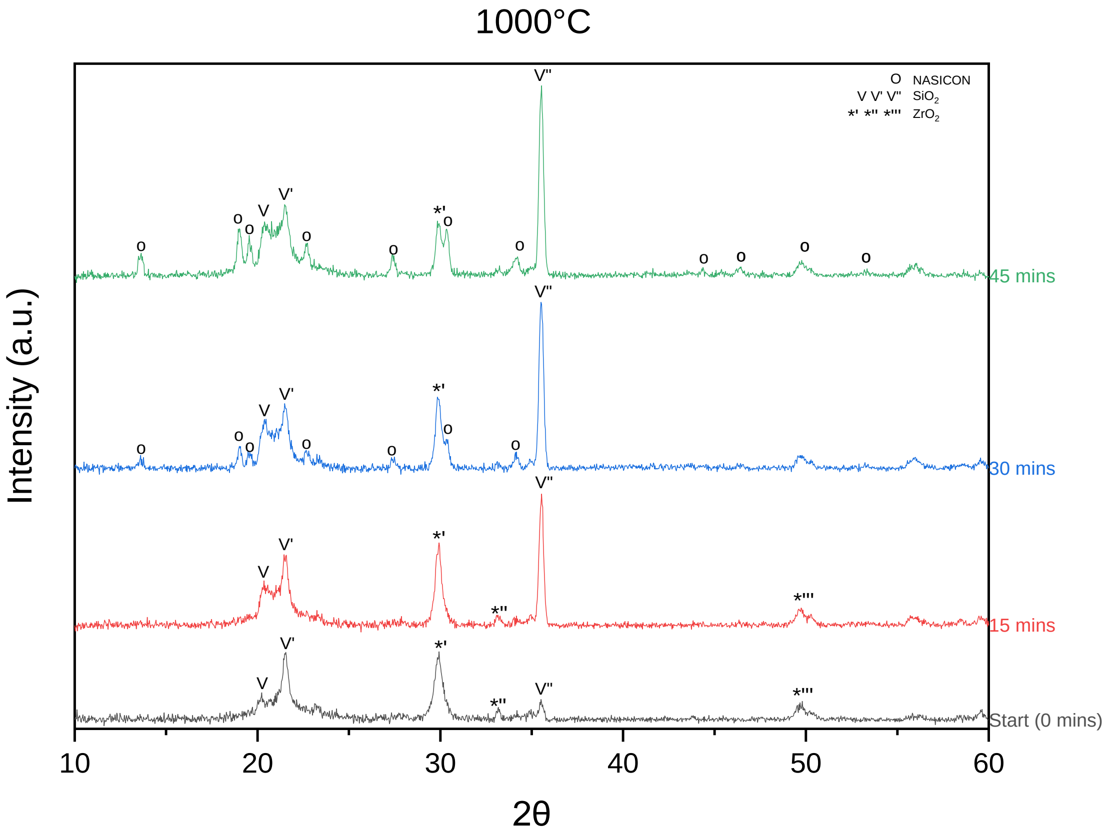

Figure 121: XRD's taken at time intervals during the thermal stage experiment. Graph shows the evolution of the NASICON peaks.

Thermal stage XRD data shows NASICON starts to form at 1000°C after 30 minutes (Figure 121). Peak intensity slightly increases over time and after 1 hour 30 mins the intensity of the NAISCON peaks stays constant. The presence of carbon hinders the formation of NASICON (as it is attached to the Zr), so when the C is removed the structure can form/grow. This is demonstrated in the DSC-TGA data in Chapter 5, which shows an exothermic peak at 977ºC for Cl-TA chemistry NASICON powder. This explains why at 950°C NASICON takes 1 hour 45 minutes to form, but only takes 30 minutes to form at 1000°C.

Once NASICON has formed the secondary phase present in the NASICON is the doublet peak at 30.3º (*') which is ZrO_2. The SiO_2 peak at 36º formed instantly at 1000°C, and the intensity of the peak is much greater than the 950ºC thermal stage experiment.

6.9 Electrochemistry

EIS was performed on a NASICON sol thin film ($ZrOCl_2.8H_2O$) spray coated onto a quartz substrate (120°C) and sintered conventionally at 1000°C (XRD data for sample in Figure 105). The EIS data was collected to assess its conductivity relative to equivalent NASICON pellets reported in literature. To determine the ionic conductivity of the synthesised NASICON, the thin film dimensions were measured (Figure 122) and reported to be: thickness (t) = 0.25 cm, contact area of the electrode (A) = 2.5×10^{-3} cm^2 (film thickness x diameter of disc = 10 microns x 2.5 cm) and (R_t) = 39 MΩ (extracted from EIS data).

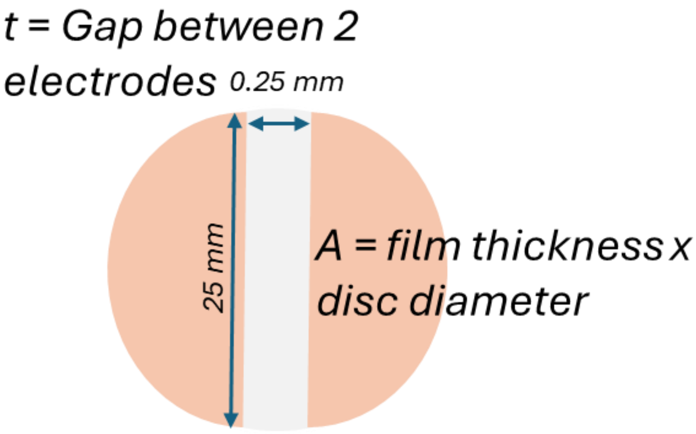

Figure 122: Diagram illustrating the dimensions used to calculate the ionic conductivity of the thin film sample.[175]

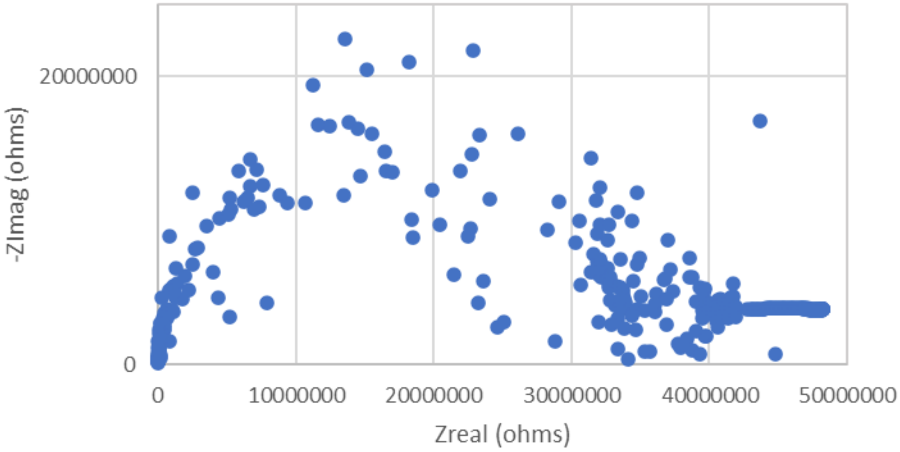

Figure 123: Nyquist plot of EIS data from NASICON thin film on quartz conventionally sintered (1000°C).

Due to the SiO_2 phase and the inhomogeneity of the film, the EIS data could not be modelled using Z-view. However, a value from the Nyquist plot (Figure 123) was used to approximate the ionic conductivity.

Equation 20

$$\sigma_t = \frac{t}{A\ x\ R_t} = \frac{0.25}{39\ x\ 10^6\ x\ 2.5\ x\ 10^{-3}} = 2.56\ x\ 10^{-6}\ Scm^{-1}$$

The ionic conductivity of the film (2.56 x 10^{-6} Scm^{-1}, Equation 20) is three orders of magnitude lower than that of the solid-state pellet presented in Chapter 4 (1.95 x 10^{-3} Scm^{-1}) and values reported in literature. The inclusion of this data quantitively demonstrates the degree of improvement in film homogeneity required to enhance thin film conductivity in future work.

6.10 Conclusion

This chapter successfully sintered a NASICON thin film on a quartz substrate, using water-based sol precursor chemicals, by spray coat deposition and reaction phase sintering. Demonstrating a novel way of making NASICON films. GI-XRD data suggests peaks at 20.6º, 21.7º and 36º are SiO_2 phases linked to a quartz substrate reaction, and not a secondary phase within the NASICON. Thermal XRD experiments showed that 50 layers of the precursor sol spray coated on quartz forms NASICON after 30 minutes at 1000ºC on the thermal stage. Thermal XRD experiments also showed NASICON can form at 950ºC (after 1 hour 45 minutes), but not at temperatures 900ºC and lower.

Chapter 7 – Sol NIR Sintered NASICON

7.1 Introduction

NIR typically operates at 800-1200 nm wavelengths, Figure 124 shows the wavelengths at which the NIR machine emits radiation, which is dependent on the lamp power settings (0-100%). The NIR wavelengths absorbed, and temperature reached are determined by the material being irradiated.

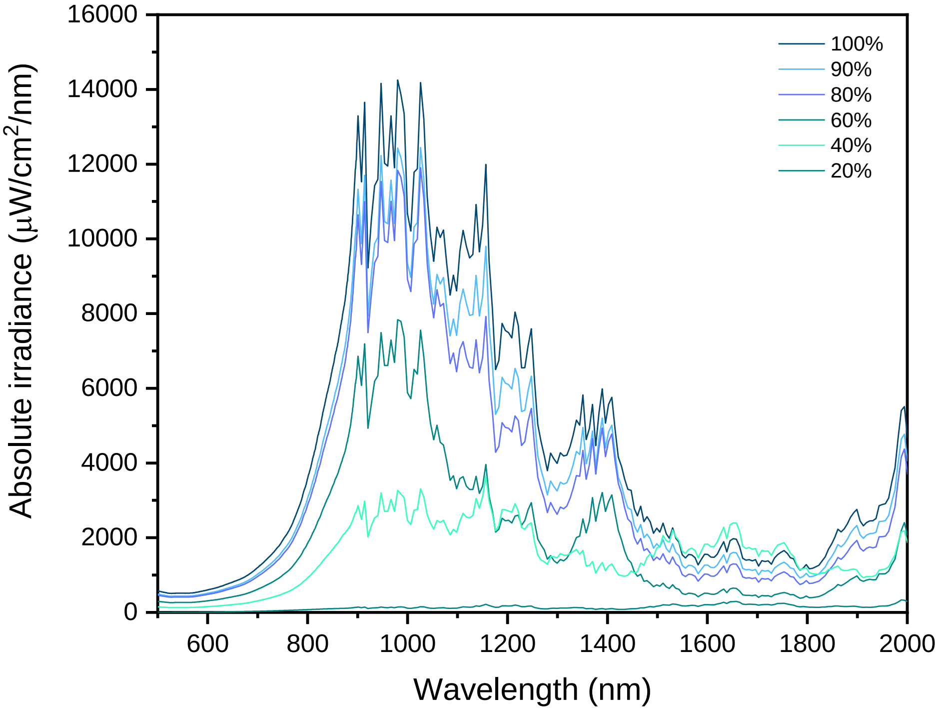

Figure 124: Output emission of NIR lamp, collection method defined in Chapter 3.[172]

Figure 125 illustrates the mechanism by which NIR radiation heats a substrate and thin film through absorbance. In this diagram the substrate absorbs and reflects the near infrared radiation, transmitting it as heat to the transparent thin film.

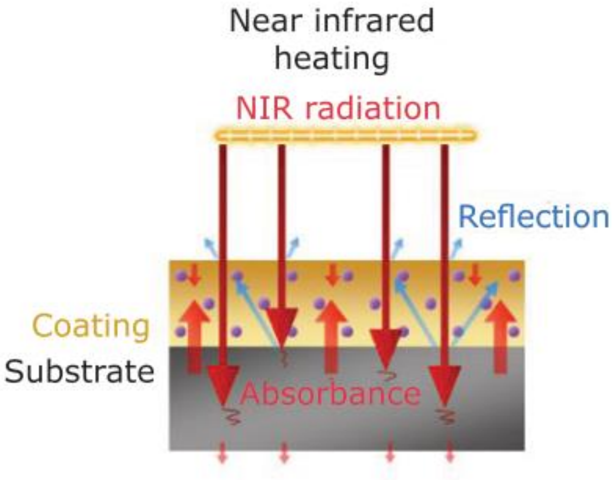

Figure 125: Diagram illustrating NIR absorption.[172]

The quartz substrates used in this thesis are transparent to incoming radiation (Figure 126); the wavelengths pass through the quartz and no heating occurs. Therefore, other substrates and techniques that absorb radiation in the NIR region were tested. For instance, graphite substrates were tested to see if transferred heat from the substrate to the thin film can facilitate the sintering of the sol.

Furthermore, Chapter 5 and 6 work showed that when heated at 750°C for one hour in a conventional oven, the samples turned black. This black coloration is associated with the appearance of carbon (C^0) from an incomplete oxidation of the carbon from the tartaric acid (C^{-4}). My work therefore utilises this black colour to absorb NIR radiation at the wavelengths specific to the NIR lamps and heats the film, shown in Figure 126 and Figure 127. At the higher temperatures achieved during NIR radiation treatment, this carbon (C^0) reacts with O_2 (combustion reaction, exothermic) generating CO_2 (C^{+4}) causing this black carbon (C^0) to disappear and causing the film to turn white. DSC-TGA data in Chapter 5 shows that this combustion reaction occurs above 950°C.

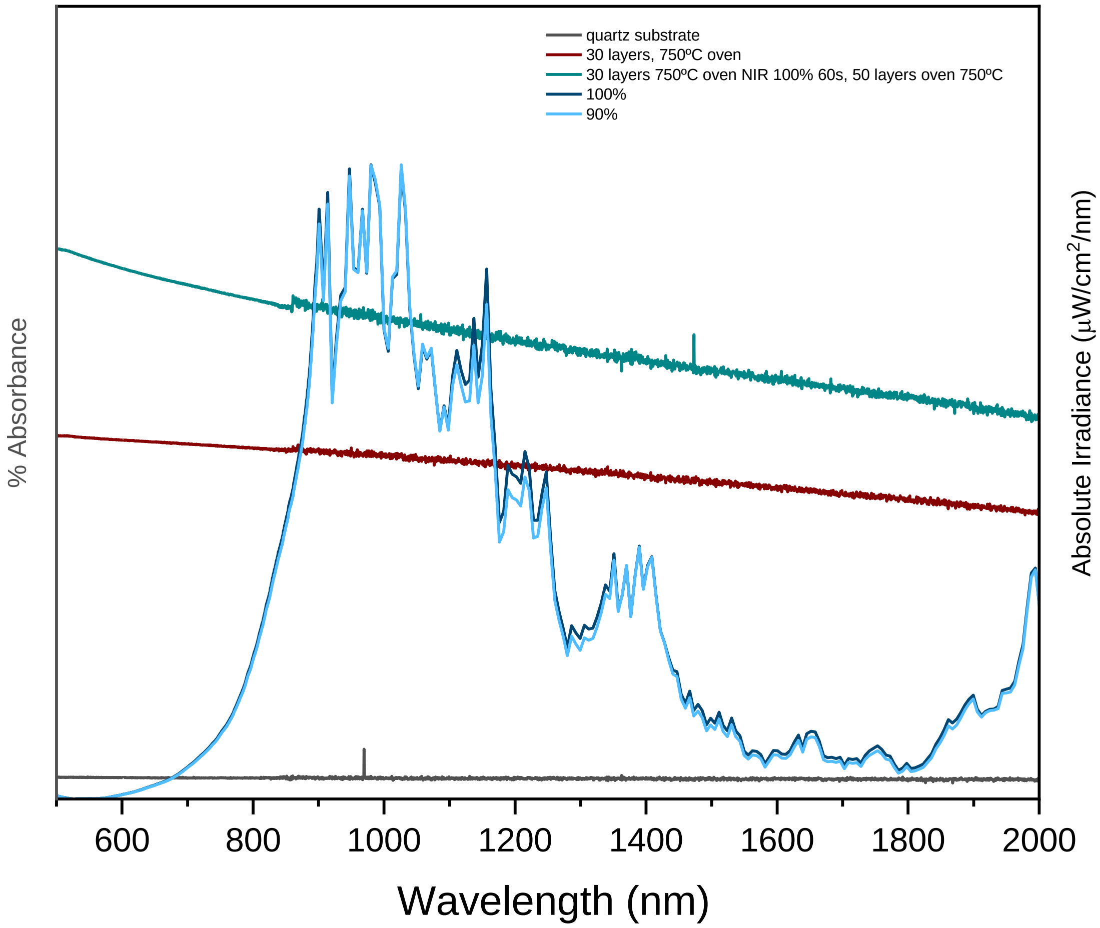

Figure 126: UV-Vis-NIR data of black: quartz sample; red: sample after 30 layers and 750ºC oven treatment; green: sample after 30 layers and 750ºC oven treatment NIR 100% 60s, 50 layers oven 750ºC.

Figure 127 illustrates that when the sol film is white in colouration (after drying or NIR treatment) the film does not absorb very much in the NIR wavelengths and therefore heating/sintering does not occur. Compared to the black 750ºC films which have a much higher % absorbance, it absorbs strongly at wavelengths of 600-2000 nm seen in the UV-VIS-NIR data. Another thing to note is that as the number of spray coats and therefore film thickness increases, so does the % absorbance of the film.

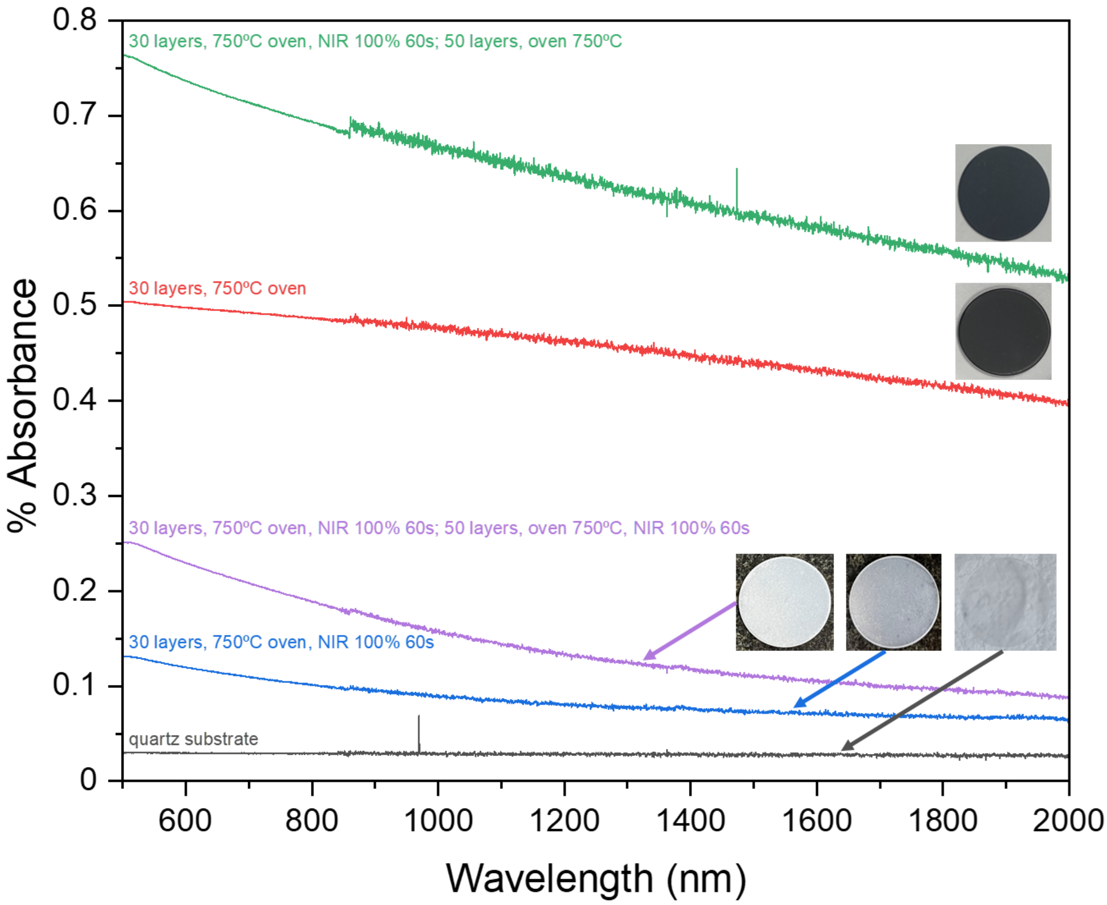

Figure 127: UV-Vis-NIR data of: black: quartz sample; blue: sample after 30 layers, 750ºC oven treatment NIR 100% 60s; purple: sample after 30 layers, 750ºC oven treatment, NIR 100% 60s, 50 layers oven 750ºC, NIR 100% 60s; red: sample after 30 layers and 750ºC oven treatment; green: sample after 30 layers, 750ºC oven treatment, NIR 100% 60s, 50 layers oven 750ºC.

This is a novel synthesis method and therefore the aim is to understand whether it is possible to sinter and therefore synthesise a NASICON sol using NIR, in turn reducing sintering times. If this is achieved, the next step is to develop a process and suitable NIR parameters to form NASICON with the required chemistry.

This chapter investigates synthesising NASICON as a thin film using the techniques developed in Chapter 6 but with NIR sintering, to apply to future applications in solid-state sodium-ion batteries. The same as the previous chapters work, it involves reaction phase sintering, in which the water-based precursor sol is directly deposited onto the substrate and sintered in-situ.

Settings must be tested to optimise the NIR for this function including length of time and % power. Other variables that interact with the ability to sinter NASICON via NIR are scoped in this chapter: substrate material, precursor chemistry, drying temperature, number of spray coated layers, 750°C oven treatment and initiator layers; describe in Table 40.

The two types of chemistry that are tested in this chapter are shown in Equation 21 and Equation 22, for all samples a 5% solid concentration is employed (in 2:1:2:3 molar ratios).

Equation 21

$$ZrO(NO_3)_2.2H_2O + NH_4H_2PO_4 + Na_2SiO_3.9H_2O + C_4H_6O_6 \rightarrow Na_3Zr_2Si_2PO_{12}$$

Equation 22

$$ZrOCl_2.8H_2O + NH_4H_2PO_4 + Na_2SiO_3.9H_2O + \ C_4H_6O_6 \ \rightarrow Na_3Zr_2Si_2PO_{12}$$

Active cooling was applied to the NIR machines electronic systems, a quartz bed was used to place the sample on and a small gap between the lamps and the bed enabled the samples being processed to reach temperatures of >1000°C.

Table 40: Table describing the sol thin film experiments undertaken.

formulation	substrate	number of layers	drying temp (°C)	NIR and oven treatments	NIR%
$ZrO(NO_3)_2.2H_2O$	alumina	100	120	30s	100%
$ZrO(NO_3)_2.2H_2O$	alumina	80	120	30s	100%
$ZrO(NO_3)_2.2H_2O$	alumina	80	120	45s	100%
$ZrO(NO_3)_2.2H_2O$	alumina	80	120	60s	100%
$ZrO(NO_3)_2.2H_2O$	alumina	80	120	15s	100%
$ZrOCl_2.8H_2O$	quartz	50	150	30s (750 oven)	100%
$ZrOCl_2.8H_2O$	quartz	50	150	30s + 60s (750 oven)	100%
$ZrOCl_2.8H_2O$	quartz	50	150	60s	100%
$ZrOCl_2.8H_2O$	quartz	50	150	60s + 60s	100%
$ZrOCl_2.8H_2O$	quartz	50	150	60s (750 oven)	100%
$ZrOCl_2.8H_2O$	quartz	50	150	60s + 30s graphite (750 oven)	100%
$ZrOCl_2.8H_2O$	quartz	50	150	60s + 60s (750 oven)	100%
$ZrOCl_2.8H_2O$	quartz	50	150	1m.min + 1m.min (750 oven)	100%
$ZrOCl_2.8H_2O$	quartz	30	120	30 spray 1000 oven	
$ZrOCl_2.8H_2O$	quartz	30+50	120	30 spray 1000 oven + 50 spray 750 oven	
$ZrOCl_2.8H_2O$	quartz	30+50	120	30 spray 1000 oven + 50 spray, NIR 60s graphite under	80%
$ZrOCl_2.8H_2O$	quartz	30+50	120	30 spray 1000 oven + 50 layers, NIR 60s graphite on top	80%
$ZrOCl_2.8H_2O$	quartz	30+50	120	30 spray 1000 oven + 50 spray 750 oven	
$ZrOCl_2.8H_2O$	quartz	30+50	120	30 spray 1000 oven + 50 spray 750 oven, NIR 100% 60s	100%
$ZrOCl_2.8H_2O$	quartz	30+50	120	30 spray 1000 oven + 50 spray 750 oven, NIR 100% 60s	100%
$ZrOCl_2.8H_2O$	quartz	30+50	120	30 spray oven 950 + 50 spray oven 750, NIR 100% 60s	100%
$ZrOCl_2.8H_2O$	quartz	30+50	120	30 spray oven 1000 + 50 spray oven 750, NIR 100% 60s	100%
$ZrOCl_2.8H_2O$	graphite	50	120	50 spray NIR 100% 30s	100%
$ZrOCl_2.8H_2O$	graphite	50	120	50 spray NIR 80% 30s	100%
$ZrOCl_2.8H_2O$	quartz	30+50	120	30 spray oven 750 NIR 90% 60s + 50 spray oven 750, NIR 100% 60s	100%
$ZrOCl_2.8H_2O$	quartz	30+50	120	30 spray oven 950 + 50 spray oven 750, NIR 60% 60s	100%
$ZrOCl_2.8H_2O$	quartz	30+50	120	30 spray oven 950 + 50 spray oven 750, NIR 80% 60s	100%
$ZrOCl_2.8H_2O$	quartz	30+50	120	30 spray oven 950 + 50 spray oven 750, NIR 100% 60s	100%
$ZrOCl_2.8H_2O$	quartz	50	120	50 spray hotplate 600, NIR 100% 60s	100%
$ZrOCl_2.8H_2O$	quartz	30+50	120	30 spray oven 750 NIR 100% 60s + 50 spray oven 750, NIR 100% 60s	100%
$ZrOCl_2.8H_2O$	quartz	30+50	120	30 spray oven 750 NIR 100% 60s + 50 spray oven 750, NIR 100% 60s	100%

7.2 Scoping experiments

Scoping experiments examined the NIR settings impact on this set of experiments - length of time and % power. Other variables scoped included substrate material (alumina, graphite and quartz), precursor chemistry (NO_3 vs Cl), drying temperature (120°C / 150°C), number of spray coated layers (100, 80 and 50), and 750°C oven treatments. Many of these variables were previously tested in Chapter 6, however they may be more suitable in synthesising NASICON via NIR sintering compared to conventional oven sintering.

7.2.1 Alumina Substrate

Alumina was tested as a substrate as the shorter sintering exposure time (60s instead of 3 hours) may reduce the Al^{2+} diffusion into the film and potentially enable a NASICON phase to form.

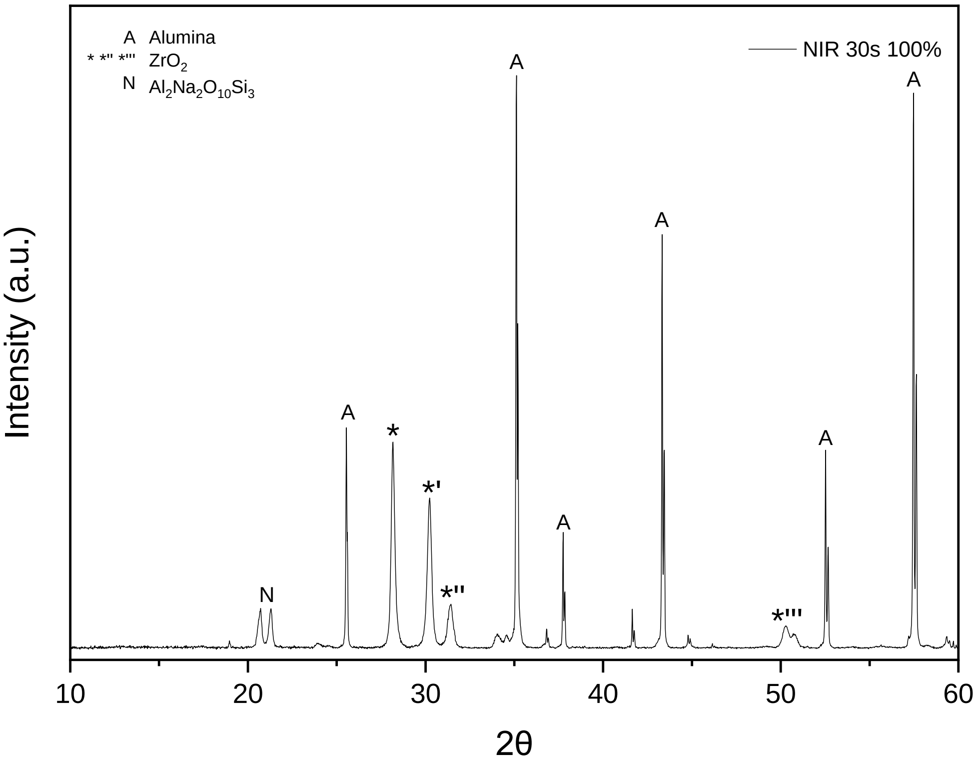

Figure 128: XRD of NASICON sol spray coated 100 layers on an alumina substrate, dried at 120°C and sintered by NIR at 100% power for 30s.

The NIR data (Figure 128) illustrates that for this chemistry, concentration, number of spray-coated layers and drying temperature, NASICON does not formed under these NIR conditions. The XRD data shows Al_2O_3 (SG 167, COD 2300448[207]) peaks at 25.6°, 35.2°, 37.8°, 43.4°, 52.6° and 57.5° attributed to the alumina substrate. The data is also dominated by tetragonal (SG 137, COD 1526427[220]; *’ / *’’’) and monoclinic (SG 14, COD 2300544[208]; * / *’’) ZrO_2 peaks at 30.3°, 50.4°, 28.3° and 31.4°. The two peaks at 21° is potentially due to the formation of an $Al_2Na_2O_{10}Si_3$ (SG 43, COD 9010485[221]) intermediate phase; however, no NASICON peaks are present.

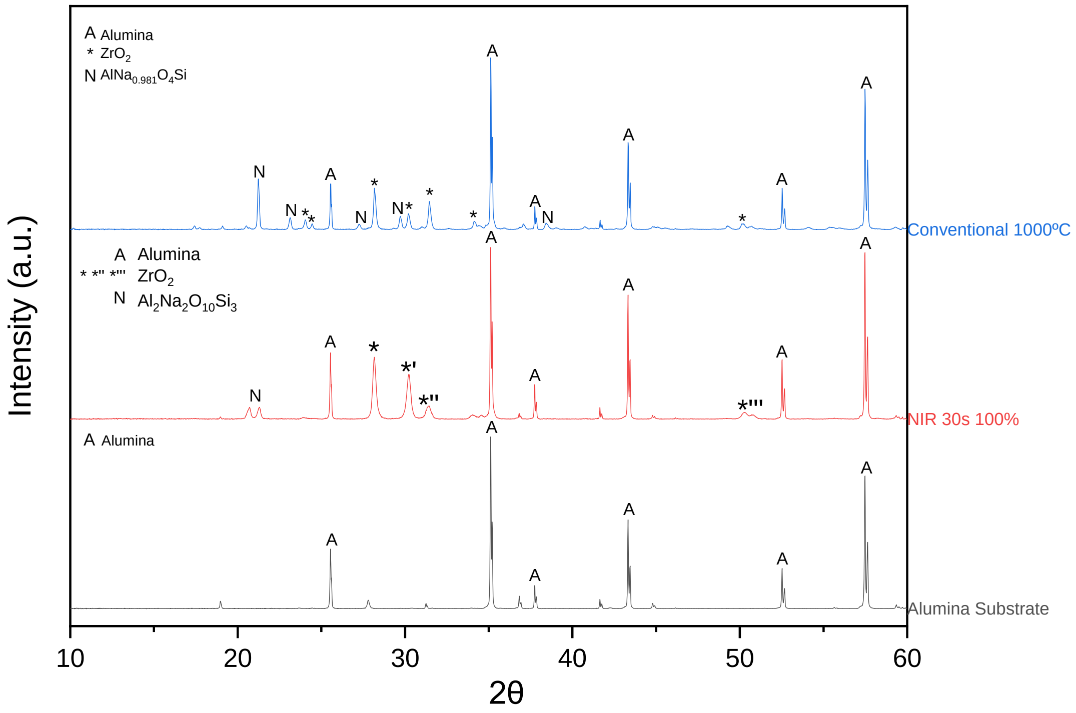

Figure 129: XRD of NASICON sol spray coated 100 layers on an alumina substrate, dried at 120ºC and sintered by NIR at 100% power for 30s. Compared to the XRD of the alumina substrate spray coated 100 layers, dried at 120ºC and conventionally sintered at 1000°C. XRD of the alumina substrate is also shown.

Figure 129 illustrates that although the XRD data shows different peaks to the conventionally sintered equivalent sample, both XRD’s are dominated by the alumina substrate peaks. In both cases NASICON has not formed, this could be due to the movement of alumina ions into the NASICON film. The conventional oven shows more intermediate phases ($Al_2Na_2O_{10}Si_3$) than the NIR film ($AlNa_{0,981}O_4Si$), this is most likely due to the extended sintering time of the conventionally heated film (3 hours). ZrO_2 secondary phases occur in both samples due to its thermal stability, a common secondary phase when sintering at high temperatures.

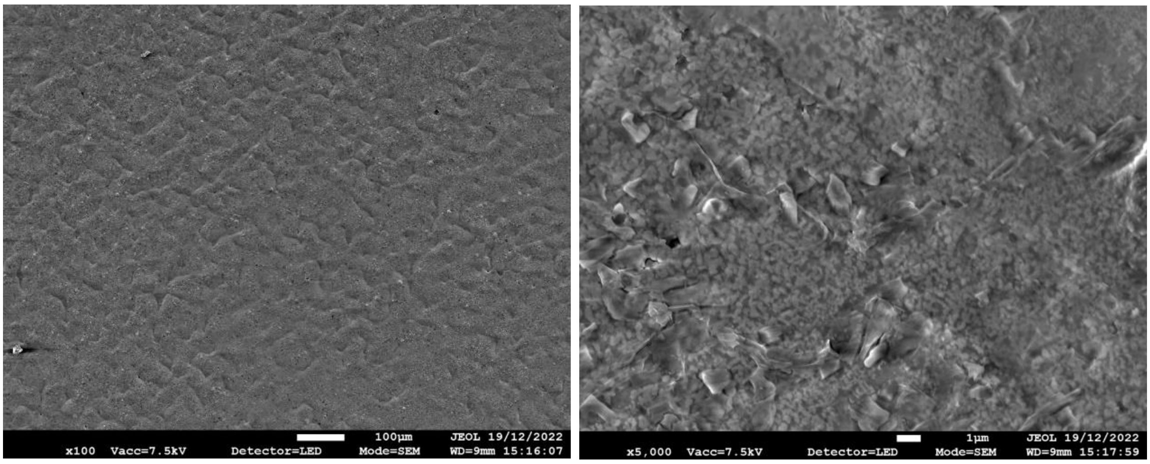

Figure 130: SEM images of sol NASICON spray coated and sintered via NIR (100% power, 30s) on a quartz substrate.

SEM images in Figure 130 show a very homogenous film, with less cracks/islands than the conventionally sintered films in Chapter 6.

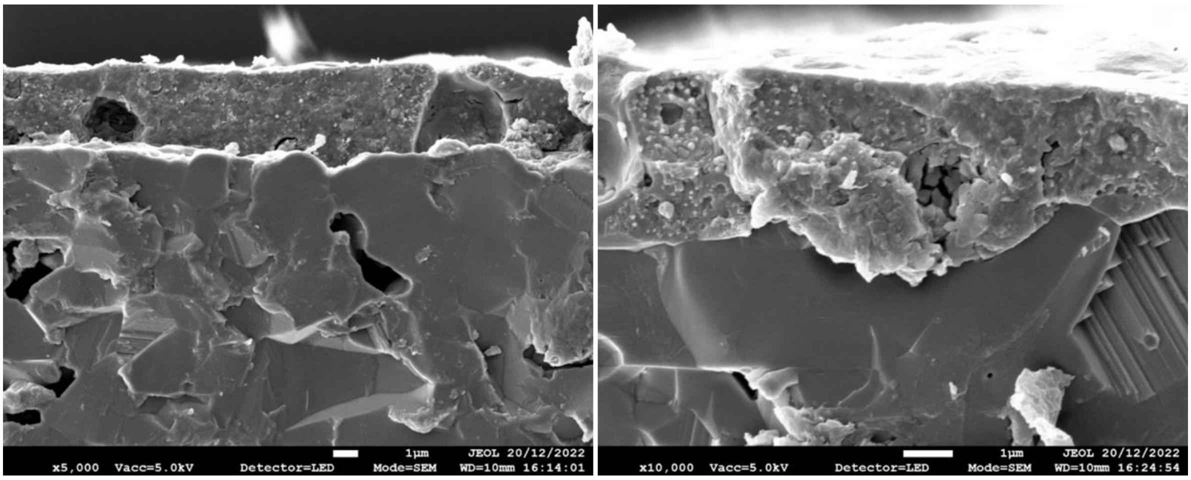

Figure 131: Cross-sectional SEM images of sol NASICON spray coated and NIR (100% power, 30s) sintered on an alumina substrate.

The cross section in Figure 131 shows the alumina sample heated using NIR. The images show two defined layers: the alumina substrate and a compact/dense film (with some pores present). This top spray coated layer is approximately 10 microns.

Scoping experiments also investigated NIR sintering for different lengths of time at 100% power, to see whether NASICON can form with different NIR exposure times. The length of NIR treatments chosen where: 15s, 30s, 45s and 60s.

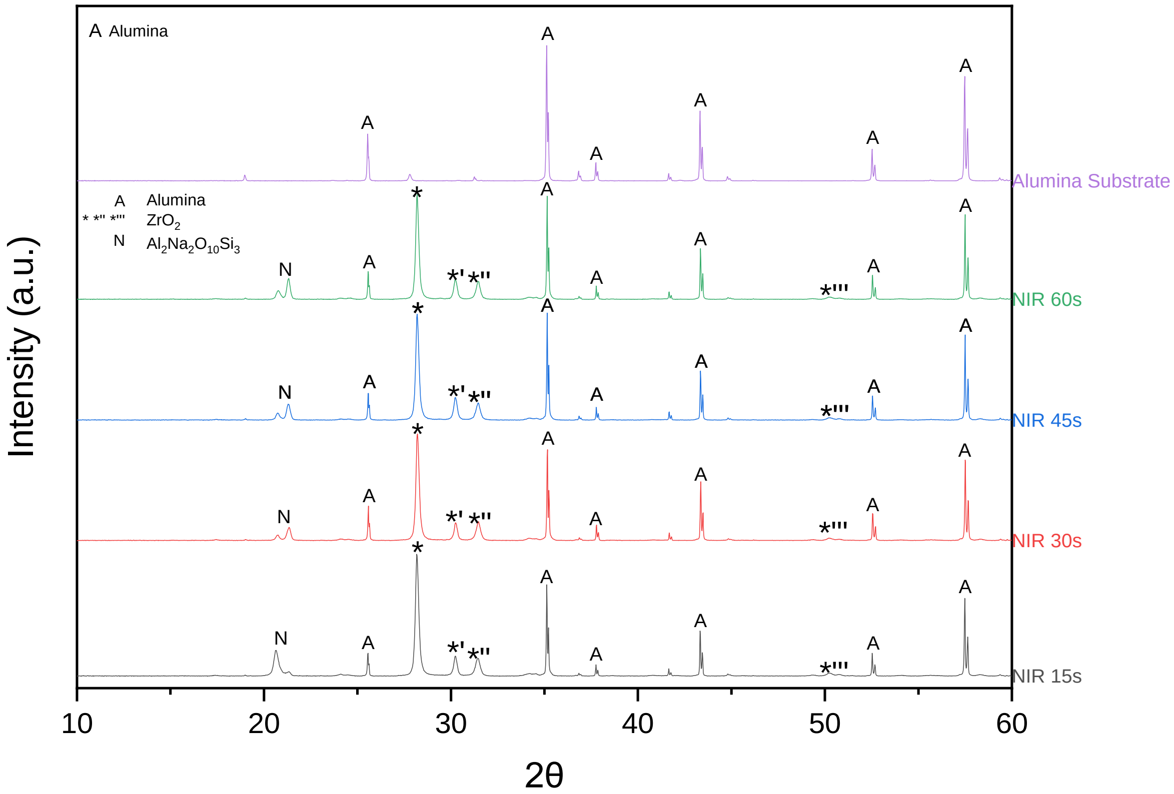

Figure 132: XRD of NASICON NO$_3$ sol spray coated 80 layers on alumina, dried at 120°C and sintered using NIR at 100% power and different exposure lengths. Compared to the XRD of the alumina substrate.

Figure 132 compares the NIR irradiated samples with the alumina substrate, and illustrates that at all NIR exposure lengths, NASICON does not form as a thin film on alumina. Phases of ZrO_2 and $Al_2Na_2O_{10}Si_3$ are present in all the samples, with similar intensities for all XRD scans. The only difference between the samples is the shape of the peak at 21°C suggesting differences in the presence of this intermediate phase.

7.2.2 Graphite substrate

As alumina did not work as a substrate for NIR sintering, this experiment explored the application of a graphite substrate to sinter NASICON. The motive to use graphite is that the black colour absorbs more NIR radiation (Figure 133), which in turn will increase the temperature of the graphite substrate, and therefore heat and potentially reach the necessary temperature for NASICON synthesis, >950ºC.

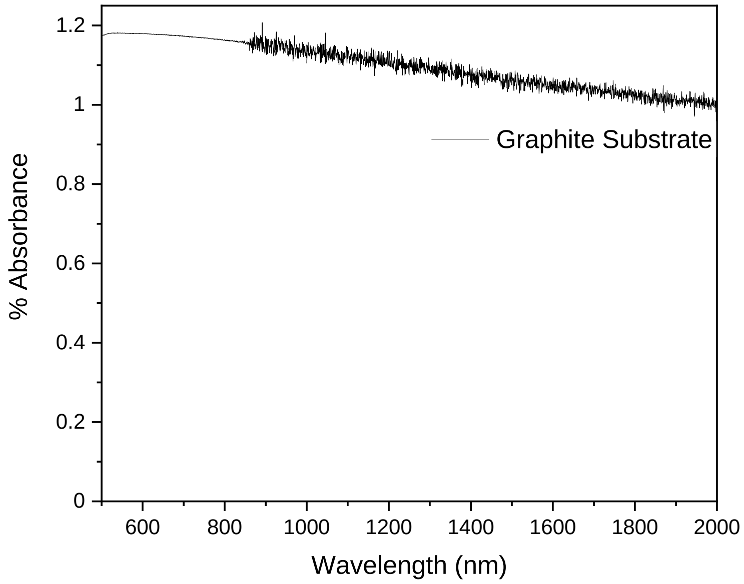

Figure 133: UV-Vis-NIR % absorbance data of the graphite substrate.

The first set of experiments placed the graphite substrate below or on-top of the spray coated quartz and used the colour of the graphite to increase the temperature through NIR absorption and attempt to sinter the NASICON through transferred heat (Figure 134 (a) and (b)).

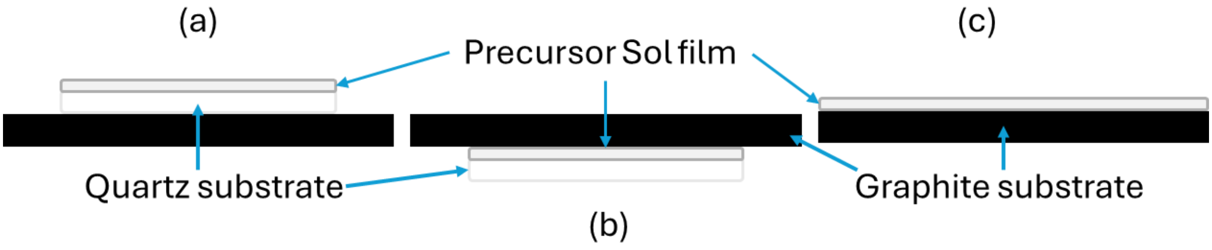

Figure 134: Diagram illustrating the graphite samples set-up: (a) quartz spray coated sample on-top of graphite substrate (b) quartz spray coated sample on-top of graphite substrate (c) graphite substrate directly spray coated.

The quartz samples were coated with 30 layers and sintered in the oven at 1000°C, then another 50 layers was spray coated on-top. The samples placed below or above the spray coated quartz sample were then placed in the NIR at 80% for 60s.

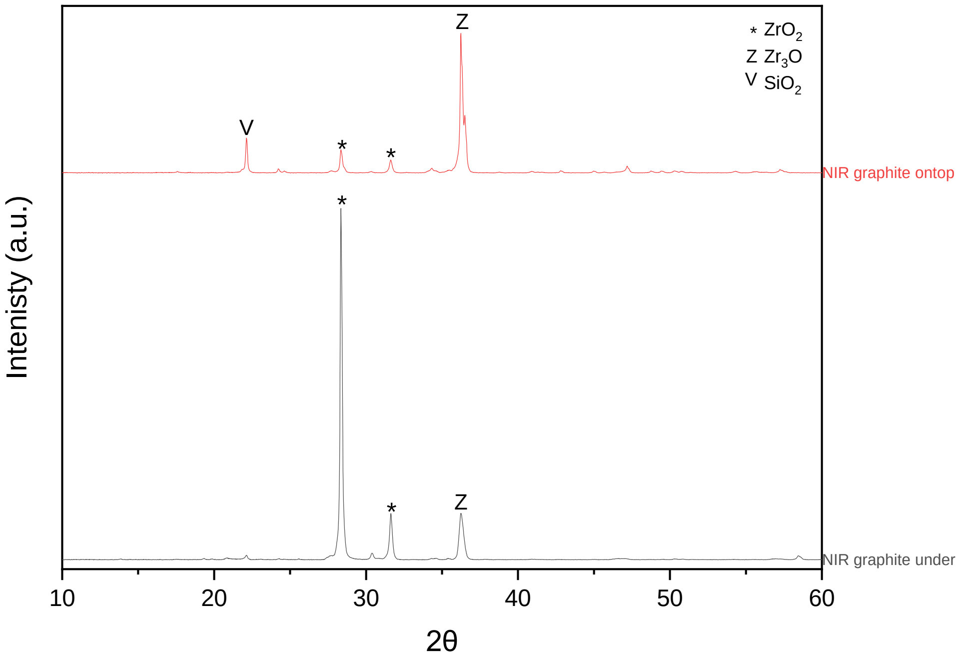

Figure 135: XRD of NASICON ZrOCl2.8H2 sol spray coated on quartz (30 layers) and sintered at 1000°C in a conventional oven, followed by a second spray coat (50 layers) and NIR treated at 80% for 60s. 1.3 - graphite placed under the sample during NIR treatment; 1.4 - graphite placed on top of the sample during NIR treatment.

The XRD data (Figure 135) shows that NASICON has not formed for either sample. Analysis indicated the potential phases for these films:

- Graphite on top: SiO_2 (SG 92, COD 9015087[222]) at 22.1º; ZrO_2 (SG 14, COD 2108453[187]) at 28.3º and 31.4º; and Zr_3O (SG 167, COD 1535864[223]) at 36.3º.
- Graphite under: ZrO_2 (SG 14, COD 2300544[208]) at 28.3º and 31.6º; and ZrO_3 (SG 167, COD 1535864[223]) at 36.3º

ZrO_2 secondary phases are the most likely phase to occur because this compound has the highest thermal stability (compared to volatile Na and P). A silica phase is present suggesting the sample could have reached a high temperature of >800ºC, as this peak is seen at this temperature in the thermal stage experiments (Chapter 6).

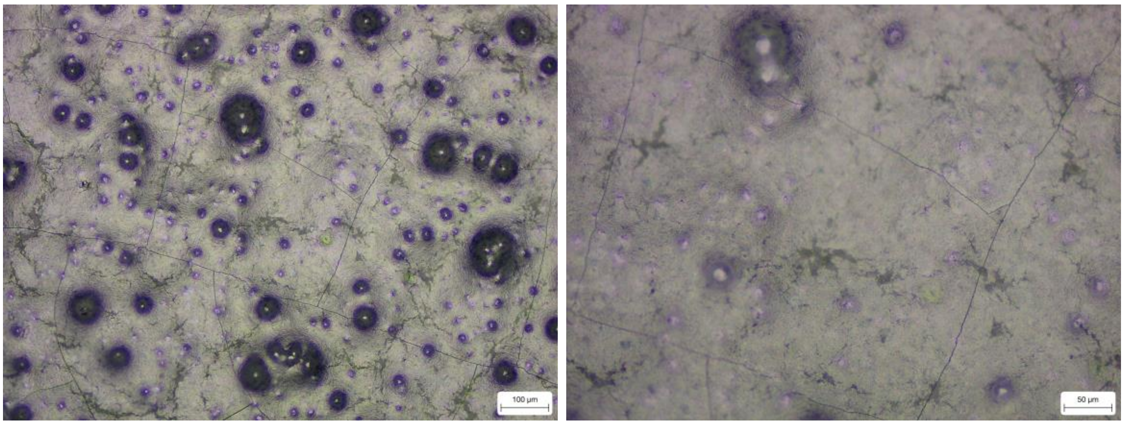

Figure 136: Optical microscope images of NASICON ZrOCl2.8H2 sol spray coated on quartz (30 layers) and sintered at 1000°C in a conventional oven, followed by a second spray coat (50 layers) and NIR treated at 80% for 60s with graphite placed under the sample. Images at x10 and x20 magnification.

Optical microscope images of the film (Figure 136) show a non-homogeneous film with dark spots/areas, confirming with the XRD data that this method should not be explored further.

The next set of experiments attempted to spray coat the sol directly onto graphite substrate (Figure 134 (c)) and NIR sinter. The chemistry of the film did not have tartaric acid precursor as the graphite contains carbon and Chapter 5 powder experiments proved NASICON can form without the presence of tartaric acid. Two samples at two different NIR % powers were tested: 100% for 30s and 80% for 30s.

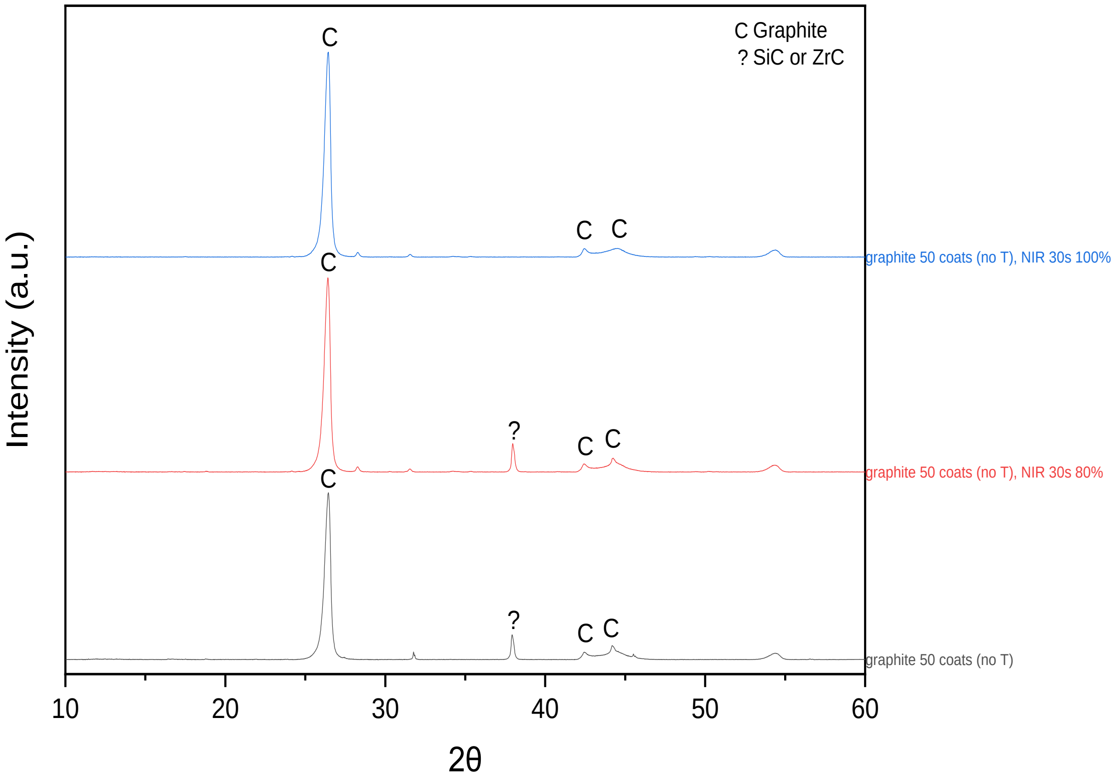

Figure 137: XRD of NASICON sol ($ZrOCl_2.8H_2O$ without tartaric acid) on a graphite substrate. Black: 50 spray coats, no heat treatment; Red: 50 spray coats, NIR treated at 80% for 30 seconds; Blue: 50 spray coats, NIR treated at 100% for 30 seconds.

XRD data in Figure 137 illustrates that NASICON does not form when coated on graphite and treated with NIR. The data is dominated by C/graphite peaks (SG 194, COD 9011577[224]) at 26.4º, 42.3º and 44.2º. As suggested in the DSC-TGA data in Chapter 5, C can hinder NASICON formation as it oxidises and reacts with components in the film. Therefore, the large amount of C present in the graphite substrate could cause intermediates of SiC (COD 1011053[225]) and/or ZrC (COD 1539492[226]), which stops NASICON formation and could be attributed to the peak at 38º. An alternative theory is that the graphite is reaching extreme temperatures causing many of the volatile components of the sol to burn off. While additional research is needed to confirm this, this thesis focussed on using alternative substrates and techniques to refine the thin film synthesis of NASICON using NIR.

7.2.3 Quartz Substrate and using 750°C oven treatment

Quartz was utilised as a substrate, as Chapter 6 proved through conventional sintering (oven) NASICON thin films can successfully synthesise on this substrate.

As seen previously in the sol powder work (Chapter 5), when the NASICON precursor is treated at 750°C the NASICON turns black. I decided to utilise this in the NIR work, as NIR absorption increases when the material is black. Therefore, in this work some samples are treated at 750°C, turning the film black, and then treating this black sample with NIR radiation to attempt to initiate NIR in-situ sintering.

This experiment is looking at depositing the Zirconium Chloride chemistry sol as a thin film onto quartz substrates using a spray gun (50 coats). The aim of the experiment is to trial a range of different NIR treatments in combination with conventional oven treatments to see if it is possible to sinter NASICON using NIR, scoping the potential of the equipment for this application.

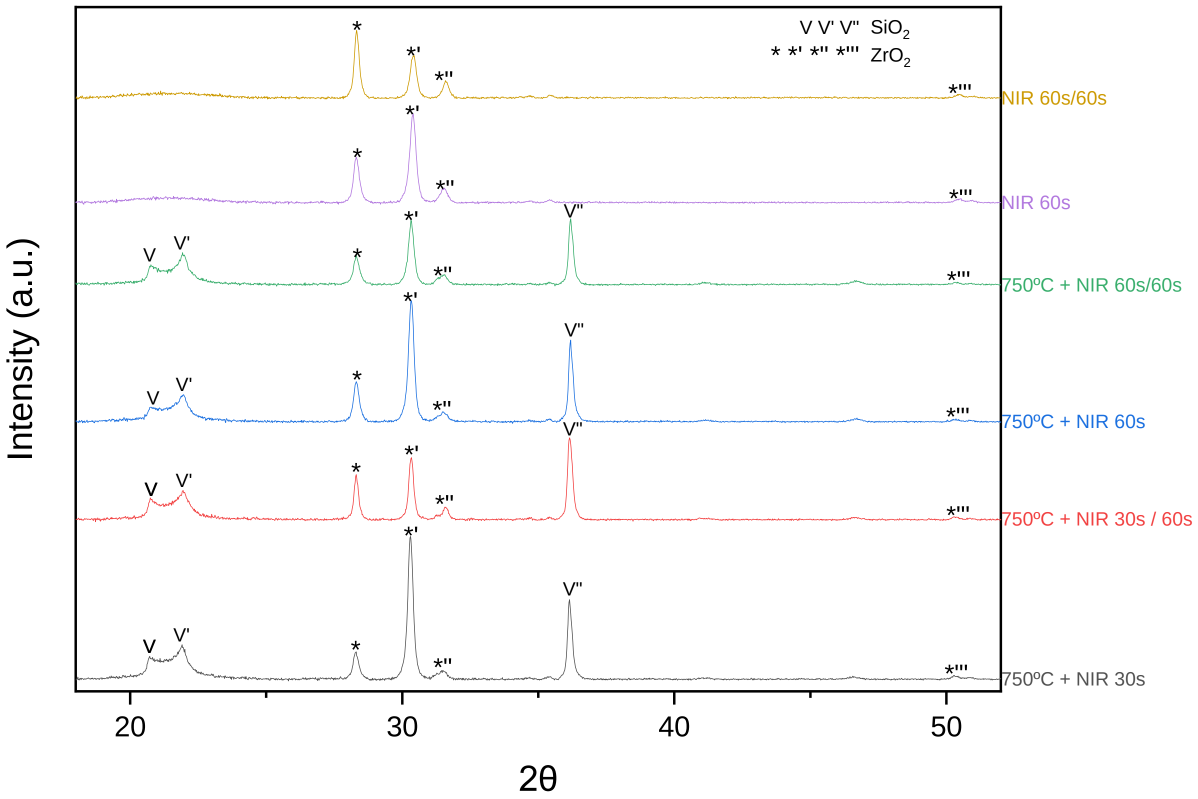

Figure 138: All XRD’s are samples with NASICON sol (ZrOCl2.8H2O) spray coated onto quartz. Black XRD: sample heated at 750°C in conventional oven and treated on the NIR at 100% for 30 seconds. Red XRD: sample heated at 750°C in conventional oven and treated on the NIR at 100% for 30, then treated at 100% for 60s. Blue XRD: sample heated at 750°C in conventional oven and treated on the NIR at 100% for 60 seconds. Green XRD: sample heated at 750°C in conventional oven and treated on the NIR at 100% for 60s and then treated again at 100% for 60s. Purple XRD: treated on the NIR at 100% for 60s. Yellow XRD: treated on the NIR at 100% for 60s and then treated again at 100% 60s.

For the XRDs without the 750°C heat treatment, both the fused SiO_2 and the dried precursor sol absorb poorly in the NIR wavelengths, as they are white/clear in colour. Therefore, direct NIR heating of the sprayed sol does not result in a temperature high enough to form NASICON, and only ZrO_2 phases form; the temperature is not high enough to allow the conversion of the quartz substrate.

The XRD data (Figure 138) illustrates that for the samples heated at 750°C before NIR radiation at this chemistry, concentration, number of spray-coated layers and drying temperature in all the above experiments tested NASICON is not formed under this range of conditions. The NIR samples have formed SiO_2 and ZrO_2 XRD peaks in different phases:

- ZrO_2 tetragonal (SG 137, COD 1526427[220]; *’/*’’’) at 30.3° and 50.4°

- ZrO_2 monoclinic (SG 14, COD 2300544[208]; */*") at 28.3º and 31.4º
- SiO_2 orthorhombic (SG 1, COD 9013393[214]; V) at 20.6º
- SiO_2 tetragonal (SG 92, COD 9001578[215]; V'/V") at 21.7º and 36º

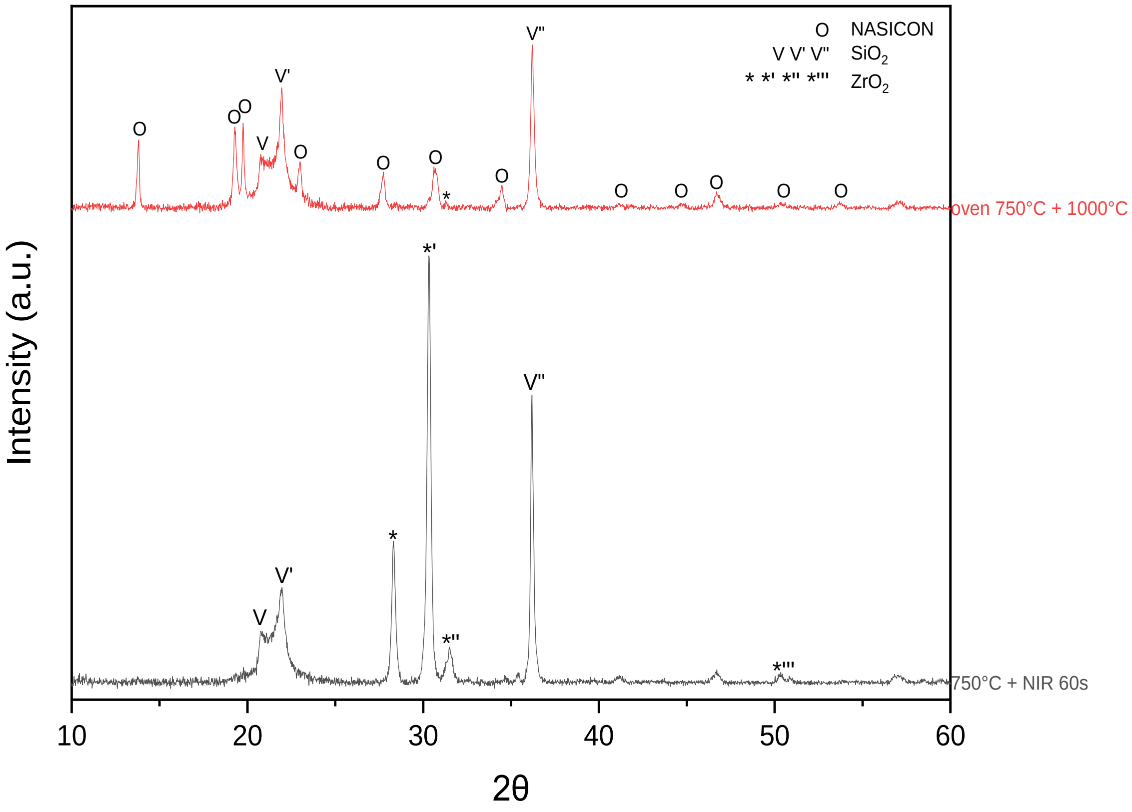

Figure 139: XRD's of samples with NASICON sol ($ZrOCl_2.8H_2O$) spray coated onto quartz. Black XRD: sample treated at 750°C in conventional oven and treated on the NIR at 100% for 60 seconds. Red XRD: sample heated at 750°C and sintered at 1000°C in conventional oven.

Figure 139 illustrates the difference between the conventional oven thin film sample and the NIR treated sample. Both samples have the same chemistry, concentration, drying temperature, and number of spray coated layers; the only difference is one sample is treated at 1000°C in the oven and one is treated at 100% for 60s with NIR. Both samples have formed the secondary phases at 20.6º, 21.7º and 36º peaks, suggesting the silicon has renucleated in both the oven and under NIR treatment. Although NASICON has not formed in this NIR case, it does suggest that due to the black colour of the film, enough NIR has been absorbed to increase the temperature high enough to allow the conversion of the quartz substrate. Thermal stage XRD experiments show that the SiO_2 peak at 21.7º occurs at 800ºC, whereas the 20.6º and 36º SiO_2 peaks occur at 950ºC. Similar peak intensity of the SiO_2 phases in the XRD data shown here (Figure 139) occur in the thermal stage XRD data after 30 minutes at 1000ºC. This confirms that the NIR samples reach at least 1000ºC, far exceeding temperature of previous NIR work in literature. Therefore, as the sample reaches this temperature there is potential for NASICON to be sintered using this intermediate 750°C step.

Collating all the information from the quartz substrate NIR experiments, formation of NASICON does not occur using NIR and only 50 layers due to 3 possible hyptheses:

- The sintering time is too short for these samples, for instance it takes 30 mins at 1000ºC to form NASICON on a thermal stage.
- The sample is too thin, therefore there is not enough of the carbon-rich intermediate film, in turn causing insufficient absorption of NIR.
- A higher or lower temperature might be needed to sinter NASICON at this short radiation time (60s).
- Reaction is occurring between the substrate and the sol at high intensities.

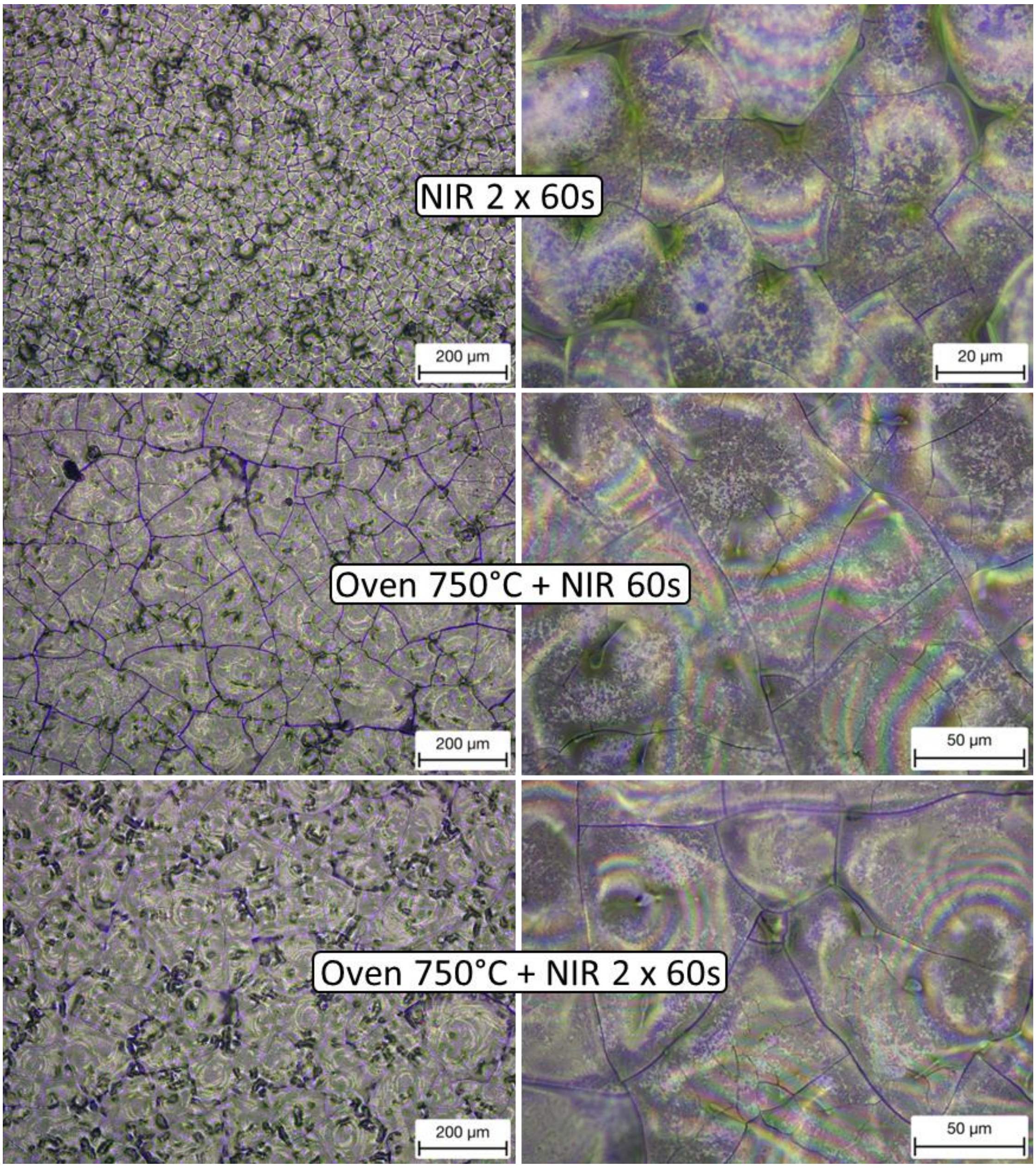

Figure 140: Optical microscope images of NASICON ZrOCl2.8H2 sol spray coated on quartz.

Figure 140 illustrates that at the stated oven/NIR treatments the morphology and homogeneity of the films are very similar. All optical images display cracks in the film and darks areas.

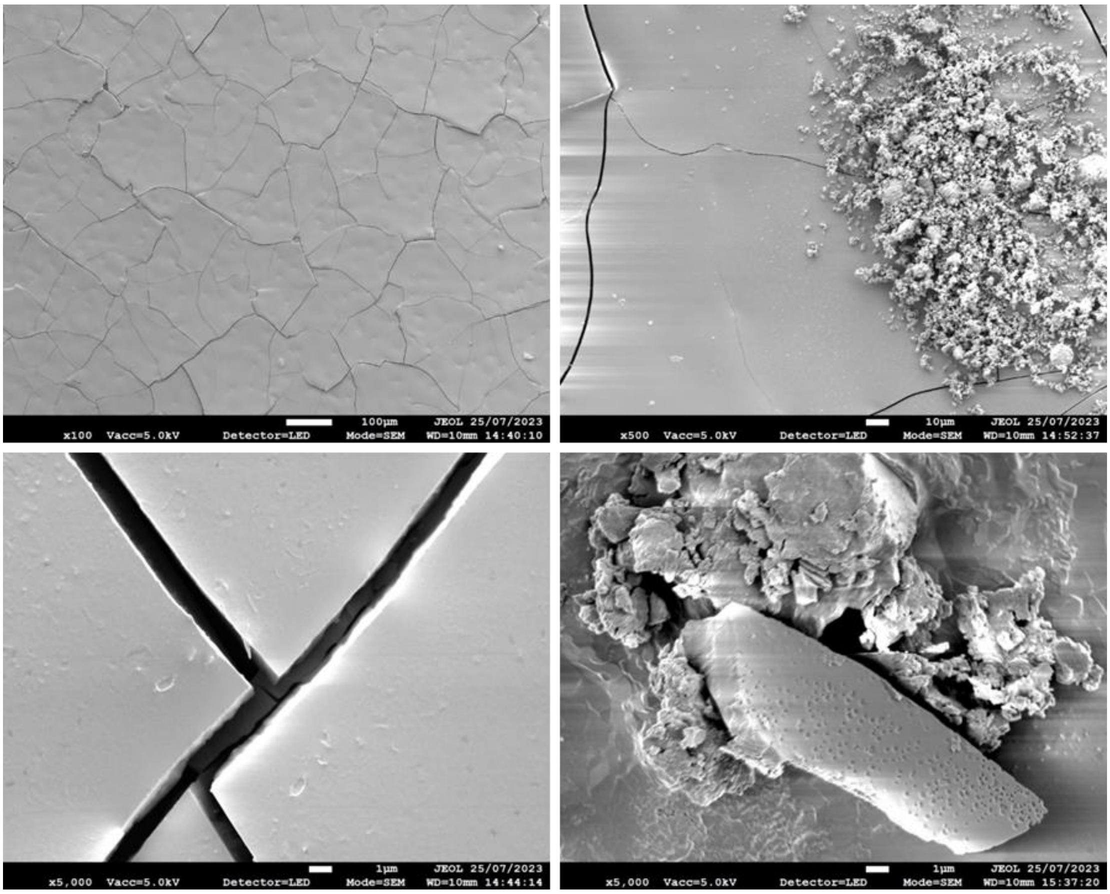

Figure 141: SEM images of NASICON ZrOCl2.8H2O sol spray coated on quartz and NIR treated. Images at x100, x 500 and x5,000 magnification.

SEM images in Figure 141 show in more detail that NASICON has not formed as no crystal structures are present; the film appears to look like the glassy regions of SiO_2 seen in previous samples.

7.3 Initiator layer and 750°C oven treatment

Troughton et al.'s[148] paper described a substrate-driven nucleation and substrate orientated crystal growth during rapid NIR sintering. Therefore, this next set of experiments is looking at depositing 30 layers of the chloride chemistry sol onto a quartz substrate and sintering in a conventional oven, creating an initiator layer which initiates the NASICON crystal phase growth/grain orientation. After which another 50 layers were deposited and conventionally heated at 750°C, forming the black carbon-rich intermediate precursor material to enable NIR sintering. The sample is then NIR treated (100% for 60s), which should allow sintering and NASICON formation in the correct phase.

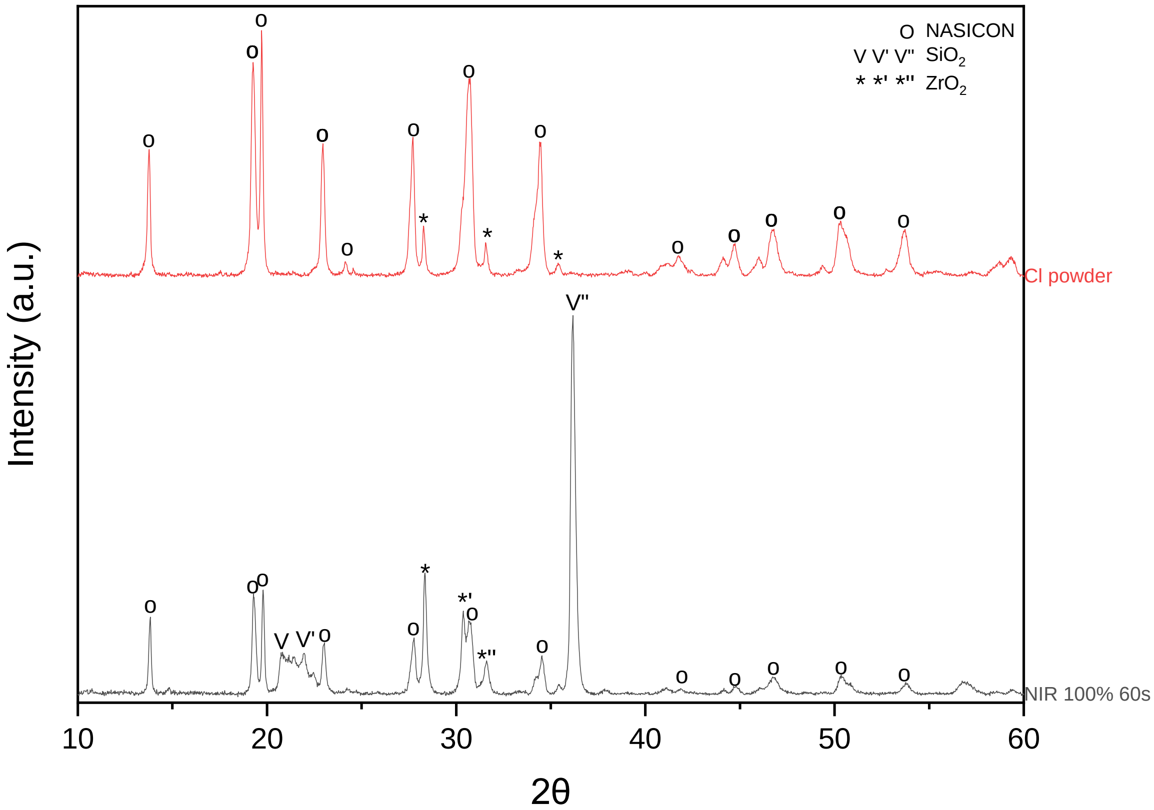

Figure 142: XRD of NASICON sol ($ZrOCl_2.8H_2O$) spray coated onto quartz (30 layers) and sintered conventionally at 1000°C; followed by a second spray coat (50 layers), heated in the oven at 750°C and sintered using the NIR at 100% for 60 seconds. Compared to the XRD of the NASICON sol chloride powder.

XRD data in Figure 142 compares the final NIR treated thin film sample with the NASICON powder equivalent. This shows that NASICON has formed after NIR treatment, as the characteristic NASICON (SG 15, COD 1529665[191]) peaks are present at 13.8°, 19.2°, 22.8°, 27.5°, 30.5°, 34.1°, 41°, 44°, 50.5° and 53°. Some ZrO_2 (SG 14, COD

2300544[208]; * / *") (SG 137, COD 1526427[220]; *') secondary phases are present at 28.3°, 31.4° and 30.3°. SiO_2 (SG 1, COD 9013393[214]) (SG 91, COD 9001578[215]) phases from the quartz substrate are also present at 20.6°, 21.7° and 36°. After the NIR treatment the black colouration has gone and the sample become white, suggesting the combustion reaction between the C and O_2 has occurred (DSC-TGA data) and confirming that NASICON has formed.

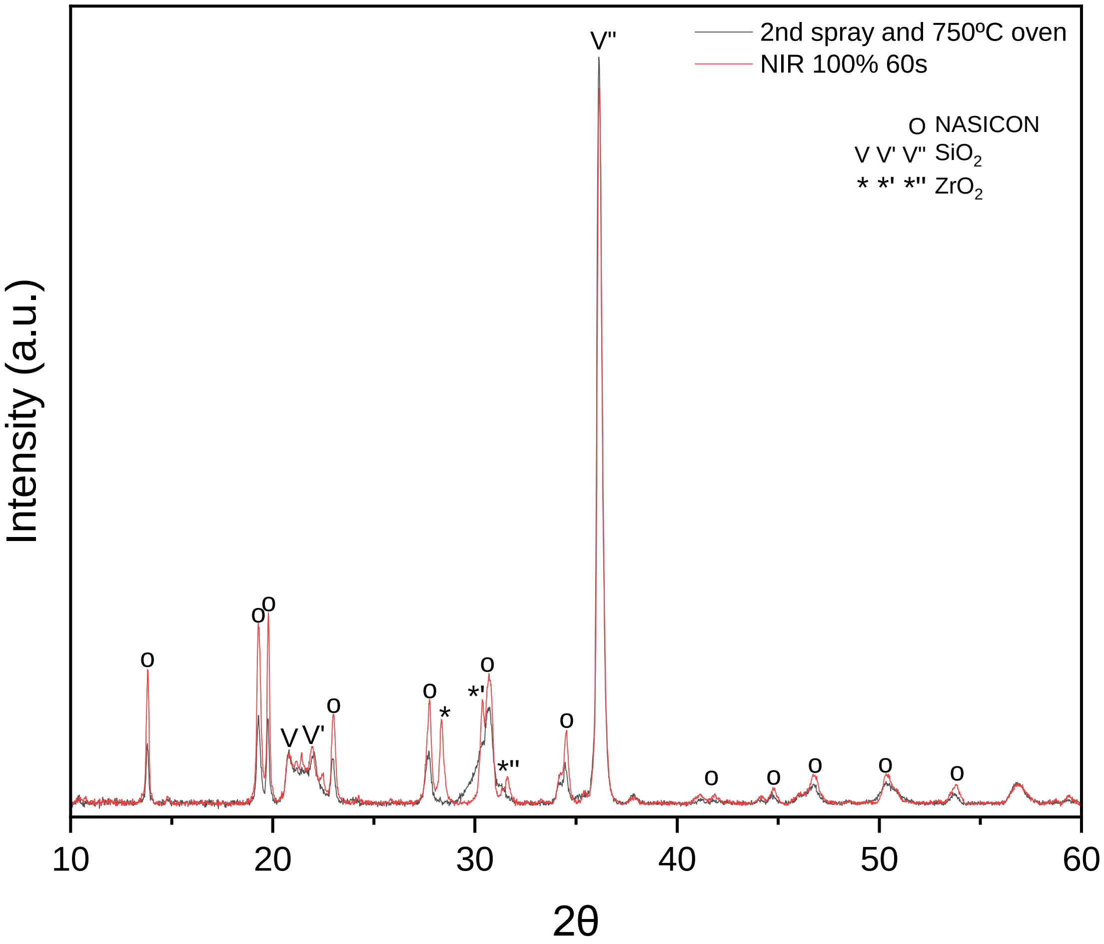

Figure 143: XRD of NASICON sol ($ZrOCl_2.8H_2O$) spray coated onto quartz. 1.5: 30 layers sintered conventionally at 1000°C; followed by a second spray coat (50 layers), heated in the oven at 750°C. 1.6: 30 layers sintered conventionally at 1000°C; followed by a second spray coat (50 layers), heated in the oven at 750°C and sintered using the NIR at 100% for 60 seconds.

The XRD data in Figure 143 compares the sample post the second spray and 750°C treatment, with the final NIR treated sample. The NASICON peaks at 13.8°, 19.2°, 22.8°, 27.5°, 30.5° and 34.1° have all almost doubled in intensity. As the intensity of the quartz secondary phase peaks at 20.6°, 21.7° and 35.5° have not increase by as much, this proves that NASICON has formed from the NIR treatment, which is a novel finding. Increasing the films thickness (30 + 50 coats) introduced more C into the film and improved the films ability to absorb NIR radiation; this in turn generated more energy in the combustion reaction, enabling sintering and NASICON phase formation.

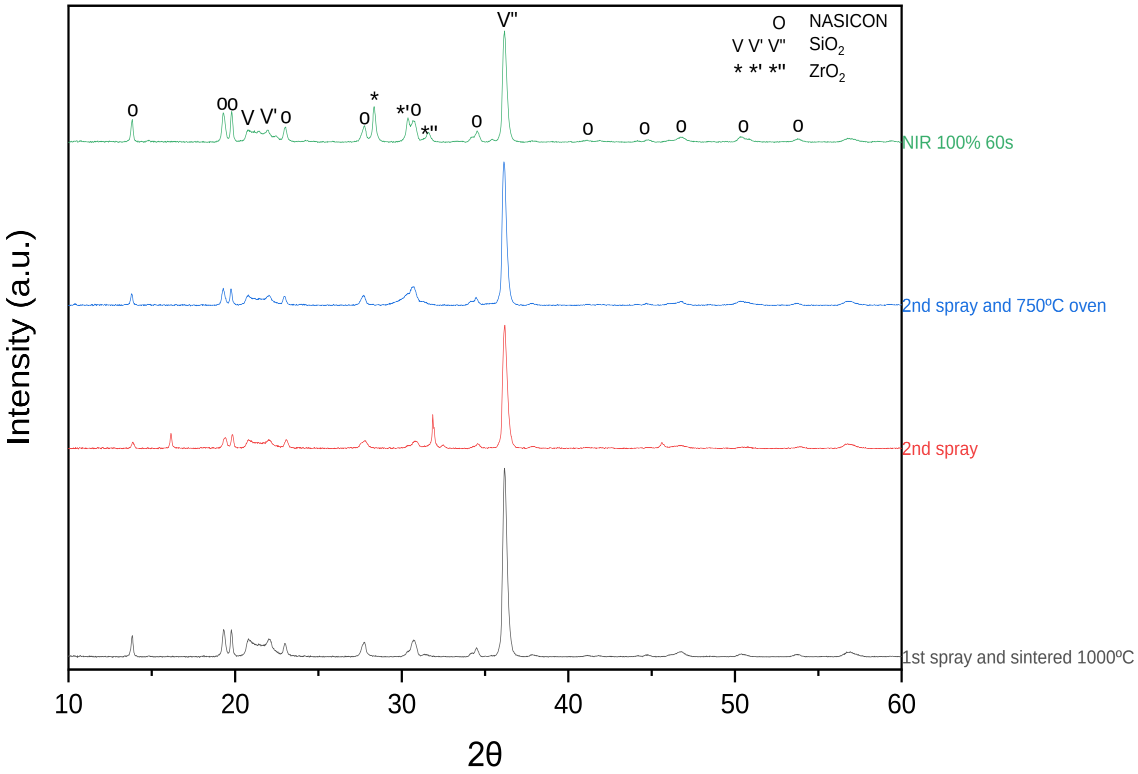

Figure 144: XRD of NASICON sol ZrOCl2.8H2O on a quartz substrate at different stages in the sintering process. Black 1.1: 30 layers sintered at 1000°C in conventional oven; Red 1.2: 30 layers sintered at 1,000°C in conventional oven, 2nd spray coat (50 layers); Blue 1.5: 30 layers sintered at 1,000°C in conventional oven, 2nd spray coat (50 layers) and heated at 750°C in conventional oven; Green 1.6: 30 layers sintered at 1,000°C in conventional oven, 2nd spray coat (50 layers) and heated at 750°C in conventional oven, sintered via NIR treatment at 100% for 60 seconds.

Figure 144 shows how the peaks differ after each step in the synthesis route. NASICON initially forms after the 1st conventional oven treatment at 1000°C. After the secondary spray coat the intensity of the NASICON peaks decrease slightly due to the precursor films on top. The peaks at 16.1° and 31.9° also appear in the XRD data at this stage, analysis suggests they could be SiO_2, Zr_3O or $Zr(SiO_4)$ phases. After the second 750°C oven treatment these two peaks are no longer present, and after the final NIR sintering step the NASICON peaks increase in intensity.

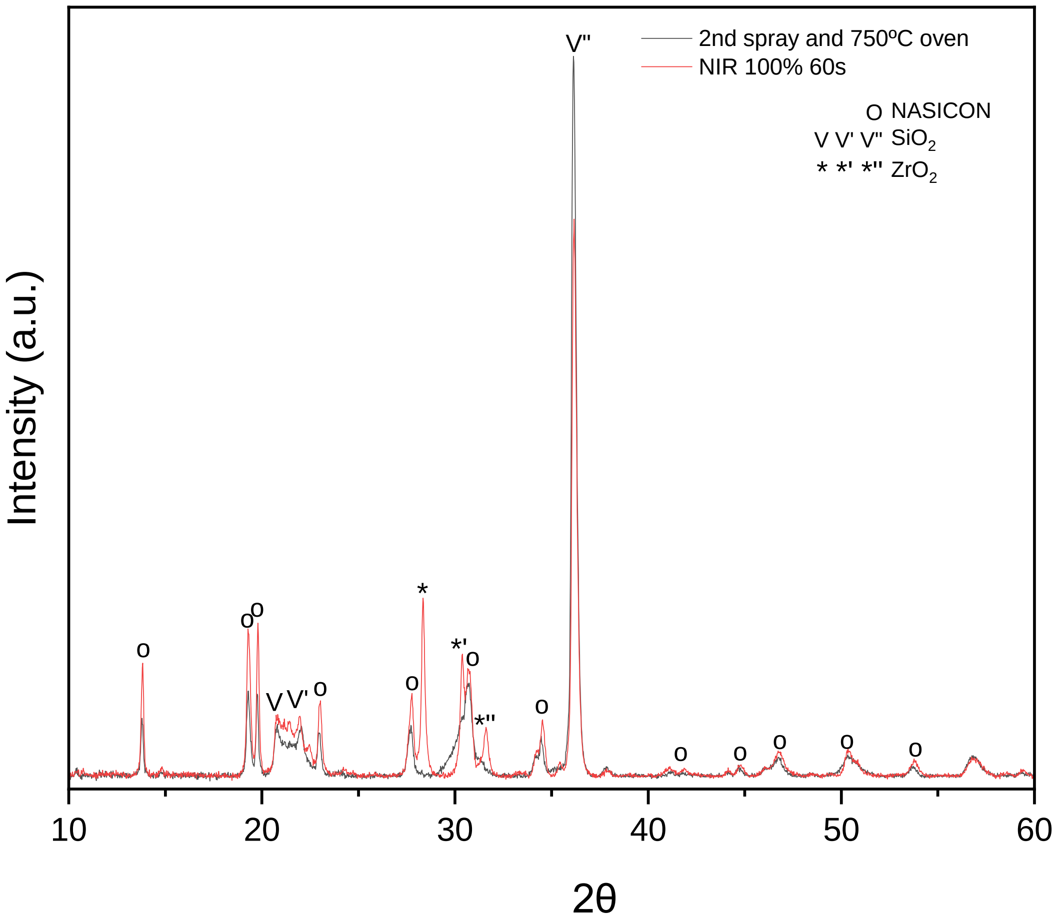

Figure 145: XRD of NASICON sol ($ZrOCl_2.8H_2O$) spray coated onto quartz. 1.5: 30 layers sintered conventionally at 1000°C; followed by a second spray coat (50 layers), heated in the oven at 750°C. 1.7: 30 layers sintered conventionally at 1000°C; followed by a second spray coat (50 layers), heated in the oven at 750°C and sintered using the NIR at 100% for 60 seconds.

Figure 145 is another sample synthesised using the exact same synthesis route. This sample proves the repeatability of the experiment, and how NIR absorption can be used to synthesise NASICON crystals. In the experiment the NASICON XRD peaks have also increased after the NIR treatment, and the intensity of the secondary phase peaks have remained the same or increased very slightly.

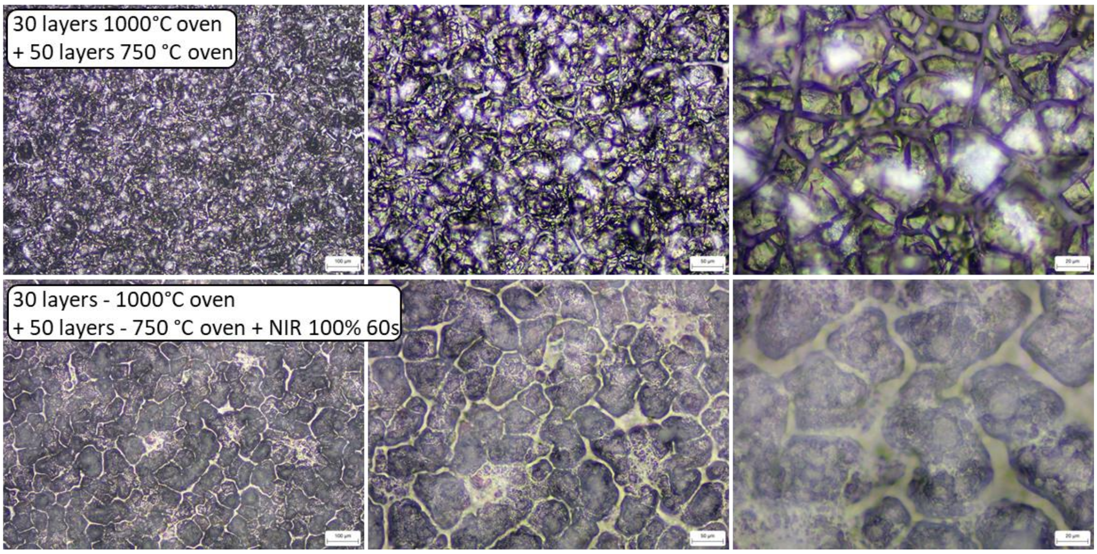

Figure 146: Optical microscope images of NASICON $ZrOCl_2.8H_2O$ sol spray coated on quartz (30 layers) and sintered at 1000°C, followed by a second spray coat (50 layers) and heated at 750°C, both in a conventional oven. Sample was then NIR treated at 100% for 60 seconds. Images at x10, x20 and x50 magnification.

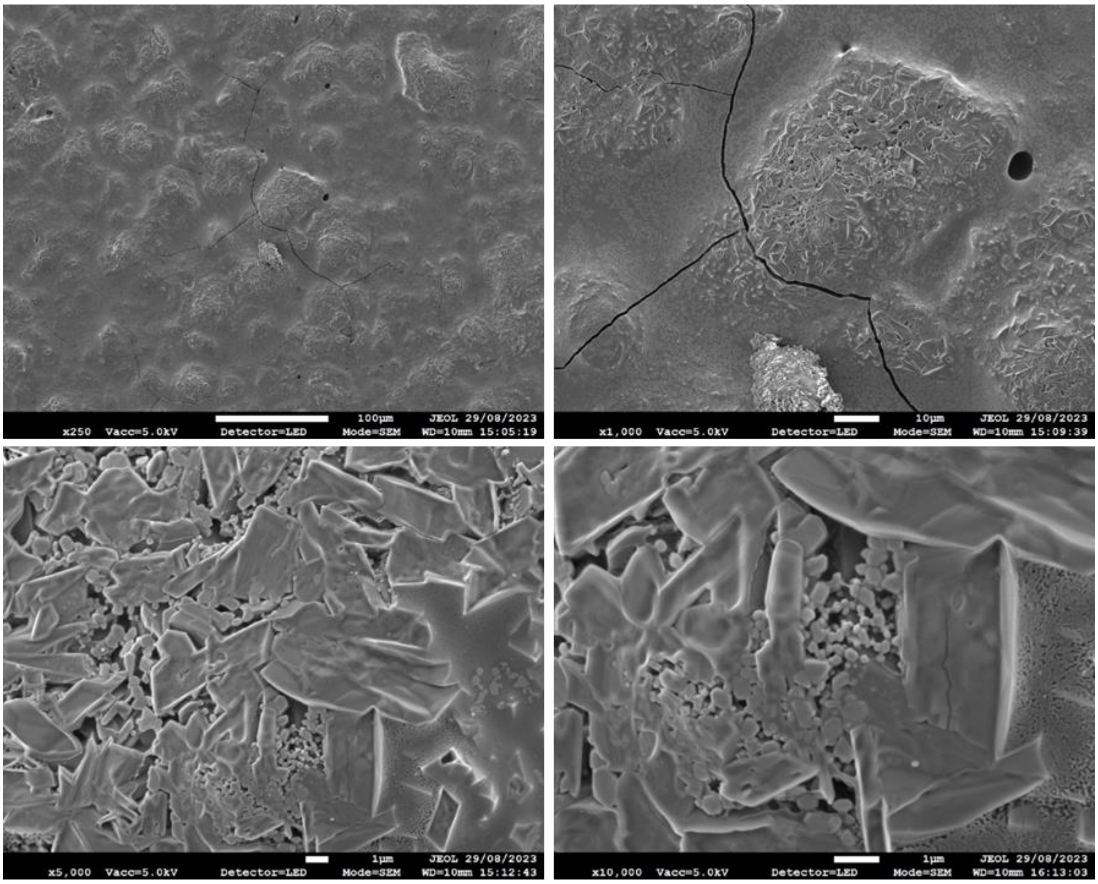

Figure 147: SEM images of NASICON $ZrOCl_2.8H_2O$ sol spray coated on quartz (30 layers) and sintered at 1000°C, followed by a second spray coat (50 layers) and heated at 750°C, both in a conventional oven. Sample was then NIR treated at 100% for 60 seconds. Images at x250, x1,000, x5,000 and x10,000 magnification.

Both the optical images (Figure 146) and SEM images (Figure 147) show the formation of islands. The SEM images show crystal formation in these islands, with the SiO_2 glassy phase between them, verifying the XRD data.

7.3.1 Oven sintering temperature of initiator layer

The aim of this experiment is to refine the previous work, examining the synthesis of the initiator layer to see if this alters the phase formation. The same synthesis steps are applied however it looks to sinter the initiator layer at a lower temperature (950°C, chosen from thermal XRD data in Chapter 6), in the hope that this can decrease the intensity of the SiO_2 phase. This work also synthesises the initiator layer without using tartaric acid as a precursor chemical, as this showed low secondary phases in the sol powder work in Chapter 5. The two experiments carried out were:

- 30 layers 1000°C oven, 50 layers 750°C oven and 100% 60s NIR
- 30 layers **950°C** oven, 50 layers 750°C oven and 100% 60s NIR

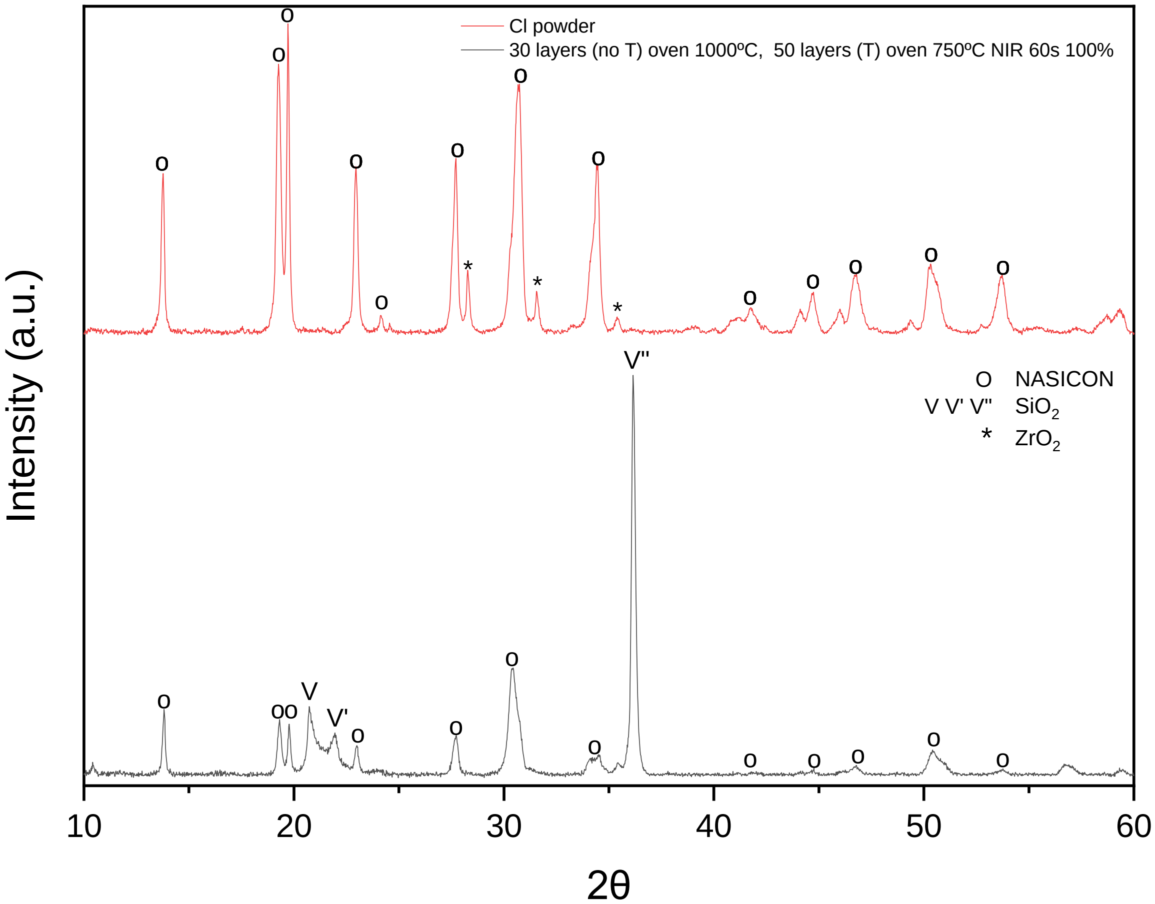

Figure 148: XRD of NASICON sol ($ZrOCl_2.8H_2O$ without tartaric acid) spray coated onto quartz (30 layers) and sintered conventionally at 1,000°C; followed by a second spray coat (50 layers), heated in the oven at 750°C and sintered using the NIR at 100% for 60 seconds. Compared to the XRD of the NASICON sol chloride powder.

Figure 148 shows that when using an initiator layer without tartaric acid present sintered at 1000°C, NASICON can form via NIR radiation. Analysis shows the NIR sample has less ZrO_2 secondary phase peaks compared to the chloride powder, however the SiO_2 phases are still present from the quartz substrate. ZrO_2 phases are present in the Cl powder due to the extended (3 hour) sintering times; and the SiO_2 phases are present in the thin film sample due to the conversion of the quartz at the surface of the substrate under NIR radiation.

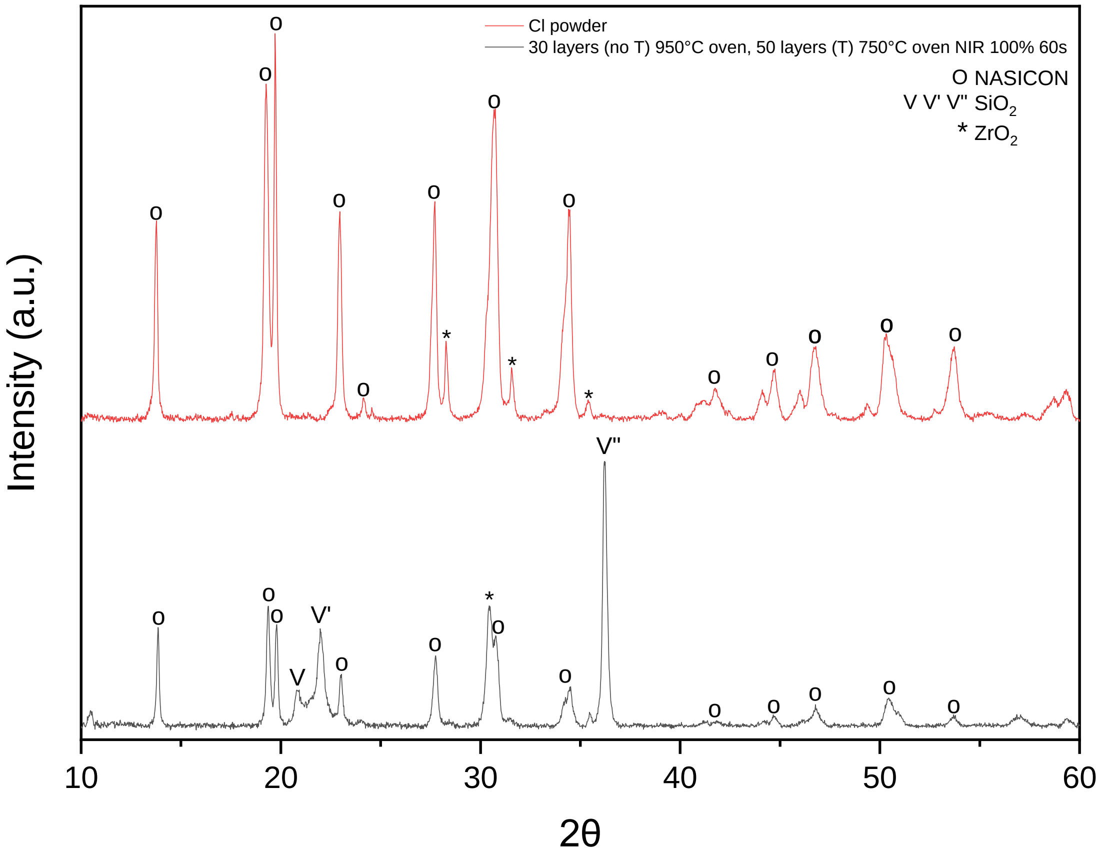

Figure 149: XRD of NASICON sol (ZrOCl2.8H2O without tartaric acid) spray coated onto quartz (30 layers) and sintered conventionally at 950°C; followed by a second spray coat (50 layers), heated in the oven at 750°C and sintered using the NIR at 100% for 60 seconds. Compared to the XRD of the NASICON sol chloride powder.

XRD data in Figure 149 data shows that NASICON does form when an initiator layer is synthesised at the lower temperature of 950°C and tartaric acid is not present. The intensity of the NASICON peaks after the NIR is much greater than the NASICON peaks in Figure 148 (1000°C initiator layer), however the intensity of the SiO_2 phase is very similar.

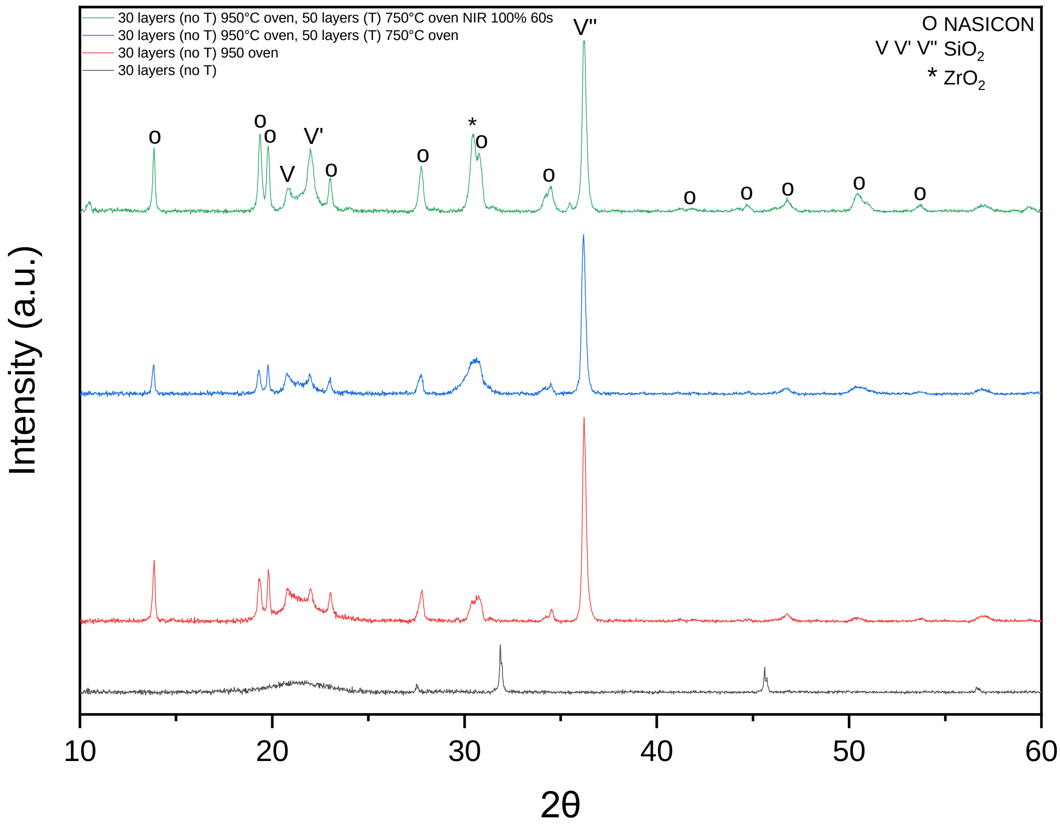

Figure 150: XRD of NASICON sol ($ZrOCl_2.8H_2O$ without tartaric acid) on a quartz substrate at different stages in the sintering process. Black: 30 layers not sintered; Red: 30 layers sintered at 950°C in conventional oven; Blue: 30 layers sintered at 950°C in conventional oven, 2nd spray coat (50 layers) and heated at 750°C in conventional oven; Green: 30 layers sintered at 950°C in conventional oven, 2nd spray coat (50 layers) and heated at 750°C in conventional oven, sintered via NIR treatment at 100% for 60 seconds.

Figure 150 shows the transformation of the thin film after each thermal treatment, illustrating that the intensity of the NASICON peaks increase after NIR radiation. This data continues to show the repeatability of this novel NIR synthesis method.

7.3.2 NIR % power

This experiment looks to expand upon the previous work, with the aim to determine whether the % power effects NIR NASICON sintering. As the last set of data proved NASICON can form using an initiator layer sintered at 950°C, this temperature has been selected for the initiator layer sintering, and tartaric acid is used as a precursor chemical (to stabilise the sol and improve spray coating technique). The following NIR settings were tested: 60%, 80% and 100% power, all for 60 seconds.

- 30 layers 950°C oven, 50 layers 750°C oven – 60%, 80% and 100% 60s NIR

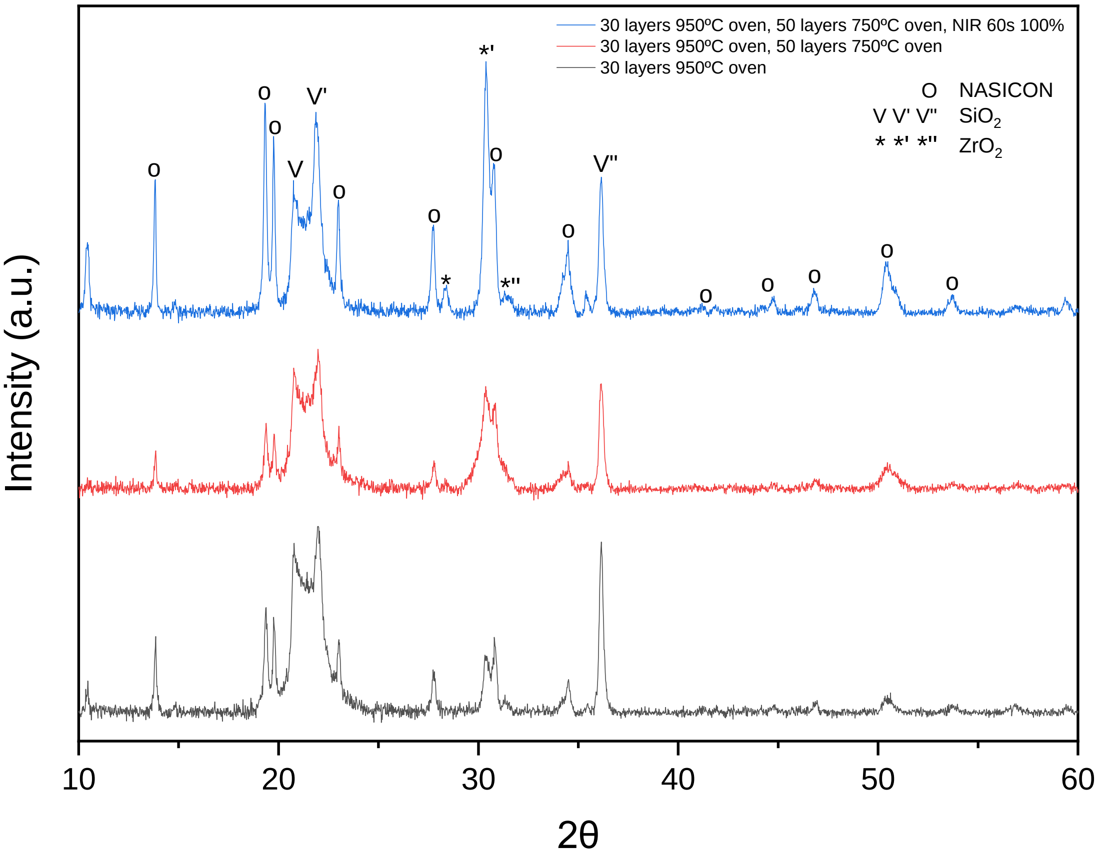

Figure 151: XRD of NASICON sol ($ZrOCl_2.8H_2O$) spray coated onto quartz at different stages in the sintering process. Black: 30 layers sintered at 950°C in conventional oven; Red: 30 layers sintered at 950°C in conventional oven, 2nd spray coat (50 layers) and heated at 750°C in conventional oven; Blue: 30 layers sintered at 950°C in conventional oven, 2nd spray coat (50 layers) and heated at 750°C in conventional oven, sintered via NIR treatment at 100% for 60 seconds.

Figure 151 shows that NASICON forms when the initiator layer is sintered at 950°C and a tartaric acid precursor chemical is used. In Figure 151 the intensity of the NASICON peaks increase after NIR. Secondary phases of ZrO_2 (28.3°, 30.3° and 31.4°) and the SiO_2

phases (20.6º, 21.7º and 35.5º) are present. More ZrO_2 phases are present in this XRD data for samples sintered in these conditions than previous samples. This could be due to ZrO_2 phases present in the initiator layer, causing the preferential growth of this phase in the subsequent layers.

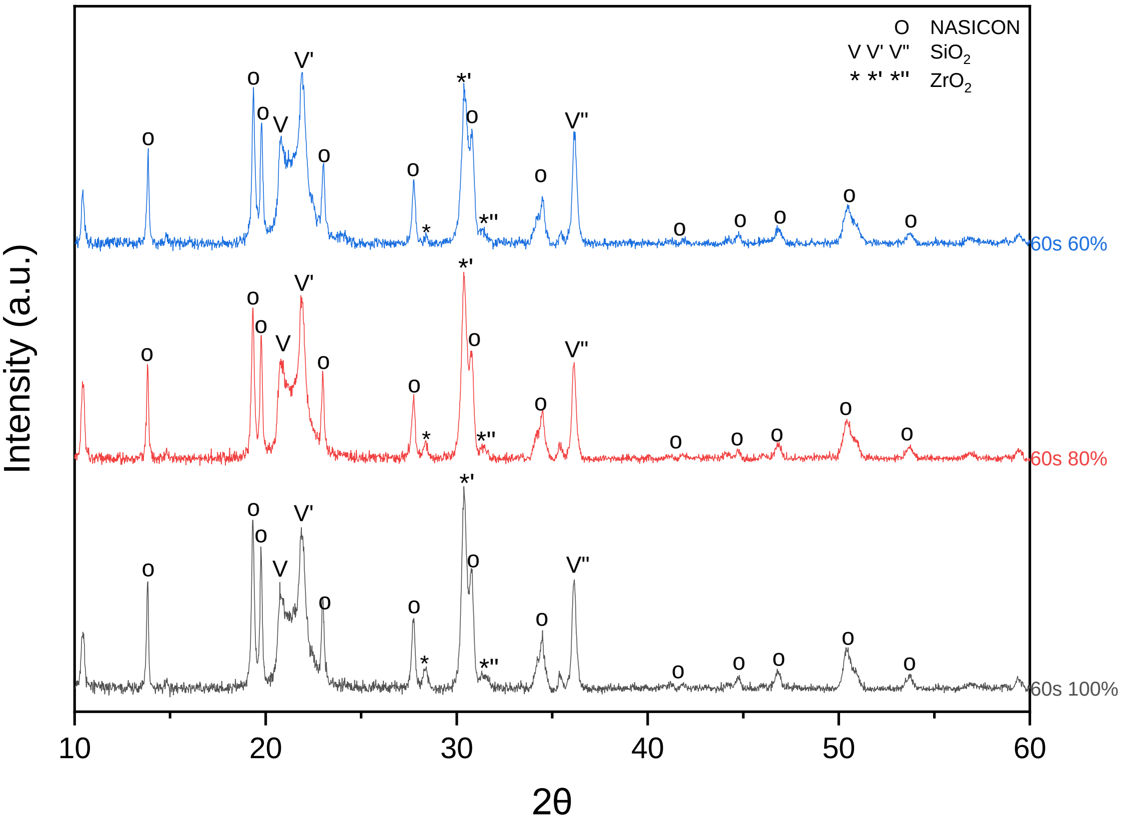

Figure 152: XRD of NASICON sol ($ZrOCl_2.8H_2O$) spray coated onto quartz (30 layers) and sintered conventionally at 950°C; followed by a second spray coat (50 layers), heated in the oven at 750°C, sintered at different NIR power percentages. Black: 100%; Red: 80%; Blue: 60%.

Figure 152 suggests that increasing or decreasing the NIR power during the final sintering step does not change the intensity of the NASICON XRD peaks significantly.

7.4 Using only NIR

The next stage is to utilise this initiator layer refined in the previous experiments to sinter NASICON, but without the high temperature conventional oven sintering step (at 950°C or 1000°C). The 750°C oven steps will continue to be employed to ensure the film has the black colour necessary to initiate sintering through NIR absorption. The initiator layer will also be used to help grain orientation, and a layer separation from the quartz substrate which could affect crystal growth due to its conversion at these temperatures.

The following synthesis method is used:

- 30 layers 750°C oven + **NIR 100% 60s**, 50 layers 750°C oven + 100% 60s NIR

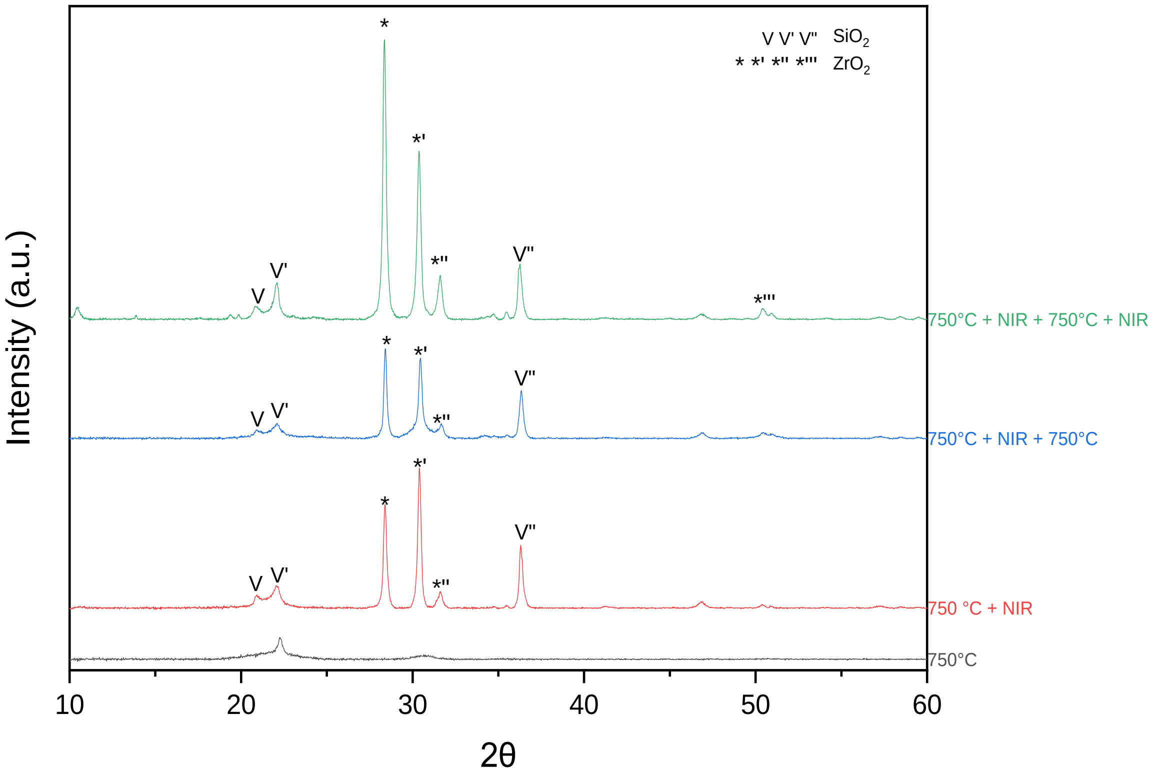

Figure 153: XRD of NASICON sol ($ZrOCl_2.8H_2O$ on a quartz substrate at different stages in the sintering process. Black: 30 layers heated at 750°C in conventional oven; Red: 30 layers heated at 750°C in oven, NIR treated at 100% 60s; Blue: 30 layers heated at 750°C in oven, NIR treated at 100% 60s; 2nd spray coat (50 layers) and heated at 750°C in conventional oven; Green: 30 layers heated at 750°C in oven, NIR treated at 100% 60s; 2nd spray coat (50 layers) and heated at 750°C in conventional oven, sintered via NIR treatment at 100% 60s.

NASICON does not form during the first NIR treatment as the film is not as opaque (black) at 30 layers, so does not absorb enough NIR.

Figure 153 shows the sample has not formed NASICON after the second NIR treatment, but formed the distinctive tetragonal (SG 137, COD 1526427[220]; *’ / *”’) and monoclinic (SG 14, COD 2300544[208]; * / *”) ZrO_2 peaks at 30.3º, 50.4º, 28.3º and 31.4º. Orthorhombic (SG 1, COD 9013393[214]; V) and tetragonal (SG 92, COD 9001578[215]; V’/V”) SiO_2 phases have also formed from the conversion of the quartz substrate at 20.6º, 21.7º and 36º. These peaks show that temperature of the sample has exceeded 1000°C using NIR, however NASICON phase formation has not occurred. At 19.2º NASICON crystal growth may have initiated, this suggests this particular sample did not reach a high enough temperature for long enough to sinter NASICON (60 s), potentially due to low C content. Therefore, a thicker film and longer NIR sintering times should be investigated in the future.

To determine if these non-NASICON phases are within the film or substrate XRD-GI characterisation was carried out on this sample.

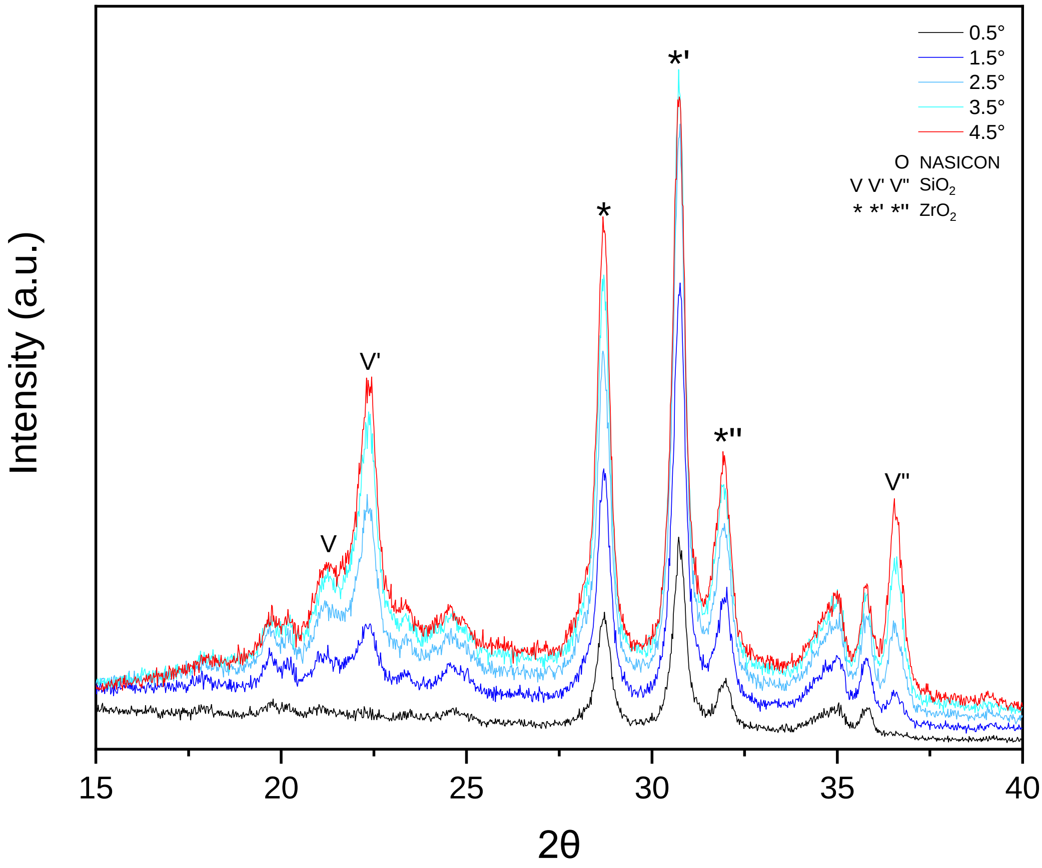

Figure 154: XRD-GI of thin film $ZrCl_2.8H_2O$ NASICON on quartz: 30 layers heated at 750°C in oven, NIR treated at 100% 60s; 2nd spray coat (50 layers) and heated at 750°C in conventional oven, sintered via NIR treatment at 100% 60s. XRD angles used are: 0.5°, 1.5°, 2.5°, 3.5° and 4.5°.

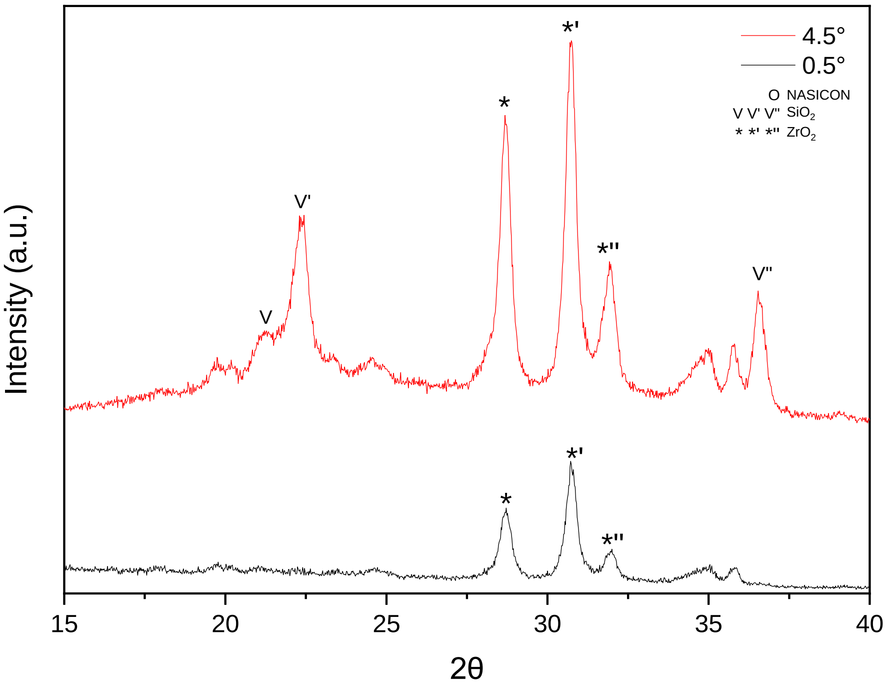

Figure 155: XRD-GI of thin film ZrCl2.8H2O NASICON on quartz: 30 layers heated at 750°C in oven, NIR treated at 100% 60s; 2nd spray coat (50 layers) and heated at

750°C in conventional oven, sintered via NIR treatment at 100% 60s. XRD angles used are: 0.5°and 4.5°

XRD-GI data in Figure 154 and Figure 155 show that at the lowest angle (0.5º, top layer) only the ZrO_2 peaks are present, suggesting these peaks are secondary phases within the film. The intensity of these three secondary phase peaks increases as the angle of the XRD increases. At increased angles (4.5º, substrate surface) the SiO_2 phase peaks are present, proving again that they are linked to the renucleation of the quartz substrate. This XRD-GI data implies that the crystal film phase is thin/broken, allowing the signal to come through and therefore shows a difference in texture compared to the oven samples.

The next set of experiments used the same parameters, however the % power of NIR used on the initiator layers is lower at 90%.

- 30 layers 750°C oven + **NIR 90% 60s**, 50 layers 750°C oven + 100% 60s NIR

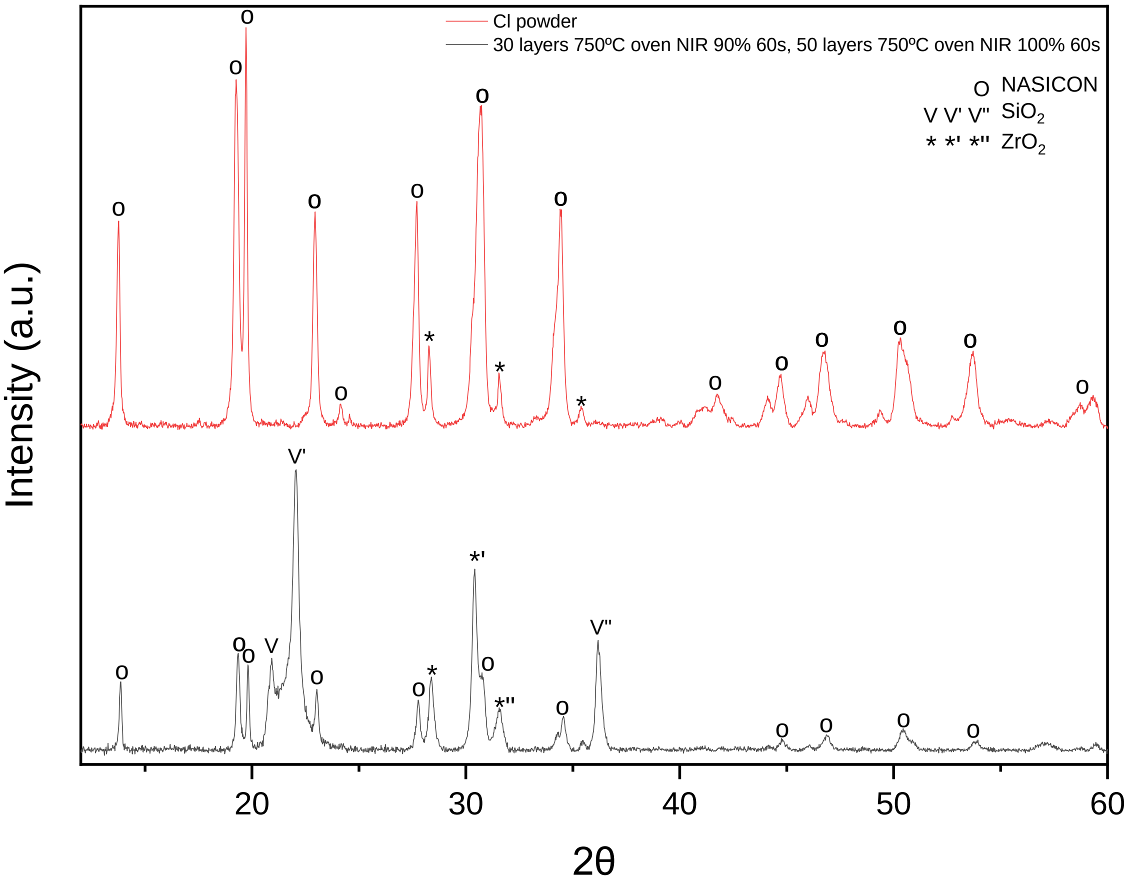

Figure 156: XRD of NASICON sol (ZrOCl2.8H2O) spray coated onto quartz (30 layers) and heated at 750°C and NIR treated at 90% for 60s; followed by a second spray coat (50 layers), heated in the oven at 750°C and sintered using the NIR at 100% for 60 seconds. Compared to the XRD of the NASICON sol chloride powder.

XRD data in Figure 156 shows that NASICON can be synthesised through NIR sintering alone, a completely novel innovation! This technique combines the power of NIR with the presence of carbon residue, increasing NIR absorption and facilitating NASICON crystallisation. XRD analysis showed NASICON (SG 15, COD 1529665[191]) peaks formed at 13.8º, 19.2º, 22.8º, 27.5º, 30.5º, 34.1º, 41º, 44º, 50.5º and 53º.

ZrO_2 (SG 14, COD 2300544[208]; * / *”) (SG 137, COD 1526427[220]; *’) secondary phase peaks are present in the film at 28.3º, 31.4º and 30.3º. NaCl evaporation occurs at high temperatures (Chapter 5) which could remove some Na from the NASICON structure, enabling ZrO_2 secondary phase formation. Therefore, future work could use a greater excess of Na precursors. Phases relating to the conversion of quartz occurring at 20.6º 21.7º and 36º, and are analysed as orthorhombic and tetragonal SiO_2 phases (SG 1, COD 9013393[214]; V) (SG 91, COD 9001578[215]; V’ and V”). The NIR samples have more zirconyl-based phases than the conventional oven thin film samples (Chapter 6), and the SiO_2 peak has a higher intensity in the conventional oven samples.

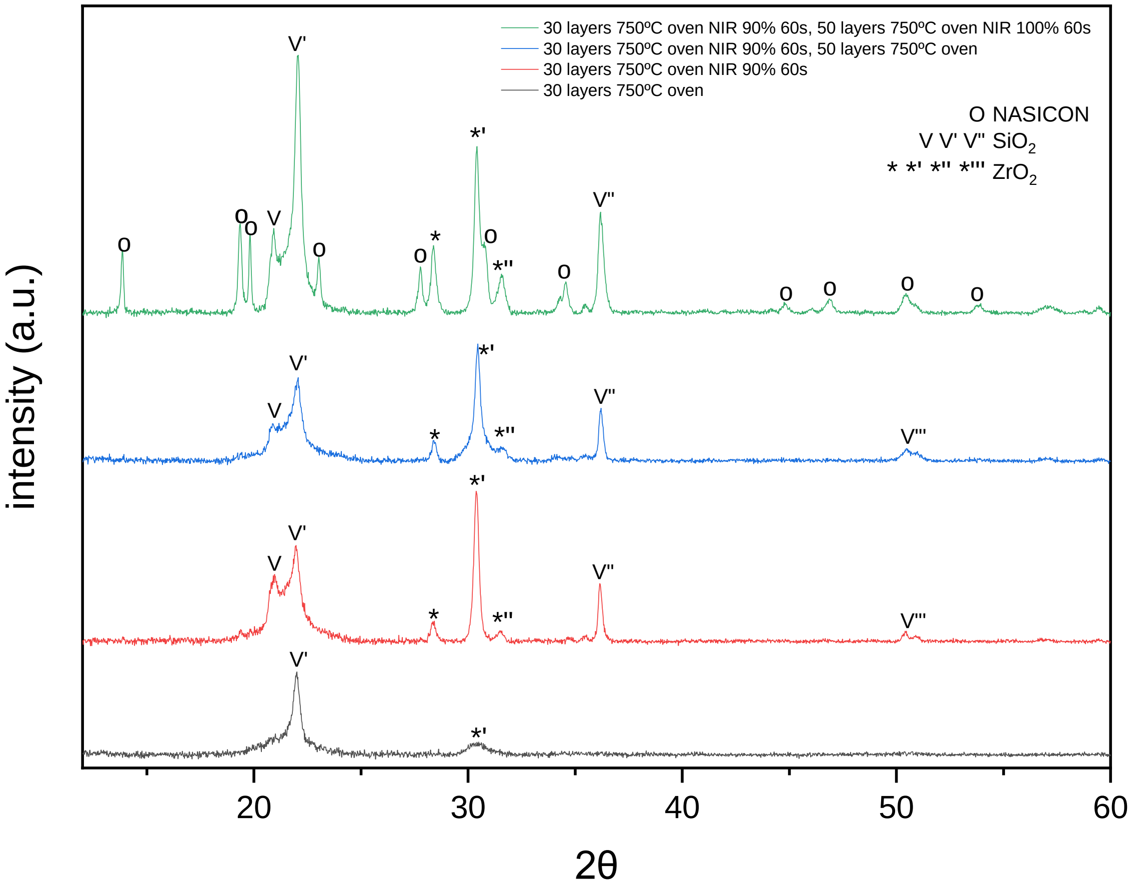

Figure 157: XRD of NASICON sol (ZrOCl2.8H2O) spray coated onto quartz at different stages in the sintering process. Black: 30 layers heated at 750°C in conventional oven; Red: 30 layers heated at 750°C in conventional oven, NIR treated at 90% for 60s; Blue: 30 layers heated at 750°C in conventional oven, NIR treated at 90% for 60s, 2nd spray coat (50 layers) and heated at 750°C in conventional oven; Green: 30 layers heated at 750°C in conventional oven, NIR treated at 90% for 60s, 2nd spray coat (50 layers) and heated at 750°C in conventional oven, sintered via NIR treatment at 100% for 60 seconds.

XRD data in Figure 157 shows that the ZrO_2 secondary phases are present after the first NIR treatment, however their intensity is a lot lower than those in Figure 153. This could influence the subsequent formation of NASICON, therefore the 90% NIR treatment forms an initiator phase that is more preferential for NASICON crystal growth in the subsequent layers. Furthermore, this sample potentially has a higher C content than the previous sample (Figure 153), enabling sintering.

NASICON formation occurs in this case because a thicker film (80 layers in total) is used, which absorbs more NIR (shown in UV-vis-NIR graph, Figure 127). This results in a higher carbon content in the film and therefore more energy in the combustion reaction, thus enabling higher temperatures for sintering and the formation of the NASICON phase.

Future work should investigate the influence of film thickness on NASICON formation using NIR radiation.

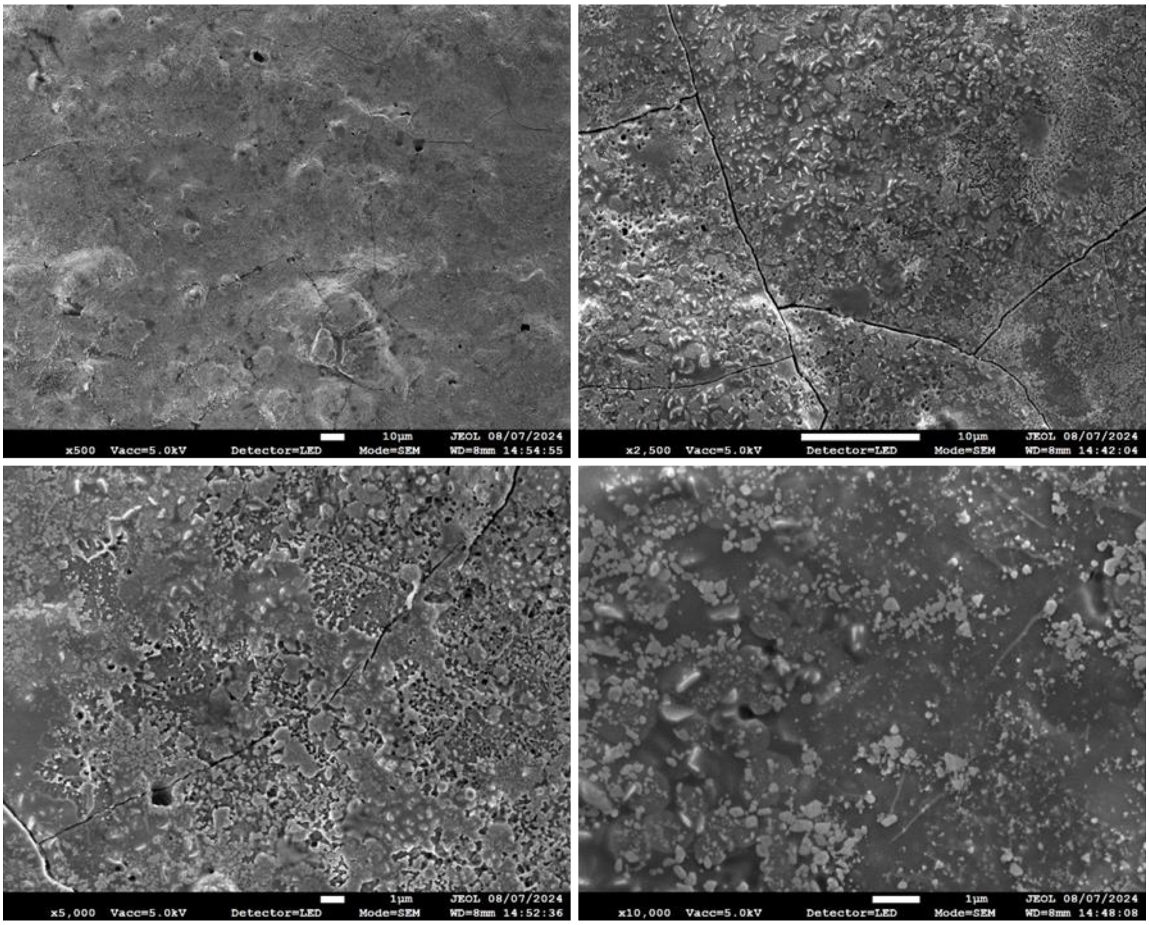

Figure 158: SEM images of successfully NIR sintered NASICON sol film on quartz.

The conventionally heated films showed islands of NASICON connected by SiO_2 glassy phases (Chapter 6). The NIR sintered film shown in Figure 158 is more uniform at the micron level; the SiO_2 and NAISCON phases are not as distinct. Furthermore, the particle size of the NIR samples appear smaller than the conventional oven equivalents. However, at the submicron level the SiO_2 phase is evident between the small NASICON grains.

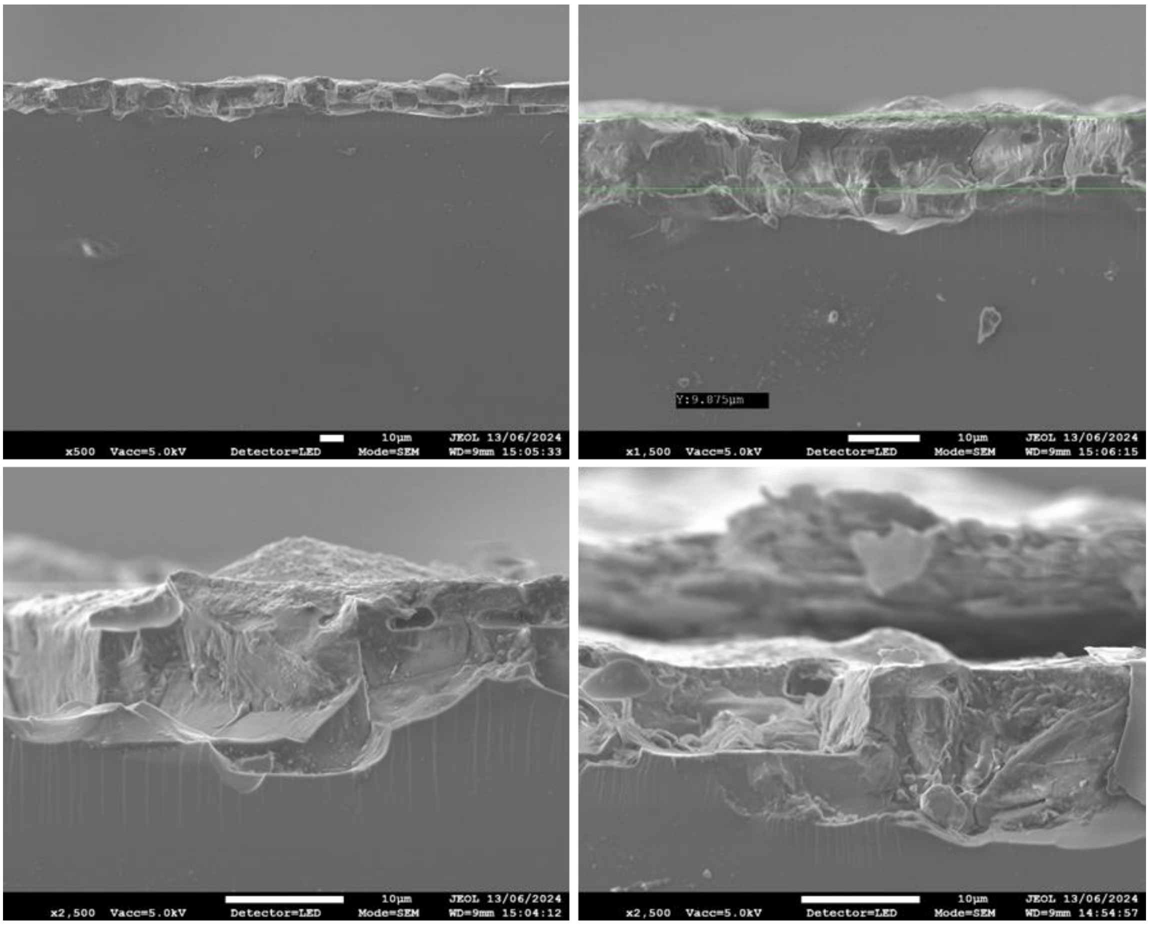

Figure 159: Cross-section SEM images of successfully NIR sintered NASICON sol film on quartz.

Cross section SEM images (Figure 159) show the film to be dense and roughly ~10 µm thickness. This is the same as the conventionally sintered samples, proving the spray coating technique is repeatable. The SEM images show 2 distinct layers, this could be a quartz and SiO_2 layer with NASICON islands on the surface, or quartz and a NASICON layer. A hypothesis for this could be due to the C content of the film during sintering. As stated in previous chapters, C hinders NASICON crystal growth. During NIR sintering carbon can be removed from the surface of the film more easily. Therefore, better crystal growth occurs at the surface and C is trapped at lower layer (close to quartz substrate).

This experiment demonstrates the first NASICON sintered by NIR, reducing the sintering time from 3 hours to 60s (Table 41).

Table 41: Illustrating the thermal treatments and NIR sintering times.

Synthesis steps	**Time**	**Heating Parameters**
Oven	1 hour	750ºC
NIR	60 seconds	90%
Oven	1 hour	750ºC
NIR	60 seconds	100%
Total sintering time	60 seconds	
Total heating time	2 hours 60 s	

7.4.1 Electrochemistry

EIS was performed on the NASICON sol thin film successfully sintered via 750°C conventional heating and NIR processing steps: 30 layers 750°C oven + **NIR 90% 60s**, 50 layers 750°C oven + 100% 60s NIR. The XRD data for the sample electrochemically analysed is in Figure 156. The EIS measurements were performed to evaluate the ionic conductivity relative to equivalent NASICON pellets reported in literature. The thin film dimensions required for EIS analysis are the same as those describe in Chapter 6 (Figure 122). For the NIR processed sample the values are: (t) = 0.25 cm, (A) = 2.5 x 10^{-3} cm^2 and (R_t) = 50 MΩ, determined from the EIS data.

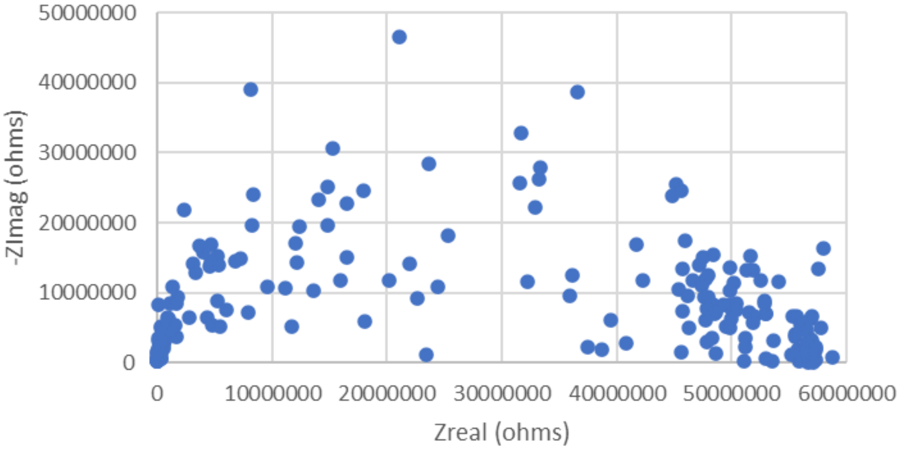

Figure 160: Nyquist plot of EIS data from NASICON thin film on quartz NIR sintered.

As the film is inhomogeneous the EIS data could not be modelled using Z-view, therefore a value from the Nyquist plot (Figure 160 and Figure 123) was used to approximate the ionic conductivity.

Equation 23

$$\sigma_t = \frac{t}{A\ x\ R_t} = \frac{0.25}{50\ x\ 10^6\ x\ 2.5\ x\ 10^{-3}} = 2\ x\ 10^{-6}\ Scm^{-1}$$

The ionic conductivity (2 x 10^{-6} Scm^{-1}, Equation 23) is in the same order of magnitude as the thin film EIS data in Chapter 6. However, it is considerably lower than the solid-state pellet data in Chapter 4 (1.95 x 10^{-3} Scm^{-1}) and further work must be carried out on the homogeneity of the film.

7.5 Conclusion

This work presents the first successful demonstration of NASICON thin films sintered using Near-Infrared Radiation (NIR). A novel process was developed utilising: a water-based precursor sol spray-coated onto quartz substrates, 750°C heat treatments and NIR radiation sintering. This 750°C heat step enabled the formation of a black carbon-rich intermediate film, which increased NIR absorption and enabled NASICON crystallisation.

This novel NIR method ensures rapid processing times, with faster NASICON sintering of 60 seconds, compared to conventional heating at >950°C for several hours in a conventional oven, reducing energy required. Sol thin film work took 3 hours to sinter compared to 60s NIR sintering, making this method x180 faster. This method could be used to sinter in-situ and reduce undesirable reactions with the electrode materials during sintering – due to the speed of sintering limiting time for diffusion. Furthermore, this method shows promise for applications in a wide range of ceramic coatings and is suitable for industrial scale up.

Future work needs to be done on film thickness, length of NIR sintering and film homogeneity to improve the conductivity of the film.

Chapter 8: Conclusions

8.1 Summary

This thesis has demonstrated the successful synthesis of NASICON through multiple innovative approaches.

The solid-state synthesis method yielded NASICON pellets with significantly improved phase purity compared to literature[79], as evidence by Rietveld refinement revealing only 1.5% ZrO_2 secondary phase formation (GOF Rwp 7.72% and χ^2 1.62). EIS measurements carried out showed a total ionic conductivity of 1.95 x 10^{-3} Scm^{-1} for the synthesised NASICON pellet, which aligns with the values reported in literature[79,175,195] (in the order of x 10^{-3} Scm^{-1}).

Furthermore, NASICON powder synthesis via the sol technique proved successful, with both chloride and nitrate precursor chemistries producing NASICON powder in alumina crucibles. The method resulted in NASICON formation at reduced conventional sintering temperatures (1000°C), with <2% ZrO_2 secondary phase formation comparable with literature values.[133,135,124]

A novel approach for NASICON thin film fabrication was developed, utilising water-based sol precursor chemicals (via particulate sol synthesis), spray coat deposition, and reaction phase sintering on quartz substrates. A NASICON thin film was successfully prepared and characterised using SEM and XRD. GI-XRD analysis attributed the non-NAISCON peaks at 20.6°, 21.7° and 36° to be SiO_2 phases linked to a quartz substrate reaction, and not a secondary phase within the NASICON itself.

Finally, this research presents the first successful demonstration of NASICON thin films sintering using NIR radiation. This innovative process incorporates a water-based precursor sol spray-coated onto quartz substrates, followed by 750°C heat treatments and NIR radiation sintering. The films were characterised as NASICON via XRD.

During this thesis there were several issues encountered and overcome to ensure NASICON formed via the solid-state or particulate sol synthesis methods.

The reaction of NASICON with the substrates/crucibles was a common issue for both solid-state and sol techniques. During the solid-state synthesis it was proven that the crucibles affected the composition of the NASICON formed during the sintering step, particularly Al^{3+} diffusion from alumina crucibles. A powder bed method was utilised and successfully synthesised NASICON as a free pellet using the solid-state technique. Furthermore, NASICON could not form on the alumina substrates as a thin film, due to the Al^{3+} diffusion, therefore quartz was utilised instead.

Quartz also caused issues during conventional and NIR sintering, as XRD data exhibited SiO_2 peaks. GI-XRD confirmed NASICON formed on-top of a SiO_2 structure, therefore the SiO_2 present was not a secondary phase within the NASICON. Therefore, the SiO_2 could be a transformation of just the quartz or an intermediate layer, on the surface of the substrate or the bottom part of the NASICON film. This could occur due to a higher temperature than 1000ºC being reached, due to the presence of carbon in the system causing an exothermic reaction (suggested by DSC-TGA data), or due to the presence of Na in NASICON lowering the quartz melting point and facilitating the formation of SiO_2 structure at a lower temperature than expected.

The high sintering temperature and its relation to secondary phases is a challenge in NASICON synthesis, therefore work in this thesis looked to determine the temperatures at which NASICON forms, preferably with low secondary phase compositions.

During the solid-state synthesis, characterisation at each processing step was carried out to determine the stage at which NASICON formation occurs. It was determined that chemical changes start to occur during the high temperature calcination step (1100°C) and NASICON is fully formed during the sintering step (1180°C or 1200°C), with densification at this stage. Secondary phases of ZrO_2 could have been reduced by optimising sintering time and temperature further, however 1.5% weight of ZrO_2 exceeded expectations from literature so was not a necessary parameter to refine.

For the sol thin film work thermal XRD experiments were used to determine the lowest temperature at which NASICON formed on quartz. Data showed NASICON can form at 950ºC (after 1 hour 45 minutes) and at 1000ºC (after 30 minutes) on the thermal stage but not at temperatures 900ºC and lower.

For the thin films sintered using NIR the temperature of the sample could not be measured during NIR sintering, yet analysis of the XRD data suggested that temperatures higher than 1000ºC were reached, due to the presence of SiO_2 phases. The synthesis also required the investigation of many NIR variables to enable the NAISCON formation, but was ultimately successful.

Both conventional and NIR sintered films contained ZrO_2 based secondary phases. It appeared ZrO_2 tetragonal secondary phases occurred at a lower sintering temperature or not enough sintering time, and ZrO_2 monoclinic phase formed at a higher temperature. The ZrO_2 secondary phase could be caused by NaCl evaporation, removing some Na from the structure and generating ZrO_2 secondary phases, therefore excess Na precursor chemicals could be used to reduce this.[196] This secondary phase could also be due to excessive temperatures being reached, which promotes ZrO_2 formation.[88,89,79] However, many tetragonal ZrO_2 phases formed via NIR sintering, suggesting the longer exposure times could be needed. Therefore, further work on NIR parameters for sintering is needed.

The temperature also affects film homogeneity, the films prepared conventionally and via NIR treatment were not homogeneous, therefore this is something to be looked at in the future.

Use of tartaric acid was also an area that needed attention, as introducing carbon changed the reaction mechanism and NASICON formation (DSC-TGA data). Cl without TA chemistry precursors formed the purest NASICON powder, meaning it had the lowest ZrO_2 secondary phases. However, without TA the sol is very unstable and starts to gel quickly, therefore TA is a necessary additive in thin film/spray coating work. Furthermore, it was found that at 750°C the formation of a black carbon-rich intermediate film formed due to the presence of TA, which increased NIR absorption and enabled NASICON crystallisation.

As described above the challenges of NASICON synthesis was overcome during the PhD, and the aims of the project were successfully carried out. This work has produced NASICON with low percentage secondary phases (<2%, Rietveld refinement) using both solid-state and sol synthesis techniques, with improved understanding of chemical mechanisms of the synthesis techniques through XRD, DSC-TGA and SEM analysis.

NASICON thin films were successfully conventionally synthesised using an innovative spray coating technique from water-based sol at reduced sintering temperatures of 950°C. A novel method of sintering NASICON as a thin film using near infrared radiation was successfully carried out, using a carbon intermediate to increase NIR absorption in thin film. The novel technique reduced sintering times from 3 hours (conventional thin film) to 60s (NIR thin film), x180 faster (Table 42). Sol NIR thin film work reduced processing times from 70 hours (solid state pellets) to 2 hours 2 mins (NIR thin film).

Table 42: Illustrating the processing/sintering times and temperatures employed to prepare NASICON during this thesis.

	Sintering time	**Sintering temp**	**Total oven + NIR time**
Solid-state pellet	16 hours	1180 °C	70 hours
Sol Powder	3 hours	1000 °C	16 hours
Sol thin film	3 hours	950 °C	3 hours
Sol thin film NIR	60 seconds	NIR 90% + 100% power	2 hours + 2 mins

This novel NIR method ensures rapid processing times, with faster NASICON sintering of 60 seconds, compared to conventional heating at >950°C for several hours in a conventional oven, reducing energy required. This method shows proof of concept that NIR thin films could be used to sinter electrolyte materials in Na-ion batteries in-situ. This could reduce undesirable reactions with the electrode materials during sintering – due to the speed of sintering limiting time for diffusion. Furthermore, this method shows promise for applications in a wide range of ceramic coatings and is suitable for industrial scale up.

8.2 Further work

Further work to arise from this thesis should involve the sol thin film technique as this has the most promise. As alluded to above, three areas of this work need further work.

Firstly, to reduce the conversion of the quartz substrate generating the SiO_2 XRD peaks. Initial experiments on increasing film thickness have looked promising, using the conventional oven and NIR exposure decreased the SiO_2 peaks. However, this may not reduce the conversion of SiO_2 but increase the NASICON synthesised above, more GI-XRD experiments need to be done to verify this. Other substrates could also be tested that interact less with the high temperatures and NASICON, as well as testing substrates that are similar to the Na-ion battery electrodes (if utilised for this application).

Film homogeneity needs to progress to improve the conductivity of the NASICON thin films. Processing temperatures, pH, film thickness, and types of solvents used are all areas of investigation that could improve the homogeneity of the film. Once a homogenous film is formed conventionally and through NIR sintering, then the conductivity of thin films can be analysed.

Thirdly, more repeats of the NIR work should be carried out with the application of a non-contact temperature probe to understand the temperatures being reached by the samples. Once this is understood more detailed evaluation of NIR parameters need further testing and refinement for sintering, including length of time and % power needed to synthesise NASICON.

If these three challenges are overcome work must be done to in-situ sinter NASICON on an electrode. The carbon in the electrodes may help or hinder NASICON formation via NIR sintering, as C prohibits NASICON growth but also enables NIR sintering through absorption. An interlayer may be used if the concentration of C is a limiting factor, and more stable glassy carbons could be used in the electrodes.

Energy calculations for the NIR technique compared to the conventional sintering of thin films would also be useful data to collate in the future.

Bibliography

1 *Net Zero Technical report*, 2019.

2 S. H. Kim, J. H. Kim, S. J. Cho and S. Y. Lee, *Adv. Energy Mater.*, 2019, **9**, 1–10.

3 A. S. Rao, K. R. Rashmi, D. V. Manjunatha, A. Jayarama, S. Prabhu and R. Pinto, *Int. J. Hydrogen Energy*, 2019, **44**, 23762–23774.

4 Z. Yang, Y. Luo, X. Gao and R. Wang, *ChemElectroChem*, 2020, **7**, 2599–2607.

5 E. Scoccimarro, O. Cattaneo, S. Gualdi, F. Mattion, A. Bizeul, A. M. Risquez and R. Quadrelli, *Commun. Earth Environ.*, 2023, **4**, 208.

6 J. P. Holdren, *Popul. Environ.*, 1991, **12**, 231–255.

7 K. Dong, G. Hochman, Y. Zhang, R. Sun, H. Li and H. Liao, *Energy Econ.*, 2018, **75**, 180–192.

8 S. Feng and I. Lazkano, *Energy Policy*, 2025, **198**, 114447.

9 X. Liu, S. Chen, Z. Xiong, K. Li and Y. Zhang, *Prog. Mater. Sci.*, 2022, **130**, 100978.

10 M. Winter and R. J. Brodd, *Chem. Rev.*, 2004, **104**, 4245–4270.

11 L. Castel, How to Improve the Performance of Sodium-ion Batteries Using Various Carbon Anodes Designs, https://www.azom.com/article.aspx?ArticleID=22278.

12 P. Kurzweil, *J. Power Sources*, 2010, **195**, 4424–4434.

13 V. Deshpande, C. Doerrer, M. S. Dyer, H. El-shinawi, N. Fleck, J. T. S. Irvine, H. J. Lee, G. Li, E. Liberti, I. Mcclelland, C. I. Thomas, S. J. Turrell, M. Vestli and C. K. Williams, *J. Phys. Energy*, 2020, **2**, 0–52.

14 Nature Editorial, *Nature*, 2021, **595**, 7–7.

15 A. M. Domingues, R. G. de Souza and J. V. R. Luiz, *Energy Res. Soc. Sci.*, 2024, **118**, 103756.

16 M. S. Ziegler and J. E. Trancik, *Energy Environ. Sci.*, 2021, **14**, 1635–1651.

17 M. S. Ziegler, J. Song and J. E. Trancik, *Energy Environ. Sci.*, 2021, **14**, 6074–6098.

18 A. Yao, S. M. Benson and W. C. Chueh, *Nat. Energy*, DOI:10.1038/s41560-024-01701-9.

19 K. Mukai, T. Inoue, Y. Kato and S. Shirai, *ACS Omega*, 2017, **2**, 864–872.

20 L. Xiang, X. Li, J. Xiao, L. Zhu and X. Zhan, *Adv. Powder Mater.*, 2024, **3**, 100181.

21 C. Vaalma, D. Buchholz, M. Weil and S. Passerini, *Nat. Rev. Mater.*, 2018, **3**, 18013.

22 M. T. Castro, M. R. B. Domalanta, J. A. D. R. Paraggua and J. D. Ocon, *J. Energy Storage*, 2024, **94**, 112414.

23 A. Rudola, R. Sayers, C. J. Wright and J. Barker, *Nat. Energy*, 2023, **8**, 215–218.

24 H. Che, S. Chen, Y. Xie, H. Wang, K. Amine, X. Z. Liao and Z. F. Ma, *Energy Environ. Sci.*, 2017, **10**, 1075–1101.

25 L. Zhang, Y. Liu, Y. You, A. Vinu and L. Mai, *Interdiscip. Mater.*, 2023, **2**, 91–110.

26 L. Zhang, Y. Liu, Y. You, A. Vinu and L. Mai, *Interdiscip. Mater.*, 2023, **2**, 91–110.

27 Z. Moradi, A. Lanjan, R. Tyagi and S. Srinivasan, *J. Energy Storage*, 2023, **73**, 109048.

28 A. Mahmoudzadeh Andwari, A. Pesiridis, S. Rajoo, R. Martinez-Botas and V. Esfahanian, *Renew. Sustain. Energy Rev.*, 2017, **78**, 414–430.

29 J. Ma, B. Chen, L. Wang and G. Cui, *J. Power Sources*, 2018, **392**, 94–115.

30 J.-J. Kim, K. Yoon, I. Park and K. Kang, *Small Methods*, 2017, **1**, 1700219.

31 X. Gao, Z. Xing, M. Wang, C. Nie, Z. Shang, Z. Bai, S. X. Dou and N. Wang, *Energy Storage Mater.*, 2023, **60**, 102821.

32 L. Zhang, P. Zhang, C. Chang, W. Guo, Z. H. Guo and X. Pu, *ACS Appl. Mater. Interfaces*, 2021, **13**, 46794–46802.

33 Y. L. Ni'Mah, M. Y. Cheng, J. H. Cheng, J. Rick and B. J. Hwang, *J. Power Sources*, 2015, **278**, 375–381.

34 M. M. E. Jacob, S. R. S. Prabaharan and S. Radhakrishna, *Solid State Ionics*, 1997, **104**, 267–276.

35 Z. Moradi, A. Lanjan, R. Tyagi and S. Srinivasan, *J. Energy Storage*, 2023, **73**, 109048.

36 G. Åvall and P. Johansson, *J. Chem. Phys.*, DOI:10.1063/5.0005397.

37 N. Tapia-ruiz, A. R. Armstrong, H. Alptekin, M. A. Amores, H. Au, J. Barker, R. Boston, W. R. Brant, J. M. Brittain, Y. Chen, M. Chhowalla, Y. Choi, S. I. R. Costa, M. C. Ribadeneyra, S. A. M. Dickson, E. I. Eweka, J. D. Forero-saboya, C. P. Grey, Z. Li, S. F. L. Mertens, R. Mogensen, L. Monconduit, D. M. C. Ould, R. G. Palgrave, P. Poizot, A. Ponrouch, S. Renault, E. M. Reynolds, A. Rudola, R. Sayers, D. O. Scanlon, S. Sen, V. R. Seymour, B. Silv, G. S. Stone, C. I. Thomas, M. Titirici, J. Tong, T. J. Wood, D. S. Wright and R. Younesi, *J. Phys. Energy*, 2021, **3**, 031503.

38 Z. Gao, H. Sun, L. Fu, F. Ye, Y. Zhang, W. Luo and Y. Huang, *Adv. Mater.*, DOI:10.1002/adma.201705702.

39 V. Thangadurai, H. Kaack and W. J. F. Weppner, *J. Am. Ceram. Soc.*, 2003, **86**, 437–440.

40 J. Awaka, N. Kijima, H. Hayakawa and J. Akimoto, *J. Solid State Chem.*, 2009, **182**, 2046–2052.

41 R. Murugan, V. Thangadurai and W. Weppner, *Angew. Chemie Int. Ed.*, 2007, **46**, 7778–7781.

42 E. J. Cussen, *J. Mater. Chem.*, 2010, **20**, 5167–5173.

43 V. Thangadurai and W. Weppner, *Adv. Funct. Mater.*, 2005, **15**, 107–112.

44 F. Zheng, M. Kotobuki, S. Song, M. O. Lai and L. Lu, *J. Power Sources*, 2018, **389**, 198–213.

45 S. Akhtar, W. Lee, M. Kim, M. S. Park and W. S. Yoon, *J. Electrochem. Sci. Technol.*, 2021, **12**, 1–20.

46 Q. Abbas, M. Mirzaeian, A.-G. Olabi and D. Gibson, in *Encyclopedia of Smart Materials*, Elsevier, 2021, pp. 382–392.

47 B. Dunn, H. Kamath and J.-M. Tarascon, *Science (80-.).*, 2011, **334**, 928–935.

48 H.-L. Yang, B.-W. Zhang, K. Konstantinov, Y.-X. Wang, H.-K. Liu and S.-X. Dou, *Adv. Energy Sustain. Res.*, DOI:10.1002/aesr.202000057.

49 T. Famprikis, P. Canepa, J. A. Dawson, M. S. Islam and C. Masquelier, *Nat. Mater.*, 2019, **18**, 1278–1291.

50 K. Xu, *Chem. Rev.*, 2004, **104**, 4303–4417.

51 Y. Lu, L. Li, Q. Zhang, Z. Niu and J. Chen, *Joule*, 2018, **2**, 1747–1770.

52 L. Fan, S. Wei, S. Li, Q. Li and Y. Lu, *Adv. Energy Mater.*, 2018, **8**, 1702657.

53 J. Kim, K. Yoon, I. Park and K. Kang, *Small Methods*, DOI:10.1002/smtd.201700219.

54 H. Peng, Y. Fang, J. Wang, P. Ruan, Y. Tang, B. Lu, X. Cao, S. Liang and J. Zhou, *Matter*, 2022, **5**, 4363–4378.

55 R. Koerver, I. Aygün, T. Leichtweiß, C. Dietrich, W. Zhang, J. O. Binder, P. Hartmann, W. G. Zeier and J. Janek, *Chem. Mater.*, 2017, **29**, 5574–5582.

56 E. J. Cheng, A. Sharafi and J. Sakamoto, *Electrochim. Acta*, 2017, **223**, 85–91.

57 L. Wang, D. Liu, T. Huang, Z. Geng and A. Yu, *RSC Adv.*, 2020, **10**, 10038–10045.

58 P. Kehne, C. Guhl, Q. Ma, F. Tietz, L. Alff, R. Hausbrand and P. Komissinskiy, *J. Power Sources*, 2019, **409**, 86–93.

59 Z. Geng, Y. Huang, G. Sun, R. Chen, W. Cao, J. Zheng and H. Li, *Nano Energy*, 2022, **91**, 106679.

60 J. M. Valle, C. Huang, D. Tatke, J. Wolfenstine, W. Go, Y. Kim and J. Sakamoto, *Solid State Ionics*, DOI:10.1016/j.ssi.2021.115712.

61 S. M. Lee, S. T. Lee, D. H. Lee, S. H. Lee, S. S. Han and S. K. Lim, *J. Ceram. Process. Res.*, 2015, **16**, 49–53.

62 B. Santhoshkumar, D. L.R. Khanna, M. B. Choudhary, P. Lokeswara Rao, K. V. Ramanathan, A. K. Bera, S. M. Yusuf and B. Pahari, *Chem. Phys. Lett.*, 2021, **776**, 1–8.

63 H. Park, K. Jung, M. Nezafati, C. S. Kim and B. Kang, *ACS Appl. Mater. Interfaces*, 2016, **8**, 27814–27824.

64 Y. B. Rao and L. N. Patro, .

65 A. Martucci, S. Sartori, M. Guglielmi, M. L. Di Vona, S. Licoccia and E. Traversa, *J. Eur. Ceram. Soc.*, 2002, **22**, 1995–2000.

66 S. Narayanan, S. Reid, S. Butler and V. Thangadurai, *Solid State Ionics*, 2019, **331**, 22–29.

67 H. .-P. Hong, DOI:https://doi.org/10.1016/0025-5408(78)90075-2.

68 F. Sudreau, D. Petit and J. P. Boilot, 1989, **90**, 78–90.

69 Z. Deng, J. Gu, Y. Li, S. Li, J. Peng, X. Li, J. Luo, Y. Huang, C. Fang, Q. Li, J. Han, Y. Huang and Y. Zhao, *Electrochim. Acta*, 2019, **298**, 121–126.

70 T. Lan, C. L. Tsai, F. Tietz, X. K. Wei, M. Heggen, R. E. Dunin-Borkowski, R. Wang, Y. Xiao, Q. Ma and O. Guillon, *Nano Energy*, 2019, **65**, 104040.

71 H. Gao, L. Xue, S. Xin, K. Park and J. B. Goodenough, *Angew. Chemie Int. Ed.*, 2017, **56**, 5541–5545.

72 M. A. Sawhney, M. Wahid, S. Muhkerjee, R. Griffin, A. Roberts, S. Ogale and J. Baker, *ChemPhysChem*, DOI:10.1002/cphc.202100860.

73 J.B. Goodenough, H.Y-P. Hong, J.A. Kafalas, *Mater. Res. Bull.*, DOI:https://doi.org/10.1016/0025-5408(76)90077-5.

74 H. .-P. Hong, *Mater. Res. Bull.*, 1976, **11**, 173–182.

75 Y. Noguchi, E. Kobayashi, L. S. Plashnitsa, S. Okada and J. I. Yamaki, *Electrochim. Acta*, 2013, **101**, 59–65.

76 G. Paściak, W. Mielcarek, K. Prociów and J. Warycha, *Ceram. Int.*, 2014, **40**, 12783–12787.

77 J. W. Fergus, *Solid State Ionics*, 2012, **227**, 102–112.

78 N. Anantharamulu, K. Koteswara Rao, G. Rambabu, B. Vijaya Kumar, V. Radha and M. Vithal, *J. Mater. Sci.*, 2011, **46**, 2821–2837.

79 A. Jalalian-Khakshour, C. O. Phillips, L. Jackson, T. O. Dunlop, S. Margadonna and D. Deganello, *J. Mater. Sci.*, 2020, **55**, 2291–2302.

80 M. L. Di Vona, S. Licoccia, L. Montanaro and E. Traversa, *Chem. Mater.*, 1999, **11**, 1336–1341.

81 S. Song, H. M. Duong, A. M. Korsunsky, N. Hu and L. Lu, *Sci. Rep.*, 2016, **6**, 1–10.

82 M. Guin and F. Tietz, *J. Power Sources*, 2015, **273**, 1056–1064.

83 Z. Liang, F. Du, N. Zhao and X. Guo, *Chinese J. Struct. Chem.*, 2023, **42**, 100108.

84 Z. Zhang, Z. Zou, K. Kaup, R. Xiao, S. Shi, M. Avdeev, Y. S. Hu, D. Wang, B. He, H. Li, X. Huang, L. F. Nazar and L. Chen, *Adv. Energy Mater.*, 2019, **9**, 1–14.

85 M. Amores, P. J. Baker, E. J. Cussen and S. A. Corr, *Chem. Commun.*, 2018, **54**, 10040–10043.

86 Z. Deng, G. Sai Gautam, S. K. Kolli, J. N. Chotard, A. K. Cheetham, C. Masquelier and P. Canepa, *Chem. Mater.*, 2020, **32**, 7908–7920.

87 Y. B. Rao, K. K. Bharathi and L. N. Patro, *Solid State Ionics*, 2021, **366–367**, 115671.

88 S. D. Choi and J. W. Park, *Sensors Mater.*, 1996, **8**, 505–511.

89 J. S. Lee, C. M. Chang, Y. Il Lee, J. H. Lee and S. H. Hong, *J. Am. Ceram. Soc.*, 2004, **87**, 305–307.

90 Z. Yang, B. Tang, Z. Xie and Z. Zhou, *ChemElectroChem*, 2021, **8**, 1035–1047.

91 R. O. Fuentes, F. M. Figueiredo, M. R. Soares and F. M. B. Marques, *J. Eur. Ceram. Soc.*, 2005, **25**, 455–462.

92 M. Guin, F. Tietz and O. Guillon, *Solid State Ionics*, 2016, **293**, 18–26.

93 O. Guillon, J. Gonzalez-Julian, B. Dargatz, T. Kessel, G. Schierning, J. Räthel and M. Herrmann, *Adv. Eng. Mater.*, 2014, **16**, 830–849.

94 G. Lee, E. A. Olevsky, C. Manière, A. Maximenko, O. Izhvanov, C. Back and J. McKittrick, *Acta Mater.*, 2018, **144**, 524–533.

95 F. Lalère, J. B. Leriche, M. Courty, S. Boulineau, V. Viallet, C. Masquelier and V. Seznec, *J. Power Sources*, 2014, **247**, 975–980.

96 S. Zhang, B. Quan, Z. Zhao, B. Zhao, Y. He and W. Chen, *Mater. Lett.*, 2004, **58**, 226–229.

97 A. Essoumhi, C. Favotto, M. Mansori and P. Satre, *J. Solid State Chem.*, 2004, **177**, 4475–4481.

98 A. Ignaszak, P. Pasierb, R. Gajerski and S. Komornicki, *Thermochim. Acta*, 2005, **426**, 7–14.

99 Y. B. Rao and L. N. Patro, *Mater. Lett.*, DOI:10.1016/j.matlet.2021.130267.

100 H. Park, K. Jung, M. Nezafati, C. Kim and B. Kang, *ACS Appl. Mater. Interfaces*, 2016, **8**, 27814–27824.

101 S. He, Y. Xu, Y. Chen and X. Ma, *J. Mater. Chem. A*, 2020, **8**, 12594–12602.

102 A. Tang, C. Yang and P. Hu, *J. Phys. Conf. Ser.*, 2022, **2351**, 4–10.

103 M. K. Chong, Z. Zainuddin, F. S. Omar and M. H. H. Jumali, *Ceram. Int.*, 2022, **48**, 22147–22154.

104 S. Narayanan, S. Reid, S. Butler and V. Thangadurai, *Solid State Ionics*, 2019, **331**, 22–29.

105 M. Kimura, K. T. Tseng, J. Wolfenstine and J. Sakamoto, *Solid State Ionics*, 2024, **411**, 116561.

106 R. Griffin, K. Hooper, C. Charbonneau and J. Baker, *Johnson Matthey Technol. Rev.*, 2021, **66**, 32–43.

107 S. Wünscher, R. Abbel, J. Perelaer and U. S. Schubert, *J. Mater. Chem. C*, 2014, **2**, 10232–10261.

108 D. Bryant, I. Mabbett, P. Greenwood, T. Watson, M. Wijdekop and D. Worsley, *Org. Electron.*, 2014, **15**, 1126–1130.

109 C. Wen, Z. Luo, H. Liang, X. Liu, W. Lei and A. Lu, *Appl. Phys. A Mater. Sci. Process.*, 2022, **128**, 1–12.

110 R. O. Fuentes, F. M. Figueiredo, F. M. B. Marques and J. I. Franco, *Solid State Ionics*, 2001, **140**, 173–179.

111 K. Kwatek, W. Ślubowska, J. L. Nowiński, A. T. Krawczyńska, I. Sobrados and J. Sanz, *Materials (Basel).*, 2021, **14**, 5729.

112 W. H. Sutton and W. A. Johnson, 1980, 311–320.

113 F. Tietz, *AIMS Mater. Sci.*, 2017, **4**, 1305–1318.

114 W. Lan, D. Lu, R. Zhao and H. Chen, *Int. J. Electrochem. Sci.*, 2019, **14**, 9695–9703.

115 J. M. McKittrick, University of Colorado, 1988.

116 J. A. S. Oh, L. He, A. Plewa, M. Morita, Y. Zhao, T. Sakamoto, X. Song, W. Zhai, K. Zeng and L. Lu, *ACS Appl. Mater. Interfaces*, 2019, **11**, 40125–40133.

117 R. O. Fuentes, F. M. B. Marques and J. I. Franco, *Bol. Soc. Esp. Cerám. Vidr.*, 1999, **38**, 631–634.

118 M. Borlaf and R. Moreno, *Open Ceram.*, 2021, **8**, 100200.

119 C. J. Brinker and G. W. Scherer, *Sol-gel science: the physics and chemistry of sol-gel processing*, Academic press, 2013.

120 B. E. Yoldas and I. K. Lloyd, *Mater. Res. Bull.*, 1983, **18**, 1171–1177.

121 A. K. Cheetham and C. F. Mellot, *Chem. Mater.*, 1997, **9**, 2269–2279.

122 P. Porkodi, V. Yegnaraman, P. Kamaraj, V. Kalyanavalli and D. Jeyakumar, *Chem. Mater.*, 2008, **20**, 6410–6419.

123 N. Y. Turova, E. P. Turevskaya, V. G. Kessler and M. I. Yanovskaya, Eds., Springer US, Boston, MA, 2002, pp. 107–125.

124 Y. Shimizu and T. Ushijima, 2000, **132**, 143–148.

125 M. E. D. Z. Rodrigo F. Silva*, *Thin Solid Films*, 2004, **449**, 86–93.

126 L. L. Hench and J. O. N. K. West, 1990, 33–72.

127 D. A. Skoog, D. M. West, F. J. Holler and S. R. Crouch, *Fundamentals of analytical chemistry*, Saunders College Pub. Fort Worth, 1996, vol. 33.

128 S. D. Burnside, V. Shklover, C. A. Barbe, K. Brooks, P. Comte, F. Arendse-Duriaux, M. Jirousek and M. Graetzel, *Mater. Res. Soc. Symp. - Proc.*, 1998, **519**, 59–64.

129 M. I. Tejedor-Tejedor, F. M. Vichi and M. A. Anderson, *J. Porous Mater.*, 2005,

12, 201–214.

130 J. G. Mahy, F. Deschamps, V. Collard, C. Jérôme, J. Bartlett, S. D. Lambert and B. Heinrichs, *J. Sol-Gel Sci. Technol.*, 2018, **87**, 568–583.

131 R. C. Bhave and B. I. Lee, *Mater. Sci. Eng. A*, 2007, **467**, 146–149.

132 L. Luan, S. Liu and D. Sun, *J. Solid State Chem.*, 2009, **182**, 1462–1467.

133 Y. Shimizu, Y. Azuma and S. Michishita, *J. Mater. Chem.*, 1997, **7**, 1487–1490.

134 Y. Shimizu, S. Michishita and T. Murata, *Jpn. J. Appl. Phys.*, 1995, **34**, L833–L836.

135 Y. Shimizu, S. Michishita and T. M. Takahiro Murata, *Jpn. J. Appl. Phys.*, 1995, **34**, L833.

136 P. Jiang, G. Du, Y. Shi, F. She, P. Guo, G. Qian, X. Lu, F. Xie and X. Lu, *Chem. Eng. J.*, 2023, **451**, 138771.

137 X. Wang, Z. Liu, Y. Tang, J. Chen, D. Wang and Z. Mao, *J. Power Sources*, 2021, **481**, 228924.

138 J. Perelaer, R. Abbel, S. Wünscher, R. Jani, T. Van Lammeren and U. S. Schubert, *Adv. Mater.*, 2012, **24**, 2620–2625.

139 M. J. Carnie, C. Charbonneau, P. R. F. Barnes, M. L. Davies, I. Mabbett, T. M. Watson, B. C. O'Regan and D. A. Worsley, *J. Mater. Chem. A*, 2013, **1**, 2225–2230.

140 K. Hooper, M. Carnie, C. Charbonneau and T. Watson, *Int. J. Photoenergy*, DOI:10.1155/2014/953623.

141 I. Mabbett, J. Elvins, C. Gowenlock, C. Glover, P. Jones, G. Williams and D. Worsley, *Prog. Org. Coatings*, 2014, **77**, 494–501.

142 C. Charbonneau, K. Hooper, M. Carnie, J. Searle, B. Philip, D. Wragg, T. Watson and D. Worsley, *Prog. Photovoltaics Res. Appl.*, 2014, **22**, 1267–1272.

143 D. A. Brennan, Swansea University, 2018.

144 S. J. Potts, Y. C. Lau, T. Dunlop, T. Claypole and C. Phillips, *J. Mater. Sci.*, 2019, **54**, 8163–8176.

145 F. Jeschull, D. Brandell, M. Wohlfahrt-Mehrens and M. Memm, *Energy Technol.*, 2017, **5**, 2108–2118.

146 F. C. Krebs, R. Søndergaard and M. Jørgensen, *Sol. Energy Mater. Sol. Cells*, 2011, **95**, 1348–1353.

147 J. Troughton, M. J. Carnie, M. L. Davies, C. Charbonneau, E. H. Jewell, D. A. Worsley and T. M. Watson, *J. Mater. Chem. A*, 2016, **4**, 3471–3476.

148 J. Troughton, C. Charbonneau, M. J. Carnie, M. L. Davies, D. A. Worsley and T. M. Watson, *J. Mater. Chem. A*, 2015, **3**, 9123–9127.

149 A. Sandmann, C. Notthoff and M. Winterer, *J. Appl. Phys.*, 2013, **113**, 1–6.

150 Y. Oh, S.-N. Lee, H.-K. Kim and J. Kim, *J. Electrochem. Soc.*, 2012, **159**, H777–

H781.

151 H. J. Hwang and H. S. Kim, *J. Nanosci. Nanotechnol.*, 2015, **15**, 5028–5034.

152 R. Danaei, T. Varghese, M. Ahmadzadeh, J. McCloy, C. Hollar, M. Sadeq Saleh, J. Park, Y. Zhang and R. Panat, *Adv. Eng. Mater.*, 2019, **21**, 1–6.

153 R. Dharmadasa, B. Lavery, I. M. Dharmadasa and T. Druffel, *ACS Appl. Mater. Interfaces*, 2014, **6**, 5034–5040.

154 R. Dharmadasa, I. M. Dharmadasa and T. Druffel, *Adv. Eng. Mater.*, 2014, **16**, 1351–1361.

155 S. R. Dhage, H. S. Kim and H. T. Hahn, *J. Electron. Mater.*, 2011, **40**, 122–126.

156 H. S. Kim, S. R. Dhage, D. E. Shim and H. T. Hahn, *Appl. Phys. A Mater. Sci. Process.*, 2009, **97**, 791–798.

157 S. H. Park, W. H. Chung and H. S. Kim, *J. Mater. Process. Technol.*, 2014, **214**, 2730–2738.

158 D. J. Lee, S. H. Park, S. Jang, H. S. Kim, J. H. Oh and Y. W. Song, *J. Micromechanics Microengineering*, 2011, **21**, 1–7.

159 S. H. Park and H. S. Kim, *Thin Solid Films*, 2014, **550**, 575–581.

160 D. Tobjörk, H. Aarnio, P. Pulkkinen, R. Bollström, A. Määttänen, P. Ihalainen, T. Mäkelä, J. Peltonen, M. Toivakka, H. Tenhu and R. Österbacka, *Thin Solid Films*, 2012, **520**, 2949–2955.

161 A. Denneulin, A. Blayo, C. Neuman and J. Bras, *J. Nanoparticle Res.*, 2011, **13**, 3815–3823.

162 K. Hooper, Swansea University, 2014.

163 J. Baker, K. Hooper, S. Meroni, A. Pockett, J. McGettrick, Z. Wei, R. Escalante, G. Oskam, M. Carnie and T. Watson, *J. Mater. Chem. A*, 2017, **5**, 18643–18650.

164 S. H. Huang, C. K. Guan, P. H. Lee, H. C. Huang, C. F. Li, Y. C. Huang and W. F. Su, *Adv. Energy Mater.*, 2020, **10**, 1–9.

165 A. Ahmad, C. Glasgow and T. A. Wheat, *Solid State Ionics*, 1995, **76**, 143–154.

166 Y. L. Huang, A. Caneiro, M. Attari and P. Fabry, *Thin Solid Films*, 1991, **196**, 283–294.

167 H. Perthuis, G. Velasco and P. Colomban, *Jpn. J. Appl. Phys.*, 1984, **23**, 534.

168 S. Mudenda and G. M. Kale, *J. Mater. Chem. A*, 2015, **3**, 12268–12275.

169 M. Sozak, T. Nazarenus, J. Exner, J. Kita and R. Moos, *J. Mater. Sci.*, 2023, **58**, 10108–10119.

170 R. Inada, K. ichi Ishida, M. Tojo, T. Okada, T. Tojo and Y. Sakurai, *Ceram. Int.*, 2015, **41**, 11136–11142.

171 J. Exner, T. Nazarenus, D. Hanft, J. Kita and R. Moos, *Adv. Mater.*, DOI:10.1002/adma.201908104.

172 R. Griffin, K. Hooper, C. Charbonneau and J. Baker, *Johnson Matthey Technol. Rev.*, 2022, **66**, 32–43.

173 D. D. Le Pevelen, in *Encyclopedia of Spectroscopy and Spectrometry*, ed. J. C. B. T.-E. of S. and S. (Second E. Lindon, Elsevier, Oxford, 2010, pp. 2559–2576.

174 H. Gao and J. B. Goodenough, *Angew. Chemie*, 2016, **128**, 12960–12964.

175 S. Naqash, Q. Ma, F. Tietz and O. Guillon, *Solid State Ionics*, 2017, **302**, 83–91.

176 K. Qiao, T. Zhang, K. Wang, S. Yuan, S. Zhang, L. Wang, Z. Wang, P. Peng, J. Cai, C. Liu and W. Wang, *Front. Bioeng. Biotechnol.*, 2021, **9**, 1–16.

177 T.-H. Le, D. T. T. Le and N. Van Tung, *J. Chem.*, 2021, **2021**, 1–9.

178 A. Ghule, R. Murugan and H. Chang, *Thermochim. Acta*, 2001, **371**, 127–135.

179 D. K. Smith and W. Newkirk, *Acta Crystallogr.*, 1965, **18**, 983–991.

180 C. A. Fyfe, H. Gies, G. T. Kokotailo, C. Pasztor, H. Strobl and D. E. Cox, *J. Am. Chem. Soc.*, 1989, **111**, 2470–2474.

181 P. H. Wei, *Zeitschrift fuer Krist. Krist. Krist. Krist.*, 1935, **92**, 355–362.

182 J. R. Chelikowsky, H. E. King and J. Glinnemann, *Phys. Rev. B*, 1990, **41**, 10866–10869.

183 A. . Belik, A. A.; Bykov, A.B.; Ivanov-Shits, A.K.; Verin, I.A.; Golubev, A.M.; Nistyuk, *Crystallogr. Reports*, 2000, **45**, 902.

184 A. A. Voronkov, N. G. Shumyatskaya and Y. A. Pyatenko, *J. Struct. Chem.*, 1971, **11**, 866–867.

185 P. Rudolf, A. Clearfield and J. Jorgensen, *Solid State Ionics*, 1986, **21**, 213–224.

186 K. R. Whittle, G. R. Lumpkin and S. E. Ashbrook, *J. Solid State Chem.*, 2006, **179**, 512–521.

187 H. Fukui, M. Fujimoto, Y. Akahama, A. Sano-Furukawa and T. Hattori, *Acta Crystallogr. Sect. B Struct. Sci. Cryst. Eng. Mater.*, 2019, **75**, 742–749.

188 M. B. Boisen, G. V Gibbs and M. S. T. Bukowinski, *Phys. Chem. Miner.*, 1994, **21**, 269–284.

189 Y. Zhao, Z. Liu, J. Xu, T. Zhang, F. Zhang and X. Zhang, 2019, **783**, 219–225.

190 R. Inada, K. Kimura, K. Kusakabe, T. Tojo and Y. Sakurai, *Solid State Ionics*, 2014, **261**, 95–99.

191 J. P. Boilot, G. Collin and P. Colomban, *Mater. Res. Bull.*, 1987, **22**, 669–676.

192 M. Amores, T. E. Ashton, P. J. Baker, E. J. Cussen and S. A. Corr, *J. Mater. Chem. A*, 2016, **4**, 1729–1736.

193 B. H. Toby, *Powder Diffr.*, 2006, **21**, 67–70.

194 L. B. McCusker, R. B. Von Dreele, D. E. Cox, D. Louër and P. Scardi, *J. Appl. Crystallogr.*, 1999, **32**, 36–50.

195 K. Hayashi, K. Shima and F. Sugiyama, *J. Electrochem. Soc.*, 2013, **160**, A1467–

A1472.

196 N. S. Bell, C. Edney, J. S. Wheeler, D. Ingersoll and E. D. Spoerke, *J. Am. Ceram. Soc.*, 2014, **97**, 3744–3748.

197 P. Bouvier, E. Djurado, G. Lucazeau and T. Le Bihan, *Phys. Rev. B*, 2000, **62**, 8731–8737.

198 D. Wang, Y. Guo, K. Liang and K. Tao, *Sci. China Ser. A Math.*, 1999, **42**, 80–86.

199 A. Tiliakos, M. Iordache and A. Marinoiu, *Appl. Sci.*, 2021, **11**, 8432.

200 J. Amaro-Gahete, D. Esquivel, J. R. Ruiz, C. Jiménez-Sanchidrián and F. J. Romero-Salguero, *Appl. Catal. A Gen.*, 2019, **585**, 117190.

201 Y. Ruan, S. Song, J. Liu, P. Liu, B. Cheng, X. Song and V. Battaglia, *Ceram. Int.*, 2017, **43**, 7810–7815.

202 S. Bai, M. Cao, Y. Jin, X. Dai, X. Liang, Z. Ye, M. Li, J. Cheng, X. Xiao, Z. Wu, Z. Xia, B. Sun, E. Wang, Y. Mo, F. Gao and F. Zhang, *Adv. Energy Mater.*, DOI:10.1002/aenm.201301460.

203 C. J. Howard, R. J. Hill and B. E. Reichert, *Acta Crystallogr. Sect. B Struct. Sci.*, 1988, **44**, 116–120.

204 J. Newsam, A. Cheetham and B. Tofield, *Solid State Ionics*, 1980, **1**, 377–393.

205 H. Kohler and H. Schulz, *Mater. Res. Bull.*, 1985, **20**, 1461–1471.

206 M. Winterer, R. Delaplane and R. McGreevy, *J. Appl. Crystallogr.*, 2002, **35**, 434–442.

207 M. Schreyer, L. Guo, S. Thirunahari, F. Gao and M. Garland, *J. Appl. Crystallogr.*, 2014, **47**, 659–667.

208 M. Winterer, R. Delaplane and R. McGreevy, *J. Appl. Crystallogr.*, 2002, **35**, 434–442.

209 L. Lutterotti and P. Scardi, *J. Appl. Crystallogr.*, 1990, **23**, 246–252.

210 A. Kaliyaraj Selva Kumar, Y. Zhang, D. Li and R. G. Compton, *Electrochem. commun.*, 2020, **121**, 106867.

211 M. A. Sawhney and J. Baker, *Coatings*, DOI:10.3390/coatings13040689.

212 M. Matinfar and J. A. Nychka, *Adv. Colloid Interface Sci.*, 2023, **322**, 103036.

213 P. Vulic, V. Kahlenberg and J. Konzett, *Am. Mineral.*, 2008, **93**, 1072–1079.

214 J. H. Konnert and D. E. Appleman, *Acta Crystallogr. Sect. B Struct. Crystallogr. Cryst. Chem.*, 1978, **34**, 391–403.

215 R. T. Downs and D. C. Palmer, *Am. Mineral.*, 1994, **79**, 9–14.

216 P. R. Rudolf, A. Clearfield and J. D. Jorgensen, *J. Solid State Chem.*, 1988, **72**, 100–112.

217 S. Lee and H. Xu, *Acta Crystallogr. Sect. B Struct. Sci. Cryst. Eng. Mater.*, 2019, **75**, 160–167.

218 W. H. Baur and A. A. Khan, *Acta Crystallogr. Sect. B Struct. Crystallogr. Cryst. Chem.*, 1971, **27**, 2133–2139.

219 W. W. Van Den Hoogenhof and D. K. G. De Boer, *Spectrochim. Acta Part B At. Spectrosc.*, 1993, **48**, 277–284.

220 N. Igawa and Y. Ishii, *J. Am. Ceram. Soc.*, 2001, **84**, 1169–1171.

221 H.-W. Wang and D. L. Bish, *Am. Mineral.*, 2008, **93**, 1191–1194.

222 P. Dera, J. D. Lazarz, V. B. Prakapenka, M. Barkley and R. T. Downs, *Phys. Chem. Miner.*, 2011, **38**, 517–529.

223 P. Dubertret, A.; Lehr, *Comptes Rendus des Seances l'Academie des Sci.*, 1968, **Serie C**, 820–822.

224 P. Trucano and R. Chen, *Nature*, 1975, **258**, 136–137.

225 H. Ott, *Naturwissenschaften*, 1925, **13**, 319–319.

226 K. Aigner, W. Lengauer, D. Rafaja and P. Ettmayer, *J. Alloys Compd.*, 1994, **215**, 121–126.